

# Wideband focal-plane arrays with improved scanning capabilities

***Citation for published version (APA):***

Dubok, A. (2023). *Wideband focal-plane arrays with improved scanning capabilities*. [Phd Thesis 1 (Research TU/e / Graduation TU/e), Electrical Engineering]. Eindhoven University of Technology.

***Document status and date:***

Published: 13/04/2023

***Document Version:***

Publisher's PDF, also known as Version of Record (includes final page, issue and volume numbers)

***Please check the document version of this publication:***

- A submitted manuscript is the version of the article upon submission and before peer-review. There can be important differences between the submitted version and the official published version of record. People interested in the research are advised to contact the author for the final version of the publication, or visit the DOI to the publisher's website.
- The final author version and the galley proof are versions of the publication after peer review.
- The final published version features the final layout of the paper including the volume, issue and page numbers.

[Link to publication](#)

***General rights***

Copyright and moral rights for the publications made accessible in the public portal are retained by the authors and/or other copyright owners and it is a condition of accessing publications that users recognise and abide by the legal requirements associated with these rights.

- Users may download and print one copy of any publication from the public portal for the purpose of private study or research.
- You may not further distribute the material or use it for any profit-making activity or commercial gain
- You may freely distribute the URL identifying the publication in the public portal.

If the publication is distributed under the terms of Article 25fa of the Dutch Copyright Act, indicated by the "Taverne" license above, please follow below link for the End User Agreement:

[www.tue.nl/taverne](http://www.tue.nl/taverne)

***Take down policy***

If you believe that this document breaches copyright please contact us at:

[openaccess@tue.nl](mailto:openaccess@tue.nl)

providing details and we will investigate your claim.

# Wideband focal-plane arrays with improved scanning capabilities

Aleksei Dubok

This research was financially supported by NWO-TTW as part of the FREEBEAM OTP project nr. 12409.

A catalog record is available from the Eindhoven University of Technology Library.

Title: Wideband Focal-Plane-Arrays with improved scanning capabilities

Author: Aleksei Dubok

Eindhoven University of Technology, 2023 - Proefschrift

ISBN: 978-90-386-5708-0

NUR: 959

Cover design: Aleksei Dubok

Copyright ©2023 by Aleksei Dubok

All rights reserved. No part of this publication may be reproduced, stored in a retrieval system, or transmitted in any form or by any means without the prior written consent of the author.

# Wideband focal-plane arrays with improved scanning capabilities

## PROEFSCHRIFT

ter verkrijging van de graad van doctor aan de Technische  
Universiteit Eindhoven, op gezag van de rector magnificus  
prof.dr.ir. F.P.T. Baaijens,  
voor een commissie aangewezen door het College voor  
Promoties, in het openbaar te verdedigen  
op donderdag 13 april 2023 om 13:30 uur

door

Aleksei Dubok

geboren te Pskov, Rusland

Dit proefschrift van het proefontwerp is goedgekeurd door de promotoren en de samenstelling van de promotiecommissie is als volgt:

voorzitter:	prof.dr.ir. P.H.N. de With
1 <sup>e</sup> promotor:	prof.dr.ir. A.B. Smolders
2 <sup>e</sup> promotor:	prof.dr.ir. G. Gerini
leden:	prof. dr. M. Ivashina (Chalmers University)
	prof.ir. A.M.J. Koonen
	prof.dr.ir. P.G.M. Baltus
	prof.dr.ir. M.J. Bentum

*Het onderzoek of ontwerp dat in dit proefschrift wordt beschreven is uitgevoerd in overeenstemming met de TU/e Gedragscode Wetenschapsbeoefening.*

To my wife  
To my son  
To my parents



# CONTENTS

---

Contents .....	7
Summary .....	11
List of Abbreviations and Symbols .....	13
1. Introduction .....	19
2. Focal Plane Arrays .....	25
2.1. History of FPA.....	25
2.2. FPA concept versus phased arrays.....	25
2.3. Features and applications of FPAs.....	27
2.4. Challenges of modern FPAs .....	30
2.5. Optical beamforming for FPAs.....	31
3. FPA: Design Framework.....	33
3.1. Array design challenges <sup>1</sup> .....	33
3.1.1. Introduction.....	33
3.1.2. Wideband limit for antenna design .....	34
3.1.3. Design of wideband array element.....	35
3.1.4. Additional bandwidth improvement .....	36
3.1.5. Focal-plane arrays.....	39
3.1.6. Conclusion .....	42
3.2. Reflector for narrow-range scanning <sup>1</sup> .....	43
3.2.1. Introduction.....	43
3.2.2. Illumination limitations of classical prime-focus FPAs .....	44
3.2.3. Double parabolic reflector configuration .....	47
3.2.4. Optimization of double reflector configuration for FPA.....	49
3.2.5. Conclusion .....	53
3.3. Reflector theory and reflector for wide range application <sup>1</sup> .....	55
3.3.1. Introduction.....	55
3.3.2. Mathematical model of reflector .....	55
3.3.3. Reflector comparison .....	56
3.3.4. Conclusion .....	58

4.	Reflector synthesis for Wide-Scanning Focal Plane Arrays <sup>1</sup> .....	59
4.1.	Introduction.....	59
4.2.	Limitations of classical parabolic prime-focus reflectors and ideal array illumination .....	61
4.3.	Mathematical principles of reflector synthesis based on geometrical optics .....	65
4.3.1.	Two-dimensional center-fed single-reflector model .....	65
4.3.2.	Two-dimensional center-fed double-reflector model.....	70
4.3.3.	Three-dimensional offset single-reflector model .....	72
4.3.4.	Three-dimensional offset double-reflector model.....	75
4.4.	Optimization of single and double-reflector configurations .....	77
4.4.1.	Axially symmetric single reflector .....	78
4.4.2.	Axially symmetric double-reflector .....	80
4.4.3.	Offset single reflector.....	84
4.4.4.	Offset double reflector .....	85
4.4.5.	Comparison of all configurations .....	89
4.5.	Experimental validation .....	92
4.6.	Conclusion .....	98
4.7.	Extreme Scanning Double Shaped-Reflector Antenna with Multiple Interactions for Focal Plane Array applications <sup>1</sup> .....	99
4.7.1.	Introduction .....	99
4.7.2.	Illumination challenges for conventional FPAs .....	100
4.7.3.	Reflector system with double sub-reflector interaction.....	101
4.7.4.	Conclusions .....	108
5.	FPA Design and Implementation .....	109
5.1.	Arrays investigation <sup>1</sup> .....	109
5.1.1.	Introduction .....	109
5.1.2.	Wideband array design.....	109
5.1.3.	3D wideband focal plane connected-array concept.....	113
5.1.4.	Conclusions .....	118
5.2.	Wideband Phased-Array Feeds for Focal Plane Arrays: Design and Implementation <sup>1</sup> .....	119
5.2.1.	Introduction .....	119
5.2.2.	Design Challenges of wideband antenna elements for PAFs .....	120
5.2.3.	Integration of wideband PAFs and reflectors.....	122
5.2.3.1.	PAFs total radiation efficiency and active wideband performance using a classical prime-focus reflector.....	122

5.2.3.2.	The reflector aperture efficiency in the case of a classical prime-focus reflector .....	126
5.2.4.	FPA prototyping and measurements .....	129
5.2.4.1.	Array prototypes for probe measurements of the (passive) input reflection coefficients .....	130
5.2.4.2.	Array prototypes with mini SMP connectors for element pattern measurements.....	135
5.2.4.3.	Evaluation of the active wideband performance of the PAF with the classical prime-focus reflector and the complex offset double-reflector system.....	142
5.2.4.4.	Far-field pattern measurements of the complex offset double-reflector fed by modified bow-tie antennas .....	148
5.2.5.	FPA system capability .....	153
5.2.5.1.	FPA system analysis .....	154
5.2.5.2.	Equivalent phased-array configuration .....	158
5.2.6.	Conclusions .....	161
6.	FPA demonstrator <sup>1, 2</sup> .....	163
6.1.	Introduction .....	163
6.2.	Overall system concept.....	165
6.3.	Broadband wide-scan focal-plane arrays .....	167
6.4.	Optical beamforming using ring resonators.....	168
6.5.	Active phased-array feed using low-noise amplifiers with a large dynamic range .....	170
6.6.	System demonstrator .....	173
6.7.	Conclusions and future research directions .....	175
7.	Focal-Plane Arrays with Improved Scan Capabilities <sup>1</sup> .....	177
7.1.	Introduction .....	177
7.2.	Double-reflector antenna with improved scan capabilities .....	179
7.2.1.	Multi-variable optimization goal .....	182
7.2.2.	Maximization of EIRP within the defined scan range .....	185
7.2.3.	Minimum RATA .....	187
7.2.4.	Maximization of EIRP and the minimum RATA .....	190
7.2.5.	Array size minimization .....	192
7.2.6.	Summary of optimizations.....	194
7.3.	Array size minimization for different sub-reflector sizes .....	195
7.4.	Array size minimization for two-dimensional scanning .....	200
7.5.	Conclusion .....	207
8.	Conclusion and recommendations.....	209

---

8.1.	Thesis overview .....	209
8.2.	Recommendations.....	211
	Bibliography .....	215
	List of publications.....	229
	Acknowledgments.....	233
	Curriculum Vitae.....	235

## SUMMARY

---

In the past decades, focal-plane arrays (FPAs) have become an interesting alternative to conventional horn-fed reflector antennas in a number of applications, e.g. in radio astronomy and Ka-band satellite communications.

The presented work has been performed as part of the NWO FREEBEAM project: fiber to RF-FREEspace multiBEAM converter. This project investigated novel multi-beam wideband antenna systems with optical beamforming. The aim of the project has been to develop a hybrid system using an FPA that combines the benefits of phased arrays and traditional reflector-based solutions. In addition, a novel optical interface to the FPA was used, which provides an ultra-wideband interface and a compact versatile solution enabling fast beam steering. The main applications are radio astronomy, satellite communications, satellite TV, broadband internet via satellite, 5G/6G point-to-point wireless communications, and low-cost Ka-band (30-40 GHz) multi-function radar. For the next generation of radio astronomy, FPAs offer high sensitivity in combination with a large field of view (FoV) at a relatively low price.

One of the fundamental limitations of FPAs is the small number of simultaneously active array elements limiting the achievable effective isotropic radiated power (EIRP). A low EIRP level limits the use of low-cost silicon integrated circuits. In addition, it is an issue to realize wide-angle scanning, which is related to the challenge to provide a proper exposure of the FPA even for relatively small scan angles of the main beam, due to the significant beam deviation in the focal plane. Moreover, there are bandwidth limitations related to mutual coupling between array elements. Therefore, in this work, various reflector configurations have been investigated in order to improve the FPA illumination and increase the number of simultaneously active elements, during beam scanning over a wide instantaneous bandwidth. At the same time, array designs with improved active impedance matching performance and reflector illumination have been investigated and realized including the integration with a low noise amplifier (LNA).

A new concept for optimal array illumination by the reflector has been proposed. The idea is based on increasing the number of active elements of the FPA in order to overcome the main limitation of conventional FPA systems in which only a very small region in the focal plane is illuminated and the necessity to achieve a uniform distribution of power and phase along the array elements, which is required for optical beamforming. This allows for an increase in the achievable EIRP and system sensitivity.

We have developed reflector optimization software based on geometrical optics which was used to achieve one of the main project challenges: wide-angle scanning with a reflector up to  $\pm 20^\circ$  in the azimuth plane with potential capacity to operate in the scan range up to  $\pm 30^\circ$  in azimuth and  $\pm 3^\circ$  in elevation. Different single and double reflector configurations systems have been optimized for this purpose and verified with commercial software. The final double-reflector configuration achieves the required scanning range with a compact

array of which almost half of the array elements are active during scanning. The scanning capabilities have been significantly improved as compared to classical prime focus and double-parabolic reflectors. The phase linearity between the array elements has been sufficiently improved in order to use optical beamforming.

Consequently, the co-design of arrays and reflectors has been investigated in the frame of this project in order to use the full capability of the wideband antenna and wide-scan range reflector and to avoid integration problems that could result in a limited active frequency band during FPA scanning. As a result, the proposed wideband array of modified bow-tie antennas with the complex double-reflector provides high radiation efficiency and shows an active frequency bandwidth of more than one octave (20 - 40 GHz) within  $\pm 20^\circ$  azimuth scan. Two types of high-efficient array configurations have been implemented in a 3D EM simulation software tool, namely the connected array and a conventional one. Those results have been successfully confirmed by several experimental validations in the near-field test facility of the Eindhoven University of Technology.

# LIST OF ABBREVIATIONS AND SYMBOLS

---

5G	5 <sup>th</sup> Generation mobile communications
5G-NR	5G-NR radio access technology for the 5G
6G	6 <sup>th</sup> Generation mobile communications
AF	Array Factor
ARC	Active reflection coefficient
BiCMOS	Bipolar Complementary Metal Oxide Semiconductor
CE	Common-emitter
CW	Continuous wave
DAC	Digital-to-analog
DM-MIMO	Distributed massive MIMO
EF	Element Factor
EIRP	Effective Isotropic Radiated Power
EM	Electromagnetic
EM	External modulator
EMI	Electromagnetic interference
FEM	Finite Element Method
FIT	Finite Integration Technique
FoV	Field of View
FPA	Focal-plane array
FREEBEAM	Fiber to RF-FREEspace multiBEAM converter
GO	Geometrical optics
HCC	Home communication controller
ICs	Integrated circuits
LNA	Low-noise amplifier
MIMO	Multiple-Input-Multiple-Output
mm-wave	Millimeter-wave

MOM	Method of moments
MZM	Mach-Zehnder modulator
NLOS	Non-line-of-sight
Oas	Optical amplifiers
ORR	Optical micro-ring resonator
OSBF	Optical Sideband Filter
PA	Power Amplifier
PAF	Phased-array feed
PC	Polarization controllers
PIC	Photonic integrated circuit
PO	Physical optics
RATA	Ratio of active versus total number of array elements
RMS	Root-mean-square
RX	Receiver
SF	Sub-array Factor
SiGe	Silicon-germanium
SLL	Side Lobe Levels
TARC	Total active antenna reflection coefficient
TE	Transverse electric
TE	Transverse electromagnetic
TEC	Thermo-electric cooling
TTD	True-time-delay
TX	Transmitter
VNA	Vector Network Analyzer

## List of Symbols

Symbol	Description
$\epsilon_0$	free-space dielectric constant
$\epsilon$	relative permittivity of the dielectric
$k$	wavenumber
$c$	speed of light
$f_0$	central operating frequency
$\Delta f$	frequency band
$\lambda$	free-space wavelength
$\lambda_0$	free-space wavelength at the central operating frequency
$J_1$	Bessel function of the first kind
$r$	aperture radius
$E$	electric field distribution
$\eta$	total antenna radiation efficiency
$\eta(r)$	aperture efficiency
$a$	maximum antenna size
$Q$	quality factor
$B$	relative bandwidth
$C$	capacitance
$S$	area of overlap of the two plates
$d$	separation between the plates
$Z_0$	free space impedance
$P_{tot}$	total power
$A_{ij}$	polynomial coefficients
$\alpha$	angle of incidence
$\tan(\alpha)$	tangent of the angle of the incident wave
$\beta$	the angle of incidence, reflector elevation incline
$\Psi$	feeding angle of the array
$D$	reflector diameter
$D_s$	sub-reflector diameter
$S(x, y, z)$	reflector surface

---

$S_s(x, y, z)$	sub-reflector surface
$M$	magnification factor
$F$	reflector focal length
$F_a$	array plane position
$L_y$	size of the array along the ydirection-direction
$B_{ij}$	sub-reflector polynomial coefficients
$Dy_s$	size of the sub-reflector in the $xy$ -plane
$Dz_s$	size of the sub-reflector in the $xz$ -plane
$z_s$	shift in the polynomial function of the sub-reflector along the $z$ -coordinate
$y_s$	shift in the polynomial function of the sub-reflector along the $y$ -coordinate
$z_b$	vertical offset between the array and reflector
$z_{\text{off}}$	reflector clearance height, the offset distance
$z_{s0}$	shift of reflector polynomial function along the $z$ -coordinate
$\Delta_y$	shift of sub-reflector polynomial function along the $y$ -coordinate
$\Delta_z$	shift of sub-reflector polynomial function along the $z$ -coordinate
$y_s$	shift of sub-reflector along the $y$ -coordinate
$z_s$	shift of sub-reflector along the $z$ -coordinate
$\theta$	angle of incidence of the incident field
$\theta_0$	incident angle on the array surface
$F_m$	focal length of the main reflector
$D_m$	diameter of the main reflector
$z_c$	array position along the $z$ -coordinate
$S_{mn}$	scattering coefficient between element $m$ and $n$ array element
$R_m$	active reflection coefficient
$a_n$	excitation vector
$M$	number of array elements
$N$	number of array elements
$d_x$	distance between array elements
$T$	total active antenna reflection coefficient
$M$	coefficient related to the Miller effect
$Z_{IN}$	input impedance

---

$R_{EQ}$	equivalent resistance
$\omega_C$	radial frequency
$\Gamma_{IN}$	reflection coefficient
$Z_S$	output impedance of the matching network
$Z_{OPT}$	optimal noise impedance of the transistor
$C_{BE}$	base-emitter capacitances
$C_{BC}$	base-collector capacitances
$R_B$	equivalent base resistance
$g_m$	trans-conductance
$L_E$	degeneration inductance



# CHAPTER ONE

## 1. INTRODUCTION

---

The continuously growing need for higher data rates in wireless communications drives new applications into the millimeter-wave (mm-wave) frequency domain. Emerging applications include base stations for 5G wireless communication, two-way satellite communication, point-to-point wireless backhaul, and commercial radar [1], [2], [3], [4]. These mm-wave applications would benefit from using advanced phased-array technologies. Phased arrays offer the ability of fast electronic beam-steering, multi-beam operation, adaptive pattern shaping, and MIMO (Multiple-Input-Multiple-Output) capabilities. However, traditional full phased-array solutions have major limitations: they are far too expensive and have a very high-power consumption due to the low efficiency of state-of-the-art mm-wave integrated circuits [5], [6]. In addition, phased arrays have high complexity and provide a limited operational bandwidth [7]. The FPA is an alternative to phased arrays, which is a hybrid solution that combines the best of both worlds: the robustness, low cost, and large bandwidth of conventional reflector-based antenna systems and the flexibility and adaptivity of phased arrays. FPAs provide electronic beam scanning over a field of view (FoV). Therefore, it has become an interesting alternative to conventional horn-fed reflector antennas.

FPAs are widely used in radio astronomy [8], satellite and point-to-point communications [9], [10], and low-cost Ka-band (30-40 GHz) multi-function radars [11]. FPAs provide a high antenna gain at low costs and allow beam scanning or multi-beam functionality [8], [12], [13]. The example of FPAs developed for the Westerbork Synthesis Radio Telescope based on a dual-polarized Vivaldi array is presented in Fig. 1.1 [14].

An interesting area of research is to investigate whether FPAs can be used to realize base stations for future mm-wave wireless communications infrastructure to meet the demands of emerging applications such as 5G-NR/6G, point-to-point wireless communications, and low-cost Ka-band (30-40 GHz) multi-function radar. Those areas could have rich possibilities for FPA implementations. These future microwave and mm-wave applications set new requirements on FPA systems such as a wide FoV covering a scan range up to  $\pm 20^\circ$ , large instantaneous bandwidth up to an octave, and a highly effective isotropic radiated power (EIRP) in transmit mode using silicon-based integrated circuits (ICs) [15].

There are a number of fundamental limits related to FPAs that need to be solved before this technology could become a widely accepted option to replace phased arrays. One of the main restrictive factors of FPAs is the limited scan range and insufficient power budget due to the limited ratio of active elements within the array [16], [17]. This leads to the necessity to use a huge number of array elements when using a traditional phased array as a feed. It is

possible to solve those issues if to design FPA systems with wide-scan capabilities. The proposed concept of this thesis demonstrates improved performance compared to conventional implementations in terms of the required number of array elements.

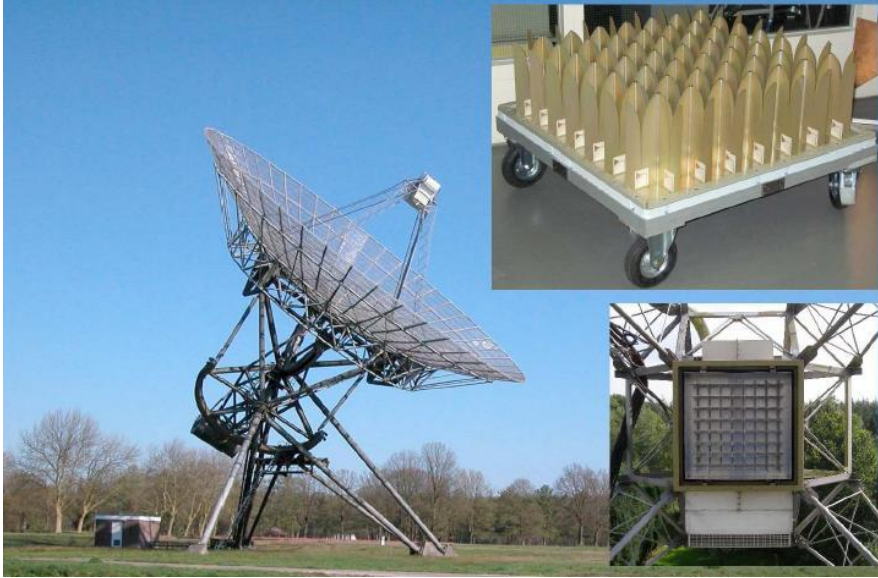


**Figure 1.1.** The WSRT telescope is equipped with a phased-array feed (PAF) using Vivaldi antenna elements. Shown in the inserts is the array in the lab (top right) and in the focal plane of the telescope (bottom right) [14].

Traditionally, reflector systems have a limited scan potential and are dedicated to applications that required high directivity within an extremely narrow angular section. Classical reflectors focus the received wavefront on a relatively small spot in the focal plane. Multi-beam operation with such reflectors is normally done by placing a few separate feeds in the focal plane (Fig. 1.2). This approach only works well over a relatively small angular range, since the point in the focal plane on which the energy is focused deviates strongly with increasing offset angle [18], [19], even for small offset angles.



**Figure 1.2.** Example of multi-beam operation with a classical reflector by placing a few separate feeds in the focal plane [20].

The use of arrays as feeds for reflector systems allows to a scan of the main beam over a wider angular range. At the same time, the focusing properties of traditional reflectors significantly deteriorate during scanning. As a result, only a small number of active array elements are typically used in the focal plane [18], [21], [22], [23]. This limits the number of simultaneously available beams or scan range [24], [25] and limits the achievable EIRP [26], [27], [28]. At the same time, the required array size grows dramatically with increased scan range requirements. Nevertheless, the array feed could compensate for the reflector defocusing to achieve a high level of EIRP over the entire scan range. At the same time, mutual reposition of the reflector and array feed, the so-called axial displacement of the array, allows to increase in the number of involved array elements within the required scan range [29]. Another important restrictive factor of existing FPA concepts is the frequency bandwidth. The demands for wideband antenna arrays and focal-plane arrays (FPA) are increasing, especially in the Ku- and Ka-band. Hence, it is necessary to make an investigation of broadband array antenna elements. At the same time, for FPAs, it is crucial to have proper reflector illumination. In order to obtain a high aperture efficiency, the array spacing needs to be close to  $\lambda_0/2$  at the highest frequency of operation [30], where  $\lambda_0$  is the free-space wavelength. As a result, the mutual coupling between the array elements is rather high and causes the active input impedance of each element to be different and highly dependent on frequency and scan angle [31], [32]. At the same time, the array element should be large enough to provide a wide bandwidth [33], which only exacerbates the situation with the mutual coupling within the array. Even for the phased array use case, where the only difference in the excitation coefficients is the phase differences between the array elements, mutual coupling significantly limits the impedance-matching bandwidth as compared to the isolated-element performance. In an FPA application, there are not only phase differences between array elements, but there is a strongly varying amplitude distribution which could lead to a further decrease in bandwidth. As a result, wideband arrays can have issues in operation when they are used as a PAF in an FPA antenna system with beam scanning. Therefore, it is necessary to investigate methods to improve both the active reflection coefficient (ARC) and total active antenna reflection coefficient (TARC) in order to obtain a wideband performance.

An additional limitation is related to the specific beamformer used in this work. To obtain a wide bandwidth we will use a novel optical beamforming network that provides multi-beam operation over a wide instantaneous bandwidth [34]. The optical beamformer utilizes true time delay (TTD) units, implemented in optical integrated circuits (ICs). These optical ICs generate frequency-independent time delays with a linear phase [35]. Therefore, a linear phase distribution along the array elements of the FPA is required in order to realize such an optical beamformer circuit [36], [37]. This sets an additional requirement for our FPA system.

This thesis is dedicated to the investigation of FPAs, its applicability, limitations, and ways of improvement. The main focus is on the wideband operation of the PAF combined with an improved scan range. The goal of our work was to overcome existing limitations and to develop a wideband FPA system, operating in the frequency band of 20-40 GHz with a scan range of up to  $\pm 20^\circ$  in the azimuth plane. The FPA should maximize the EIRP using silicon-based ICs and should minimize the beam deviation in the focal plane region during scanning. Next to this, it should accommodate optical beamforming requiring a linear phase distribution along the array elements.

We propose a new concept for optimal array illumination by the reflector, a double

reflector concept that overcomes the limited FoV and limited maximum EIRP of optimized conventional single- and double-reflector FPAs as presented in [10], [38]. The idea is based on increasing the number of simultaneously active elements in the FPA in order to overcome the limitation of a small illuminated region in traditional FPA concepts. By realizing a close to uniform amplitude distribution over the array elements, we can increase the achievable EIRP and system sensitivity, as discussed further in the thesis in chapter 4. To synthesize the optimal configuration of our new double-reflector FPA concept, we have developed a mathematical framework based on geometrical optics (GO). We have implemented this framework for single and double-reflector FPA systems. Various FPA systems with centered and offset single- and double-reflector configurations have been optimized and verified with a physical optics (PO) approach using GRASP [39]. The final double-reflector FPA configuration achieves the required scanning range with a compact PAF, which has at least half of the array elements simultaneously active during scanning.

From the PAF side, this thesis presents the outcomes which were done in the framework of the development of a wideband array for use in an FPA system. An array design with wideband capabilities is proposed and investigated against well-known antenna designs. The proposed antenna design allows us to achieve good active matching properties over a frequency band of more than one octave. At the same time, other relevant characteristics, like a high total radiation efficiency, phase-center stability, and reflector aperture efficiency remain at an acceptable level. We investigated the wide-band scan performance of the array in the case of a conventional phased array as well as in the case of an FPA system in which a complex field distribution needs to be generated for proper reflector illumination. The effects of mutual coupling in FPAs will be discussed in detail as well as the impact of mutual coupling on the antenna matching performance. The goal of the FPA antenna system was to increase the element density of the array in order to obtain a larger effective isotropic radiated power (EIRP).

A large number of array prototypes have been manufactured and tested to support the design ideas. In addition, with a novel reflector design wide-scan FPAs have been realized. This concept was tested in combination with the designed array feeds. The demonstrated simulations and measurements fully support the feasibility studies of both reflector and array concepts.

The thesis presents the following scientific contributions beyond state-of-the-art:

- The reflector optimization software based on the geometrical optics approach has been realized in order to achieve a wide scan range with single and double reflectors of  $\pm 20^\circ$  in the azimuth plane.
- All well-known types of FPA reflector configurations have been compared for applicability to operate at broadside scan and for wide-angle scanning.
- A new type of reflector concept is proposed (the complex offset double reflector) with a very compact PAF to realize wide-angle scanning over a wide bandwidth. It has been experimentally validated with a wide FoV.
- The proposed reflector configuration maximizes the ratio of active array elements in FPAs and provides the required phase linearity between the array elements to optimally use the optical beamforming.

- A wideband array of modified bow-tie antennas has been developed that provides a bandwidth of more than one octave (20 - 40 GHz) based on the active reflection coefficient and the total active antenna reflection over a scan range of  $\pm 20^\circ$  in azimuth. The details of modified bow-tie antennas are discussed further in the thesis in chapter 5.
- The experimental verification of the proposed PAF concept in combination with a novel double-reflector FPA system that provides a wide scan range.
- Investigation of the maximum achievable scan range that FPA systems can provide, in particular for the double-reflector model with wide-scan capabilities, and the investigation of the most crucial factors of wide scanning FPAs. In addition, several configurations have been explored with a wide illumination area of the array to maximize the EIRP.

The structure of the thesis is as follows. Chapter 2 describes the overall FPA concept, FPA applications, features of FPAs, and its difference as compared to traditional phased arrays. Chapter 3 provides an overview of the main design challenges of FPA: wideband limits of the PAF and issues of scanning with a reflector system. As an example, the design of a wideband array element is provided as well as an analysis of reflector configurations for narrow and wide scan-range applications. Chapter 4 is fully dedicated to the reflector synthesis for wide-scanning FPAs. An optimization algorithm based on geometrical optics is proposed for reflector optimization for wide-range scanning. Multiple single and double-reflector configurations are optimized and analyzed for FPA applications including the double shaped-reflector antenna with multiple interactions. The reflector prototype is discussed, presented, and tested for experimental validation. Chapter 5 goes deeper into the PAF analysis and design. The design of wideband arrays is investigated in detail including the design challenges for active wideband performance, issues for reflector aperture efficiency, and integration of wideband PAFs and reflectors. The chapter includes multiple FPA prototypes and measurements, and investigations of the overall FPA system capability. Chapter 6 is focused on the FPA demonstrator, which is a system-level concept and the result of a collaboration between several sub-projects. The broadband wide-scan focal-plane array designed in the framework of this thesis is combined with optical beamforming using ring resonators and low-noise amplifiers with a large dynamic range done within other research projects. Chapter 7 discusses the limits of the proposed FPA designs in terms of scan capabilities. Various reflector optimization use cases are investigated, and overall FPA's limitations are studied, for example, the achievable maximum scan range for different reflector configurations while minimizing the required array size. In addition, the options to extend our framework toward two-dimensional scanning are presented. The last chapter provides an overall conclusion and recommendations for future research on FPAs.



# CHAPTER TWO

## 2. FOCAL PLANE ARRAYS

---

### 2.1. History of FPA

The first attempts to improve the reflector antenna by placing an array in the focal plane go back to the least the 1940s. The idea has been to include beam scanning, multiple beams capabilities, improving the efficiency of the reflector, generating a specific beam pattern, and the possibility of correcting deficiencies in the reflector.

Traditionally, parabolic reflectors have been used. However, the spherical reflector already has been proposed for systems with beam scanning in 1949 [40], [41] with the application in the Arecibo radio telescope [42], [43] in the early 1960s. In addition, the shift of the array closer to the reflector than the focus also has been applied in order to realize electronic scanning without the gain reduction offered by a reflector. For such systems, the amplitude of the array illumination is sufficiently uniform [44]. Investigations in this domain began as early as 1961 [45], and by the 1970s developments were introduced into existing radar installations [46].

The possibility to correct for scan aberrations by using a PAF has been studied in [47] and [48]. Those investigations demonstrate the compensation for reflector distortions as well as beam scanning. The scanning capability of up to 15 beam widths has been demonstrated in [49] for a reflector curved in only one plane. The first investigation of multiple-beam capability with FPAs was done in 1965 [50].

The application of FPAs in geostationary satellite antennas started in the 1970s. In this application, FPAs could support the need to shape the beam pattern for illuminating a specific geographical region [51], [52], [53], [54], [55], [56], [57]. The possibility of beam reconfiguration in satellite FPAs has been studied in [58], [59]. The effects of active array performance and challenges of mutual coupling between array elements of FPAs were first investigated for circular and coaxial waveguides in [60], [61], [62], [63], [64].

### 2.2. FPA concept versus phased arrays

In a simplified way, it is possible to split the FPA system into two main components: reflector antenna and phased-array feed (PAF). The design challenges of PAFs are very similar to phased arrays. Both of these technologies are used in a number of similar applications like radars. However, there are a number of essential differences which is important to highlight in order to understand the design features of FPAs. While the prime goal of an FPA is the proper illumination of the reflector antenna, phased arrays form a self-sufficient antenna system that creates the wavefront in the far field from an array of single

antenna elements, see Fig. 2.1, where  $S_m$  is the element scattering coefficient.

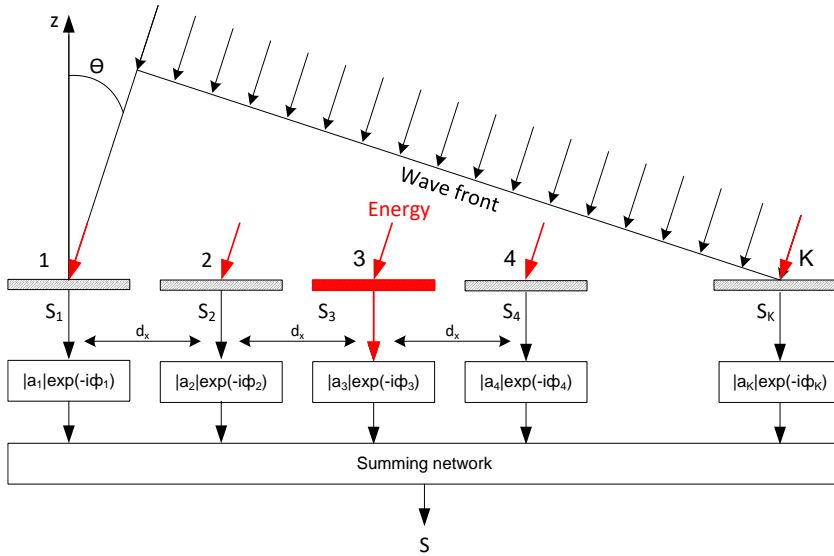


**Figure 2.1.** Phased array concept, a linear array of  $K$  elements is shown.

Like the FPA the main feature of phased-array antennas is the ability to change the shape and direction of the radiation pattern without physically moving the antenna. This is achieved by using a certain phase difference between each array element. This phase shift provides constructive interference in the desired direction (scan angle). Since phased arrays require for each channel a phase-shifter and amplifier, they are quite expensive and power-hungry. Therefore, FPAs could be a nice alternative here for phased arrays since they can achieve the same directivity with fewer array elements and as a result with a smaller number of phase shifters and amplifiers. This advantage is realized by using a combination of a phased-array feed that illuminates a reflector antenna.

The combination of an array and reflector, forming an FPA system, is illustrated in Fig. 2.2. The reflector provides the system the necessary directivity while the PAF provides the steering capability which is achieved electronically without a mechanical movement. Thus, the main advantages and benefits of reflectors and phased arrays are combined in FPAs. In the case of FPAs, there are not only phase differences between array elements, but there is a strongly varying amplitude distribution. In addition, the phase distribution is not linear like in the case of a conventional phased array. Thus, to form the proper reflector illumination or optimal reception of an incoming plane wave, a very specific phase and amplitude control of the PAF elements should be used. Typically, the center of the PAF is placed in the focal point of a reflector.

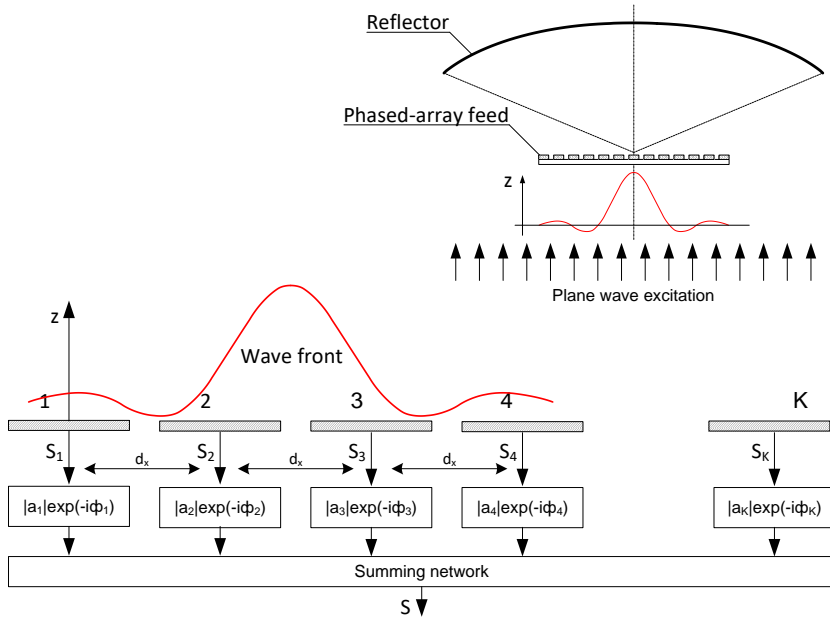


**Figure 2.2.** FPA concept where a phased-array feed (PAF) illuminates a reflector antenna.

### 2.3. Features and applications of FPAs

The combination of a reflector antenna with a PAF brings a lot of potential benefits and makes this type of technology well-suited for a number of applications. The main benefits which are well established and demonstrated in literature are:

- **Field of View (FoV).** It is possible to significantly improve the FoV of a reflector system by using PAFs [67], [68], [69], [70]. Moreover, FPAs provide near-constant and smoothly varying efficiency [71], [72] and sensitivity across the FoV [73], [74], [75].
- **Improved antenna efficiency.** The maximum effectiveness of the reflector aperture is achieved when the feed matches the focal plane field generated from an incoming plane wave on the reflector [71]. The PAF could provide the additional possibility of a better match [76], [77], [78]. In addition, there is a possibility of enhanced gain by improving the illumination from PAF [65], [79]. Associated advantages include higher EIRP on the downlink and higher gain-to-noise temperature (G/T) on the uplink, increased capacity, and smaller ground terminals [80].
- **Reduction of the scan losses and scan aberration correction.** Without a PAF scanning with reflectors is done by positioning a number of separate feeds in the focal plane of the reflector using beam switching, see Fig. 1.2. In this case, the scanning capability of the system is limited in terms of discreteness and there is no possibility to compensate of asymmetrical aberrations [71]. A combination of a reflector and PAF could give the possibility to significantly reduce the scan loss, which was demonstrated in [42] for the spherical Arecibo reflector with the linear

array of dipoles, in [44] and [81] for reflectors curved in one dimension and for two-dimensional feed arrays in [82]. Overall, the use of a single feed in the focal plane creates a significant distortion of the radiation pattern and an increase of sidelobe levels in the case of scanning [71]. According to [83], [43], [48], [76], [84], [85], [86].

- Correcting reflector surface defects. In addition to the aberration correction, it is possible to correct the reflector surface defect by phase and amplitude adjustment of individual array elements [84], [87], [88], [89]. [48] and [90] provide the empirical estimation of reflector surface correction by PAF and demonstrate the effective use of lower-cost reflectors using this technology.
- Vernier pointing. FPAs can also be used to introduce minor corrections to the beam direction [83], which can be useful to compensate for reflector misalignment due to sway and twist caused by wind, deformation due to gravity, and improper installation.
- Producing specific radiation patterns and reconfigurability. By using a PAF very specific radiation patterns can be created. There is wide flexibility in the FPA due to the electronic beamforming with control of both the phase and amplitude of each individual array element. So, the weighting of array elements could be adjusted to balance them for specific purposes like maximizing sensitivity and pattern control or interference mitigation and pattern control. This is widely used in satellite communication satellites with nonreferential 2D scanning where a geostationary satellite should cover a specific geographic region [91], [92], [93], [94], [95].
- Interference cancellation. In addition to the general reconfigurability, FPAs allow nulls to be established in the direction of an interferer [95], [96], [97], [98]. In addition, the beam widths can be reduced by using more elements in the antenna array without increasing the dimension of the reflector [99]. Moreover, with optical PAF more narrow beams could be achieved. This is also helpful to reduce interfering radiation.

The wide scan capabilities of FPAs which are investigated in this thesis open additional applications domains for FPAs. For example, it could be possible to have a simultaneous connection between several base stations due to the combined capabilities of wide scan and multi-beam. There is also a possibility of tracking multiple satellites simultaneously using electronic beam steering. There is an important note, that this is possible only on different radio frequencies. For radar applications, wide scanning with reflectors opens great opportunities in fast and high-resolution systems, which potentially could overcome the existing and widely used phased arrays. The features of multi-beam antennas using FPAs are summarized in [100], [101], [102], [103], [104], [105].

Looking at the state of the art there are a number of applications where PFAs already proven themselves as reliable and suitable technology.

- Radio astronomy. The significantly larger FoV with FPAs is beneficial for radio astronomy applications. This was done in the concept implemented by ASTRON [106] where a receiver array is placed in the focal plane of each reflector antenna to create the Square Kilometer Array (SKA). FPAs allow to sample of the

aperture field distribution using a discrete number of elements in the focal plane. As a result, the signals from the different elements are combined to generate a high-quality image.

- **Earth observation.** Traditionally, multiple-beam capabilities have been achieved by using a number of horn antennas positioned in the focal plane making a one-horn-per-beam configuration [107]. However, this leads to a loss in aperture efficiency due to aberrations and distortions associated with off-axis beams. In addition, overlapping beams are required to illuminate the service area uniformly and thus efficiently [108]. The gain reduction within those overlaps should not exceed a 3 dB drop [109]. This could be achieved with feed horns due to their large sizes and thus coarse samplings of the focal plane fields. Here FPAs could be beneficial for earth observation providing high resolution with advanced beamforming [110], [111], [112].
- **Satellite communication.** Traditionally, a high-gain reflector antenna is used for satellite communication [113]. The trend in satellite communication is to provide higher demands for high-speed internet and high-quality TV broadcasting. Thus, the FPA technology was found to be an attractive solution in this domain [108]. The multi-beam antennas provide a frequency reuse scheme for communication to the ground, at the same time each generated spot beam on the ground can be allocated to a different frequency band. Nowadays, FPAs are being used for direct-broadcast satellites (DBS), personal communication satellites (PCS), military communication satellites, and high-speed Internet applications [114]. In addition, FPAs have also been successfully implemented in geosynchronous satellites as well as low earth orbit (LEO) and medium earth orbit (MEO) satellites [115], [116]. Examples of commercial satellites employing frequency reuse multi-beam antennas include INTELSAT IV-A (1975), INTELSAT V (1981), INTELSAT VI (1989), NASA's ACTS satellite, and ITALSAT [117], [118].

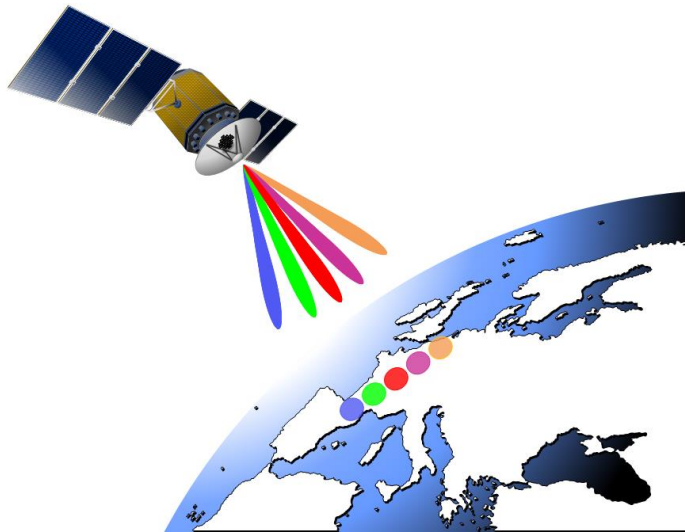


**Figure 2.3.** Conceptual drawing of frequency reuse for satellite communication (downlink).

- VSAT ground-based terminals. Traditionally, home-satellite terminals use a dish reflector antenna system with a single feed. The antenna should be precisely aligned mechanically and directed to the specific satellite. This implies that the home-satellite users cannot switch their connection without mechanically moving the dish antenna or cannot form more than one satellite link at the same time. Using reflectors with PAFs for very small aperture terminals (VSAT) is significantly improving the performance of satellite communication, users can switch the satellite link without the need to mechanically realign their antenna system [119], [120]. In addition, it is possible to connect with several satellites simultaneously without replicating the antenna system. Traditionally, multi-satellite connections are formed by replicating the antenna system for each radio beam [121]. It is also simplifying the alignment process and allowing it to sustain harsh weather conditions.

#### 2.4. Challenges of modern FPAs

As we could see from the previous paragraph there are a large number of applications where FPAs could be the best suitable practical solution. Nevertheless, there are a number of challenges, which are typical for this technology. Some of them like a limited scan potential and limited active frequency bandwidth are the main subject of this thesis. However, there are other challenges related to FPAs, which are important to consider:

- Design complexity. Overall design complexity is much higher compared to classical reflector solutions in which a simpler feed configuration is used. In addition, the mechanical design of FPAs is more complex as compared to phased arrays of similar size due to the combination of reflector and PAF.
- Necessity to use complex field distributions in the PAF (Fig. 2.2), which could provide a larger impact of mutual coupling [121], [122].
- The PAF requires a dense array configuration with, as a result, high mutual coupling. This sets challenges to provide a good active matching performance towards the commonly used standard impedance of  $50\ \Omega$  [124].
- All mentioned challenges also require special demands for beamforming electronics. Each array element should have a separate transceiver IC, including a low-noise amplifier (LNA), power amplifier (PA), and a beamforming vector modulator to adjust amplitude and phase [124]. As a result, there are higher demands for system calibration due to the increased number of feed elements, more complicated beamforming electronics, and complex beamforming algorithms.
- In addition, these electronics could have a high-power consumption, and substantial power requirements and, as a result, will require cooling. This puts additional demands on operational temperatures which could be difficult to achieve [125], [126].
- The overall complexity of the FPA system and its operational algorithm could affect the system's reliability.

### 2.5. Optical beamforming for FPAs

The work in this thesis is part of the FREEBEAM project [34]. FREEBEAM can be classified into three subsystems: a focal plane array with a reflector, an optically controlled RF multi-beamformer system, and a low-noise amplifier system. The project demands a multi-beam functionality with more than one radio beam. The radio frequency range required to be covered is 20 GHz (20 – 40 GHz). The wideband capability of the designed FPA system is achieved by using optical beamforming. [128] presents detailed information about the novel optical beamforming network design for the antenna system presented in this thesis, [34]. The optical beamformer utilizes a true time delay (TTD), implemented in a photonic integrated circuit (PIC). These PICs generate frequency-independent time delays (linear phase) [35], therefore alleviating the beam-squinting problem prevalent in wideband beamformers. A dispersive optical TTD device generates wavelength-dependent time delays and thus can be used to generate simultaneous multiple beams by using light sources of different wavelengths with the beams at different radio frequencies and with the possibility to be fed by just a single fiber from a remote multi- $\lambda$  transmitter site. In addition, TTD includes immunity to electromagnetic interference (EMI), scalability, and a low weight thanks to the high level of photonic integration of the optical beamformer circuits.

The usage of optical beamformers puts a special requirement on the phase distribution linearity along the array elements of the FPA. It is an important requirement for the realization of a compact TTD optical beamformer circuit [129]. Therefore, an additional antenna design target for the development of our FPA system is a linear phase distribution along the elements of the PAF.



# CHAPTER THREE

## 3. FPA: DESIGN FRAMEWORK

---

### 3.1. Array design challenges<sup>1</sup>

This chapter discusses the main design challenges of wideband antenna elements which can be used in focal-plane arrays. A novel electrically small wideband antenna is presented. It is based on a bow-tie antenna. The proposed antenna shows excellent input matching properties over a frequency band of more than one octave and nearly reaches the theoretical Chu-Harrington limit. It is shown that the central element of a five-element feed array, operating at a center frequency of 30 GHz, realizes an input matching bandwidth of 24.4 GHz.

#### 3.1.1. Introduction

Electronic phased-array antennas became a widespread technology in the past decades in a number of applications, such as long-range and multi-function radars. However, there are limiting factors to use this technology at higher frequencies, such as bandwidth limitation [130]. Nevertheless, the demand for wideband antenna arrays and focal-plane arrays is increasing especially in the Ku- and Ka-band. Therefore, it is necessary to make an investigation of broadband antenna elements that can be used in an array environment.

This chapter presents the work which was done in the framework of the development of a wideband focal-plane array (FPA), operating in the frequency band from 20-40 GHz. The challenge is to optimize the array elements over a 20 GHz bandwidth for optimal efficiency and for a frequency-stable phase-center. In addition, the element pattern should be suitable for reflector illumination.

In comparison to the well-known and widely used Vivaldi phased-array feed [131], our design achieves a wideband operation using a smaller occupied area for each of the array elements. In addition, our concept significantly improves the phase-center stability, which is a major drawback of the Vivaldi concept.

In this chapter, we will investigate the fundamental limitations of these wideband antenna elements.

<sup>1</sup>Current paragraph 3.1 is published as a conference paper: A. Dubok, A. Al-Rawi, M. Herben and A. B. Smolders, "Fundamental challenges for wideband antenna elements in focal-plane arrays," in The 9th European Conference on Antennas and Propagation, Lisbon Portugal, 2015, and included here in its entirety without any changes.

### 3.1.2. Wideband limit for antenna design

Antenna dimensions are strongly related to the frequency of operation and the required bandwidth. For electrically-small antennas, the ratio between the maximum achievable frequency bandwidth and the antenna dimension is defined by the well-known Chu-Harrington limit [132], [133], and [134], which sets a lower limit on the quality factor and related bandwidth. The Chu-Harrington limit is given by:

$$(3.1) \quad Q = \frac{1}{k^3 a^3} + \frac{1}{ka}$$

where  $k$  is the wavenumber,  $Q$  the antenna quality factor, and  $a$  the antenna size or boundary sphere surrounding the antenna as illustrated in Fig. 3.1, [133] - [134].

According to (3.1) it is possible to define a minimum antenna size for a certain value of the antenna quality factor.

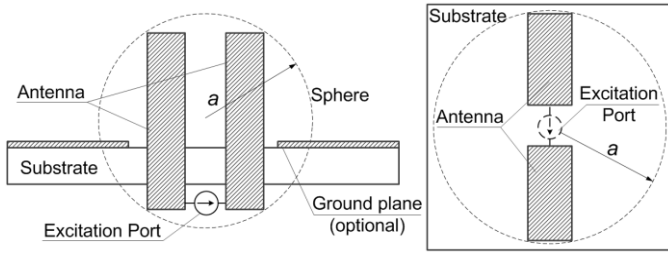


**Figure 3.1.** Illustration of boundary sphere which defines the minimum antenna size [133].

In order to obtain a direct relation between the antenna properties and its frequency band, it is necessary to change the parameters of the Chu-Harrington limit according to the:

$$k = \frac{2\pi f_0}{c}; \quad Q \cong \frac{1}{B\eta}; \quad B = \frac{\Delta f}{f_0} \quad (3.2)$$

$$\Delta f(a) = \frac{1}{\eta c} \frac{8\pi^3 f_0^4 a^3}{c^2 + 4\pi^2 f_0^2 a^2} \quad (3.3)$$

where  $\eta$  represents the total antenna radiation efficiency,  $B$  is the relative bandwidth and  $c$  is the speed of light. There is no clear definition of bandwidth in the investigated literature [132], [133], and [134]. Therefore, we decided to use the most strict variant: the frequency band is defined based on the  $S_{11}$  parameter less than -10dB.

(3.3) expresses the dependence of the bandwidth versus the minimum required antenna size  $a$ . Consequently, it is possible to estimate the minimum antenna size which could provide a certain frequency bandwidth around the central frequency  $f_0$ . Fig. 3.2 shows the theoretically achievable frequency bandwidth depending on the minimum antenna size within the investigated frequency band from 20 GHz to 40 GHz. The radiation efficiency in the initial calculation was assumed to be equal to 100% in order to get an estimation with the best possible parameters.

According to Fig. 3.2, the minimum antenna size, which theoretically could provide the required frequency bandwidth, is equal to the boundary sphere with a radius of 1.8 mm corresponding to about 36% of the free-space wavelength.

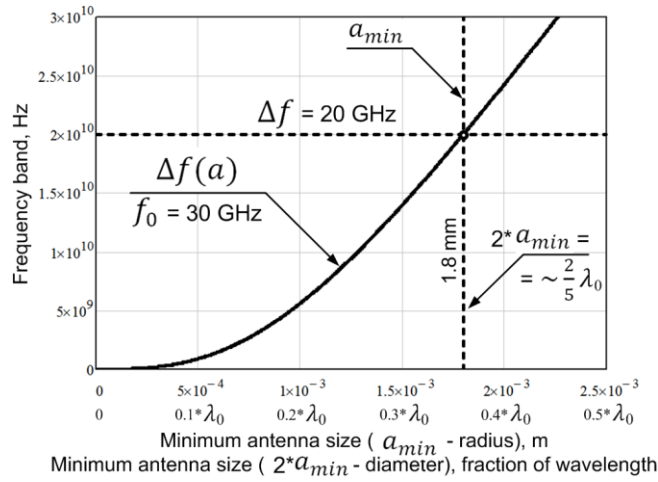


**Figure 3.2.** Theoretically achievable frequency bandwidth depending on the minimum antenna size.

### 3.1.3. Design of wideband array element

The investigation of a suitable wideband antenna concept was done based on the presented size limitations in section 3.1.2. All analyzed antennas were fit into the boundary sphere of Fig. 3.1 in order to get as close as possible to the Chu-Harrington limit. Limiting the height of the antenna, with respect to the normal of the array face, results in a more stable feed phase center [135]. The latter is important in order to avoid major de-focusing of the secondary radiation pattern [136]. In addition, only antenna configurations with a high total radiation efficiency and a far-field pattern that is suited for reflector illumination were considered. These criteria are some of the basic requirements for FPA antenna systems. The total efficiency of an antenna is the radiation efficiency multiplied by the impedance mismatch loss of the antenna when connected to a transmission line or receiver.

As a starting point, the well-known bow-tie antenna was chosen [137]. The design for the 20-40 GHz band is shown in Fig. 3.3. The bow-tie antenna is a wideband antenna type with a stable phase center, which has established itself in wideband antenna arrays and almost ideally fits into the boundary sphere of the Chu-Harrington limit. We have performed an optimization to improve the bow-tie antenna to further increase the operational bandwidth, while reducing the boundary sphere further, to approximate closer to the Chu-Harrington limit of Fig. 3.2. Optimization was organized by consistently changing the antenna geometry based on a genetic algorithm similar to the procedure described in [138].

The modified bow-tie antenna (Fig. 3.4) was designed based on the described wideband analysis methods and compared to the performance of the original bow-tie antenna. It is important to note that there are no direct connections with the ground plane of the investigated antennas. Simulations were done with CST in Transient Solver – a general-purpose 3D electromagnetic simulator [139]. The matching properties are shown in Fig. 3.5. It is clear that the bandwidth was significantly improved for the optimized configuration. In addition, the input matching in the upper range of the investigated band (33-40 GHz) is much better for the modified bow-tie antenna as compared to its classical variant. However, there are some matching issues around 20 GHz and 42 GHz. For our application, it is desirable to have

a better level of matching in order to obtain some margin in the bandwidth.

(3.3) allows us to estimate the theoretically achievable frequency bandwidth and to compare its value with the simulation results of both antenna types, see Fig. 3.6. Based on the simulation results, the total radiation efficiency used in (3.3) was assumed to be constant within the frequency band and equals 95% for the bow-tie antenna and 92% for its modified version instead of the initial 100%. From Fig. 3.6 it is clear that the modified bow-tie antenna very efficiently uses the available space. The achieved bandwidth of the standard bow-tie antenna is 15.72 GHz, while the theoretically achievable bandwidth for this antenna size is 25.84 GHz. The modified bow-tie antenna achieves a bandwidth of 25.9 GHz, while the theoretical limit is 28.87 GHz. Note that the phase center remains almost constant with a minor peak deviation of not more than half of the wavelength within the investigated frequency band for both antennas.

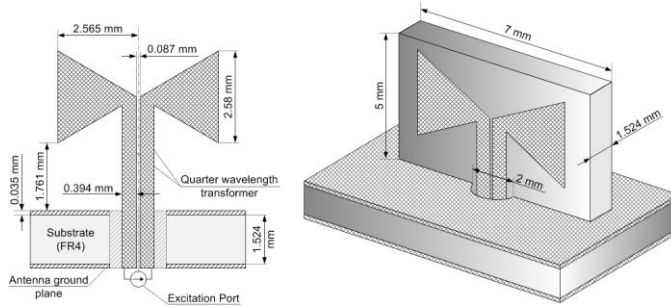


**Figure 3.3.** Cross section of a classical bow-tie antenna.

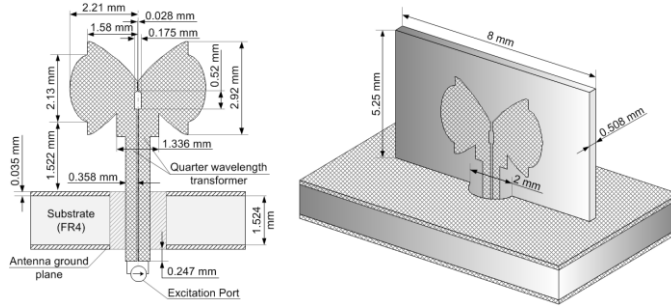


**Figure 3.4.** Cross section of the modified bow-tie antenna.

### 3.1.4. Additional bandwidth improvement

The presented modified bow-tie antenna achieves a bandwidth of 25.9 GHz and is very close to the Chu-Harrington limit of 28.87 GHz. However, there is still almost a 3 GHz difference between the theoretically achievable and actually achieved results. In addition, it was already mentioned that the matching level around 20 GHz and 42 GHz should be improved. Therefore, it is necessary to investigate some additional methods of bandwidth improvement and to try to get as close as possible to the theoretical limit. Radiation efficiency and phase-center position should remain the same.

One of the options to improve impedance matching is by implementing lumped elements within the antenna structure. Another option is to redistribute, the surface currents on the

radiating structures [140]. For that purpose, a slot configuration was realized in the modified bow-tie antenna and optimized for the matching properties in CST [139]. The resulting dimensions of the slot are presented in Fig. 3.7. The corresponding antenna surface currents distribution at 20 GHz, 30 GHz, 40 GHz, and 45 GHz are shown in Fig. 3.8. As can be seen, the surface current distribution for the antenna with an additional slot is more stable at the different frequencies. Therefore, the performance of the modified bow-tie antenna with an additional bandwidth improvement varies slowly with the frequency. As a result, this antenna has more stable radiation characteristics and impedance over a wide frequency band.

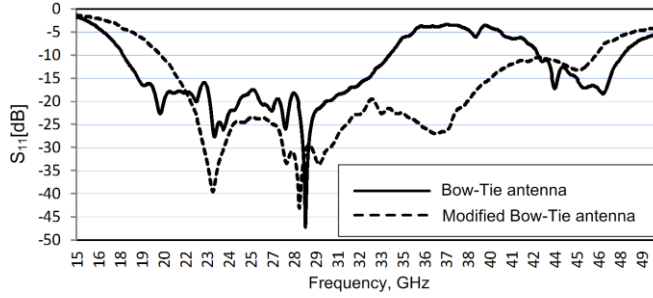


**Figure 3.5.** Simulated input matching of the standard bow-tie antenna and its modified wideband variant.

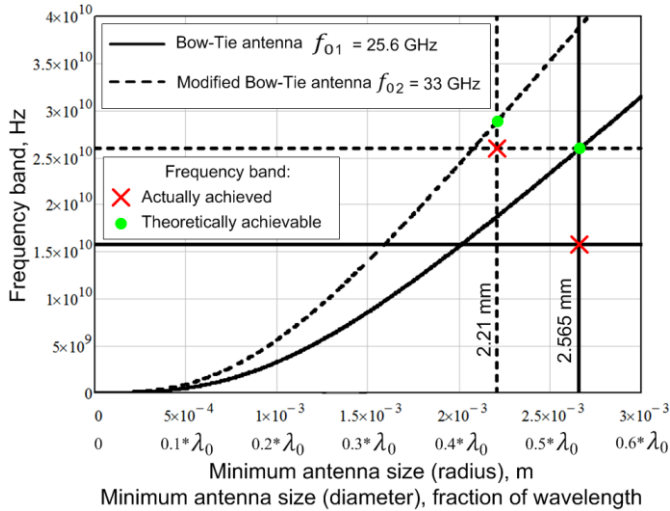


**Figure 3.6.** Evaluation of theoretically achievable and obtained bandwidth for the considered antennas.

At these high frequencies, it is not possible to use SMD-type of lumped elements, due to the parasitic. An alternative is to realize parallel plate capacitors on the antenna substrate. The theoretical capacitance of this capacitor is given by:

$$C = \frac{\varepsilon \varepsilon_0 S}{d} \quad (3.4)$$

where  $\varepsilon_0$  is the free-space dielectric constant ( $\varepsilon_0 \approx 8.854 \times 10^{-12} \text{ F}\cdot\text{m}^{-1}$ ),  $\varepsilon$  is the relative permittivity of the dielectric substrate,  $S$  is the area of overlap of the two plates and  $d$  is the separation between the plates. Consequently, additional capacitive microstrip pads could be

added on the back side of the antenna substrate in order to improve the impedance matching. The required capacity of the capacitors, dimensions, and positions of the microstrip pads were optimized by means of simulation. The resulting geometry is presented in Fig. 3.7.

The matching properties of the modified bow-tie antenna with and without the implemented bandwidth improvement features are shown in Fig. 3.9.

In order to estimate the bandwidth improvement, it is possible to make an analysis similar to Fig. 3.6 for our new antenna design. The outside antenna dimension remains the same, as well as the simulated total radiation efficiency. The central frequency is decreased by about 1 GHz according to Fig. 3.9. By substitution of all parameters in (3.3), Fig. 3.10 was obtained.

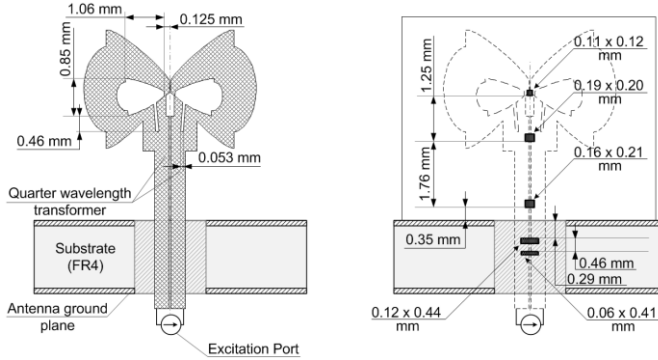


**Figure 3.7.** Additional bandwidth improvement for the modified bow-tie antenna: slots on the antenna surface and capacitive microstrip pads on the back side of the antenna.

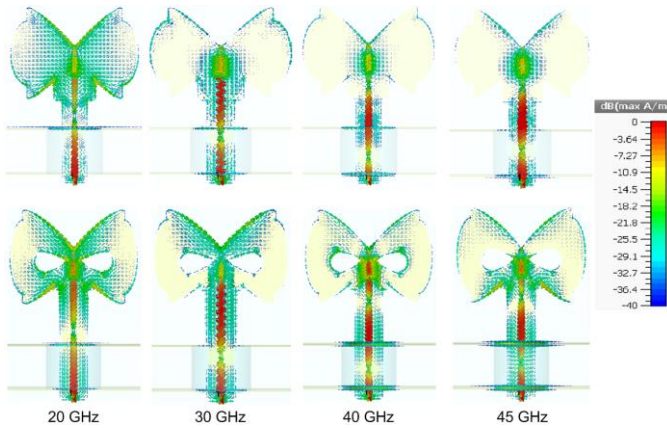


**Figure 3.8.** Currents on the surface of the modified bow-tie antenna at 20 GHz, 30 GHz, 40 GHz, and 45 GHz without and with an additional slot.

From Fig. 3.10 it is clear that the difference between the theoretically achievable and actually achieved bandwidth is significantly reduced. The modified bow-tie antenna with an additional bandwidth improvement achieves a bandwidth of 27.45 GHz, which is just slightly smaller (0.2 GHz) than the theoretical limit. As a result, it is possible to claim that the fundamental Chu-Harrington limit was almost reached by this antenna element.

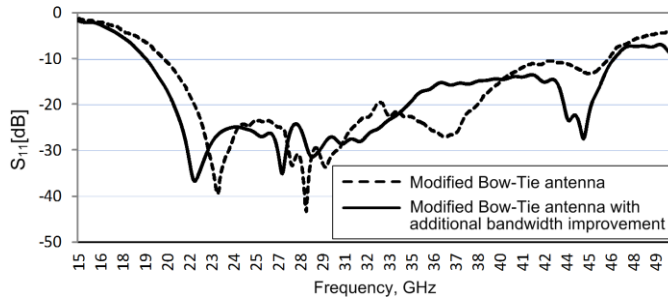


**Figure 3.9.** Simulated input matching of the modified bow-tie antenna with and without additional bandwidth improvement.

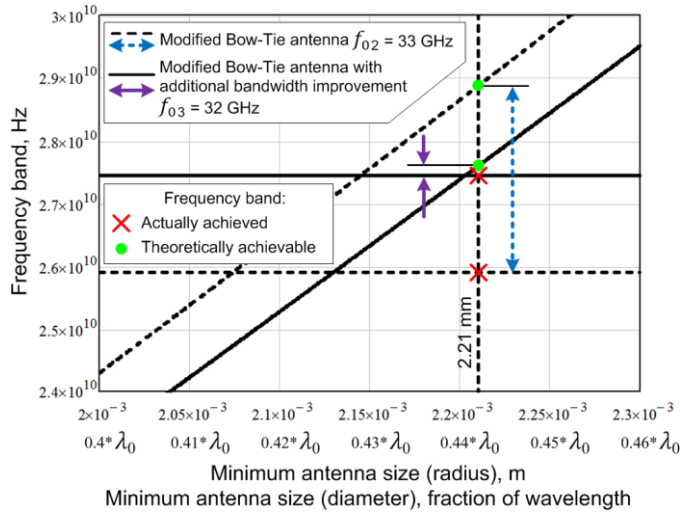


**Figure 3.10.** Evaluation of theoretically achievable and obtained bandwidth for the modified bow-tie antenna with and without additional bandwidth improvement.

### 3.1.5. Focal-plane arrays

The antenna element of section 3.1.4 is used as a starting point for the design of a feed array for a focal-plane array configuration. The element spacing was chosen equal to half a wavelength at the center frequency (30 GHz). Since the antenna elements are almost touching in this case (0.58 mm spacing between edges), it is expected that mutual coupling will deteriorate the matching performance [65].

As a first step, we have investigated a linear array with five elements, as shown in Fig. 3.11. The input matching properties of the central element of the array is shown in Fig. 3.14. The other array elements were connected to a matched load of 50 Ohm. From Fig. 3.14 it is clear that the matching properties for the central element in the array are quite different as compared to the matching properties of a single wideband array element (see Fig. 3.9). The achieved wideband properties have been deteriorated by mutual coupling between the array elements.

An interesting technique to improve the matching properties in wideband arrays are so-called connected arrays [141]. An additional electrical connection between neighboring array

elements is introduced. The matching properties of such a configuration are improved due to the fact that the connections between neighboring elements allow currents to remain nearly constant with frequency. Based on this method, connections between neighboring elements have been introduced in the array of Fig. 3.11. The position and geometry of the connection were optimized in CST [139]. The resulting connected-array configuration (Fig. 3.12) was designed based on the best-achieved matching properties. Fig. 3.14 shows the resulting matching properties as compared to the normal array configuration.

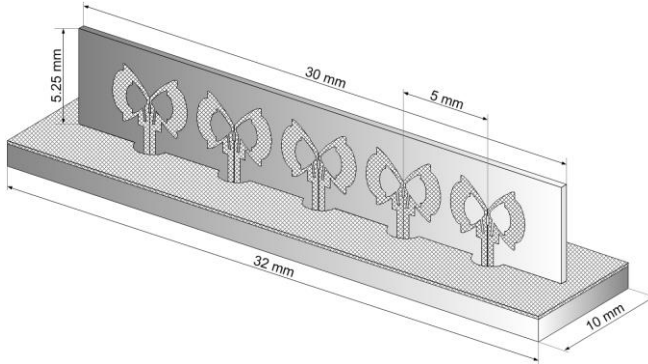


**Figure 3.11.** Cross section of an array of five modified bow-tie antenna elements in a row.

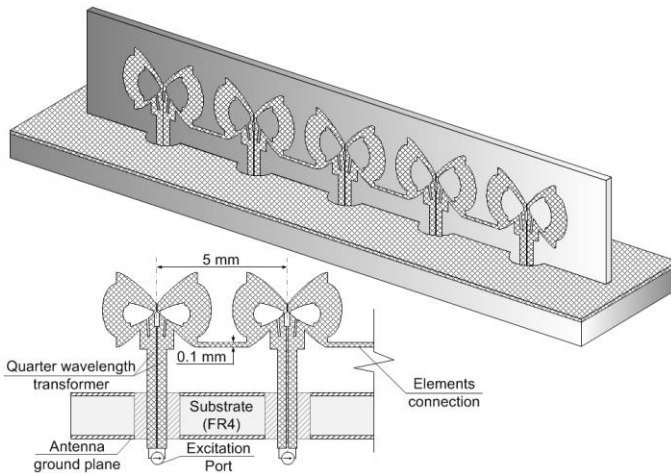


**Figure 3.12.** Cross section of a connected array of five modified bow-tie antenna elements in a row.

The surface current distributions at 30 GHz for the investigated arrays are presented in Fig. 3.13. It is clear that in the case of the connected array intentionally introduced currents can be observed between neighboring elements. This allows the redistribution of the surface currents of the individual elements and, as a result, reduces the negative effects of mutual coupling.

According to Fig. 3.14, the wideband properties for the central element in a connected array have been significantly improved as compared to a classical array configuration. The achieved bandwidth of 24.4 GHz covers the desired band from 20-40 GHz.

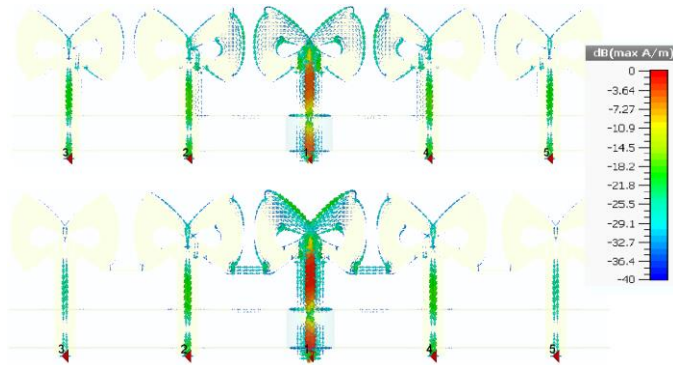


**Figure 3.13.** The surface current distribution of a normal array and a connected array at 30 GHz.

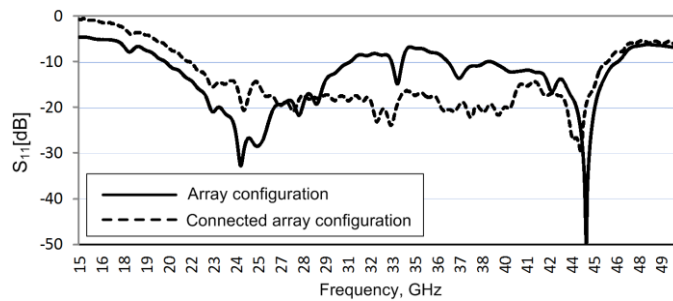


**Figure 3.14.** Simulated input matching of the central element in a normal array and a connected array defined by five modified bow-tie antenna elements in a row.

The simulated results of the total radiation efficiency for the investigated arrays and for the single array element are presented in Fig. 3.15. It is clear that in the case of a single element of section 3.1.4, the total radiation efficiency is high and exceeds 90% in a large part of the desired band. For an array configuration, due to the mutual coupling, the radiation properties have been deteriorated. However, for the central element in a connected array, the radiation properties remain higher within the desired band as compared to a classical array configuration.

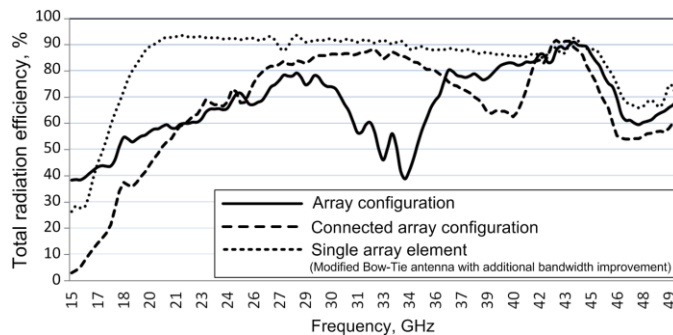


**Figure 3.15.** The simulated total radiation efficiency of the single array element and central element in a normal array and a connected array defined by five modified bow-tie antenna elements in a row.

The simulated results of the phase-center position for the investigated arrays are presented in Fig. 3.16. It is clear some ripple occurs and one significant peak for the normal array around 33 GHz. Nevertheless, for the central element of the connected array, the fluctuations almost do not exceed one wavelength.

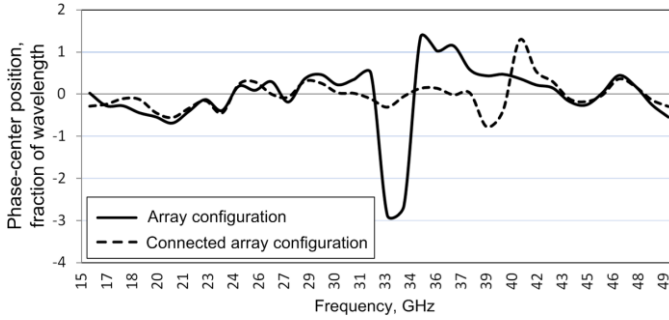


**Figure 3.16.** Simulated phase-center position of the central element in a normal array and a connected array defined by five modified bow-tie antenna elements in a row.

### 3.1.6. Conclusion

Future FPA antenna-systems require wideband properties. In this section, wideband analysis methods were proposed in order to determine the relationship between the antenna geometry and its frequency characteristics. The proposed design allows us to get good matching properties over a frequency band of more than one octave and nearly reaches the theoretical Chu-Harrington limit. At the same time, other relevant characteristics, like high total radiation efficiency and phase-center stability remain at an acceptable level.

We have presented a modified bow-tie antenna that achieves a bandwidth of 25.9 GHz, very close to the Chu-Harrington limit of 28.87 GHz. Furthermore, with an additional bandwidth improvement like slots on the antenna surface and the realization of extra capacitive elements, the bandwidth could be further improved to 27.45 GHz. In addition, the concept of connected arrays was used to obtain wideband antenna properties in an array configuration. It was shown that for a five element array, an input matching bandwidth of 24.4 GHz can be obtained.

### 3.2. Reflector for narrow-range scanning<sup>1</sup>

An optimized double-reflector antenna concept for a wideband focal plane array (FPA) configuration is presented for Ka-band applications with a limited scan range, e.g. ground terminals for satellite communication. The proposed reflector configuration allows to maximize the number of active array elements and minimizes the actual array size during scanning. In addition, the FPA configuration has been optimized for wideband optical true-time-delay (TTD) beamforming, resulting in wideband operation from 20-40 GHz. Based on a minimum required 80 % aperture efficiency at 30 GHz, the double-reflector concept allows expanding the illuminated region of the array by a factor of 60 as compared to traditional prime-focus configurations. The proposed configuration also decreases the magnification factor  $M$  by a factor of 2.5, as compared to the double-parabolic configuration for a  $\pm 1.5^\circ$  scan range.

#### 3.2.1. Introduction

In the past decades, focal-plane arrays (FPAs) have become an interesting alternative to conventional horn-fed reflector antennas in a number of applications, e.g. in radio astronomy [8] and in Ka-band satellite communication [9]. However, the small number of simultaneously active array elements is representing a serious limiting factor for this technology, in terms of the number of multiple beams or scan range [142] and the level of achievable effective isotropic radiated power (EIRP) [15]. A low EIRP level limits the use of low-cost silicon integrated circuits. In addition, it is a challenge to provide a proper exposure of the FPA even for relatively small scan angles of the main beam, due to the significant beam deviation in the focal plane (see Fig. 3.17) [143]. Therefore, it is necessary to investigate various reflector configurations in order to improve the FPA illumination and increase the number of simultaneously active elements, during beam scanning over a wide instantaneous bandwidth.

This chapter presents the outcome of a study to overcome these limitations. Our goal was to develop a wideband FPA system, operating in the frequency band 20-40 GHz. The beamforming of the array elements is done with a novel optical beamforming network, resulting in multi-beam operation over a wide instantaneous bandwidth [34]. The optical beamformer utilizes true time delay (TTD), implemented in optical integrated circuits (ICs). These optical ICs generate frequency-independent time delays (linear phase) [35], therefore alleviating the beam-squinting problem prevalent in wideband beamformers. A dispersive optical TTD device generates wavelength-dependent time delays and thus can be used to generate simultaneous multiple beams by using light sources of different wavelengths. In addition, TTD includes immunity to electromagnetic interference (EMI), scalability, and a low weight thanks to the high level of photonic integration of the optical beamformer circuits. A linear phase distribution along the array elements of the FPA is an important requirement for the realization of a compact TTD optical beamformer circuit [129]. Therefore, our antenna design targets a linear phase distribution along the array elements of the FPA.

<sup>1</sup>Current paragraph 3.2 is published as a journal paper: Dubok, A; Al-Rawi, A; Tessema, N; Tangdiongga, E; Herben, M.H.A.J; Gerini, G; Smolders, A. B, "Double Reflector Configuration for Optimal Exposure of Wideband Focal Plane Arrays with Optical Beamforming," IEEE Transactions on Antennas & Propagation, no. 10.1109/TAP.2017.2709620, 2017, and included here in its entirety without any changes.

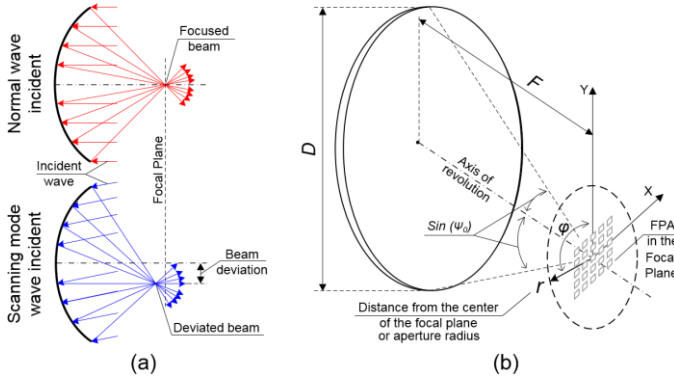


**Figure 3.17.** (a) Beam deviation during scanning (b) Geometry of the FPA system with a single reflector.

Another important requirement for our FPA system is related to the scan range. We have investigated two specific scan ranges:  $\pm 1.5^\circ$  and  $\pm 3^\circ$  for 2-dimensional scanning, which is much more challenging than 1-dimensional scanning. These are typical values for reflector installation and calibration in Ka-band, in two-way satellite communication [10], and in surveys for radio astronomy [144], respectively. In conventional FPA systems, the array is not used very efficiently, even in the case of a limited scan range. The number of simultaneously illuminated array elements is limited, due to the small region of high power density in the focal plane. In addition, the required size of the array is quite large, due to the significant spot beam deviation from the array center during scanning. As a consequence, the number of simultaneous active elements is small as compared to the total number of array elements. Therefore, the achieved EIRP levels, as well as the scan performance, are limited [15]. In summary, we have the following requirements for the FPA system:

- wide band in the range of 20-40 GHz,
- linear phase distribution in the focal region,
- wide illumination area of the array to maximize the EIRP,
- decrease beam deviation in the focal plane region during scanning.

In this chapter, we will optimize the FPA system for these requirements. For that purpose, we will investigate and compare three configurations: i) a classical prime-focus reflector, ii) a double parabolic configuration, and iii) our proposed optimized FPA configuration. We will use a classical prime focus reflector with  $F/D = 0.6$  and  $D = 0.8$  m. The array element spacing is chosen as  $\lambda_0/2$  at 40 GHz, where  $\lambda_0$  is the free-space wavelength. All simulations have been performed with GRASP [39].

### 3.2.2. Illumination limitations of classical prime-focus FPAs

For large  $F/D$  ratios and small scan angles, when neglecting the spill-over and decoupling efficiencies, the co-polar component of the electric field distribution in the focal plane of a prime-focus reflector can be approximated by:

$$E(r) = 2 \frac{J_1(kr \sin(\psi_0))}{kr \sin(\psi_0)} \quad (3.5)$$

where  $J_1$  is the Bessel function of the first kind with order 1,  $\Psi_0 = \pi/4$  is the subtended angle of the reflector,  $k$  is the wavenumber and  $r$  is the distance from the center of the focal plane or aperture radius, see also Fig. 3.17 and [145].

According to (3.5), it is clear that the same reflector operating at higher frequencies will illuminate a smaller region in the focal plane. As an example, the electric field in the focal plane for a classical prime focus reflector is presented in Fig. 3.18. The normalized power density distribution of the electric field, calculated according to (3.5), is shown in Fig. 3.19. By integrating the electric field on the focal plane and normalizing it to the total power  $P_{tot}$  received by the reflector and free space impedance  $Z_0$ , it is possible to calculate the aperture efficiency  $\eta(r)$  in the focal plane (see Fig. 3.17) [143], which is presented in Fig. 3.20:

$$\eta(r) = \frac{1}{P_{tot}} \int_0^{2\pi} \int_0^r \frac{|E(r')|^2}{2Z_0} r' dr' d\varphi \quad (3.6)$$

According to Figs. 3.17 – 3.19 the illuminated region in the focal plane is relatively small. When we assume an array element spacing of  $\lambda_0/2$  at the highest frequency (40 GHz), only two to three elements could be located in the area of maximum power density (above the -3 dB level). Fig. 3.20 shows that by considering larger array surfaces, the aperture efficiency first increases very quickly until  $r$  reaches the first Airy ring and then remains practically constant. This fact limits the number of simultaneously involved array elements, and as a result, limits the EIRP level and the beam-scanning capabilities.

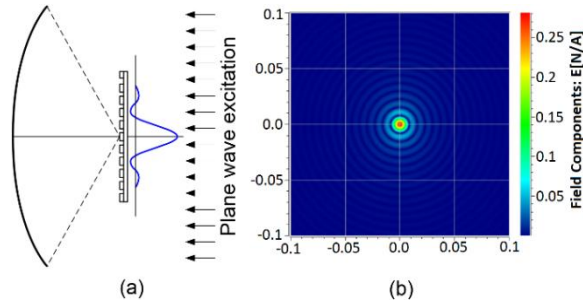


**Figure 3.18.** (a) Field distribution of a reflector antenna in the focal plane (b) 2D illustration of the Airy pattern in the focal plane of a classical prime focus reflector with  $F/D = 0.6$ ,  $f = 30$  GHz [39].

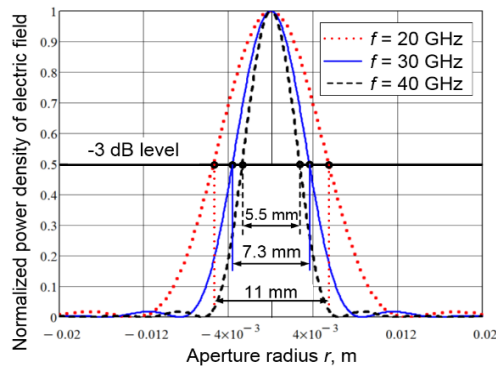


**Figure 3.19.** Normalized power density distribution of the electric field in the focal plane of a classical prime focus reflector with  $F/D = 0.6$ .

For the considered FPA system employing a wideband optical beamforming network, it is required to have a linear phase distribution along the array elements. The phase distribution in the focal plane of the investigated parabolic reflector is shown in Fig. 3.21 as well as an example of an optimal phase-distribution in the order of the optical beamformer to be used. It is clear that the phase distribution is far from linear along the aperture radius at a single frequency. If we consider the aperture area at 30 GHz for which the normalized power density is above -3 dB (see Fig 3.19), the linearity of the phase distribution shows a root-mean-square (rms) error of  $6.36^\circ$ . This will deteriorate the overall performance of our FPA system with optical beamforming [37].

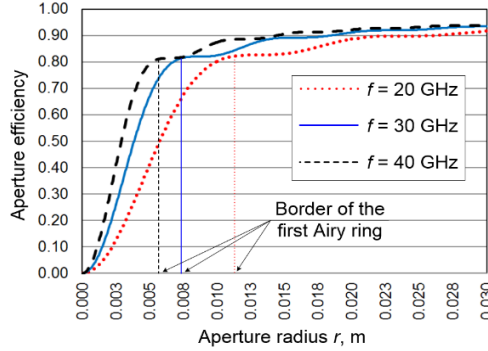


**Figure 3.20.** Aperture efficiency in the focal plane of a classical prime focus reflector with  $F/D = 0.6$ .

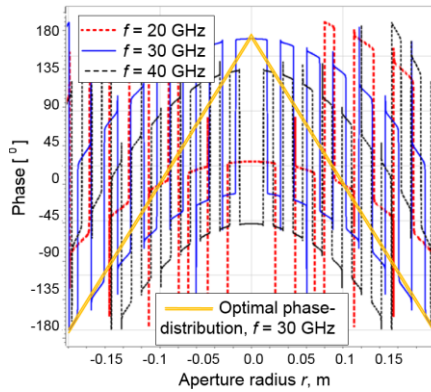


**Figure 3.21.** Phase distribution in the focal plane of a classical prime focus reflector with  $F/D = 0.6$ .

The aperture efficiency and field distribution cuts for different scan angles of the main beam are presented in Fig. 3.22. We can observe that for various scan angles of the main beam, the region of maximum power will have almost the same size, but will be shifted away from the array center. This means that the array size should be increased in order to provide scanning capabilities. However, the number of simultaneously active elements will remain the same.

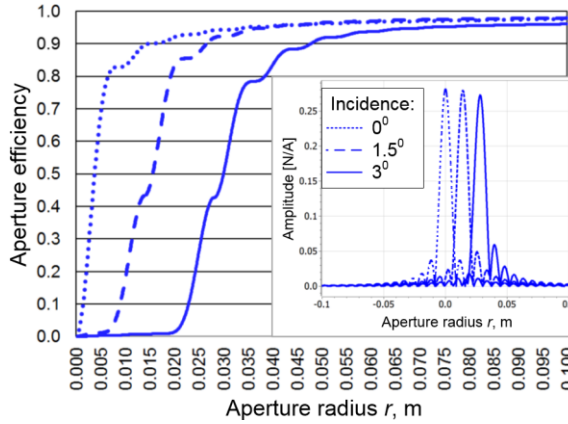


**Figure 3.22.** Aperture efficiency and electric field cuts in the focal plane for different scan angles of a classical prime focus reflector with  $F/D = 0.6$ ,  $f = 30$  GHz.

### 3.2.3. Double parabolic reflector configuration

Double parabolic reflector configurations are commonly known as imaging reflector systems [146]. They are constituted by a feeding phased array properly magnified by two reflector antennas. Such systems efficiently combine the advantages of the reflector and array antennas. They are commonly used to generate reconfigurable beams over a small angular scan range. Some sort of beam compression is realized to increase the illuminated region of the array significantly and, as a consequence, the number of simultaneously active elements. The working principle of a double parabolic reflector and the relevant geometrical dimensions are schematically shown in Fig. 3.23.

The simulated electric field distribution in the array plane for a double parabolic reflector configuration with  $F_m/D_m = 0.6$  and  $F_m/F_s = 8$  is shown in Fig. 3.24. The corresponding aperture efficiency is shown in Fig. 3.25. The size of the sub-reflector was chosen based on the array size from section 3.2.2 for the scanning case of  $\pm 3^\circ$  and aperture efficiency of 95 %,  $D_m/D_s = 4.5$  (see Fig. 3.22). The same excitation mechanism has been used. A planar array has been located at the surface of the main reflector. The sub-reflector blockage was included in the simulation. The resulting phase distribution in the array plane is presented in Fig. 3.26.

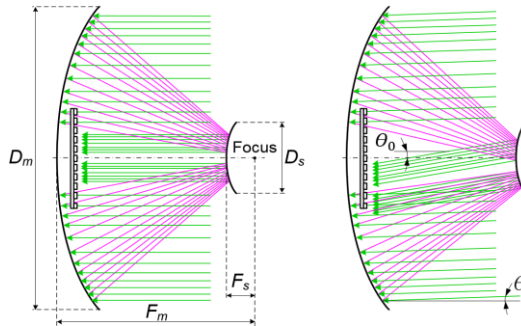


**Figure 3.23.** Symmetrical double parabolic reflector configuration.

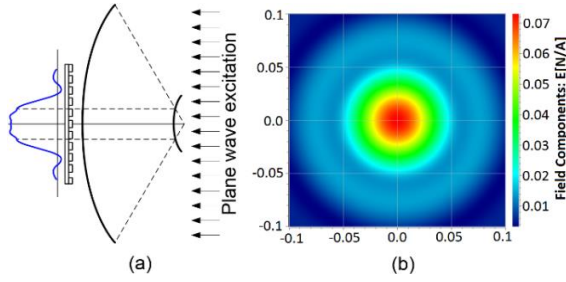


**Figure 3.24.** (a) Field distribution of a symmetrical double parabolic reflector antenna (b) corresponding 2D illustration of the field pattern in the array plane,  $F_m/D_m = 0.6$  for the main reflector,  $F_m/F_s = 8$  for sub-reflector,  $f = 30$  GHz [39].

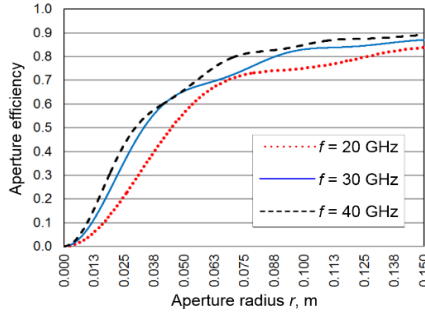


**Figure 3.25.** Aperture efficiency in the array plane of a symmetrical double parabolic reflector,  $F_m/D_m = 0.6$  for the main reflector,  $F_m/F_s = 8$  for the sub-reflector, and blockage of the sub-reflector is included.

According to Fig. 3.24 and 3.25, the illuminated region in the array plane is significantly expanded as compared to the classical prime-focus system. Based on an aperture efficiency of 80 %, the illuminated area of the array has been increased by a factor of 150, for this particular example. The aperture efficiency curve is less steep than in the case of a prime focus reflector, which indicates a broadening of the focal field distribution. In addition, the phase relation between the array elements shows an inverted V-kind of distribution as a function of  $r$  for reasonable array sizes over the entire frequency range, with a linearity error of  $3.06^\circ$  at 30 GHz.

The aperture efficiency and electric field cuts for different scan angles are presented in Fig. 3.27. The required array size in the case of scanning should be significantly increased in order to achieve sufficient aperture efficiency. The poor performance is due to the amplification of the incidence angle on the array surface, expressed by the magnification factor  $M$  [147]:

$$\theta_0 = \frac{F_m}{F_s} \theta = M \theta \quad (3.7)$$

where  $\theta$  is the angle of incidence of the incident field,  $\theta_0$  is the incident angle on the array surface (Fig. 3.23). As a result, even a small beam deviation of the incident wave causes a significant shift of the irradiated region. As a consequence, the array size should be significantly increased. Therefore, the number of active elements will be still significantly less than the number of inactive array elements. Therefore, also with this configuration, an effective exposure of the FPA cannot be achieved.

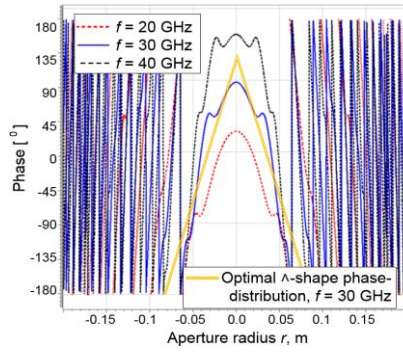


**Figure 3.26.** Phase distribution in the array plane of a symmetrical double parabolic reflector,  $F_m/D_m = 0.6$  for the main reflector,  $F_m/F_s = 8$  for the sub-reflector.

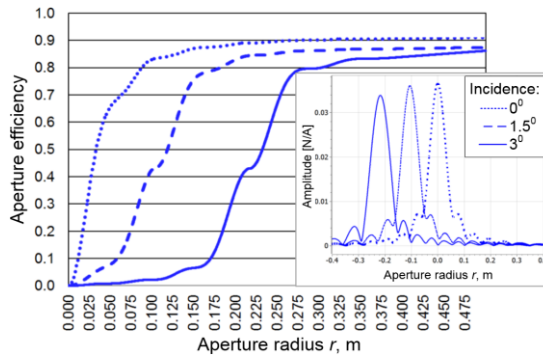


**Figure 3.27.** Aperture efficiency and electric field cuts in the array plane for different angles of incidence of the incident field of a symmetrical double parabolic reflector,  $F_m/D_m = 0.6$  for the main reflector,  $F_m/F_s = 8$  for the sub-reflector,  $f = 30$  GHz.

### 3.2.4. Optimization of double reflector configuration for FPA

Classical prime-focus reflector antennas have a relatively small illuminated region in the focal plane and do not allow the full use of the FPA capabilities. A double parabolic reflector allows increasing significantly the number of simultaneously active elements in the FPA system and can improve the linearity of the phase relation between the array elements. However, there is still the issue of the magnification of the incident angle on the projected FPA surface. Therefore, we need to find a way to decrease the magnification factor and to keep a sufficient number of active elements, at the same time. In order to do that, we have optimized the ratio between the required aperture radius for a  $1.5^\circ$  scan angle versus a  $0^\circ$  scan angle ( $AR_{1.5}$ ) and the ratio between a scan angle of  $3^\circ$  versus  $0^\circ$  scan angle ( $AR_3$ ).

As a starting point, a Cassegrain ring-focus configuration has been chosen [148]. In these systems, the electromagnetic field is focused on a single feed point located in the plane of the main reflector (see Fig. 3.28(a)). It is possible to shift the feed away from the sub-reflector and, at the same time, keep all beams focused on the feed, by optimization of the sub-reflector shape [149]. In this way, the beam can be broadened in the main reflector plane, where the array will actually be placed. If the illumination cone of the second reflector has a focus on infinity (Fig. 3.28(b)), the configuration could be considered as a double parabolic reflector

of section 3.2.3.

The field distribution in the array plane has been determined for a number of cases in which the focal point is shifted away from the original feed plane. The FPA is located at the surface of the main reflector (see Fig. 3.28(c)). The size of the sub-reflector has been defined in the same way as for the double parabolic configurations of section 3.2.3. The aperture efficiency has been calculated based on the electric field distribution according to Eq. (3.6). The required aperture radius, corresponding to an 80 % aperture efficiency at 30 GHz, is presented in Fig. 3.29 for angles of incidence of  $1.5^\circ$  and  $3^\circ$ . Wider scanning (e.g.  $5^\circ$  and  $10^\circ$ ) is an issue, due to the necessity of a larger sub-reflector resulting in significant blockage [150]. Note that blockage of the sub-reflector is included in our model.

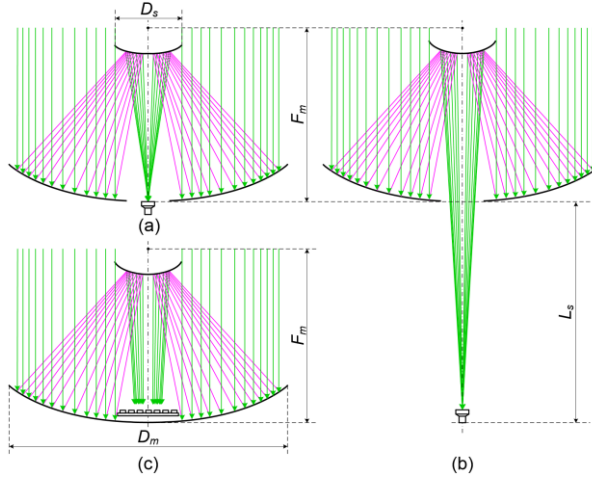


**Figure 3.28.** (a) Ring focus dual reflector (b) ring focus dual reflector with single shifted feed (c) ring focus dual reflector with FPA.

From Fig. 3.29, we can conclude that the aperture radius is increasing with increasing shifts from the feed plane ( $L_s$ ) for all considered scan angles. However, for the case of non-zero incidence ( $1.5^\circ$  and  $3^\circ$ ), the required aperture radius grows faster than for normal incidence. In order to find the optimum, the ratios  $AR_{1.5}$  and  $AR_3$  are presented in Fig. 3.30. It appears that these ratios can be optimized as a function of  $L_s$  (see Fig. 3.28(b)). According to Fig. 3.30, the minimum value of  $AR_{1.5}$  is 1.54 and the minimum of  $AR_3$  is 2.22. For the classical prime focus reflector case, according to Fig. 3.22, we find that  $AR_{1.5}=2.94$  and  $AR_3=5.87$ . For the double parabolic reflector configuration, according to Fig. 3.27, we find that  $AR_{1.5}=2.06$  and  $AR_3=3.43$ . Therefore, the proposed configuration is optimal in terms that we minimized the ratio between the required aperture radius for a  $1.5^\circ$  scan angle versus  $0^\circ$  ( $AR_{1.5}$ ) and the ratio between a scan angle of  $3^\circ$  versus  $0^\circ$  ( $AR_3$ ).

The optimization for both scan angles at the same time is not possible. Each value of  $L_s$  produces a different shape of the sub-reflector with different eccentricities. In our case, the optimal value of  $L_s$  for both cases is quite similar. Therefore, we have used  $L_s=0.22$  m as the optimal configuration. In this case, the ratio between the main reflector and the sub-reflector is  $D_m/D_s=8$ ,  $F_m/D_m=0.6$ , and  $F_s/D_s=6.9$ . The position of the sub-reflector has been chosen in such a way that we obtain an aperture efficiency level of 95 % on the sub-reflector surface for the scanning case of  $\pm 3^\circ$ .

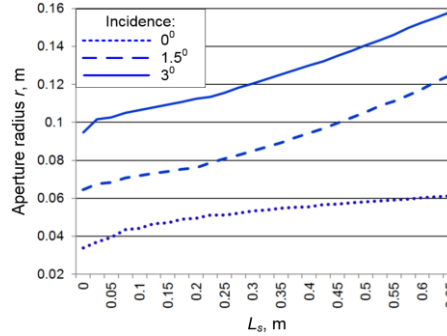


**Figure 3.29.** Aperture radius versus scan angle based on 80 % aperture efficiency for a ring focus dual reflector with FPA,  $f = 30$  GHz, blockage of sub-reflector is included.

The calculated field distribution in the array plane for the non-scanning case of the optimized symmetrical double reflector is presented in Fig. 3.31, and the corresponding aperture efficiency is in Fig. 3.32. The phase distribution in the array plane is presented in Fig. 3.33(a). The blockage of the sub-reflector is included in all these results. According to Fig. 3.31 and 3.32, the illuminated region in the array plane is significantly expanded as compared to the classical prime focus reflector in section 3.2.2. The illuminated area of the array has been increased by a factor of 60 based on an aperture efficiency of 80 %. The phase distribution between the array elements has approximately a linear V-kind of shape within the array size with an rms error of  $1.65^\circ$  at 30 GHz. For the central array element ( $r = 0$ ), the phase dependence versus frequency is very linear (rms error does not exceed 1 % at 30 GHz for all considered reflector configurations), see Fig. 3.33(b). Therefore, this configuration is more suitable for the optical beamforming network. Fig. 3.33(c) presents the phase distribution for the optical beamforming, which operates in a band 20-40 GHz, with discretization along frequency 1 GHz and  $\lambda_0/2$  distance between array elements, at the highest frequency. Fig. 3.33(d) presents the phase distribution in the array plane at 30 GHz for all investigated reflector configurations.

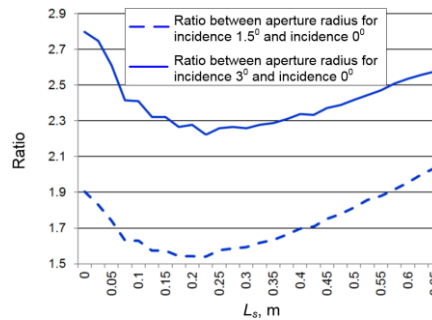


**Figure 3.30.** Ratios between aperture radius for different angles of incidence of the incident field based on 80 % aperture efficiency for a ring focus dual reflector with FPA,  $f = 30$  GHz, blockage of sub-reflector is included.

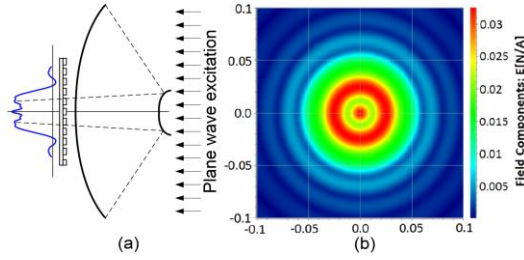


**Figure 3.31.** (a) Field distribution of an optimized symmetrical double reflector antenna (b) 2D illustration of pattern in the array plane of an optimized symmetrical double reflector,  $F_m/D_m = 0.6$  for the main reflector,  $f = 30$  GHz [39].

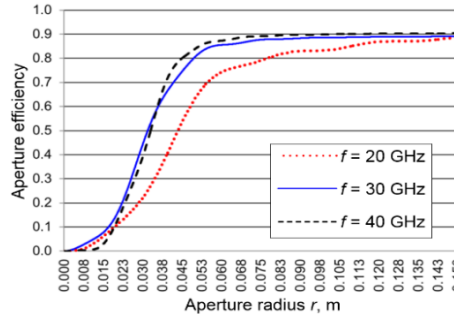


**Figure 3.32.** Aperture efficiency in the array plane of an optimized symmetrical double reflector,  $F_m/D_m = 0.6$  for the main reflector, blockage of the sub-reflector is included.

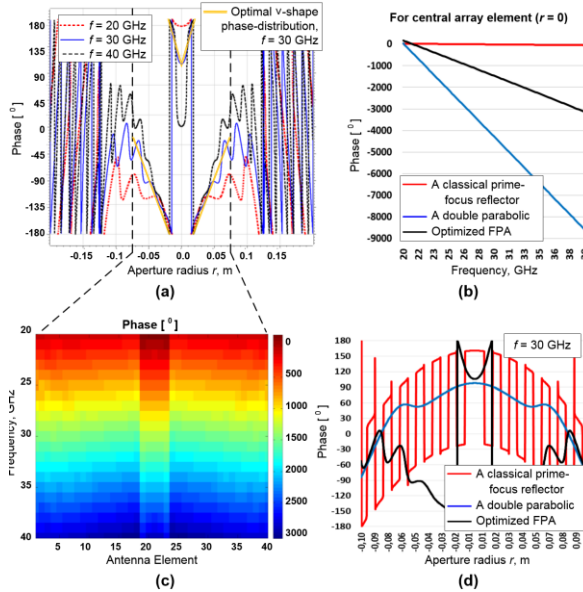


**Figure 3.33.** (a) Phase distribution in the array plane of an optimized symmetrical double reflector,  $F_m/D_m = 0.6$  for main reflector (b) Frequency dependence of the required phase for the central array element ( $r = 0$ ) for various investigated reflector configurations (c) Phase distribution between array elements of an optimized symmetrical double reflector with the discretization of  $\lambda/2$  at the highest frequency in the frequency band 20–40 GHz (d) Phase distribution in the array plane for investigated reflector configurations,  $f = 30$  GHz.

Next, we investigate the aperture efficiency and field distribution cuts for different scan angles. Results are presented in Fig. 3.34. It is clear that, with increasing scan angle, the region of maximum power becomes larger, but it is less shifted from the center, as compared to a prime-focus reflector or double-parabolic reflector. We observe a more uniform distribution of power over the array elements. This is significantly improved compared to the investigated configurations in sections 3.2.2 and 3.2.3, where there are elements with zero aperture efficiency like in Fig. 3.22 and Fig. 3.27 for the  $1.5^\circ$  and  $3^\circ$  scan cases. At the same time, the number of active elements is significantly increased. The required overall array dimensions are also much smaller as compared to the double parabolic reflector from section 3.2.3. A comparison of the investigated reflector configurations is given in Table 3.1. The comparison criteria have been analyzed for field distributions at the FPA surface at 30 GHz and for a target aperture efficiency of 80 %.

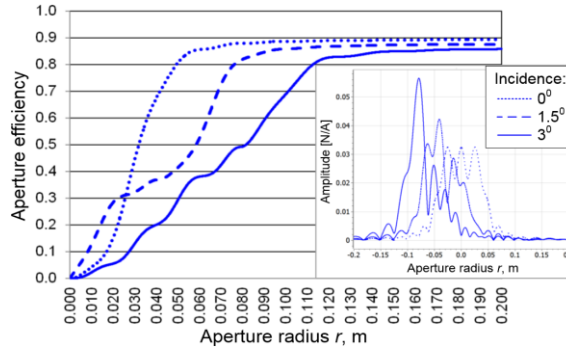


**Figure 3.34.** Aperture efficiency and electric field cuts for different angles of incidence of the incident field in the array plane of an optimized symmetrical double reflector,  $F_m/D_m = 0.6$  for the main reflector,  $f = 30$  GHz.

**Table 3.1.** Comparison of investigated reflector configurations at 30 GHz, element spacing is  $\lambda_0/2$  at 40 GHz.

Comparison Criteria	Wave incid.	Reflector configuration		
		<i>A classical prime-focus reflector</i>	<i>A double parabolic reflector</i>	<i>Optimized FPA</i>
Number of illuminated elements	$0^\circ$	8	~ 1600	~ 550
	$1.5^\circ$	8	~ 1600	~ 610
	$3^\circ$	8	~ 1600	~ 670
Required array size	$0^\circ$	0.6 cm	8.5 cm	5 cm
	$1.5^\circ$	1.9 cm	17.7 cm	7.8 cm
	$3^\circ$	3.4 cm	28 cm	11.5 cm
Scan performance: percent of active elements from the whole array	$0^\circ$	~ 100 %	~ 100 %	~ 100 %
		(Active array size is equal to the required array size)		
	$1.5^\circ$	~ 9.9 %	~ 22.8 %	~ <b>44.9 %</b>
	$3^\circ$	~ 3.1 %	~ 9.1 %	~ <b>22.7 %</b>
Phase linearity (see Fig. 3.33) and rms error		Completely nonlinear $6.36^\circ$	Linear inverted V-kind of shape $3.06^\circ$	Linear V-kind of shape $1.65^\circ$

### 3.2.5. Conclusion

We have presented a double reflector configuration that shows excellent performance of a wide frequency range in terms of maximizing the number of simultaneously active array

elements. Up to 22.7 % of elements are active simultaneously within a scan range of  $\pm 3^\circ$ . It also overcomes the well-known FPA problem of a small illuminated region in the focal plane by increasing it by a factor of 60, as compared to traditional prime-focus configurations. The phase linearity between the array elements has been improved to an rms error of  $1.65^\circ$  at 30 GHz. In addition, the scanning capabilities have been significantly improved as compared to classical prime focus and double-parabolic reflectors. The beam deviation decreased by a factor of 2.5, as compared to a double-parabolic configuration, for a scan range between  $\pm 1.5^\circ$ . Combined with wide-band photonic beamforming, this antenna configuration can result in a wideband, compact, low-weight, and energy-efficient antenna system for Ka-band communications.

### 3.3. Reflector theory and reflector for wide range application<sup>1</sup>

A mathematical analysis of reflector shaping for wide-angle scanning is presented. Parabolic, hyperbolic, and spherical reflectors are defined based on the geometrical optics method in order to have the smallest deviation of the focused beam (Fig. 3.35) during wide-angle scanning. It is shown that it is possible to expand the illuminated region of the array by a factor of 3 for parabolic reflectors with axial displacement based on an estimated 80 % aperture efficiency at 30 GHz,  $D/\lambda=80$ . Moreover, it is demonstrated that a spherical reflector has the smallest deviation from the axis of revolution during wide-angle scanning.

#### 3.3.1. Introduction

Focal-plane arrays (FPA) are considered the preferred antenna concept in a number of emerging applications [8], [9]. However, there are limiting factors for a full implementation of the advantages of this technology due to the challenges in the FPA illumination and the limitations in wide-angle scanning. In traditional FPAs, the illuminated region in the focal plane is relatively small [145]. Only a few elements can be located in the area of maximum power density. This fact limits the number of involved active elements, and as a result, this limits the EIRP level and the beam-scanning capability [15]. In addition, the required size of the feed-array should be significantly increased due to the large beam deviation from the center of the feed-array during wide-angle scanning [143]. The goal of this chapter is to investigate various reflector configurations in order to find a reflector shape that is most suitable for wide-angle scanning and could broaden the region of high-power density in FPAs.

#### 3.3.2. Mathematical model of reflector

In order to find an optimal shape for wide-angle scanning, we have defined our reflector in terms of a second-order polynomial (see also Fig. 3.35):

$$a_{11}x^2 + a_{22}y^2 + 2a_{12}xy + 2a_{13}x + 2a_{23}y + a_{33} = 0 \quad (3.8)$$

with coefficients  $a_{ij}$ . The geometrical optics approach has been applied in order to analyze the reflection properties of various reflector shapes. The considered properties are presented in Fig. 3.35. Incidence and reflection angles can be found from the equations of the incident and reflected waves and the normal to the reflector surface. These can be analytically computed from the polynomial interpretation of the reflector. For different incidence angles, the beam is focused off the axis of revolution. The beam deviation can be derived from the line equations of the reflected waves. The value of beam deviation is given by:

$$S(a_1, P_1, P_2, D) = \frac{D/2}{(P_1P_2 + 1)(P_1 - P_2)(a_1^2 + 1)} (P_1^2P_2a_1^2 - P_1^2P_2^2a_1 - P_1^2P_2 + P_1^2a_1 + P_1P_2^2a_1^2 - P_1P_2^2 + 4P_1P_2a_1 - P_1a_1^2 + P_1 + P_2^2a_1 - P_2a_1^2 + P_2 - a_1) \quad (3.9)$$

where  $a_1 = \tan(\alpha)$  is the tangent of the angle of the incident wave,  $P_1$  and  $P_2$  are polynomials defined by the reflector shape:

<sup>1</sup>Current paragraph 3.2 is published as a journal paper: Dubok, A; Al-Rawi, A; Tessema, N; Tangdionga, E; Herben, M.H.A.J; Gerini, G; Smolders, A. B, "Double Reflector Configuration for Optimal Exposure of Wideband Focal Plane Arrays with Optical Beamforming," IEEE Transactions on Antennas & Propagation, no. 10.1109/TAP.2017.2709620, 2017, and included here in its entirety without any changes.

$$P_1 = \frac{a_{12}P_3 + a_{22} \frac{D}{2} + a_{23}}{a_{11}P_3 + a_{12} \frac{D}{2} + a_{13}} \quad P_2 = \frac{a_{12}P_3 - a_{22} \frac{D}{2} + a_{23}}{a_{11}P_3 - a_{12} \frac{D}{2} + a_{13}} \quad (3.10)$$

$$P_3 = \sqrt{\frac{(D/2)^2 a_{12}^2 + D a_{12} a_{13} + a_{13}^2 - (D/2)^2 a_{11} a_{22} - D a_{11} a_{23} - a_{11} a_{33} - a_{13} - a_{12} (D/2)}{a_{11}}}$$

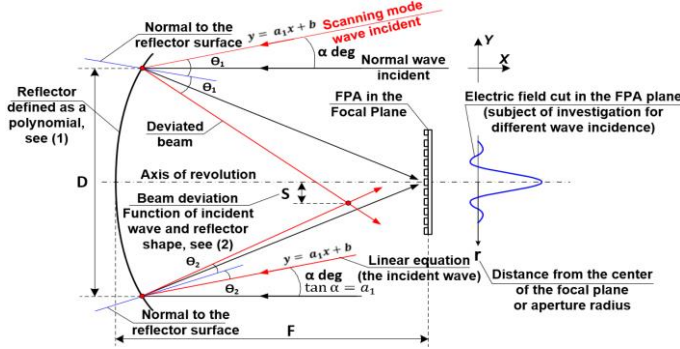


**Figure 3.35.** The displacement of the beam from the axis of revolution during scanning in XY-plane.

The range of the incident angles is defined by the wide-angle scanning requirements of the application. The goal is to find the polynomial coefficients of Eq. (3.8), which provide the smallest value of the beam deviation given by Eq. (3.9). In order to make a further analysis of a 3D reflector shape, the desired polynomial coefficients are presented in the GRASP format for a second order polynomial [39]:

$$A_{xx}x^2 + A_{xy}xy + A_{yy}y^2 + A_x x + A_y y + A_c = A_{zz}z^2 + A_z z + A_{xz}xz + A_{yz}yz \quad (3.11)$$

where the coefficients on the left side of the equation are identical to the coefficients of (3.8).

We found three different optimal reflector shapes: parabolic, hyperbolic, and spherical reflector. Nonzero coefficients of Eq. (3.11) for the parabolic shape are:  $A_{xx}=A_{yy}=0.52$ ,  $A_z=1$  or in other form  $F/D = 0.6$ , for the hyperbolic shape:  $A_{xx}=A_{yy}=2.1$ ,  $A_{zz}=1.6$ ,  $A_z=3.6$  and for the spherical shape:  $A_{xx}=A_{yy}=A_{zz}=1$ ,  $A_z=1.6$ .

### 3.3.3. Reflector comparison

The obtained reflector shapes have been analyzed in GRASP by means of physical optics [39]. The electric field in the FPA plane is computed for different wave incidence angles. When we calculate the obtained power by integrating the electric field along  $r$  and normalize it to the total power obtained by the reflector, it is possible to calculate the aperture efficiency in the FPA plane [15]. Two scanning ranges have been investigated:  $\pm 5$  degrees and  $\pm 10$  degrees. The reflector diameter is  $D = 0.8$  m,  $D/\lambda = 80$ . The aperture efficiencies, for different angles of incidence, are presented in Fig. 3.36, for the three investigated reflector configurations. It is clear that the spherical reflector has the smallest deviation, and as a result, the smallest required lateral array size in order to provide certain wide-angle scanning, which corresponds to [151].

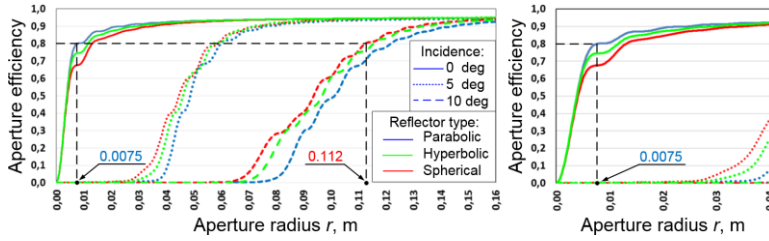


**Figure 3.36.** Aperture efficiency for different angles of incidence of the excitation waves in the FPA plane, for different reflector configurations,  $f = 30$  GHz.

In order to improve the situation with a smaller illuminated region in the focal plane, different axial displacements of the FPA have been analyzed for the investigated reflector shapes, in the case of normal-wave incidence see Fig. 3.37. Based on the simulation results, it was found that an axial displacement of  $2.25\lambda$  of the FPA towards the parabolic reflector expands the illuminated region of the array by a factor of 3 based on an 80% aperture efficiency at 30 GHz. This results in a smooth energy distribution along the feed-array elements. For hyperbolic and spherical reflectors, the best result is achieved for an axial displacement of  $1\lambda$  of the FPA outwards the reflector. This has benefits in terms of a more equal distribution of the energy along the array elements without a significant increase in the required size of the array.

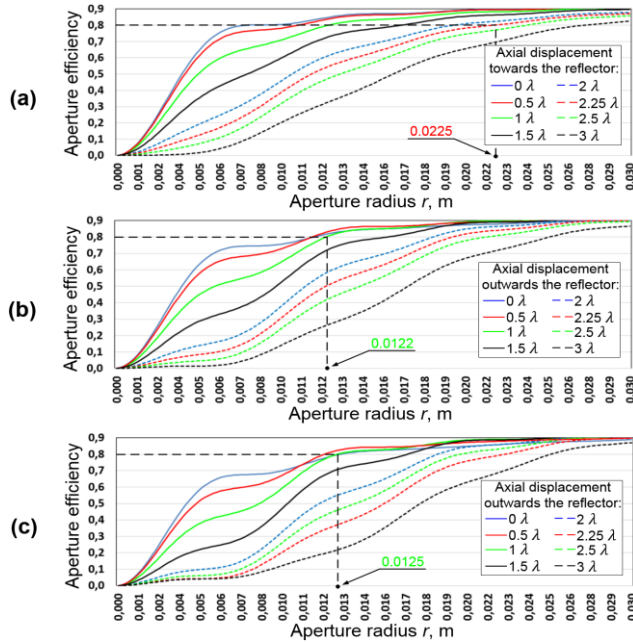


**Figure 3.37.** Aperture efficiency for different axial displacements of FPA in the case of normal-wave incidence,  $f = 30$  GHz, (a) towards the parabolic reflector, (b) outwards the hyperbolic reflector, (c) outwards the spherical reflector.

The aperture efficiency for different angles of incidence is presented in Fig. 3.38 for the investigated reflector configurations with proposed axial displacements. We can observe that the parabolic reflector has the most benefits of expanding the illuminated region for normal-

wave incidence. In addition, it has almost the same performance for wide-angle scanning as compared to the hyperbolic and spherical reflectors with optimal axial displacements. However, if we compare this parabolic displaced reflector with the original configurations without optimal axial displacements, the wide-angle scanning performance is still inferior to the spherical reflector (Fig. 3.36 and 3.38).

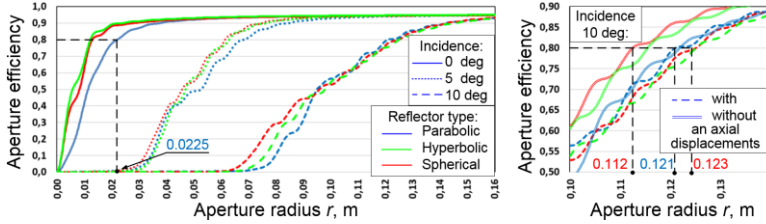


**Figure 3.38.** Aperture efficiency for different angles of incidence of the excitation waves in the FPA plane, for different reflector configurations with and without an optimal axial displacement,  $f = 30$  GHz.

### 3.3.4. Conclusion

We have presented a mathematical model for reflector shaping to minimize beam deviation during scanning. We verified this model by means of a physical optics approach in GRASP. We found that the parabolic configuration with an axial displacement of  $2.25\lambda$  towards the reflector shows the largest illuminated region of the feed-array. Whereas the spherical reflector without axial displacements is the best option for minimization of the lateral array size for wide-angle scanning operations.

# CHAPTER FOUR

## 4. REFLECTOR SYNTHESIS FOR WIDE-SCANNING FOCAL PLANE ARRAYS<sup>1</sup>

---

### Summary

A new complex offset double reflector configuration for a wideband focal plane array (FPA) is presented which is optimized for Ka-band applications with a scan range of  $\pm 20^\circ$  in the azimuth plane. This configuration is obtained by using a mathematical framework based on geometrical optics (GO) which allows us to optimize complex double-reflector FPAs with limited computational effort. The proposed reflector configuration maximizes the number of simultaneously active array elements of the phased-array feed (PAF) and minimizes the required total number of array elements for this wide scan range. To realize an aperture efficiency of at least 80% at 30 GHz, our concept allows half of the antenna elements in the array to be active during scanning for a scan range of  $\pm 10^\circ$  and at least a quarter of the array elements to be active for a scan range of  $\pm 20^\circ$ . This is a major improvement as compared to the scanning capabilities of focal-plane arrays based on conventional single and double-parabolic reflector configurations. In addition, the FPA configuration has been optimized for wideband optical true-time-delay (TTD) beamforming which requires a linear phase distribution along the array elements. We obtained a phase linearity with an rms error of  $2.81^\circ$  at 30 GHz. The experiments from the realized prototype demonstrate good agreement between simulation and measurements and fully prove the required scanning performance over a  $\pm 20^\circ$  scan range. The prototype demonstrates a high directivity up to 46 dBi at 30 GHz and 48 dBi at 40 GHz and aperture efficiency up to 83 % at 30 GHz and 77 % at 40 GHz.

### 4.1. Introduction

Focal-plane arrays (FPAs) appear to be a very interesting antenna concept that combines the benefits of phased-arrays and traditional reflector-based solutions by offering a high antenna gain, relatively low costs, and electronic beam scanning over a limited field-of-view (FoV). Therefore, it has become an interesting alternative for conventional horn-fed reflector antennas in a number of applications, e.g. in radio astronomy [8] and in satellite communication [9], [10]. Moreover, emerging applications such as 4G/5G point-to-point wireless communications, 5G new-radio millimeter-wave (mm-wave) wireless and low-cost Ka-band (30-40 GHz) multi-function radars could be areas in which FPAs can play a major role. These future microwave and mm-wave applications set new requirements on FPA

<sup>1</sup>Current chapter (paragraphs 4.1 – 4.6) is published as a journal paper: Dubok A., Al-Rawi A., Gerini G., Smolders A. B., "Reflector Synthesis for Wide-Scanning Focal Plane Arrays," IEEE Transactions on Antennas and Propagation, vol. 67, no. 3, 2019.

systems such as a wide FoV covering a scan range up to  $\pm 20^\circ$ , large instantaneous bandwidth up to an octave, and a highly effective isotropic radiated power (EIRP) in transmit mode using silicon-based integrated circuits [15].

However, there are still a lot of limitations in the state-of-the-art of FPAs that need to be improved before FPAs can be applied in several of the mentioned applications with these challenging requirements. First of all, the FoV is limited in conventional FPAs due to the significant beam deviation in the focal plane, and as a result, relatively large arrays are required in the focal plane [143], [38]. This leads to high costs and complexity of the FPA system. Secondly, the small number of simultaneously active array elements in traditional FPA systems limits the multiple-beam capability [142] and the maximum EIRP [15] that can be achieved. A third limitation in existing FPA concepts is the frequency bandwidth. In order to obtain a high aperture efficiency, the array spacing needs to be close to  $\lambda_0/2$  at the highest frequency of operation [30], where  $\lambda_0$  is the free-space wavelength. As a result, the mutual coupling between the array elements is rather high and causes the active input impedance of each element to be different and highly dependent on frequency and angle of incidence [31], [32]. The final limitation is related to the specific beamformer used in this work. To obtain a wide bandwidth we will use a novel optical beamforming network that provides multi-beam operation over a wide instantaneous bandwidth [34]. The optical beamformer utilizes true time delay (TTD) units, implemented in optical integrated circuits (ICs). These optical ICs generate frequency-independent time delays with a linear phase [35]. Therefore, a linear phase distribution along the array elements of the FPA is required in order to realize such an optical beamformer circuit [36], [37]. This sets an additional requirement for our FPA system.

In this chapter, we present the outcome of a study to overcome these limitations. The goal of our work was to develop a wideband FPA system, operating in the frequency band of 20-40 GHz with a scan range up to  $\pm 20^\circ$  in the azimuth plane. The FPA should maximize the EIRP using silicon-based ICs and should minimize the beam deviation in the focal plane region during scanning. Next to this, it should accommodate optical beamforming requiring a linear phase distribution along the array elements.

To realize these stringent requirements, we propose a new concept for optimal array illumination by the reflector. The idea is based on increasing the number of simultaneously active elements in the FPA in order to overcome the limitation of a small illuminated region in traditional FPA concepts. By realizing a close to uniform amplitude distribution over the array elements, we can increase the achievable EIRP and system sensitivity. To synthesize the optimal configuration of our new double-reflector FPA concept, we have developed a mathematical framework based on geometrical optics (GO). We have implemented this framework for single and double-reflector FPA systems. Various FPA systems with centered and offset single- and double-reflector configurations have been optimized and verified with a physical optics (PO) approach using GRASP [39]. The final double-reflector FPA configuration achieves the required scanning range with a compact phased-array feed (PAF), which has at least half of the array elements simultaneously active during scanning. In our study, we have used the classical prime-focus reflector with a diameter  $D = 0.8$  m and  $F/D = 0.6$  (with  $F$  the reflector focal length) as a reference configuration to evaluate the performance improvement of the optimized reflector configurations. The array element spacing is chosen as  $\lambda_0/2$  at the central frequency of 30 GHz.

In summary, this chapter presents the following new scientific contributions:

- a parametric mathematical framework using GO has been implemented for single and double reflector optimization for FPA systems,
- all well-known types of FPA reflectors configurations have been compared for applicability to operate at broadside scan and for wide-angle scanning,
- a new type of reflector concept is proposed with a very compact PAF to realize wide-angle scanning over a wide bandwidth,
- the proposed reflector configuration maximizes the ratio of active array elements in FPAs and provides a close-to-linear phase distribution along the PAF,
- experimental validation of a complete mm-wave FPA system with a wide FoV.

The structure of the chapter is as follows: Section 4.2 describes the illumination challenges of classical prime-focus reflectors and reflectors with our desired illumination properties called "the ideal reflector for array illumination". Section 4.3 discusses the mathematical GO framework that is used to synthesize the optimal single- and double-reflector FPA systems. In Section 4.4, we present the simulation results of the different optimized reflector configurations. Finally, in Section 4.5, we provide experimental results from the 20-40 GHz prototype FPA system with improved scanning capabilities.

#### **4.2. Limitations of classical parabolic prime-focus reflectors and ideal array illumination**

The electric-field distribution in the focal plane of a classical prime-focus reflector behaves according to the well-known distribution of so-called Airy rings, corresponding to zeros of the Bessel function of the first kind and order 1 along the aperture radius  $r$  [145]. According to [145], it is clear that the same reflector operating at higher frequencies will illuminate a smaller region in the focal plane. As an example, the electric-field in the focal plane of a classical prime-focus reflector with  $F/D = 0.6$  and  $D = 0.8$  m is presented in Fig. 4.1 for 20, 30, and 40 GHz, respectively. The phase distribution in the focal plane of the investigated parabolic reflector is shown in Fig. 4.2. It is clear that the phase distribution along the array plane is nonlinear. In the area of maximum power density (above the -3 dB level), the linearity of the phase distribution shows a root-mean-square (rms) error of  $6.36^\circ$  at 30 GHz. Since we will use the optical beamforming network as discussed in [37], this phase distribution will lead to a deterioration of the FPA performance.

The performance of a classical prime-focus reflector in the case of  $10^\circ$  angle of incidence of the incoming plane wave is provided in Fig 4.3, and for the case of  $20^\circ$ — in Fig. 4.4. The focal plane position is defined based on the location of the focal point as illustrated in Fig. 4.1. We can observe that for various angles of incidence, the region of maximum power is broadened, but significantly shifted away from the array center. This means that the array size should be increased in order to provide good scanning capabilities with high antenna efficiencies.

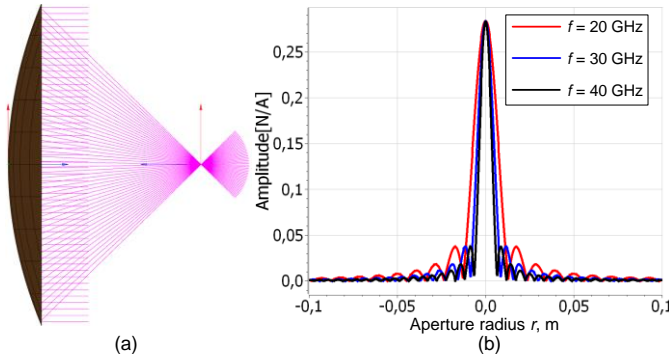


**Figure 4.1.** (a) Reflector configuration (b) electric-field cuts in the focal plane for broadside operation of a classical prime-focus reflector with  $F/D = 0.6$ ,  $D = 0.8$  m.

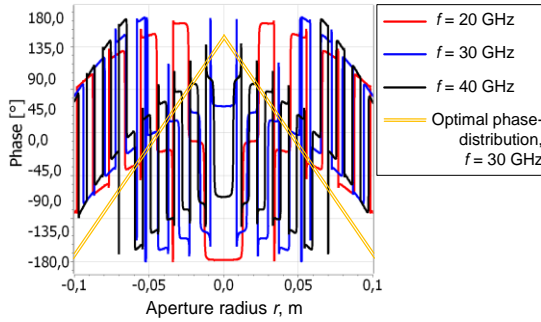


**Figure 4.2.** Phase distribution in the focal plane of a classical prime-focus reflector with  $F/D = 0.6$ ,  $D = 0.8$  m. The optimal phase distribution for our optical beamformer is also shown.

It is possible to estimate the energy distribution along the array and to calculate the aperture efficiency in accordance with [152]. The aperture efficiency distribution for the electric-field cuts of Fig. 4.1, 4.3-4.4 are presented in Fig. 4.5. The aperture efficiency estimation includes the radiation efficiency of the reflector, taper efficiency, spill-over efficiency, and polarization efficiency. It is determined according to [152]. According to Fig. 4.5, the illuminated region in the focal plane for normal incidence is relatively small. When we assume an array element spacing of  $\lambda_0/2$  at the center frequency (30 GHz), only a few elements are located in the area of maximum power density (above the -3 dB level). In addition, Fig. 4.5 shows that by considering larger array sizes, the aperture efficiency first increases very quickly until  $r$  reaches the first Airy ring and then remains almost constant. In the case of  $10^\circ$  and  $20^\circ$  angles of incidence of the incoming plane wave, the required array size is significantly increased. At the same time, most of the array elements will not be active at the same time. Therefore, the ratio of active elements to the total number of array elements is low and, as a result, the FPA is used inefficiently. This will limit the achievable EIRP level and beam scanning capabilities. Moreover, to provide scanning up to  $\pm 20^\circ$  in the azimuth plane, the dimension of the array should be at least 0.52 m to achieve an 80% aperture efficiency with a reflector size of 0.8 m. In other words, the PAF dimension is about 65% of the reflector diameter, which is undesirable. Therefore, we need to minimize the beam deviation during scanning in order to limit the FPA size and overall system cost. Another possible problem is related to the required linear phase distribution. In [152] it was shown

that even at broadside this cannot be realized with a classical prime-focus FPA.

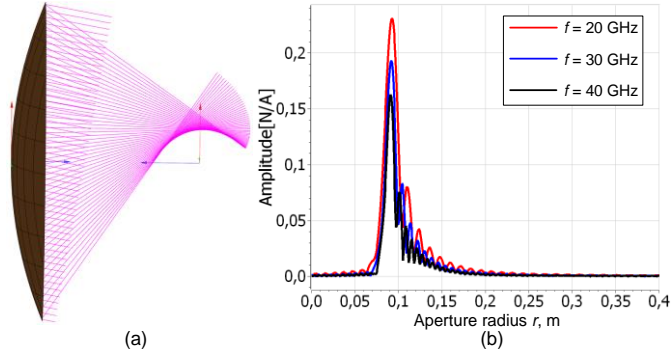


**Figure 4.3.** (a) Reflector configuration (b) electric-field cuts in the focal plane for  $10^\circ$  angle of incidence of a classical prime-focus reflector with  $F/D = 0.6$ ,  $D = 0.8$  m.

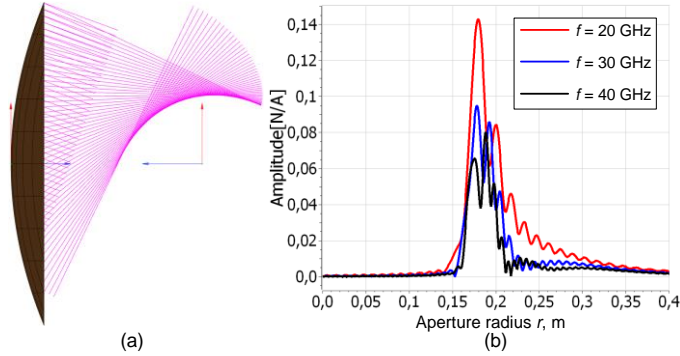


**Figure 4.4.** (a) Reflector configuration (b) electric-field cuts in the focal plane for  $20^\circ$  angle of incidence of a classical prime-focus reflector with  $F/D = 0.6$ ,  $D = 0.8$  m.

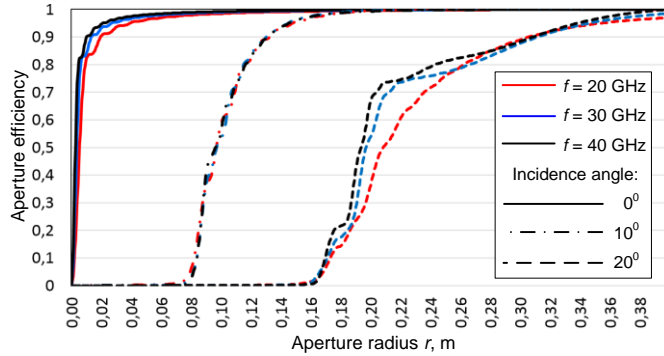


**Figure 4.5.** Aperture efficiency in the focal plane for different angles of incidence of a classical prime-focus reflector with  $F/D = 0.6$ ,  $D = 0.8$  m

In order to design an FPA system with improved PAF illumination characteristics, we first need to define the so-called “ideal” focal-plane illumination. Compared to the traditional prime-focus reflector, the ideal reflector should provide a close to uniform amplitude illumination and constant or linear phase along the PAF. To have a sufficient number of simultaneously active elements, the illuminated array size should be at least a few cm at 30

GHz. For example, using an ideal array size of  $4 \text{ cm}^2$ , 16 elements will be available with element spacing  $\lambda_0/2$  at 30 GHz. An example of the ideal amplitude and phase distribution provided by the ideal (non-physical) reflector is presented in Fig. 4.6 for broadside operation. In this case, several array elements are illuminated simultaneously.

It is possible to estimate the aperture efficiency for an “ideal” focal-plane illumination in accordance with [152]. It is obvious that for any distribution of the electric-field in the array plane an aperture efficiency of 100% could be achieved only by using an infinitely large aperture radius. Therefore, the level of the aperture efficiency of 80% has been chosen as a reference value. The aperture efficiency of a reflector with “ideal” array illumination is presented in Fig. 4.7 and can be used as a reference in the evaluation of various reflector configurations obtained during optimization. Note that the array blockage is included in Fig. 4.7. Therefore, the aperture efficiency level starts to decrease with the increasing size of the aperture radius.

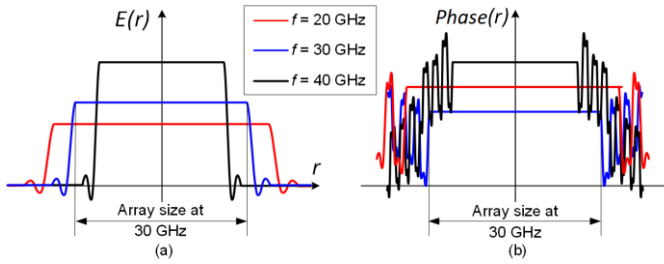


**Figure 4.6.** (a) Electric-field cuts in the array plane (b) Phase distribution in the array plane for broadside operation for a reflector with ideal array illumination.

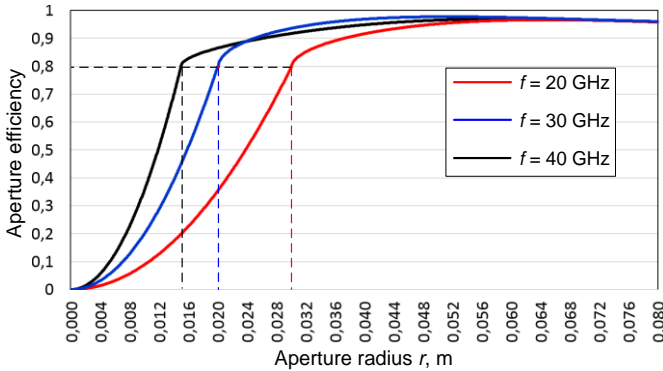


**Figure 4.7.** Aperture efficiency in the array plane for broadside operation of a reflector with ideal array illumination.

In the case of scanning, the illumination pattern would shift as illustrated in Fig. 4.8. In the ideal case, this deviation should be as small as possible in order to minimize the required overall array size. In other words, our ideal configuration resembles the traditional phased-array antenna without a reflector [32]. It is obvious that it is not possible to achieve completely the same operation properties of our FPA as for phased arrays by reflector shaping, especially in the case of wide-range scanning. Nevertheless, in our optimization of the reflector shape, we will try to achieve the ideal case as best as possible. The mathematical principles of reflector optimization are presented in the next paragraph.

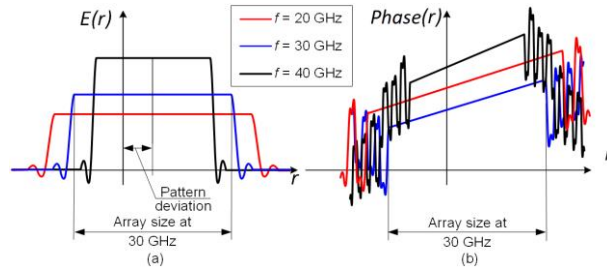


**Figure 4.8.** (a) Electric-field cuts in the array plane (b) Phase distribution in the array plane for the non-zero angle of incidence for a reflector with ideal array illumination.

### 4.3. Mathematical principles of reflector synthesis based on geometrical optics

Our goal is to develop a model of the FPA system for an arbitrary shape of the main- and sub-reflectors. To develop a model of the FPA system which could approach an “ideal” focal-plane illumination, it is necessary to optimize the shape of the main- and sub-reflectors. The optimized model is then verified using physical optics (PO) with the more accurate and computationally more intensive model. Our model uses a geometrical optics (GO) approach, which applies Snell's law according to [153], [154], and [155]. When we describe the reflector surface as a mathematical function and divide the surface into a finite number of points, it is possible to find the normal at each point of the reflector. Based on Snell's law, the reflected wave in each reflector point can be calculated. In this way, the field distribution in the array plane can be determined.

The obtained distribution of the field in the array plane can then be correlated to the ideal illumination model as described in Section 4.2 in order to set a cost function in our optimization process. As a result, the cost function will have a direct mathematical relation to the shape of the reflector surface.

Based on this approach, we have developed and implemented a GO optimization code for different types of reflectors: a two-dimensional center-fed reflector model with a single and double-reflector, and a three-dimensional offset reflector model with a single and double-reflector. A brief explanation of the mathematical principles is presented below.

#### 4.3.1. Two-dimensional center-fed single-reflector model

The symmetrical center-fed reflector can be expressed in a two-dimensional coordinate system, as shown in Fig. 4.9. In order to find an optimal shape for wide-angle scanning, we have defined our reflector in terms of a second-order polynomial (see also Fig. 4.9):

$$S(x, y) = A_{xx}x^2 + 2A_{xy}x + A_{yy}y^2 = 0, \quad (4.1)$$

where  $A_{ij}$  are polynomial coefficients which will be defined by our optimization process. The reflector center is located in the center of the coordinate system.

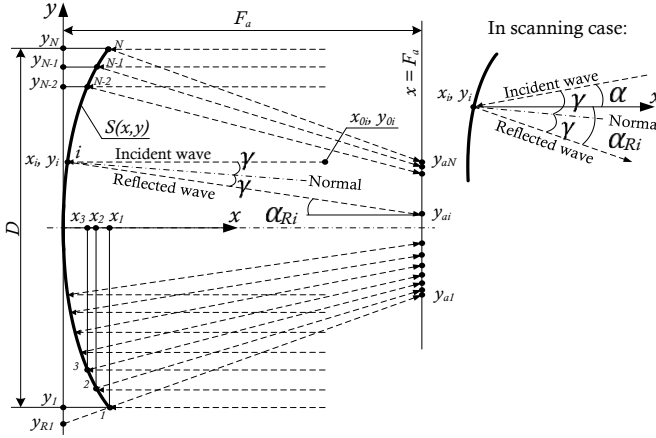


**Figure 4.9.** Two-dimensional model of the symmetric center-fed single-reflector.

Discretization of the reflector to the  $N$  points along the  $y$ -coordinate gives:

$$y_i = y_1 \dots y_N, \quad y_1 = -\frac{D}{2}, \quad y_N = \frac{D}{2}, \quad (4.2)$$

where  $D$  is the diameter of the reflector. To find the corresponding  $x$  coordinate, it is necessary to solve (4.1) as a quadratic equation:

$$x_i = -\frac{A_x \pm \sqrt{A_x^2 - A_{xx}A_{yy}y_i^2}}{A_{xx}}. \quad (4.3)$$

From the two possible solutions of  $x_i$  in (4.3), the solution with a real value should be selected in order to have a realistic shape of the reflector. In case  $S(x, y)$  is a closed surface, like part of an ellipsoid or sphere, the nearest value of  $x_i$  to the center of the coordinate system should be chosen. As a result,  $N$  reflector points are defined by the coordinates  $(x_i, y_i)$ , see Fig. 4.9.

The linear equation of the normal at point  $(x_i, y_i)$  can be set via partial derivatives of  $S(x, y)$  in the following way:

$$\frac{x - x_i}{\frac{\partial S(x_i, y_i)}{\partial x}} = \frac{y - y_i}{\frac{\partial S(x_i, y_i)}{\partial y}}, \quad (4.4)$$

where  $\frac{\partial S(x_i, y_i)}{\partial x} = 2A_{xx}x_i + 2A_x$ ,  $\frac{\partial S(x_i, y_i)}{\partial y} = 2A_{yy}y_i$ . In the form of a linear equation in  $xy$ -coordinates, the normal could be expressed as:

$$y = (x - x_i) \frac{2A_{yy}y_i}{2A_{xx}x_i + 2A_x} + y_i. \quad (4.5)$$

Snell's law states that the angle  $\gamma$  between the incidence wave and the normal to the surface is equal to the angle between the normal and the reflected wave. The  $\tan(\gamma)$  between two straight lines given by equations  $y = k_1x + b_1$  and  $y = k_2x + b_2$ , is calculated by:

$$\tan(\gamma) = \frac{k_2 - k_1}{1 + k_1 k_2}. \quad (4.6)$$

For an incidence wave, we find that:  $k_1 = \tan(\alpha)$ ,  $k_2 = \frac{2A_{yy}y_i}{2A_{xx}x_i + 2A_x}$ ; for a reflected wave we obtain:  $k_1 = \frac{2A_{xx}x_i + 2A_x}{2A_{yy}y_i}$ ,  $k_2 = \tan(\alpha_{Ri})$ . Applying Snell's law gives:

$$\tan(\gamma) = \frac{\tan(\alpha) - \frac{2A_{yy}y_i}{2A_{xx}x_i + 2A_x}}{1 + \tan(\alpha) \frac{2A_{yy}y_i}{2A_{xx}x_i + 2A_x}} = \frac{\frac{2A_{yy}y_i}{2A_{xx}x_i + 2A_x} - \tan(\alpha_{Ri})}{1 + \frac{2A_{yy}y_i}{2A_{xx}x_i + 2A_x} \tan(\alpha_{Ri})}. \quad (4.7)$$

Equation (4.7) could be solved for  $\tan(\alpha_{Ri})$  as:

$$\tan(\alpha_{Ri}) = \frac{\tan(\alpha) \left( \frac{2A_{yy}y_i}{2A_{xx}x_i + 2A_x} \right)^2 + 2 \frac{2A_{yy}y_i}{2A_{xx}x_i + 2A_x} - \tan(\alpha)}{2 \tan(\alpha) \frac{2A_{yy}y_i}{2A_{xx}x_i + 2A_x} + 1 - \left( \frac{2A_{yy}y_i}{2A_{xx}x_i + 2A_x} \right)^2}. \quad (4.8)$$

In order to define the line equation which represents the path of the reflected wave, the y-coordinate which belongs to the line equation of the reflected wave for  $x = 0$  is defined as:

$$y_{Ri} = y_i - x_i \tan(\alpha_{Ri}). \quad (4.9)$$

The array plane is a set of points located in the plane  $x = F_a$ . The y-coordinate of the reflected waves at the array plane  $y_{ai}$  gives a distribution of the field as a set of coordinates, which can be written as:

$$y_{ai} = F_a \tan(\alpha_{Ri}) + y_{Ri}. \quad (4.10)$$

According to Fig. 4.6, the optimum field distribution in the array plane provides a uniform amplitude and linear phase distribution along the array elements. To define the optimum amplitude distribution as a set of coordinates of the  $N$  reflected rays in the array plane, we have to define the ideal distribution of the coordinates of the  $N$ -points, indicated by  $y_{ai}$ . When we consider a symmetric two-dimensional reflector, the ideal focal area would be a uniform radial distribution. Translating this towards the one-dimensional representation of Fig. 4.6, the wanted distribution due to the rays reflected at the  $N$  points, would take the following form:

$$A_{ai}^w = A_{ai}^0 \left( 1 + \frac{L_y}{2} - \sqrt{\left( \frac{L_y}{2} \right)^2 + \left( A_{ai}^0 + \frac{L_y}{2} \right)^2} \right), \quad A_{ai}^0 < 0, \\ A_{ai}^w = A_{ai}^0 \left( 1 + \frac{L_y}{2} - \sqrt{\left( \frac{L_y}{2} \right)^2 - \left( A_{ai}^0 + \frac{L_y}{2} \right)^2} \right), \quad A_{ai}^0 > 0, \quad (4.11)$$

where  $A_{ai}^0 = -\frac{L_y}{2} + \frac{L_y}{N-1}(i-1)$ , for  $i = 1..N$ , where  $L_y$  is the size of the array along the y direction. It is important to note that the array size should be at least a few wavelengths. Otherwise, we will have a significant difference between the GO and PO simulation results due to the ray caustics in the array plane [156].

Based on the obtained coordinates  $y_{ai}$  and the wanted distribution, defined in (4.11), the amplitude cost function can be defined as a standard deviation:

$$Cost_{Amp} = \sqrt{\frac{1}{N} \sum_{i=1}^N (A_{ai}^w - y_{ai})^2} . \quad (4.12)$$

The wavefront has been defined in front of the reflector as a set of points with coordinates  $(x_{0i}, y_{0i})$  (see Fig. 4.9). The total length of each path for each ray can be calculated as:

$$L_i = \sqrt{(x_i - x_{0i})^2 + (y_i - y_{0i})^2} + \sqrt{(F_a - x_i)^2 + (y_{ai} - y_i)^2}. \quad (4.13)$$

In order to estimate the phase linearity along the array, the standard deviation for the phase path can be defined by:

$$Cost_{Ph} = \sqrt{\frac{1}{N} \sum_{i=1}^N ((L_i - L_{N/2})/\lambda_0)^2}. \quad (4.14)$$

Normalization to the wavelength  $\lambda_0$  makes the function invariant to the chosen frequency. One of the main optimization goals is to minimize the deviation of the field in the array plane during scanning. The deviation of the reflected waves in the array plane  $\Delta_{y_a}$  can be determined by calculation of the standard deviation of the field distributions in the case of normal incidence versus the scan case:

$$Cost_{\Delta} = \Delta_{y_a} = \sqrt{\frac{1}{N} \sum_{i=1}^N (y_{ai}^n - y_{ai})^2}, \quad (4.15)$$

where  $y_{ai}^n$  are the y-coordinates of the reflected waves at the array plane in the case of normal incidence.

In the case of scanning, the amplitude cost function should be corrected, in order to include the fact that the overall array distribution is shifted along the  $x$ -axis:

$$A_{ai}^w = A_{ai}^{wn} + \Delta_{y_a}, \quad (4.16)$$

where  $A_{ai}^{wn}$  is the distribution in the case of normal incidence.

The total cost function is a combination of amplitude, phase, and deviation cost functions with adjusted coefficients:

$$Cost = K_{sh} Cost_{\Delta} + K_{Amp} Cost_{Amp} + K_{Ph} Cost_{Ph}, \quad (4.17)$$

where  $K_{sh}$ ,  $K_{Amp}$ , and  $K_{Ph}$  are weighting coefficients, which will be determined empirically. The obtained cost function can be used to estimate how a specific shape of the reflector is suitable for the illumination of the array for a broadside or in the case of scanning. By varying the  $A_{ij}$  polynomial coefficients, the optimization algorithm provides the most optimal configuration of the reflector according to the GO approach.

It is important to note that the proposed algorithm is extremely fast and allows to check of

thousands of reflectors' shapes per second. This is one of the main reasons for using a GO model instead of a PO approach, which is more accurate. Furthermore, one of the main advantages of the presented approach is the possibility to increase the complexity of the reflector and to have minor changes in the described procedure of the cost function definition. For example, it is well known that it is not possible to obtain uniform illumination along the array with one continuous reflector. In order to have more flexibility in the reflector shaping, a discontinuity in the center of the reflector could be implemented as:

$$\begin{aligned} S(x, y) &= A_{xx}x^2 + 2A_x x + A_{yy}(y - y_0)^2 = 0 \text{ when } y > 0, \\ S(x, y) &= A_{xx}x^2 + 2A_x x + A_{yy}(y + y_0)^2 = 0 \text{ when } y < 0, \end{aligned} \quad (4.18)$$

in which  $y_0$  is a shift of the polynomial function along the  $y$ -coordinate, see Fig. 4.10. The well-known ring-focused reflector is one of the particular examples of such a configuration [148].

In this case, the only difference in the presented procedure is the expressions that define the normal at each of the  $N$  points on the reflector. The derivatives in (4.4) now take the form:

$$\begin{aligned}\frac{\partial S(x_i, y_i)}{\partial y} &= 2A_{yy}(y_i - y_0) \text{ when } y > 0, \\ \frac{\partial S(x_i, y_i)}{\partial y} &= 2A_{yy}(y_i + y_0) \text{ when } y < 0.\end{aligned}\quad (4.19)$$

All other steps are similar.

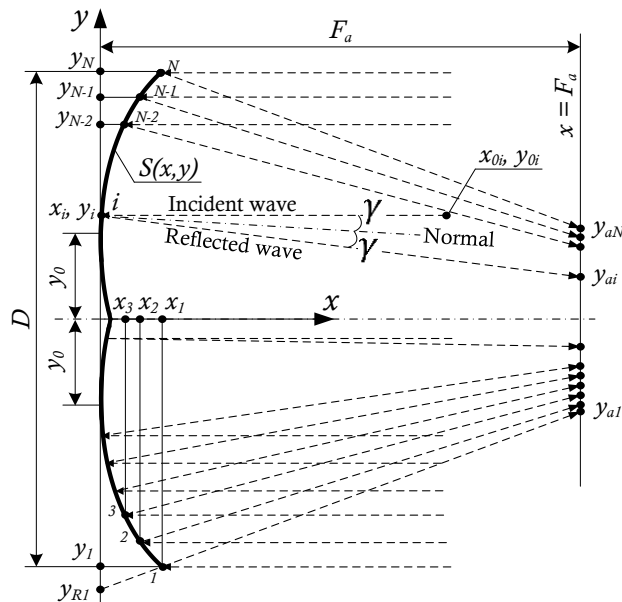


**Figure 4.10.** Two-dimensional center-fed reflector model. Single complex reflector with a discontinuity in the center.

#### 4.3.2. Two-dimensional center-fed double-reflector model

The possibilities to create a uniform amplitude and phase distribution along the array surface are limited when only a single reflector is used. Double-reflector configurations have more flexibility in terms of achieving the design goals. A special case of such configuration is the double-parabolic reflector. It is constituted by a feeding PAF properly illuminated by two reflector antennas [146, 147]. Such systems efficiently combine the advantages of the reflector and array antennas. They are commonly used to generate reconfigurable beams over a small angular scan range. In the case of a double reflector configuration, the obtained designs represent imaging reflector systems, which also could be solved as a lens antenna as demonstrated in [157]. However, the presented approach in [157] is limited to reflectors with a high magnification factor  $M = D/D_s \gg 1$ , where  $D_s$  is the size of the sub-reflector. At the same time, for double-reflector systems, relatively large sub-reflectors are required in the case of wide-angle scanning [152].

The sub-reflector surface of a double-reflector system can be defined in terms of a second-order polynomial (see also Fig. 4.11):

$$S_s(x, y) = B_{xx}(x - F_s)^2 + 2B_x(x - F_s) + B_{yy}y^2 = 0, \quad (4.20)$$

where  $F_s$  is a sub-reflector position along the  $x$ -axis and  $B_{ij}$  are sub-reflector polynomial coefficients.

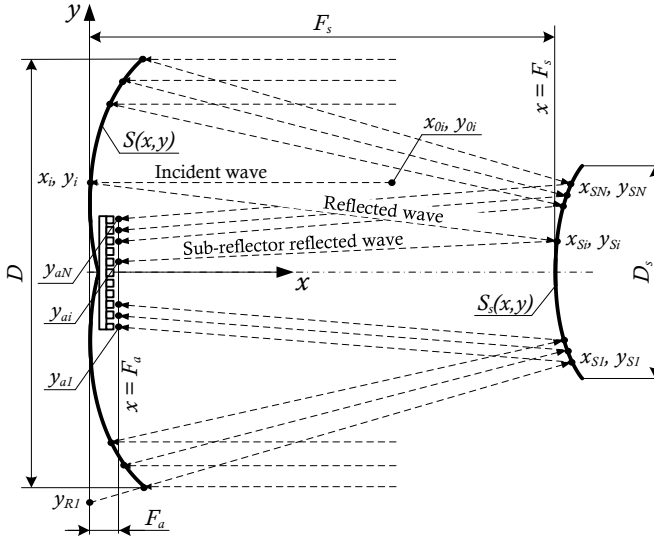


**Figure 4.11.** Two-dimensional center-fed double-reflector model.

As compared to the single-reflector case, we now have to include the interaction of the reflected waves from the main reflector with the sub-reflector surface. In order to find the coordinates of all interaction points, it is necessary to solve equation (4.20). The coordinate  $x_{Si}$  of the intersection points are found as:

$$x_{Si} = \pm \left[ \frac{2B_{yy}y_{Ri}\tan(\alpha_{Ri})B_x - 2B_{xx}B_{yy}y_{Ri}F_s\tan(\alpha_{Ri})}{(B_{yy}(\tan(\alpha_{Ri}))^2 + B_{xx})^2} - \frac{B_{xx}B_{yy}(y_{Ri})^2 + B_{xx}B_{yy}F_s^2(\tan(\alpha_{Ri}))^2 - 2B_{yy}F_s(\tan(\alpha_{Ri}))^2B_x - B_x^2}{(B_{yy}(\tan(\alpha_{Ri}))^2 + B_{xx})^2} \right]^{0.5} - \frac{B_x - F_sB_{xx} + y_{Ri}\tan(\alpha_{Ri})B_{yy}}{B_{yy}(\tan(\alpha_{Ri}))^2 + B_{xx}}. \quad (4.21)$$

Since (4.21) provides two possible solutions, the nearest value of  $x_{Si}$  to the center of the sub-reflector ( $F_s, 0$ ) should be chosen, see Fig. 4.11. The  $y$ -coordinates of the interaction points can be found by using:

$$y_{Si} = x_{Si} \tan(\alpha_{Ri}) + y_{Ri}. \quad (4.22)$$

Note that the size of the sub-reflector  $D_s$  should be at least a few wavelengths larger as compared to the GO estimation, since the diffraction from the edges of the main reflector increases the actual illuminated area of the sub-reflector.

As a next step, the linear equation of the normal to the sub-reflector point  $(x_{Si}, y_{Si})$  should be defined. After this, the procedure is similar to finding the reflected waves from the surface of the reflector described in the previous paragraph. The position of the array is in this case close to the main reflector. The phase path should include the extra wave propagation from the sub-reflector surface to the array plane.

The complexity of the sub-reflector could be increased as illustrated in Fig. 4.12. The reflector with discontinuity can be described by  $S_s(x, y)$  given by:

$$S_s(x, y) = B_{xx}(x - F_s)^2 + 2B_x(x - F_s) + B_{yy}(y - \Delta_y)^2 = 0 \text{ when } y > 0,$$

$$S_s(x, y) = B_{xx}(x - F_s)^2 + 2B_x(x - F_s) + B_{yy}(y + \Delta_y)^2 = 0 \text{ when } y < 0, \quad (4.23)$$

where  $\Delta_y$  is the shift of the polynomial function of the sub-reflector along the  $y$ -coordinate, see Fig. 4.12.

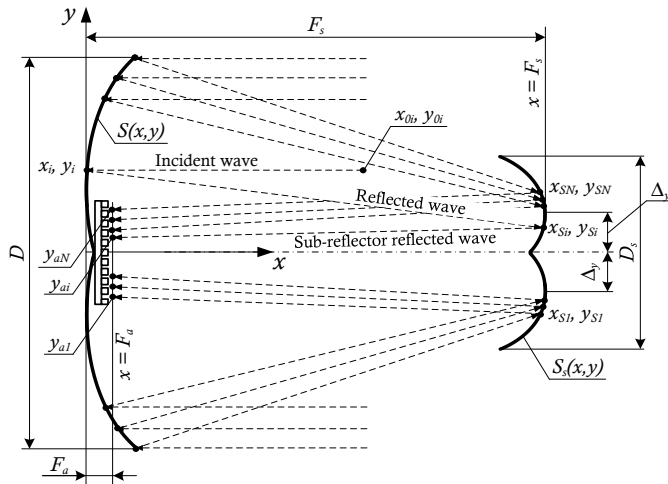


**Figure 4.12.** Two-dimensional center-fed reflector model of a complex double reflector.

In this case, the interaction points  $(x_{Si}, y_{Si})$  are calculated from the equation (4.23). The linear equation to find the normal of the points on the sub-reflector surface is adjusted to the  $\Delta_y$  value, related to the equation (4.19). The rest of the procedure is similar to the single-reflector case.

#### 4.3.3. Three-dimensional offset single-reflector model

The center-fed double-reflector model has important limitations. Due to the significant deviation of the waves reflected from the main reflector, it is required to have a sufficiently large sub-reflector to capture all reflected waves. For center-fed configurations, this leads to a significant blockage and energy loss. According to Fig. 4.5, the size of the sub-reflector should be around 65% of the main reflector in order to obtain 80% aperture efficiency in the case of  $\pm 20^\circ$  scanning range. This creates significant blockage even in the case of one-dimensional scanning. Therefore, we should investigate offset configurations, starting with a single-reflector offset configuration, as illustrated in Fig. 4.13 where a three-dimensional model is shown. We now also have to consider the  $z$ -coordinate.

The reflector surface can now be expressed in terms of a second-order polynomial (see also Fig. 4.13):

$$S(x, y, z) = A_{xx}x^2 + 2A_{xy}x + A_{yy}y^2 + A_{zz}z^2 + 2A_{yz}yz = 0, \quad (4.24)$$

where  $A_{ij}$  are polynomial coefficients. Note that the vertical offset  $z_b$  between the array and reflector (Fig. 4.13) should be at least a few wavelengths in order to avoid blockage and diffraction from the edges of the reflector and array. Mutual reflections between the reflector and array are also avoided in this case.

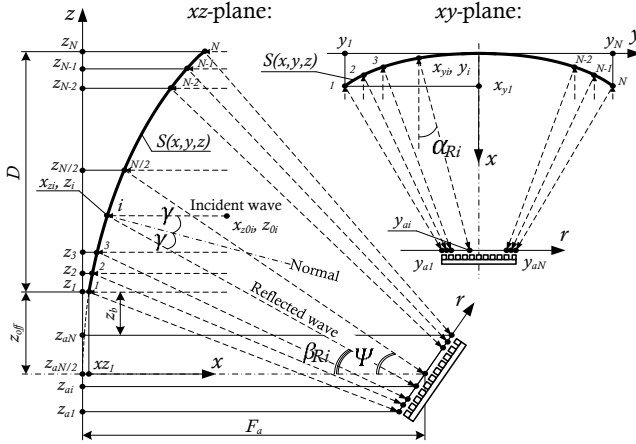


**Figure 4.13.** Three-dimensional offset single-reflector model.

The three-dimensional model is not symmetric with respect to the  $x$ -axis. Therefore, we need to investigate the wave propagation in both the  $xy$  and  $xz$ -plane. The reflector discretization along the  $y$ -axis is the same as for the center-fed reflector. Along the  $z$ -axis we now have:

$$z_i = z_1 \dots z_N, \quad z_1 = z_{\text{off}}, \quad z_N = z_1 + D. \quad (4.25)$$

We will solve (4.24) in two orthogonal planes:  $xy$  and  $xz$ . In the  $xy$ -plane, the value of  $x_{yi}$  for specific  $y_i$ -points are found as:

$$x_{yi} = -\frac{A_x}{A_{xx}} \pm \frac{\sqrt{A_x^2 - A_{xx}A_{yy}y_i^2 - 2A_{xx}A_{yz}y_i^2 z_{N/2} - A_{xx}A_{zz}z_{N/2}^2}}{A_{xx}}. \quad (4.26)$$

Similarly, the  $x_{zi}$  values for specific  $z_i$ -points in the  $xz$ -plane are found as:

$$x_{zi} = -\frac{A_x}{A_{xx}} \pm \frac{\sqrt{A_x^2 - A_{xx}A_{yy}y_{N/2}^2 - 2A_{xx}A_{yz}y_{N/2}z_i - A_{xx}A_{zz}z_i^2}}{A_{xx}}. \quad (4.27)$$

Selection of the proper coordinate  $x_{yi}$  and  $x_{zi}$  from the two options is done similarly are explained in Section 4.3.1.

There is no need for a full reflector discretization. As we will show later, the field distribution in the array plane can be estimated based on the two orthogonal cuts in the  $xy$  and  $xz$ -planes. The normal at the point  $(x_i, y_i, z_i)$  can be set via the partial derivatives in the following way:

$$\frac{x-x_i}{\frac{\partial S(x_i, y_i, z_i)}{\partial x}} = \frac{y-y_i}{\frac{\partial S(x_i, y_i, z_i)}{\partial y}} = \frac{z-z_i}{\frac{\partial S(x_i, y_i, z_i)}{\partial z}}, \quad (4.28)$$

where  $\frac{\partial S(x_i, y_i, z_i)}{\partial x} = 2A_{xx}x_i + 2A_x$ ,  $\frac{\partial S(x_i, y_i, z_i)}{\partial y} = 2A_{yy}y_i + 2A_{yz}z_i$ ,  $\frac{\partial S(x_i, y_i, z_i)}{\partial z} = 2A_{zz}z_i + 2A_{yz}y_i$ .

In a similar way the linear equation which represents the path of the incidence wave at the center of the reflector, is defined as:

$$1 = \frac{x}{y} \tan(\alpha) = \frac{x}{z} \tan(\beta), \quad (4.29)$$

where  $\alpha$  is the angle of incidence w.r.t. the  $x$ -axis in the  $xy$ -plane, and  $\beta$  the angle of incidence w.r.t. the  $x$ -axis in the  $xz$ -plane. Beam scanning is realized by varying  $\alpha$ . The angle  $\beta$  could be used to rotate the model in the  $xz$ -plane as an extra degree of freedom during optimization.

The linear equation, which represents the path of the reflected wave in the center of the reflector, is given by:

$$1 = \frac{x-x_{Ri}}{y-y_{Ri}} \tan(\alpha_{Ri}) = \frac{x-x_{Ri}}{z-z_{Ri}} \tan(\beta_{Ri}), \quad (4.30)$$

where  $\alpha_{Ri}$  is the angle of the reflected wave w.r.t. the  $x$ -axis in the  $xy$ -plane, and  $\beta_{Ri}$  – w.r.t. the  $x$ -axis in the  $xz$ -plane.

Combining (4.28), (4.29), and (4.30) provides us with more unknowns than equations. Therefore, we need to use the fact that the incoming wave is normal to the reflector surface and the reflected wave is always located in the same plane.

The equation of the plane of the incident wave, is represented by (4.31), the normal by (4.32), and the reflected wave by (4.33):

$$A + B \frac{1}{\tan(\alpha)} + C \frac{1}{\tan(\beta)} = 0, \quad (4.31)$$

$$A + B \frac{2A_{yy}y_i + 2A_{yz}z_i}{2A_{xx}x_i + 2A_x} + C \frac{2A_{zz}z_i + 2A_{yz}y_i}{2A_{xx}x_i + 2A_x} = 0, \quad (4.32)$$

$$A + B \frac{1}{\tan(\alpha_{Ri})} + C \frac{1}{\tan(\beta_{Ri})} = 0. \quad (4.33)$$

By solving (4.31)-(4.33), we can find the ratios  $B/A$  and  $C/A$ . Substituting this in (4.30) provides us  $\tan(\alpha_{Ri})$  and  $\tan(\beta_{Ri})$ . These values are sufficient for defining the intersection of the reflected wave with the array plane.

The rest of the procedure is similar to the two-dimensional model and should be applied to the  $xy$  and  $xz$ -planes.

The feeding angle of the array  $\Psi$  (Fig. 4.13) calculated in the  $xz$ -plane can be determined in the following way:

$$\Psi = \arctan \left[ \frac{z_{N/2}}{F_a - x_{zN/2}} \right]. \quad (4.34)$$

The total cost function is now a combination of the achieved properties in the  $xy$  and  $xz$ -planes:

$$Cost = K_{xy} Cost_{xy} + K_{xz} Cost_{xz}, \quad (4.35)$$

where  $K_{xy}$  and  $K_{xz}$  are weighting coefficients, which have been determined empirically.

The offset single reflector with a discontinuity is not investigated since it is extremely difficult to produce it. However, it is interesting to investigate a case where the whole polynomial function of the reflector is shifted along the  $z$ -coordinate with a value of  $z_0$ , see Fig. 4.14:

$$S(x, y, z) = A_{xx}x^2 + 2A_x x + A_{yy}y^2 + A_{zz}(z - z_0)^2 + 2A_{yz}y(z - z_0) = 0. \quad (4.36)$$

When we combine the shift of the polynomial function with a rotation of the whole system with angle  $\beta$ , the analogy with the classical center-fed configuration could be found. In the classical center-fed configuration, in the case of non-zero plane-wave incidence, the field in the focal plane will have a natural broadening (Fig. 4.14). This effect could be used in order to increase the illuminated region of the array in the  $xz$ -plane. The procedure to obtain the total cost function is similar to the previous case.

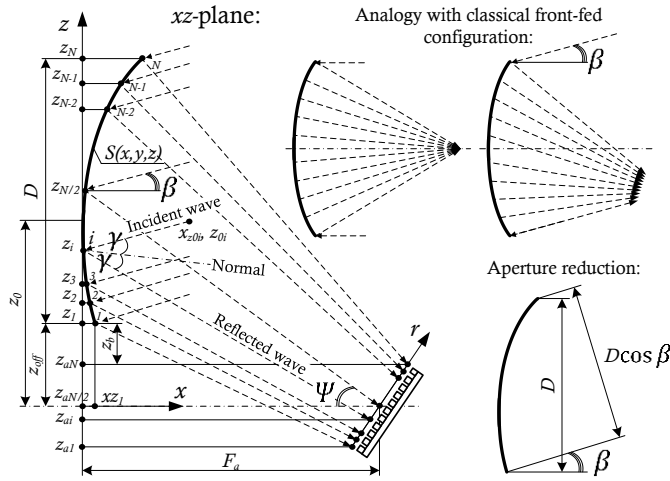


**Figure 4.14.** Three-dimensional offset reflector model using a complex reflector.

#### 4.3.4. Three-dimensional offset double-reflector model

For double-reflector systems, relatively large sub-reflectors are required in the case of scanning. By using an offset configuration, the blockage can be avoided.

The sub-reflector surface can be defined in terms of a second-order polynomial (see also Fig. 4.15):

$$S_s(x, y, z) = B_{xx}(x - F_s)^2 + 2B_x(x - F_s) + B_{yy}y^2 + B_{zz}z^2 + 2B_{yz}yz = 0. \quad (4.37)$$

The vertical offset between the sub-reflector and main reflector  $z_b$  should be at least a few wavelengths in order to avoid sub-reflector blockage. In addition, a proper choice of the array position  $z_c$  allows to avoid mutual reflections between the main reflector, sub-reflector and array. The waves reflected from the main reflector are defined in a similar as in the case of a single reflector. The intersection of the reflected wave from the main reflector and the sub-reflector surface is defined by the system of equations (4.30) and (4.37). Solving this system provides the interaction points on the sub-reflector surface:  $x_{ysi}$  and  $y_{si}$  (in the  $xy$ -plane),  $x_{zsi}$  and  $z_{si}$  (in the  $xz$ -plane).  $Dy_s$  is the size of the sub-reflector in the  $xy$ -plane,  $Dz_s$  – in the  $xz$ -plane (see Fig. 4.15).

The reflected wave from the surface of the sub-reflector is defined similarly to the reflection from the main reflector. The position of the array is again close to the main reflector. In addition, extra design features are applied to the sub-reflector geometry. The polynomial function describing the sub-reflector is now shifted along the  $z$ -coordinate by  $z_{s0}$ , see Fig. 4.16:

$$S_s(x, y, z) = B_{xx}(x - F_s)^2 + 2B_x(x - F_s) + B_{yy}y^2 + B_{zz}(z - z_{s0})^2 + 2B_{yz}y(z - z_{s0}) = 0. \quad (4.38)$$

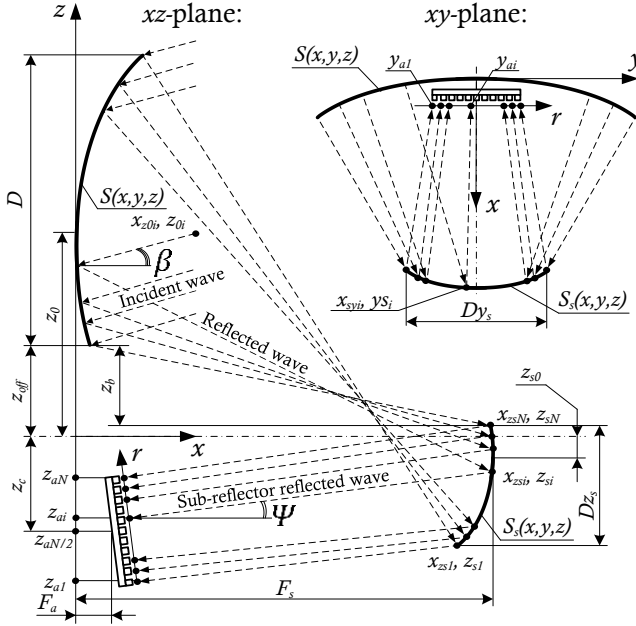


**Figure 4.15.** Three-dimensional offset double-reflector model.

In addition, the sub-reflector with two different discontinuities in the  $xy$  and  $xz$ -planes is defined by:

$$\begin{aligned}
 S_s(x, y, z) &= B_{xx}(x - F_s)^2 + 2B_x(x - F_s) + B_{yy}(y - y_s)^2 + B(z - x_s - z_{s0})^2 \\
 &\quad + 2B_{yz}(y - y_s)(z - z_s - z_{s0}) = 0 \text{ when } y > 0, z > 0, \\
 S_s(x, y, z) &= B_{xx}(x - F_s)^2 + 2B_x(x - F_s) + B_{yy}(y + y_s)^2 + B_{zz}(z - z_s - z_{s0})^2 \\
 &\quad + 2B_{yz}(y + y_s)(z - x_s - z_{s0}) = 0 \text{ when } y < 0, z > 0, \\
 S_s(x, y, z) &= B_{xx}(x - F_s)^2 + 2B_x(x - F_s) + B_{yy}(y - y_s)^2 + B_{zz}(z + z_s - z_{s0})^2 \\
 &\quad + 2B_{yz}(y - y_s)(z + x_s - z_{s0}) = 0 \text{ when } y > 0, z < 0, \\
 S_s(x, y, z) &= B_{xx}(x - F_s)^2 + 2B_x(x - F_s) + B_{yy}(y + y_s)^2 + B_{zz}(z + z_s - z_{s0})^2 + \\
 &\quad 2B_{yz}(y + y_s)(z + x_s - z_{s0}) = 0 \text{ when } y < 0, z < 0,
 \end{aligned} \tag{4.39}$$

where  $z_s$  is a shift in the polynomial function of the sub-reflector along the  $z$ -coordinate and  $y_s$  a shift along the  $y$ -coordinate, see Fig. 4.16.

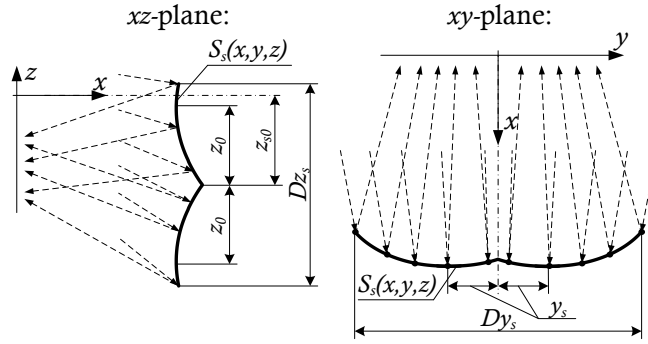


**Figure 4.16.** Complex sub-reflector model of the three-dimensional offset reflector.

In summary, in this section, we have derived a direct relation between the shape of the reflectors and the total cost function. The shape of the reflectors can be expressed in terms of polynomial coefficients as in (4.1), (4.18), (4.20), (4.23), (4.24), and (4.36) – (4.39) including design features like reflector shape discontinuities and the shifts of the polynomial function along the coordinates axis. The total cost function is presented as a combination of different optimization goals in (4.17) and (4.35). By varying the ratio between the cost functions of the amplitude distribution (4.12), the phase linearity along the array (4.14), and the deviation of the field in the array plane during scanning (4.15), it is possible to optimize the reflectors for a particular application.

#### 4.4. Optimization of single and double-reflector configurations

We have optimized the single and double-reflector configurations with the mathematical model of section 4.3 for two specific situations: 1) no scanning (broadside) and 2) beam scanning up to  $\pm 20^\circ$ . For broadside operation, the goal is to obtain a uniform amplitude and linear phase distribution as defined for the ideal reflector (Fig. 4.6). In the case of scanning, an additional goal is the minimization of the illumination deviation (Fig. 4.8). The following reflector configurations have been investigated for broadside operation:

- parabolic reflector with an axially displaced array,
- single reflector with discontinuity,
- complex double reflector,
- offset single reflector,
- complex offset double reflector.

The following reflector configurations have been investigated for wide-angle scanning:

- complex double center-fed reflector,
- complex offset double reflector.

The single reflector configurations have already been investigated for wide-angle scanning in [150]. All investigated configurations include the axial displacement of the array. We have used a PAF with a length of 4 cm, which corresponds to  $40\lambda_0$  at 30 GHz. The size of the main

reflector is 80 cm. All optimizations have been done with our mathematical GO model implemented in MATLAB and are dedicated exclusively to reflector shape optimization. We have used a Monte Carlo type of algorithm to minimize the cost function in the optimization. The resulting optimized reflector configurations have been simulated in GRASP [39] by means of PO and GO. The PO simulations include the physical theory of diffraction [39]. A comparison of all configurations is provided in section 4.4.5.

#### 4.4.1. Axially symmetric single reflector

The optimal configuration of the center-fed single parabolic reflector of Fig. 4.9 is obtained with an axially displaced PAF towards the reflector. The obtained optimal polynomial coefficients and other relevant variables are provided in Table 4.1.

**Table 4.1.** Optimal polynomial coefficients and variables of a parabolic reflector with an axially displaced PAF.

Variable	Obtained value	Variable	Obtained value
$A_{xx}$	0.4572	$A_{zz}$	4.753
$A_{yy}$	4.753	$A_{yz}$	0
$A_x$	-4.8023	$F_a$	0.48 m
$D$	0.8 m		

The obtained geometry has a ratio  $F/D = 0.6$ , which gives the smallest deviation of the focused beam according to [150]. The reflector configuration is presented in Fig. 4.17(a), the electric-field cuts in the array plane based on PO simulation in Fig. 4.17(b), the electric-field cuts in the array plane based on GO simulation in Fig. 4.17(c) and the phase distribution based on PO simulation is provided in Fig. 4.17(d). The PO simulations include the physical theory of diffraction [39].

Since the optimization algorithm is based on GO, both PO and GO simulation results are provided. However, the overall performance of the optimized reflector system should be based on the PO simulation results, since the computational precision is much higher.

According to Fig. 4.17(c), the illuminated region is matched with the desired array size of 4 cm. The amplitude distribution is not uniform but significantly improved as compared to the classical prime-focus reflector, where GO simulations provide a delta function in the center of the array. In Fig. 4.17(b), the electric-field cuts in the array plane demonstrate that the array illumination region is much broader as compared to the classical prime-focus reflector (Fig. 4.1). The aperture efficiency of the optimized configuration is presented in Fig. 4.18.

According to Fig. 4.18, the aperture efficiency increases much smoother with an increase in the array size as compared to the classical prime-focus reflector (Fig. 4.5). This indicates that we have obtained a more uniform field distribution along the array.

According to Fig. 4.17(d), the phase distribution in the array plane is quite nonlinear. However, it is significantly improved as compared to the classical prime-focus reflector. The linearity of the phase distribution at 30 GHz shows an rms error of  $3.1^0$ .

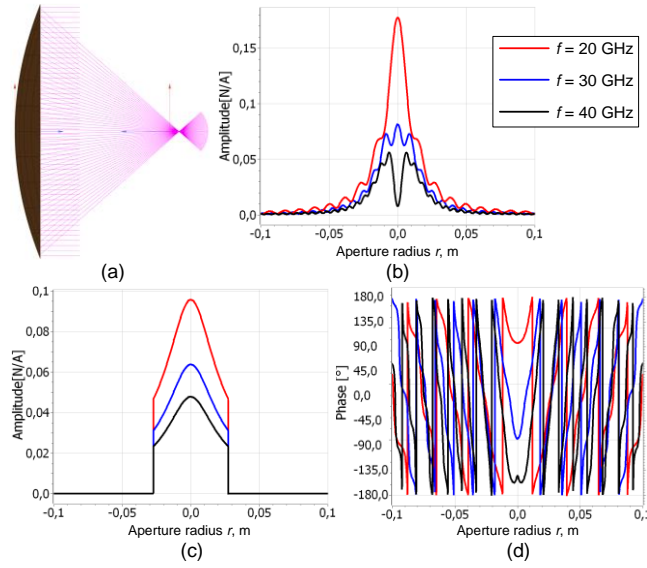


**Figure 4.17.** (a) Single-reflector configuration with the axially-displaced array, broadside situation (b) electric-field cuts in the array plane based on PO simulation (c) electric-field cuts in the array plane based on GO simulation (d) Phase distribution based on PO simulation in the array plane.

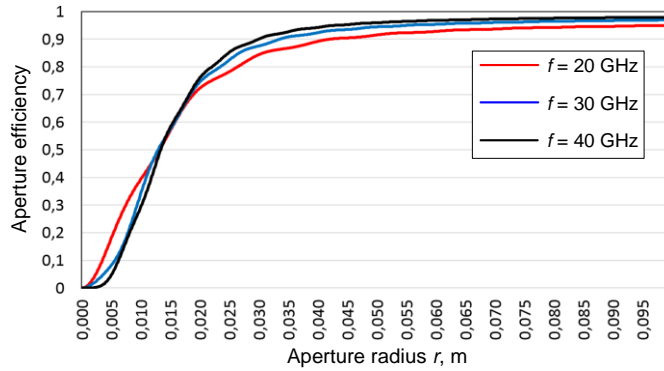


**Figure 4.18.** Aperture efficiency in the array plane for broadside operation of a parabolic reflector with an axially displaced array. PO simulations.

Next, we have optimized a single parabolic reflector with discontinuity as shown in Fig. 4.10. The obtained optimal polynomial coefficients and other relevant variables are provided in Table 4.2.

**Table 4.2.** Optimal polynomial coefficients and variables of a single reflector with discontinuity.

Variable	Obtained value	Variable	Obtained value
$A_{xx}$	0.151	$A_{yz}$	0
$A_{yy}$	2.0985	$F_a$	0.48 m
$A_x$	-2.115	$y_0$	0.0312 m
$A_{zz}$	2.0985	$D$	0.8 m

The reflector configuration and corresponding field distribution in the array plane are shown in Fig. 4.19. The corresponding aperture efficiency is presented in Fig. 4.20. From Fig. 4.19(c) it is clear that the field distribution is more uniform over the array as compared to the optimized parabolic reflector with the axially displaced array, see Fig. 4.17(c). Therefore, adding extra complexity using a discontinuity in the center of the reflector allows us to get closer to the wanted ideal array illumination. The phase distribution in the array plane of Fig. 4.19(d) is quite similar to the previous configuration. The linearity of the phase distribution at 30 GHz shows an rms error of  $2.02^\circ$ .

#### 4.4.2. Axially symmetric double-reflector

Double-reflector concepts (Fig. 4.12) provide more degrees of freedom for optimization as compared to single-reflector configurations. We have optimized the center-fed double-reflector for two specific cases: 1) broadside scan and 2) wide-angle scanning up to  $\pm 20^\circ$  in the azimuth plane. For the broadside-scan case, the obtained optimal polynomial coefficients and other relevant dimensions are provided in Table 4.3.

The discontinuity variables  $\Delta_y$  and  $y_0$  are equal to zero. Therefore, both optimized reflectors have a continuous shape and are easy to produce. The size of the sub-reflector  $D_s$  is significantly smaller than the main reflector, limiting the reduction of the aperture efficiency due to blockage to about 0.5%. The field distribution in the array plane using GO and PO is provided in Fig. 4.21 and the aperture efficiency is in Fig. 4.22.

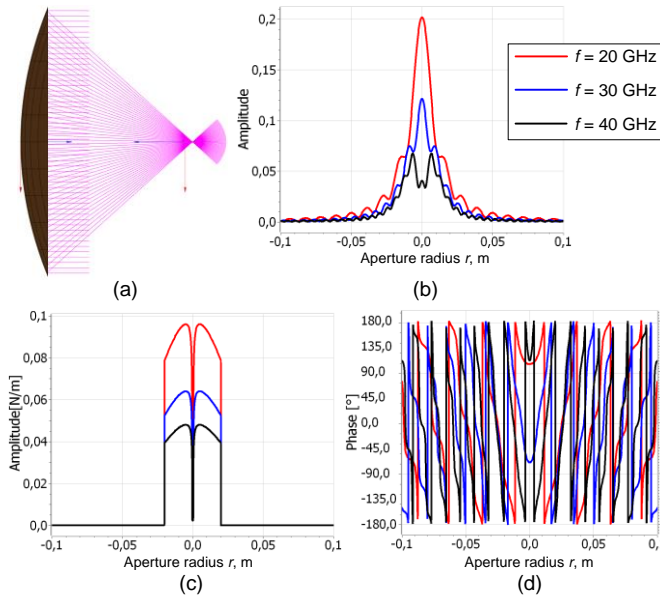


**Figure 4.19.** (a) Single-reflector configuration with discontinuity in the center, broadside situation (b) electric-field cuts in the array plane based on PO simulation (c) electric-field cuts in the array plane based on GO simulation (d) Phase distribution based on PO simulation in the array plane.

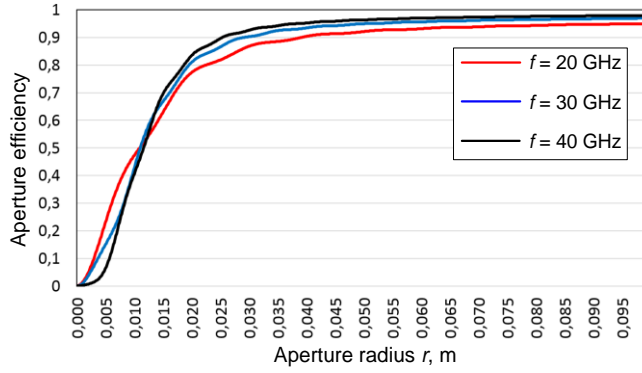


**Figure 4.20.** Aperture efficiency in the array plane for broadside operation of a single reflector with discontinuity. PO simulations.

**Table 4.3.** Optimal polynomial coefficients and dimensions of a complex double reflector. Optimized for broadside scan only.

Variable	Obtained value	Variable	Obtained value
$A_{xx}$	0.0735	$B_{xx}$	2.952
$A_{yy}$	1.215	$B_{yy}$	4.977
$A_x$	-1.325	$B_x$	-0.456
$A_{zz}$	1.215	$B_{zz}$	4.977
$A_{yz}$	0	$B_{yz}$	0
$F_s$	0.507 m	$F_a$	0.1 m
$\Delta_y$	0 m	$y_0$	0 m
$D_s$	0.054 m	$D$	0.8 m

The distribution in the array plane based on the GO simulation of Fig. 4.21(c) matches quite closely to the ideal uniform field distribution. The PO simulation results of Fig. 4.21(b) show that the illumination region is a bit wider than the desired array size of 4 cm. This is due to diffraction in the double-reflector configuration [158]. There is good phase linearity along the array elements according to Fig. 4.21(d). The linearity of the phase distribution at 30 GHz shows an rms error of  $1.45^\circ$ . The aperture efficiency of Fig. 4.22 is quite close to the aperture efficiency for the broadside operation of a reflector with ideal array illumination (Fig. 4.7).

Next, we will investigate wide-angle scanning of the double-reflector FPA. According to [150], wide-angle scanning up to  $\pm 20^\circ$  requires a very large sub-reflector. For center-fed models, this leads to significant blockage and energy loss. In addition, double-reflector configurations have another limitation in the case of scanning caused by the amplification of the angle of incidence on the array surface [146], [147]. As a result, even a small beam deviation of the incident wave causes a significant shift of the illuminated array region. As a consequence, the array size should be very large. Nevertheless, it is interesting to investigate a fictitious model of the complex double-reflector in the case of wide-angle scanning, where the effects of blockage are ignored. This model allows to estimate the potential to use double-reflector configurations for wide-angle scanning and can be used as a reference model for offset configurations.

The obtained optimal polynomial coefficients and other relevant dimensions are shown in Table 4.4.

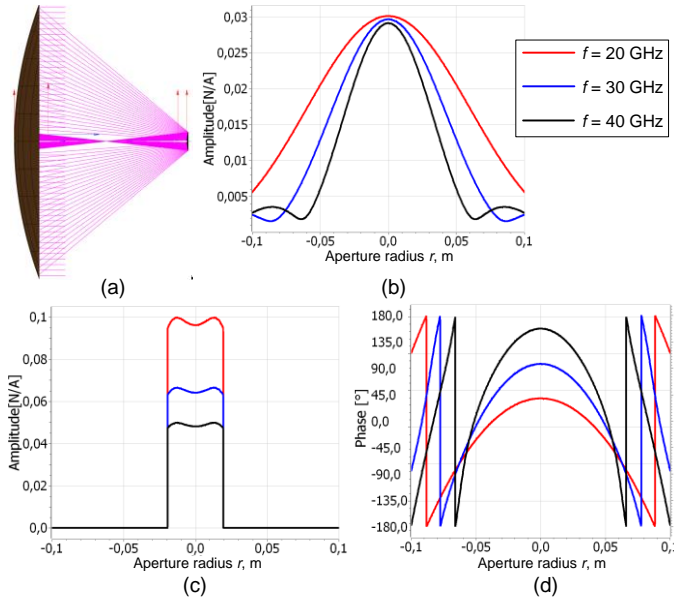


**Figure 4.21.** (a) Double-reflector configuration, broadside situation (b) electric-field cuts in the array plane based on PO simulation (c) electric-field cuts in the array plane based on GO simulation (d) Phase distribution based on PO simulation in the array plane.

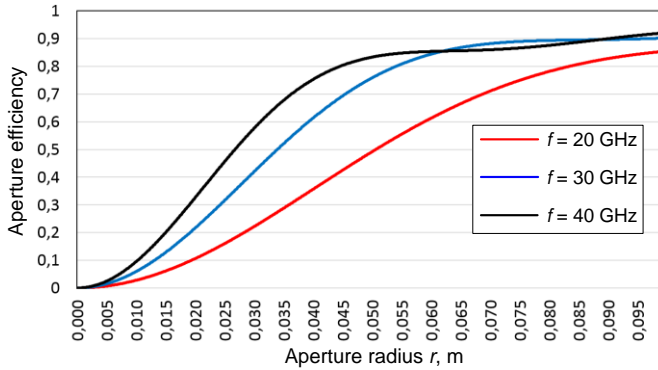


**Figure 4.22.** Aperture efficiency in the array plane for broadside operation of a complex double-reflector.

**Table 4.4** Optimal polynomial coefficients and dimensions of a complex double reflector for wide-angle scanning up to  $\pm 20^\circ$  (fictitious model that ignores blocking).

Variable	Obtained value	Variable	Obtained value
$A_{xx}$	1.692	$B_{xx}$	0.116
$A_{yy}$	1.1285	$B_{yy}$	-3.768
$A_x$	-4.922	$B_x$	-2.862
$A_{zz}$	1.1285	$B_{zz}$	-3.768
$A_{yz}$	0	$B_{yz}$	0
$F_s$	0.41 m	$F_a$	0.1 m
$\Delta_y$	0	$y_0$	0
$D_s$	0.89 m	$D$	0.8 m

Similar to the broadside case, the discontinuity variables  $\Delta_y$  and  $y_0$  are zero. As a result, both reflectors have a continuous shape. The size of sub-reflector  $D_s$  is not limited for this configuration and, as a result, the blockage is 100%. It makes this model completely fictitious. The resulting field distribution in the array plane and aperture efficiency are shown in Fig. 4.23-4.25.

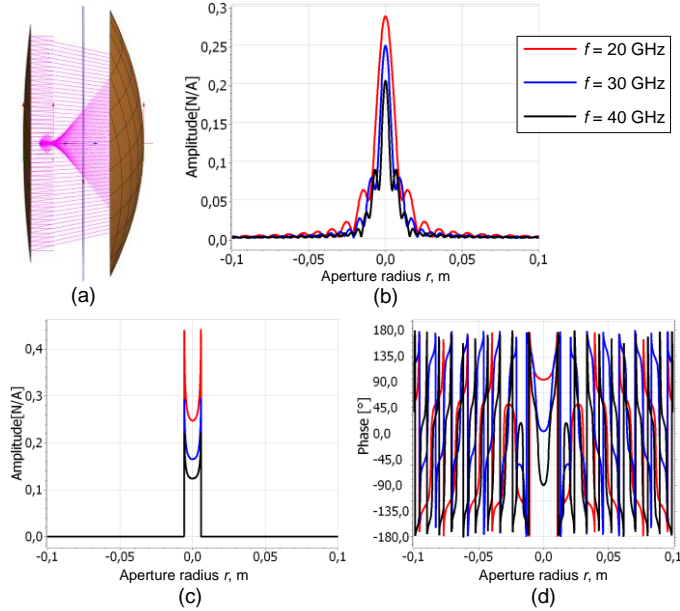


**Figure 4.23.** (a) Complex double-reflector configuration optimized for wide-angle scanning, broadside situation (b) electric-field cuts in the array plane based on PO (c) electric-field cuts in the array plane based on GO (d) Phase distribution based on PO simulation in the array plane. Blocking has been ignored.

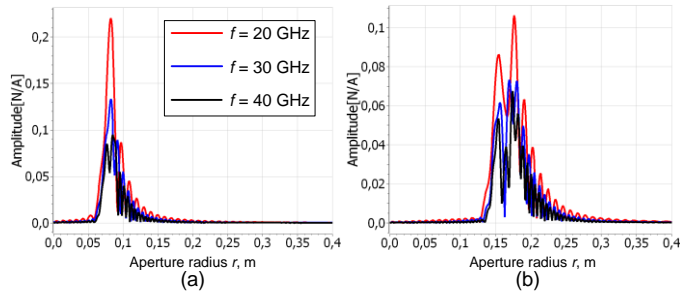


**Figure 4.24.** (a) Electric-field cuts for  $10^\circ$  angle of incidence, (b) electric-field cuts for  $20^\circ$  scanning based on PO simulation of a complex double reflector for wide scanning (blocking ignored).

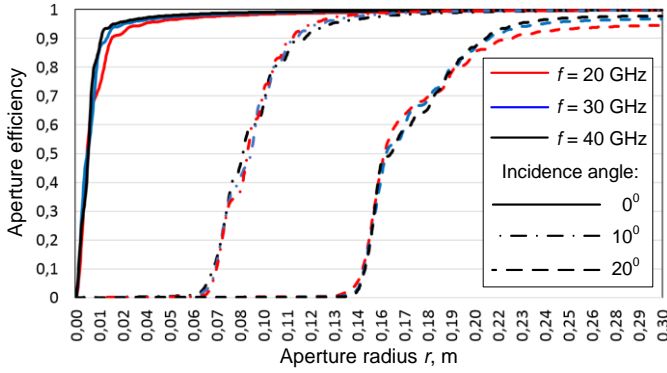


**Figure 4.25.** Aperture efficiency in the array plane for different scan angles of a complex double-reflector optimized for wide scanning (blocking ignored).

The performance at the broadside has been sacrificed in order to improve the scanning properties. When comparing the field distribution for  $10^\circ$  and  $20^\circ$  scanning with the field distribution of a classical prime-focus reflector (Fig. 4.3 – 4.4), we can conclude that the realized field deviation is about 25% smaller. In addition, to provide scanning up to  $\pm 20^\circ$  in the azimuth plane, the linear size of the array should be at least 0.39 m for an 80% aperture efficiency (Fig. 4.25). A classical prime-focus reflector requires an array size of at least 0.52 m. Therefore, the fictitious model of the complex double-reflector allows to prove the concept of wide scanning. Since a large sub-reflector is required, we need to use an offset configuration, which will be investigated in section 4.3.4.

#### 4.4.3. Offset single reflector

By using an offset configuration, blockage of the PAF and sub-reflector can be avoided. First, we will investigate the offset single-reflector FPA of Fig. 4.14. Table 4.5 summarizes the optimal polynomial coefficients and other relevant dimensions of the offset single-reflector model of Fig. 4.14.

**Table 4.5** Optimal polynomial coefficients and dimensions of an offset single reflector.

Variable	Obtained value	Variable	Obtained value
$A_{xx}$	1.4	$F_a$	0.68 m
$A_{yy}$	512.6	$z_0$	0.076 m
$A_x$	-492.3	$z_{off}$	0.1 m
$A_{zz}$	488.9	$\psi$	$54^\circ$
$A_{yz}$	0	$\beta$	$5.3^\circ$
$D$	0.8 m		

We can observe that the reflector shape is close to a parabolic shape, since  $|A_{xx}| \ll |A_x|$ , and has almost the same focusing properties in the offset and azimuth planes, since  $A_{yy} \cong A_{zz}$ . The shift of the polynomial function  $z_0$  is less than  $z_{off}$ . Therefore, the symmetry point is outside the actual reflector surface. The field distribution in the array plane and aperture efficiency of the optimized offset single-reflector are shown in Fig. 4.26 and Fig. 4.27, respectively.

The performance of the single offset reflector with axially displaced PAF is quite similar

to the center-fed single reflector. According to Fig. 4.26(c), the illuminated region is close to the required size of 4 cm. The amplitude distribution is not uniform, but significantly improved as compared to the classical prime-focus reflector (Fig. 4.1). The linearity of the phase distribution in the array has an rms error of  $3.57^\circ$  at 30 GHz. The aperture efficiency has a much smoother behavior as compared to the classical prime-focus reflector (Fig. 4.5), which corresponds to a more uniform distribution of the electric-field within the array.

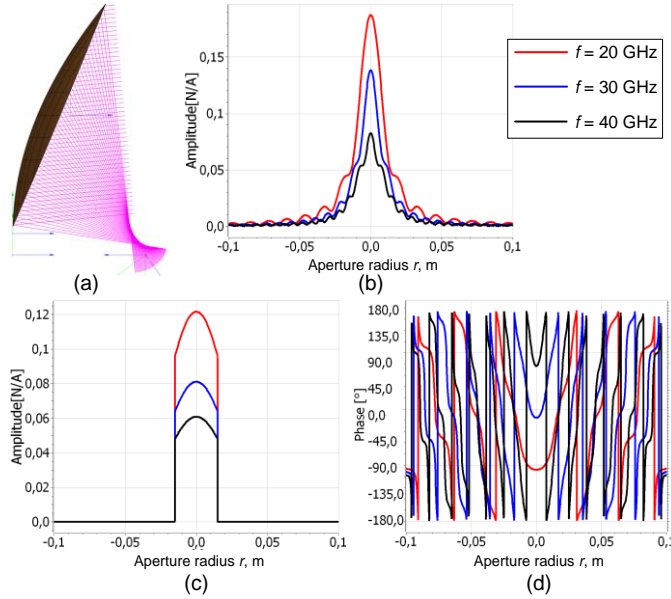


**Figure 4.26.** (a) Offset single-reflector configuration, broadside situation (b) electric-field cuts in the array plane based on PO simulation (c) electric-field cuts in the array plane based on GO simulation (d) Phase distribution based on PO simulation in the array plane.

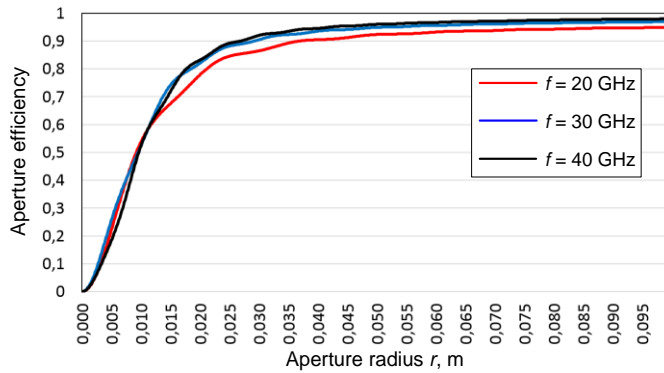


**Figure 4.27.** Aperture efficiency in the array plane for broadside operation of the optimized single offset reflector.

#### 4.4.4. Offset double reflector

By using an offset configuration, we overcome the sub-reflector blockage problem as reported in section 4.3.2. Two optimized versions of the offset double-reflector FPA of Fig.

4.15 have been investigated: 1) broadside scan and 2) wide-angle scanning up to  $\pm 20^\circ$  in the azimuth plane.

For the broadside-scan case, the obtained optimal polynomial coefficients and other relevant dimensions are provided in Table 4.6.

**Table 4.6** Optimal polynomial coefficients and dimensions of a complex offset double reflector for broadside scan.

Variable	Obtained value	Variable	Obtained value
$A_{xx}$	159	$B_{xx}$	21
$A_{yy}$	960	$B_{yy}$	-886
$A_x$	-910	$B_x$	-120
$A_{zz}$	930	$B_{zz}$	-935
$A_{yz}$	0	$B_{yz}$	0
$F_s$	0.552 m	$F_a$	0 m
$\Delta_y$	0 m	$Dz_s$	0.19 m
$z_0$	0 m	$Dy_s$	0.19 m
$\psi$	$0^\circ$	$\beta$	$0^\circ$
$Z_{off}$	0.1 m	$D$	0.8 m

The discontinuity variable  $\Delta_y$  is equal to zero so that both reflectors have a continuous shape.  $F_a = 0$  and  $\psi = 0^\circ$ , which means that the PAF is located in the center of the coordinate system and is oriented along the  $yz$ -plane in the model of Fig. 4.15. The sub-reflector dimensions  $Dz_s$  and  $Dy_s$  are almost a quarter of the main reflector dimension, but due to the offset configuration, no blockage occurs. The field distribution and aperture efficiency are shown in Fig. 4.28 and Fig. 4.29, respectively.

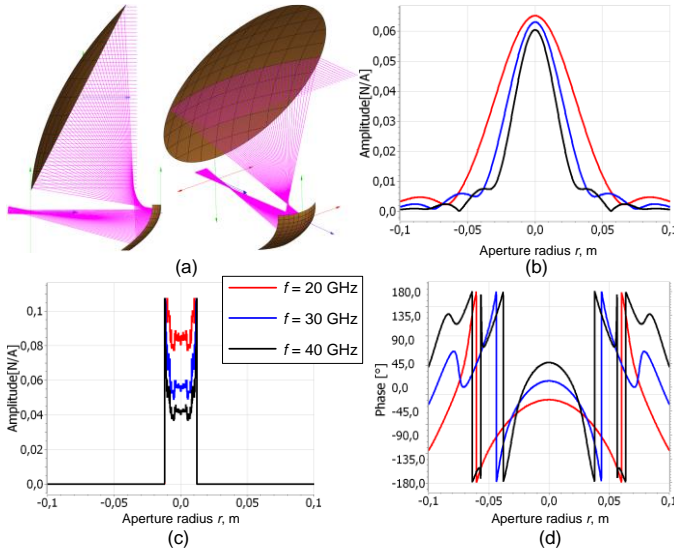


**Figure 4.28.** (a) Offset double-reflector configuration optimized for broadside-scan (b) electric-field cuts in the array plane based on PO simulation (c) electric-field cuts in the array plane based on GO simulation (d) Phase distribution based on PO simulation in the array plane.

From Fig. 4.28(c), we can observe that the field distribution is much more uniform as

compared to the offset single reflector of Fig. 4.26(c). In fact, the performance is similar to the center-fed double-reflector systems, but now avoids blockage of the large sub-reflector. The phase linearity in the array plane shows an rms error of  $1.91^\circ$  at 30 GHz, which is significantly better than the obtained with the offset single reflector.

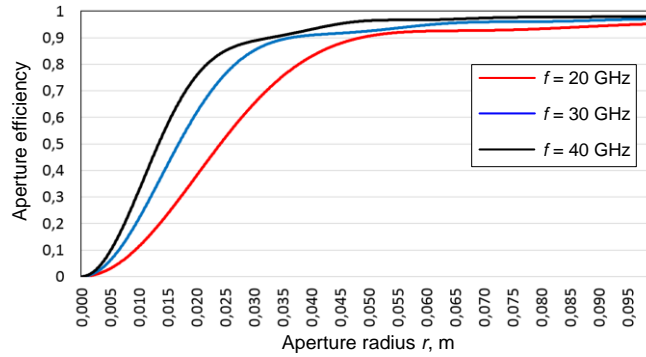


**Figure 4.29.** Aperture efficiency in the array plane optimized for broadside operation of a complex offset double-reflector.

Next, we have optimized the complex offset double reflector for wide-angle scanning. This configuration has been used to construct a prototype for experimental validation, see section 4.5. For that reason, additional manufacturing-related requirements have been applied to this design. Although the offset configuration allows a large sub-reflector size, we have limited the dimension to 83 cm. In addition, we have avoided a discontinuity in the surface of the main reflector. Thus, potentially the offset double-reflector configuration could achieve an even better performance if no production limits will be applied.

The optimal polynomial coefficients and other relevant dimensions of the optimized complex offset double-reflector of Fig. 4.16 for wide-angle scanning are provided in Table 4.7.

**Table 4.7** Optimal polynomial coefficients and other dimensions of a complex double offset reflector for wide-angle scanning up to  $\pm 20^\circ$ .

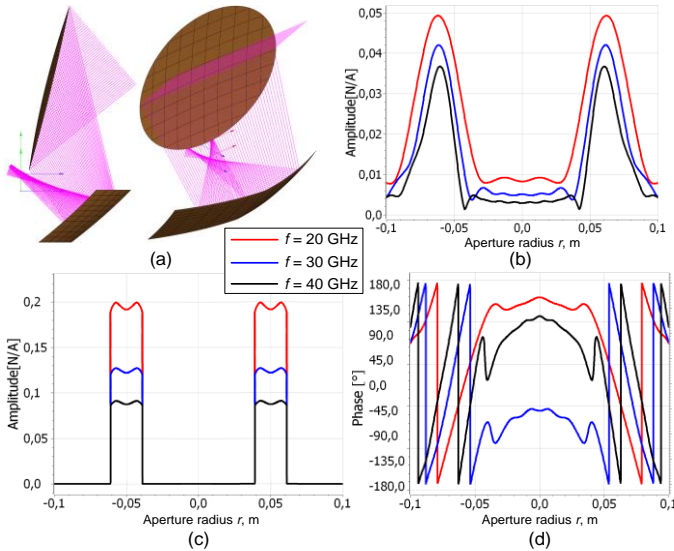
Variable	Obtained value	Variable	Obtained value
$A_{xx}$	0	$B_{xx}$	30.45
$A_{yy}$	190	$B_{yy}$	-168.73
$A_x$	-550.5	$B_x$	-124.61
$A_{zz}$	140.1	$B_{zz}$	-219.92
$A_{yz}$	0	$B_{yz}$	0
$F_s$	0.79 m	$F_a$	0 m
$z_s$	-0.081 m	$y_s$	-0.102 m
$z_0$	-0.45 m	$z_{s0}$	0.49 m
$z_{off}$	0.1 m	$z_c$	-0.08 m
$Dz_s$	0.255 m	$Dy_s$	0.83 m
$\Psi$	$-27.67^\circ$	$\beta$	$39.42^\circ$
$D$	0.8 m		

In this case, the sub-reflector of the optimized configuration has a discontinuity since  $z_s$  and  $y_s$  are not equal to zero. Furthermore,  $F_a = 0$  and  $\Psi = -27.67^\circ$ , which implies that the PAF is located in the center of the coordinate system and has a slight rotation in the offset

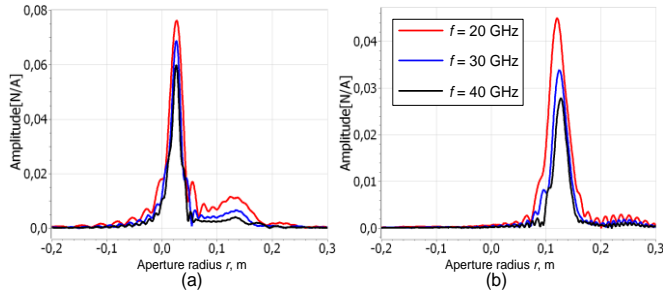
plane, see also Fig. 4.16. The dimensions of the sub-reflector,  $Dz_s$  and  $Dy_s$ , are relatively large as compared to the size of the main reflector, but there is no blockage between the reflectors. The field distribution and aperture efficiency for various scan angles of the optimized configuration are shown in Fig. 4.30 – 4.33.

Fig. 4.30 demonstrates the interesting properties of the optimized configuration. In the case of broadside operation, the field distribution is not focused in the center of the array plane. The sub-reflector discontinuity creates extra broadening in the case of broadside operation. For scan angles larger than  $8^\circ$  there is the amplitude dominance of one of the two focal points due to the fact that the illumination is shifted mainly to one of the two sub-reflector parts.

According to the GO simulation results of Fig. 4.30(c), the electric-field cuts in the array plane have been split into the two illumination regions with a quite uniform distribution. The PO simulation results of Fig. 4.30(b) show that the illuminated region for broadside operation is relatively large (about 20 cm) with two distinct field maxima. From PO simulations we found that for scan angles below  $12^\circ$ , the illumination region is smaller as compared to the broadside-scan case. For larger scan angles, between  $12^\circ$  and  $20^\circ$ , the illuminated region is larger than for the broadside-scan case. At the same time, the aperture efficiency distribution (Fig. 4.33), has a significantly smoother behavior than all previously investigated configurations. This results in a more uniform field distribution over the PAF. The PAF should have a length of about 28 cm based on an 80% aperture efficiency in order to provide scanning up to  $\pm 20^\circ$  in the azimuth plane. This is significantly better as compared to the scanning capabilities of the classical prime-focus reflector. Moreover, the linearity of the phase distribution at 30 GHz shows an rms error of  $2.81^\circ$ . The PAF width is equal to 4 cm, in line with the results for broadside operation.



**Figure 4.30.** (a) Optimized complex offset double-reflector configuration for wide-angle scanning, broadside situation (b) electric-field cuts in the array plane based on PO simulation (c) electric-field cuts in the array plane based on GO simulation (d) Phase distribution based on PO simulation in the array plane for broadside operation.



**Figure 4.31.** (a) Electric-field cuts for  $10^\circ$  angle of incidence (b) Electric-field cuts for  $20^\circ$  angle of incidence based on PO simulation of a complex offset double reflector optimized for wide-angle scanning.

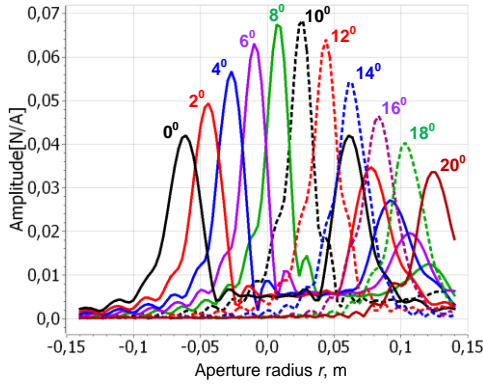


**Figure 4.32.** Electric-field cuts in the array plane of the optimized complex offset double reflector based on PO simulation for various scan angles,  $f = 30$  GHz.

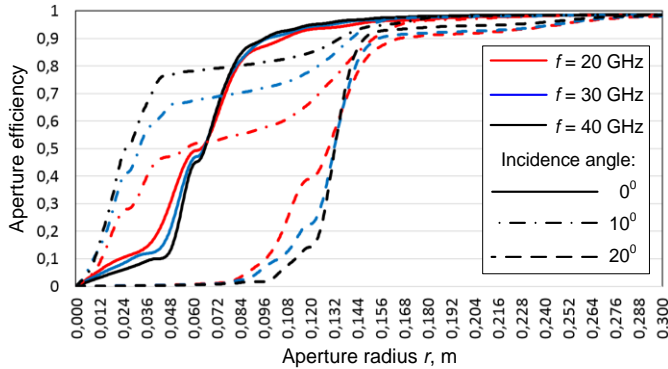


**Figure 4.33.** Aperture efficiency in the array plane for various scan angles of the optimized complex offset double reflector for wide scanning.

#### 4.4.5. Comparison of all configurations

Although a GO-mathematical framework was used to find the optimized geometries, we will use PO to compare the performance of all configurations. Let us first consider the optimized geometries for broadside operation. Fig. 4.34 shows the realized aperture

efficiencies at the center frequency. The classical prime-focus reflector (Fig. 4.1) is added as a reference case.

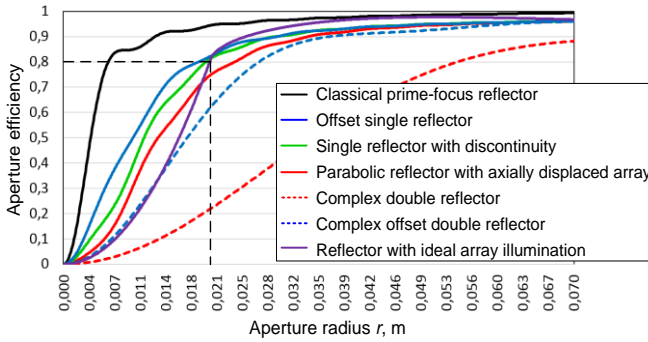


**Figure 4.34.** Realized aperture efficiencies of all optimized reflector configurations for broadside operation based on PO simulations,  $f = 30$  GHz.

The optimization goal has been set for an array size of 4 cm or 2 cm array radius. Therefore, the reflector with ideal array illumination reaches an aperture efficiency of 80% at a 2 cm radius. The required array size has been estimated for all configurations based on 80% aperture efficiency. Table 4.8 summarized the required array size and the realized phase linearity over the array.

**Table 4.8** Comparison of optimized reflector configurations for broadside operation, PO simulation model is used.

Reflector configuration	Array size (radius) for 80% aperture efficiency at 30 GHz	Phase linearity: rms error at 30 GHz
Reflector with ideal array illumination	2 cm	$0^0$
Classical prime-focus reflector	0.6 cm	$6.36^0$
Parabolic reflector with an axially displaced array	2.4 cm	$3.1^0$
Single reflector with discontinuity	1.95 cm	$2.02^0$
Complex double-reflector (including blockage)	5.5 cm	$1.45^0$
Single offset reflector	1.9 cm	$3.57^0$
Complex double offset reflector	2.7 cm	$1.91^0$

According to Fig. 4.34, and Table 4.8, the center-fed single reflector with discontinuity and the offset single reflector provides the best fit with the ideal FPA reflector system. Both of them include an axial displacement of the feed array. The realized array size is approx. three times larger as compared to the classical prime-focus reflector, which provides a significant increase in the realized EIRP. Nevertheless, according to Fig. 4.34, the best results for extending the field distribution along the array plane are obtained with the double-reflector configurations (center-fed and offset reflectors). The required array size of the center-fed double reflector is larger than the optimization goal. This can be explained by diffraction effects, which are more significant in the case of center-fed double reflectors [158]. The complex offset double reflector has a higher complexity and achieves a performance closer to the design goal. To sum up, the complex double offset reflector demonstrates the best performance in amplitude and phase uniformity along the array.

A comparison of the reflector systems optimized for wide-angle scanning is provided in Fig. 4.34 – 4.35 and Table 4.9, and the aperture efficiency distribution along the array is presented in Fig. 4.35 for  $10^\circ$  scan angle and in Fig. 4.36 - for  $20^\circ$ . The complex double center-fed reflector for wide scanning is a fictional model since we have ignored the blockage from the large sub-reflector.

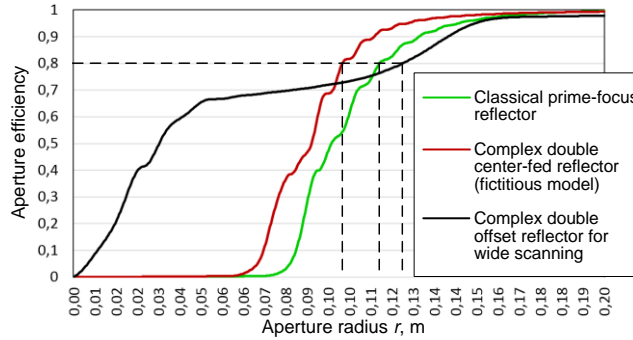


**Figure 4.35.** Comparison of optimized reflector configurations for  $10^\circ$  angle of incidence based on PO simulations,  $f = 30$  GHz.

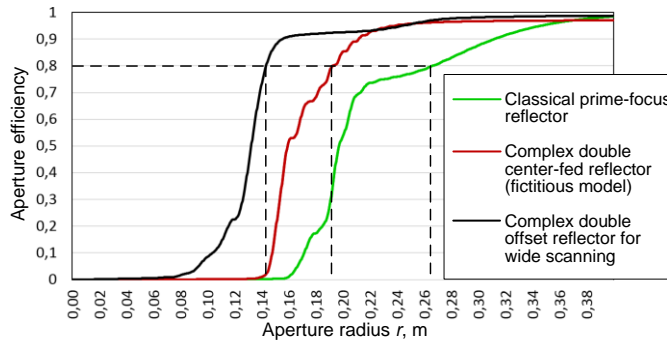


**Figure 4.36.** Comparison of optimized reflector configurations for  $20^\circ$  angle of incidence based on PO simulations,  $f = 30$  GHz.

According to Fig. 4.35 – 4.36 and Table, 4.9 the best performance is obtained with the complex offset double reflector configuration. The required array size is almost two times smaller as compared to the classical prime-focus reflector for  $\pm 20^\circ$  scanning in the azimuth plane. At the same time, the aperture efficiency has the smoothest distribution along the array, resulting in a high percentage of simultaneously active array elements. For  $10^\circ$  scanning about 44.6% of the array elements are active. Moreover, the complex offset double reflector also provides the best phase linearity. The advantages of this system over the center-fed double-reflector can be explained by the additional design complexity. The optimization of the non-symmetrical geometry has been done for two orthogonal planes, while for a symmetric center-fed configuration the geometry is the same in all planes. Therefore, independent optimization of scanning and non-scanning planes is a clear advantage of offset configurations.

**Table 4.9** Comparison of optimized reflector configurations for wide scanning operation, based on PO simulations.

Reflector configuration	Array size for 80% aperture efficiency at 30 GHz and percent of active elements from the whole array (for ±20° scanning)			Phase linearity: rms error at 30 GHz for broadside operation
	Scanning range			
	±0°	±10°	±20°	
Reflector with ideal array illumination	4 cm 100%	4 cm 100%	4 cm 100%	0°
Classical prime-focus reflector	1.2 cm 2.3%	23 cm 7.7%	52 cm 19%	6.36°
Complex double center-fed reflector(fictitious model)	2 cm 5.1%	21 cm 11.5%	39 cm 16.7%	3.28°
Complex double offset reflector	16 cm 28%	25 cm 44.6%	28 cm 21.4%	2.81°

#### 4.5. Experimental validation

Based on the analysis of the various optimized configurations, it is clear that the complex offset double reflector configuration is the most promising design in the frame of the requirements of our FPA system. Therefore, this reflector configuration has been chosen for prototyping and experimental validation. The realized prototype is shown in Fig. 4.37 and was measured in the near-field facility at the Eindhoven University of Technology.



**Figure 4.37.** Photo of the prototype using a complex offset double reflector setup.

The array-plane illumination is measured with a horn antenna with a frequency range of 26.4 - 40.1 GHz, as shown in Fig. 4.38. Relevant simulation models have been realized in GRASP and simulated by means of PO [39].

In order to test the required scanning capability up to  $\pm 20^\circ$  in the azimuth plane, an experimental validation with a synthesized PAF has been done. A horn antenna has been placed in different positions along the array plane and related radiation patterns have been measured. According to Table 4.9, the array size should be 28 cm. Therefore, we first measured the far-field patterns with the feed located in the center of the array (Fig. 4.39) and then shifted the feed in steps of 2 cm until it reaches the edge of the array at 14 cm shift (Fig. 4.40 – 4.46).

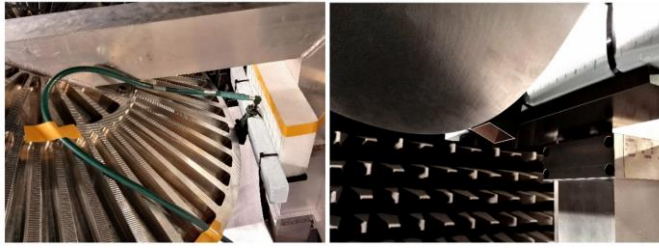


**Figure 4.38.** Photo of experiments with horn feed to measure the array-plane field distribution.

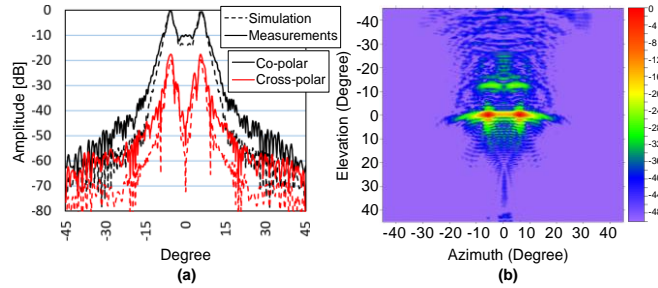


**Figure 4.39.** (a) Far-field pattern in azimuth plane (b) 2D far-field image with feed at the center of the array, 30 GHz.

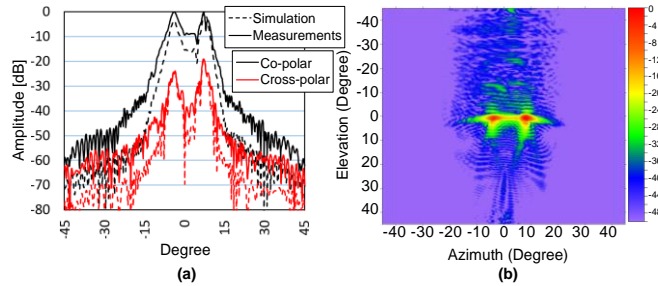


**Figure 4.40.** (a) The far-field pattern in the azimuth plane (b) 2D far-field image with feed displacement from the array center 2 cm, 30 GHz.

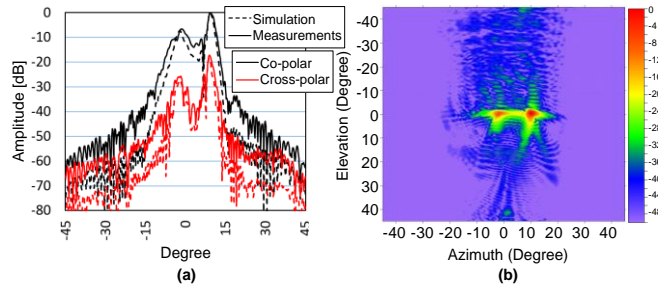


**Figure 4.41.** (a) The far-field pattern in the azimuth plane (b) 2D far-field image with feed displacement from the array center 4 cm, 30 GHz.

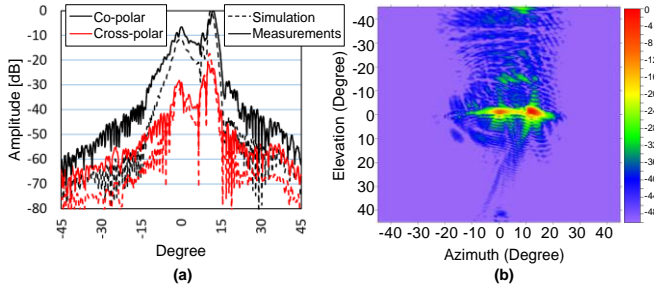


**Figure 4.42.** (a) The far-field pattern in the azimuth plane (b) 2D far-field image with feed displacement from the array center 6 cm, 30 GHz.

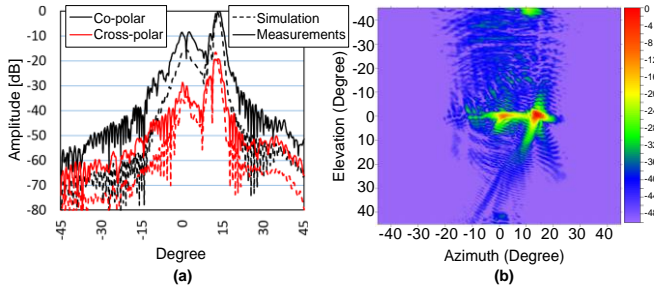


**Figure 4.43.** (a) The far-field pattern in the azimuth plane (b) 2D far-field image with feed displacement from the array center 8 cm, 30 GHz.

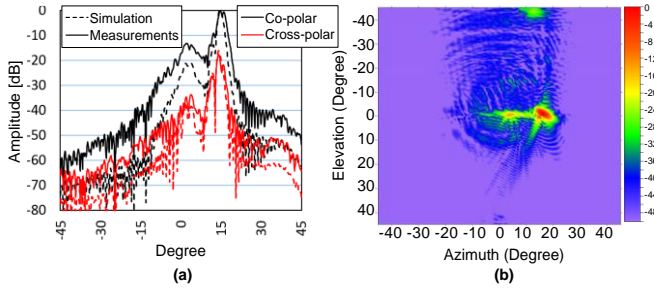


**Figure 4.44.** (a) The far-field pattern in the azimuth plane (b) 2D far-field image with feed displacement from the array center 10 cm, 30 GHz.

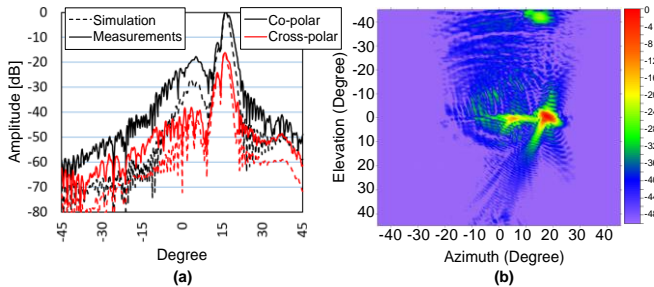


**Figure 4.45.** (a) The far-field pattern in the azimuth plane (b) 2D far-field image with feed displacement from the array center 12 cm, 30 GHz.

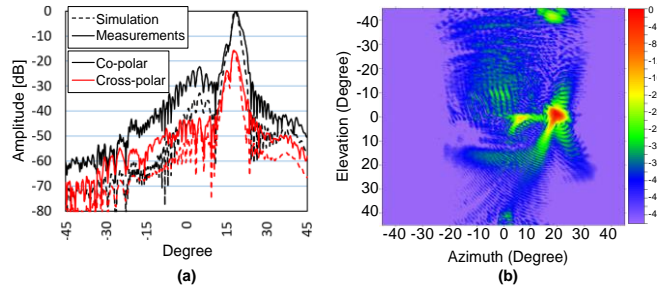
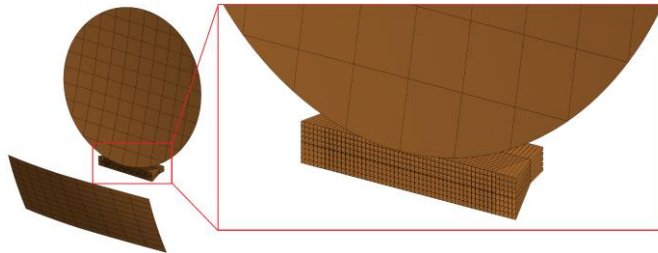


**Figure 4.46.** (a) The far-field pattern in the azimuth plane (b) 2D far-field image with feed displacement from the array center 14 cm, 30 GHz.

The agreement between simulation and measurement is in all cases quite good. The differences in sidelobe levels are mainly due to the large support structure of the reflector in the prototype of Fig. 4.37. This was not included in the simulation. Similar to the field distribution in the array plane for the receive case (see Fig. 4.28), the far-field pattern provides a bi-focal kind of distribution when only a single array element is used. Moreover, the difference between the co-polar and cross-polar components of the electric field is sufficiently high and it is not less than 20 dB.

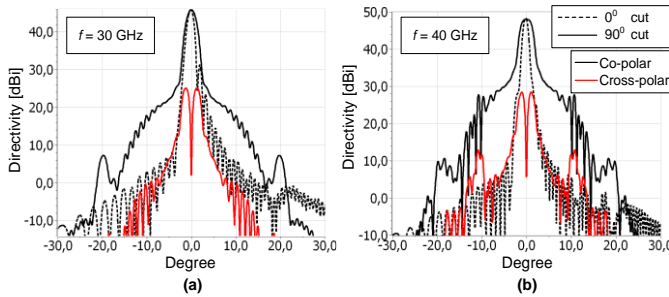
For the maximum feed displacement of 14 cm (Fig. 4.46), the main lobe deviation is about  $17^\circ$ . This is less than the required  $20^\circ$ , but could be improved somewhat by using additional phase control.

To prove the scan performance of the realized reflector prototype, we have done additional simulations with an array of horn antennas, as illustrated in Fig. 4.47. The horn antennas have the same dimensions as used in the experiments. The amplitude and phase of the individual horns have been adjusted by conjugate field matching according to the field distribution in the array plane for the receive case (Fig. 4.30(b) and Fig. 4.30(d)). In this way, it is possible to estimate the reflector directivity using GRASP [39]. Since we have used an ideal horn model, the mutual coupling between array elements is ignored as well as feed mismatch efficiency and phase efficiency. Nevertheless, the radiation efficiency of the reflector, taper efficiency, spill-over efficiency, and polarization efficiency are included. In other words, all parameters related to the actual reflector design are considered. We have investigated the performance at the scan angles  $0^\circ$ ,  $5^\circ$ ,  $10^\circ$ ,  $15^\circ$ , and  $20^\circ$  at 30 GHz and 40 GHz. In addition, array spacings of  $0.6\lambda_0$ ,  $0.7\lambda_0$  and  $0.8\lambda_0$  have been investigated, where  $\lambda_0$  corresponds to the wavelength at 30 GHz. Simulation results are presented in Figs. 4.48 – 4.53.



**Figure 4.47.** The complex offset double-reflector configuration fed by an array of horn antennas.

Fig. 4.48, 4.50, and 4.52 present the broadside operation of the complex double offset reflector configuration. The  $90^\circ$ -cuts correspond to the scan plane or the azimuth plane. In the  $0^\circ$ -plane, the patterns show similar behavior as classical prime-focus reflectors.



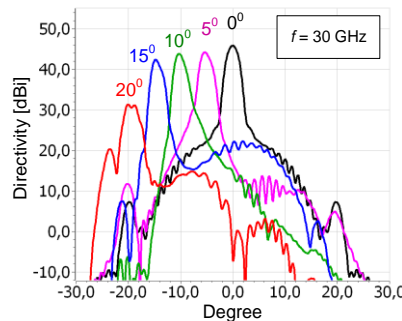
**Figure 4.48.** The directivity of the complex offset double reflector configuration with elements spacing of  $0.8\lambda_0$  for (a)  $f = 30$  GHz, (b)  $f = 40$  GHz.

Fig. 4.49, 4.51, and 4.53 show the predicted performance of the prototype in the case of scanning. Excitations of the array elements have been optimized to realize the scanning performance up to  $20^\circ$ . We can observe that for a scanning range of  $\pm 15^\circ$ , the directivity drop is limited to only a few dB and remains above 40 dBi. This proves the scanning capabilities of this reflector system. The variation in beam directivity across the scan range could be improved by overcoming the prototype production limitations based on the proposed design methods.

Table 4.10 summarizes the realized directivity and reflector efficiencies.

**Table 4.10** Performance of the prototype with different array element spacings at,  $f=30$  GHz.

Number of array elements (horns) and element spacing (for $\lambda_0 = 1$ cm)	Directivity [dB]		Reflector aperture efficiency	
	Frequency		Frequency	
	30 GHz	40 GHz	30 GHz	40 GHz
180 horns, $0.8\lambda_0$	45.801	48.008	78 %	73 %
200 horns, $0.7\lambda_0$	45.913	48.183	80 %	76 %
230 horns, $0.6\lambda_0$	46.071	48.239	83 %	77 %



**Figure 4.49.** Directivity of the complex offset double reflector configuration with element spacing of  $0.8\lambda_0$  for different scan angles,  $f = 30$  GHz.

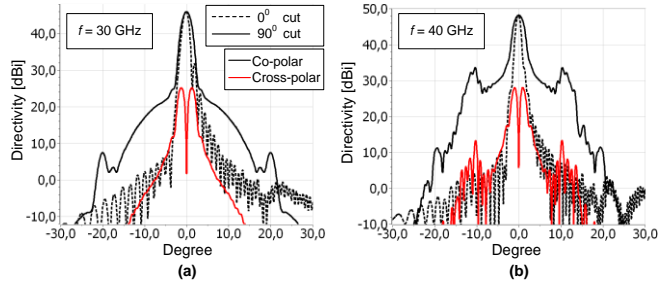


**Figure 4.50.** The directivity of the complex offset double reflector configuration with element spacing of  $0.7\lambda_0$  at 30 GHz for (a)  $f = 30$  GHz, (b)  $f = 40$  GHz.

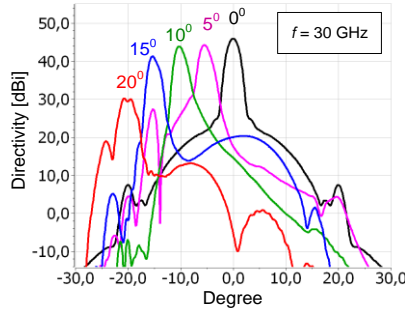


**Figure 4.51.** The directivity of the complex offset double reflector configuration with element spacing of  $0.7\lambda_0$  for different scanning performance,  $f = 30$  GHz.

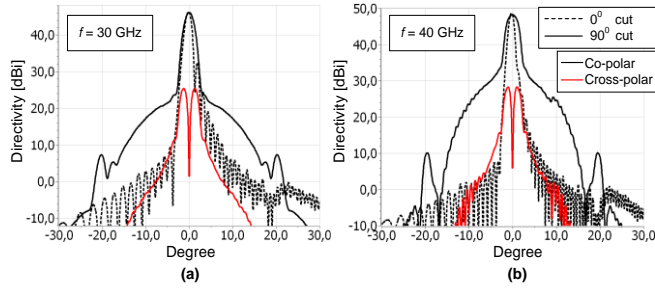


**Figure 4.52.** The directivity of the complex double offset reflector configuration with element spacing of  $0.6\lambda_0$  at 30 GHz for (a)  $f = 30$  GHz, (b)  $f = 40$  GHz.

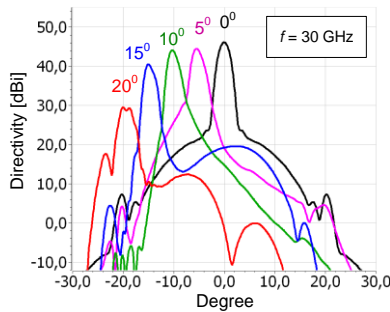


**Figure 4.53.** The directivity of the complex double offset reflector configuration with element spacing of  $0.6\lambda_0$  for different scan angles,  $f = 30$  GHz.

Table 4.10 summarizes the realized directivity and reflector efficiencies. According to Table 4.10, there is a trade-off between the size of the feed array, the number of horn antennas, and the realized efficiency. A higher directivity and reflector aperture efficiency are obtained by using a smaller array grid and more array elements. Nevertheless, even an  $0.8\lambda_0$  element spacing is physically not possible to realize in practice, since the horns are too large. Therefore, one of the crucial challenges for wideband operation is to investigate array elements that could cover the entire frequency range of 20-40 GHz with a well-behaved embedded element pattern and at the same time have compact dimensions below  $0.6\lambda_0$ . References [31], [33] describe array concepts that could meet these stringent requirements.

#### 4.6. Conclusion

In sections 4.1-4.6, a mathematical framework, based on GO, is presented to optimize wide-scanning single- and double-reflector focal plane arrays. The suggested evaluation method allows to compare of all configurations with an ideal case. An optimized new complex offset double-reflector configuration has been designed, produced, and experimentally validated.

The final complex offset double-reflector configuration achieves the intended scanning range using a compact array which allows half of the array elements to be active during scanning within the scan range of  $\pm 10^\circ$  and at least a quarter of the array elements active within a scan range of  $\pm 20^\circ$ . The scanning capabilities have been significantly improved as compared to classical prime-focus and double-parabolic reflectors. The well-known FPA problem of a small illuminated region in the focal plane has been successfully overcome. In addition, the phase linearity between the array elements of the PAF has been sufficiently improved in order to allow an optical beamforming concept (2.81° rms linearity error at 30 GHz). The experiments demonstrate a very good agreement with simulations and fully prove the required scanning performance within the  $\pm 20^\circ$  scan range with high directivity and reflector aperture efficiency up to 83 % at 30 GHz and 77 % at 40 GHz.

#### 4.7. Extreme Scanning Double Shaped-Reflector Antenna with Multiple Interactions for Focal Plane Array applications<sup>1</sup>

##### Summary

A new type of focal plane array (FPA) reflector antenna concept is proposed with a very wide field-of-view over a wide bandwidth (20-40 GHz) for ground terminals for Ka-band satellite communication and multi-function radars. The proposed concept maximizes the percentage of active array elements up to 90% within the required scanning range of  $\pm 10^\circ$  along the azimuthal plane. It combines the advantages of phased arrays in terms of wide-angle scanning and of FPA systems in terms of high antenna gain. This FPA system achieves a 15 dB higher antenna gain as compared to a phased array with a size equal to the feed array of the proposed reflector system. Based on a minimum required 80% aperture efficiency at 30 GHz, the illuminated array region is increased by a factor of 20<sup>0</sup> as compared to traditional prime-focus configurations. In addition, the FPA configuration significantly reduces the required overall array size by a factor of 1.5 as compared to conventional double-parabolic reflector configurations. Moreover, the scanning capabilities have been significantly improved as compared to classical prime-focus and double-parabolic reflectors. Since a large part of the array is active, we can obtain highly effective isotropic radiated power (EIRP).

##### 4.7.1. Introduction

Focal-plane arrays (FPAs) provide a high antenna gain at low costs and allow beam scanning or multi-beam functionality [12], [8], [159], [146], [160], [13]. However, the field-of-view (FoV) is limited. In addition, conventional FPAs only allow a small number of array elements to be active simultaneously for a particular beam. This limits the use of this concept in several emerging applications in terms of the number of multiple beams or scan range [142] and level of achievable effective isotropic radiated power (EIRP) [15]. A low EIRP level limits the use of low-cost silicon integrated circuits. In addition, it is a challenge to provide a proper exposure of the FPA within a wide scan range, due to the significant beam deviation in the focal plane [143]. Moreover, a wide scan range would require a large array size. As a consequence, the number of simultaneous active elements is small as compared to the total number of array elements. In this chapter, we will present a double reflector concept that overcomes the limited FoV and limited maximum EIRP of optimized conventional single- and double-reflector FPAs as presented in [10], [38].

We have set the following challenging design goals for the FPA system:

- wide illumination area of the array for each scan angle to maximize the EIRP,
- decreased beam deviation in the focal plane region during scanning, reducing the required number of array elements,
- maximize the percentage of active array elements within the required scanning range,
- wide operational bandwidth between 20-40 GHz.

<sup>1</sup>Current paragraph 4.7 is published as a journal paper: Dubok, A.; Al-Rawi, A.; Gerini, G.; Smolders, A.B., "Extreme Scanning Focal-plane Arrays using a Double," Transactions on Antennas and Propagation. Communication, vol. 68, no. 7, pp. 5686-5690, 2020 and included here in its entirety without any changes.

To realize these stringent requirements, we propose a new type of reflector antenna in which the sub-reflector has a double interaction with the electromagnetic waves focused by the main reflector. In this way, we obtain a large illuminated focal plane region. In order to optimize this configuration, we have developed a mathematical framework [12] based on geometrical optics (GO) [161]. Our optimized models have been validated with simulations in GRASP [39].

This chapter presents the following new scientific contributions:

- a new type of FPA reflector antenna concept is proposed with a very wide field-of-view over a wide bandwidth,
- our configuration has unique features that maximize the ratio of active array elements of the FPA for each scan angle within a scan range of  $\pm 10^\circ$  along the azimuth plane which allows to use Silicon-based transceivers.

The chapter is organized as follows. In section 4.7.2, a short overview of conventional single and double-reflector FPA systems is presented based on [12], [162], [150], and [163]. In section 4.7.3 we will introduce our novel reflector system with double sub-reflector interaction. Note that in this chapter we will focus on the receive case. Using the approach of [12], the related transmit situation can be investigated.

#### 4.7.2. Illumination challenges for conventional FPAs

The most widespread-used single-reflector antenna is the classical prime-focus reflector with a parabolic shape. The electric-field distribution in the focal plane of a classical prime-focus reflector behaves according to the well-known distribution of so-called Airy rings, corresponding to zeros of the Bessel function of the first kind and order 1 along the aperture radius  $r$  [143]. According to [143], it is clear that the same reflector operating at higher frequencies will illuminate a smaller region in the focal plane.

According to [162], for a classical prime-focus reflector with  $F/D = 0.6$  and  $D = 0.8$  m only a few array elements are required in the area of maximum power density (above the -3 dB level). In addition, in the case of scanning the required aperture size is significantly increased. At the same time, most of the array elements are inactive. Moreover, in order to provide scanning capabilities of  $\pm 10^\circ$  in the azimuth plane, the horizontal dimension of the array should be at least 0.23 m to obtain 80% aperture efficiency, which corresponds to about 29% of the size of the reflector [150]. Therefore, minimization of the beam deviation during scanning is an important factor to limit the required array size and overall system cost.

According to [150] the spherical reflector without axial displacements is the best option for minimizing the lateral array size for wide-angle scanning operations with single reflector systems. Nevertheless, the array for  $\pm 10^\circ$  scanning should be at least 0.22 m for 80% aperture efficiency with a reflector size of  $D=0.8$  m [150]. Therefore, the spherical reflector also results in a low ratio of active versus the total number of elements.

Next to single-reflector systems, we have investigated the limitations of double-reflector systems [12]. Their main advantage is an increased illuminated region in the focal plane and, as a consequence, the number of simultaneously active elements. The most widespread example of a double-reflector system is the double-parabolic reflector with two proportional parabolic shapes. According to [162] for these configurations, the aperture efficiency for

different angles of incidence shows that the required array size in the case of scanning should be significantly increased in order to achieve sufficient aperture efficiency. The issue in performance is due to the amplification of the incidence angle on the array surface, expressed by the magnification factor  $M$  [147]:

$$\theta_0 = \frac{F_m}{F_s} \theta = M \theta, \quad (4.40)$$

where  $\theta$  is the angle of incidence of the incident field and  $\theta_0$  is the incident angle on the array surface,  $F_m$  is the focal length of the main reflector, and  $F_s$  is the focal length of the sub-reflector.

In [162] two variants of double-parabolic reflector configurations were investigated. The first variant uses a ratio between reflectors of  $F_m/F_s = 8$ , and the second variant uses  $F_m/F_s = 4$ , where  $F_m$  is the focal length of the main reflector, and  $F_s$  is the focal length of the sub-reflector. For broadside operation, the illuminated area of the array has been increased by a factor of 150 for the first configuration, and 230 – for the second. In addition, the magnification factor  $M$  for the second configuration is lower and a significantly smaller array is required for  $\pm 5^\circ$  and  $\pm 10^\circ$  scanning.

Double reflector configurations also could be solved as a lens antenna according to [163]. Nevertheless, the presented approach in [163] is limited to reflectors with a high magnification factor  $M = D_m/D_s \gg 1$ , where  $D_m$  is the diameter of the main reflector and  $D_s$  is the diameter of the sub-reflector. However, for double-reflector systems, relatively large sub-reflectors are required in the case of wide-angle scanning [162]. This issue is overcome in [12] by a mathematical framework of the FPA system for an arbitrary shape of the main- and sub-reflectors. As an outcome, the complex offset dual reflector with sub-reflector discontinuity has been proposed for wide scanning operation. The obtained design achieves scanning capabilities up to  $\pm 20^\circ$  in the azimuth plane with an array with overall dimensions  $28 \text{ cm} \times 4 \text{ cm}$  or  $28\lambda_0 \times 4\lambda_0$ , where  $\lambda_0$  is the wavelength at the center frequency 30 GHz. In addition, for  $10^\circ$  scanning about 44.6% of the array elements are active.

Based on the investigated variants of the classical double-parabolic reflector configurations we can conclude that it is feasible to improve the illumination challenge of FPAs with sub-reflector optimization. With a smaller magnification factor  $M$ , a smaller array will be required in the case of scanning to  $\pm 10^\circ$ . However, at the same time, a smaller magnification factor results in less focused beams on the surface of the array even in the non-scanning case. This means that also in the orthogonal direction (elevation), a much larger array is required. To overcome these problems, our proposal is to use two sub-reflectors, each having a lower value of  $M$ . These sub-reflectors could be combined in one surface with double-ray interaction. In this way, it is possible to realize a low magnification factor, while still maintaining a focused beam on the array in the focal plane. The operation principle of such a system is presented in section 4.7.3.

#### 4.7.3. Reflector system with double sub-reflector interaction

Fig. 4.54 demonstrates the reflector system with double sub-reflector interaction. Note that this reflector configuration is a logical continuation of the configuration presented in [12]. Additional features of Fig. 4.54 could also be seen in Figs. 5-8 of [12]. The electromagnetic waves reflected from one side of the sub-reflector surface have a second interaction with the

other side of the sub-reflector before impinging the array in the focal plane. The main advantage of this system is the possibility of extra control of the waves interacting with the array surface. The obvious disadvantages are the design complexity and the sufficient size of the sub-reflector, which is comparable to the size of the main reflector. It is obvious that such a system could be considered only in offset-reflector models. Nevertheless, our new concept provides unique performance in terms of maximizing the ratio of active versus the total number of array elements.

In order to optimize the reflector system with double sub-reflector interaction, it is necessary to develop a model of the FPA system for an arbitrary shape of the main- and sub-reflectors. The performance of the optimized system is then verified using a more accurate and computationally more intensive model based on the method of moments (MOM) in GRASP [39]. Mathematical details, optimization goals, and cost function definitions of our mathematical model are presented in [12].

The main reflector surface  $S(x, y, z)$  for the configuration of Fig. 4.54 can be expressed in terms of a second-order polynomial:

$$S(x, y, z) = A_{xx}x^2 + 2A_x x + A_{yy}y^2 + A_{zz}(z - z_0)^2 + 2A_{yz}y(z - z_0) = 0, \quad (4.41)$$

where  $A_{ij}$  are polynomial coefficients. The offset between sub and main reflector  $z_b$  (Fig. 4.54) should be at least a few wavelengths in order to have no significant blockage effects and not have a significant difference between the GO and MOM simulation results due to the ray caustics in the array plane [156], [154].  $z_0$  is the offset of the polynomial function of the main reflector along the  $z$ -coordinate, see Fig. 4.54. In addition, a proper choice of the array position  $z_c$  allows to avoid mutual reflections between the main reflector, sub-reflector, and array. The position of the array is close to the main reflector or in its plane ( $F_a = 0$ ).

The sub-reflector surface  $S_s(x, y, z)$  can also be defined in terms of a second-order polynomial (see also Fig. 4.54):

$$\begin{aligned} S_s(x, y, z) &= B_{xx}(x - F_s)^2 + 2B_x(x - F_s) + B_{yy}(y - y_s)^2 + B_{zz}(z - z_s - z_{s0})^2 \\ &\quad + 2B_{yz}(y - y_s)(z - z_s - z_{s0}) = 0, \quad y > 0, z > 0, \\ S_s(x, y, z) &= B_{xx}(x - F_s)^2 + 2B_x(x - F_s) + B_{yy}(y + y_s)^2 + B_{zz}(z - z_s - z_{s0})^2 \\ &\quad + 2B_{yz}(y + y_s)(z - z_s - z_{s0}) = 0, \quad y < 0, z > 0, \\ S_s(x, y, z) &= B_{xx}(x - F_s)^2 + 2B_x(x - F_s) + B_{yy}(y - y_s)^2 + B_{zz}(z + z_s - z_{s0})^2 \\ &\quad + 2B_{yz}(y - y_s)(z + z_s - z_{s0}) = 0, \quad y > 0, z < 0, \\ S_s(x, y, z) &= B_{xx}(x - F_s)^2 + 2B_x(x - F_s) + B_{yy}(y + y_s)^2 + B_{zz}(z + z_s - z_{s0})^2 + \\ &\quad 2B_{yz}(y + y_s)(z + z_s - z_{s0}) = 0, \quad y < 0, z < 0, \end{aligned} \quad (4.42)$$

where  $B_{ij}$  are the polynomial coefficients,  $z_{s0}$  is a shift of the polynomial function of the reflector along the  $z$ -coordinate,  $F_s$  is the sub-reflector position along the  $x$ -axis,  $z_s$  describes the discontinuity of the sub-reflector along the  $z$ -coordinate and  $y_s$  – along the  $y$ -coordinate, respectively, see Fig. 4.54. The dotted lines in Fig. 4.54 stand for the polynomial function of the main reflector surface  $S(x, y, z)$  and the sub-reflector surface  $S_s(x, y, z)$ . The actual sub-

reflector surface is illustrated by the solid line in Fig. 4.54, which is part of the polynomial function.

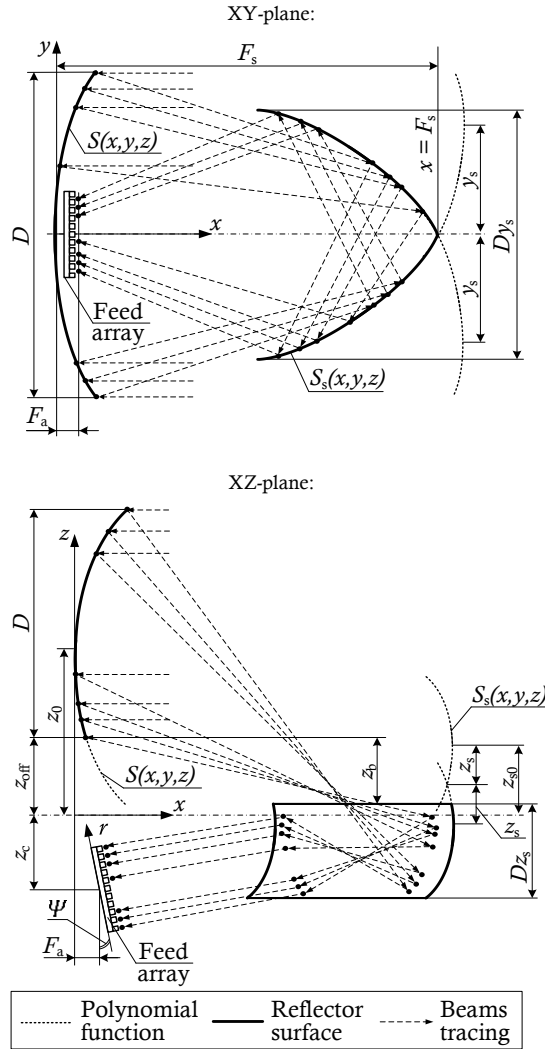


**Figure 4.54.** Reflector system with double sub-reflector interaction.

We used the mathematical framework of [12] to optimize the antenna system of Fig. 4.54 to meet our requirements. The goal is to minimize the size of the array during scanning and to achieve the highest ratio between the active and total number of elements within this array. The scanning has been investigated along the azimuth direction. In the orthogonal vertical direction, an array size of 4 cm is used for all scan angles, which corresponds to  $4\lambda_0$  at the center frequency of 30 GHz. The diameter of the main reflector is  $D=0.8$  m. For the reflector model of Fig. 4.54, the obtained optimal polynomial coefficients and variables using GO are shown in Table 4.11.

**Table 4.11** Optimal polynomial coefficients and variables of a reflector system with double sub-reflector interaction. Optimization is done with GO.

Variable	Obtained value	Variable	Obtained value
$A_{xx}$	$88.84 \text{ m}^2$	$B_{xx}$	$0 \text{ m}^2$
$A_{yy}$	$474.6 \text{ m}^2$	$B_{yy}$	$-871.4 \text{ m}^2$
$A_x$	$-465.5 \text{ m}^{-1}$	$B_x$	$-110.5 \text{ m}^{-1}$
$A_{zz}$	$336.3 \text{ m}^2$	$B_{zz}$	$-729.8 \text{ m}^2$
$A_{yz}$	$0 \text{ m}^2$	$B_{yz}$	$0 \text{ m}^2$
$F_s$	$0.812 \text{ m}$ or $81.2\lambda_0$	$F_a$	$0 \text{ m}$ or $0\lambda_0$
$z_s$	$0.177 \text{ m}$ or $17.7\lambda_0$	$y_s$	$-0.0745 \text{ m}$ or $-7.45\lambda_0$
$z_0$	$-0.023 \text{ m}$ or $-2.3\lambda_0$	$z_{s0}$	$0.157 \text{ m}$ or $15.7\lambda_0$
$z_{\text{off}}$	$0.1 \text{ m}$ or $10\lambda_0$	$z_c$	$-0.01 \text{ m}$ or $-1\lambda_0$
$Dz_s$	$0.335 \text{ m}$ or $33.5\lambda_0$	$Dy_s$	$0.774 \text{ m}$ or $77.4\lambda_0$
$\psi$	$-12.23^\circ$	$D$	$0.8 \text{ m}$ or $80\lambda_0$

The optimal sub-reflector has a non-continuous shape since the discontinuity variables  $z_s$  and  $y_s$  are not equal to zero. The parameters  $z_c = -0.01 \text{ m}$ ,  $F_a = 0$  and  $\psi = -12.23^\circ$  indicates that the array is shifted 1 cm or  $1\lambda_0$  from the center of the coordinate system and is slightly rotated in the offset plane, see Fig. 4.54. The dimensions of the sub-reflector,  $Dz_s$  and  $Dy_s$ , are comparable to the dimensions of the main reflector, but there is no blockage effect.

In the case of broadside operation, the reflector configuration is illustrated in Fig. 4.55. Fig. 4.56 illustrates the beam tracings between different parts of the antenna system. In all simulations, linear polarization is assumed. For broadside incidence, the polarization is along the  $z$ -axis. Fig. 4.57 shows the corresponding electric-field cuts in the array plane for  $x = 0$  along the  $y$ -coordinate of Fig. 4.56 based on GO and MOM simulations, respectively. The electric-field cuts in the array plane along the  $y$ -coordinate of Fig. 4.56, based on MOM simulation for  $5^\circ$  and  $10^\circ$  scanning, are presented in Fig. 4.58 for the  $x = 0$  cut in the array plane. A two-dimensional illustration of the field patterns in the array plane for different incidence angles is presented in Fig. 4.59. The aperture efficiency, calculated according to the MOM simulation results of Fig. 4.57(b) and Fig. 4.58, is presented in Fig. 4.60. The aperture efficiency estimation includes the radiation efficiency of the reflector, taper efficiency, spill-over efficiency, polarization efficiency. It is determined according to [162].

The electric-field cuts of Fig. 4.57 demonstrate the interesting properties of the optimized configuration. In the case of broadside operation, the electric-field distribution is significantly broadened along the scan plane as compared to conventional single and double-reflector systems [162]. Based on the GO simulation results we can conclude that the array is illuminated close to uniform. The MOM simulation results show similar behavior with some distortions in the electric-field distribution along the array. This is caused by diffraction effects at the edges of the reflectors. In the case of  $5^\circ$  and  $10^\circ$  scanning (Fig. 4.58), the electric-field cuts have almost the same distribution as the broadside case and the same size as the required array. This leads to the observation that almost all array elements are active within the required scan range of  $\pm 10^\circ$  in azimuth, which is a unique feature of our optimized concept. In addition, Fig. 4.59 demonstrates that the array could be relatively compact along the non-scanning plane and that for the entire scanning range the same array dimension is required. We included the radiation efficiency of the reflector, taper efficiency, spill-over efficiency, and polarization efficiency in the simulations. In other words, all parameters related to the actual reflector design are considered. The aperture efficiency versus aperture radius for the different angles of incidence (Fig. 4.60), shows a much smoother behavior as compared to

the conventional reflector systems presented in [12], [162], [150], and [163]. This is due to the more uniform distribution of the electric field within the array. In addition, according to the aperture-efficiency distribution of Fig. 4.60, the dimension of the array in the azimuth plane should be about 63.6 cm to obtain 80% aperture efficiency in the scan range up to  $\pm 10^\circ$  in the azimuth plane or  $63.6\lambda_0$ . As a result, an array with the overall size of 63.6 cm x 4 cm or  $63.6\lambda_0 \times 4\lambda_0$  is required for the proposed reflector system.

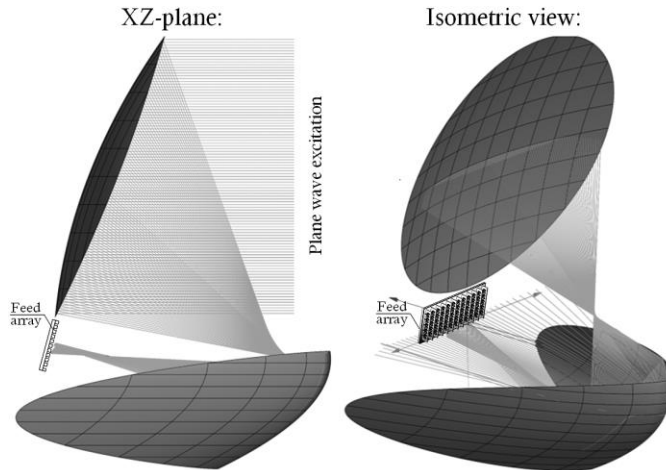


**Figure 4.55.** Simulation model of a system with double sub-reflector interaction.

Based on an 80% aperture efficiency, it is possible to estimate the required array size for wide-scanning operation. In addition, based on the overall field distribution, we can evaluate the percentage of simultaneously active array elements. The number of active elements is defined as the minimum number of array elements that are required to be involved in order to achieve an aperture efficiency of 80% (see Fig. 4.60). The obtained results are summarized in Table 4.12 for 30 GHz. At other frequencies, the results are similar since Fig. 4.60 demonstrates that the aperture efficiency distribution does not vary significantly over the frequency range from 20-40 GHz.

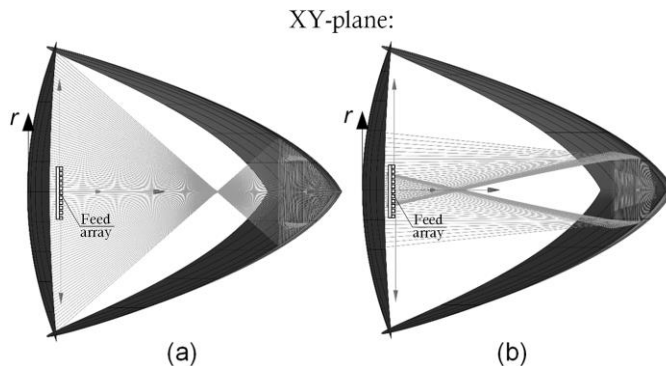


**Figure 4.56.** (a) beam tracing between the main reflector and the sub-reflector (b) beam tracing between the sub-reflector and array plane.

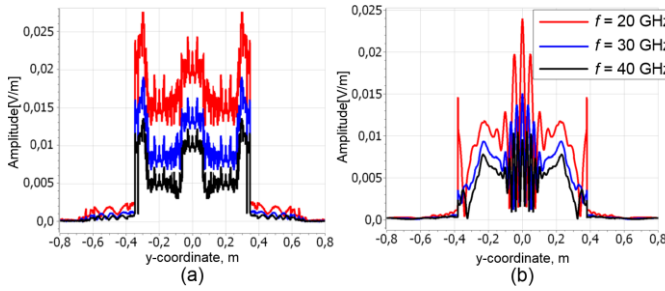


**Figure 4.57.** (a) Electric-field cuts in the array plane based on GO simulations (b) electric-field cuts in the array plane based on MOM simulation. Results for broadside operation are shown of the optimized system with double sub-reflector interaction.

According to Table 4.12, there is a trade-off between the size of the required array for scanning within  $\pm 10^\circ$ , the percentage of active elements, and reflector configuration complexity. The most widespread classical prime-focus reflector requires an array of 23 cm or  $23\lambda_0$ , but only 15.2% of array elements are active for this case. The spherical reflector improves this ratio up to 20.9% with almost the same array size. The more complicated complex offset double reflector achieves 44.6% of elements usage with a slightly bigger array of 25 cm or  $25\lambda_0$  [12]. An even higher ratio could be obtained with symmetrical double-parabolic reflectors, up to 48% for  $F_m/F_s = 8$  configuration. However, the required array size, in this case, is enormous and eliminates the advantage of using FPAs over conventional phased arrays [162]. The proposed reflector system with double sub-reflector interaction has a reasonable array size of 63.6 cm or  $63.6\lambda_0$  and, due to the more complicated mechanism of rays intersection with the sub-reflector surface, achieves a wide FoV over a wide bandwidth (Fig. 4.60). For scan angles up to  $5^\circ$  about 89% of array elements is active and for a scan angle of  $10^\circ$  almost the whole array is active. Clearly, our new reflector concept with double sub-reflector interaction outperforms the conventional single and double-reflector systems. Therefore, we can conclude that our new optimized concept provides wide-angle scanning capabilities using a relatively small array and, at the same time, offers a high number of active array elements for each scan angle. The latter allows to realize of a high EIRP using low- to medium-power silicon-based amplifiers.

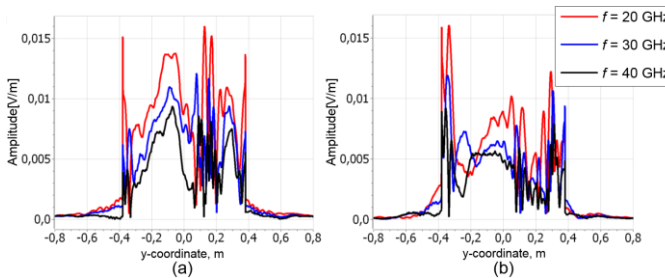


**Figure 4.58.** (a) Electric-field cuts for  $5^\circ$  incidence angle (b) Electric-field cuts for  $10^\circ$  incidence angle. MOM simulation results are shown of the optimized system with double sub-reflector interaction.

Based on the antenna reciprocity theorem it is possible to claim that the obtained reflector system will achieve adequate radiation patterns in terms of gain and side lobe values, as has been demonstrated in [12] since the obtained electric-field cuts (Fig. 4.57 – 4.58) could be

successfully synthesized by an active array in the focal plane with proper beamforming within the sufficient array size [164].

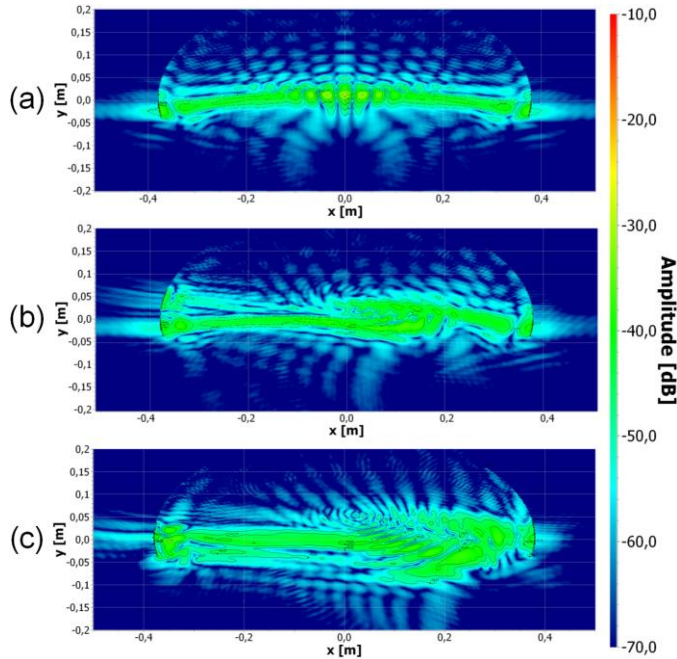


**Figure 4.59.** Two-dimensional illustration of the field pattern in the array plane based on MOM simulations of a system with double sub-reflector interaction for (a) broadside operation (b)  $5^\circ$  incidence angle (c)  $10^\circ$  incidence angle,  $f = 30$  GHz.

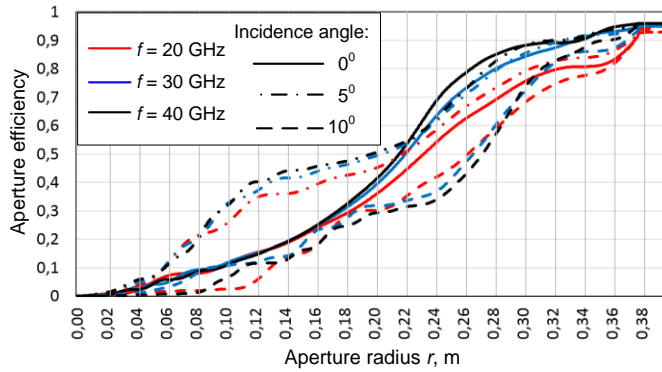


**Figure 4.60.** Aperture efficiency in the array plane for different incidence angles of a reflector system with double sub-reflector interaction.

The overall array size of our FPA systems is 63.6 cm or  $63.6\lambda_0$  in the scanning plane and 4 cm or  $4\lambda_0$  in elevation. This means that we need 1024 elements with an element spacing of  $\lambda_0/2$  at the center frequency of 30 GHz. A conventional phased-array of equivalent size could only provide an antenna gain of about 33 dBi, whereas our FPA system could potentially achieve an antenna gain of approx. 48 dBi, which is 15 dB higher as compared to the corresponding phased-array. It is important to note that this comparison is related to the equivalent size of the array since it is the most complex and costly part of the system. The

overall size of an FPA is primarily defined by reflectors, which, however, represent a relatively cheap and passive part of the system.

**Table 4.12** Comparison of investigated reflector configurations for wide scanning operation.

Reflector configuration	Array size for 80% aperture efficiency at 30 GHz and percentage of active elements (for $\pm 10^\circ$ scanning)		
	Scanning range		
	$\pm 0^\circ$	$\pm 5^\circ$	$\pm 10^\circ$
Classical prime-focus reflector [162]	1.2 cm	11.6 cm	23 cm
	$1.2\lambda_0$	$11.6\lambda_0$	$23\lambda_0$
	5.2%	11.3%	15.2%
Spherical reflector [150]	2.8 cm	12 cm	22.4 cm
	$2.8\lambda_0$	$12\lambda_0$	$22.4\lambda_0$
	12.5%	15.6%	20.9%
Symmetrical double-parabolic reflector, $F_m/F_s = 8$ [162]	18.4 cm	96 cm	336 cm
	$18.4\lambda_0$	$96\lambda_0$	$336\lambda_0$
	2.7%	28.6%	48%
Symmetrical double-parabolic reflector, $F_m/F_s = 4$ [162]	22.8 cm	47.6 cm	98 cm
	$22.8\lambda_0$	$47.6\lambda_0$	$98\lambda_0$
	11.6%	20.2%	25.5%
Complex offset double reflector [12]	16 cm	19 cm	25 cm
	$16\lambda_0$	$19\lambda_0$	$25\lambda_0$
	28%	33.6%	44.6%
<b>This work:</b> reflector system with double sub-reflector interaction	<b>56.4 cm</b>	<b>56.4 cm</b>	<b>63.6 cm</b>
	<b><math>56.4\lambda_0</math></b>	<b><math>56.4\lambda_0</math></b>	<b><math>63.6\lambda_0</math></b>
	<b>89%</b>	<b>89%</b>	<b>100%</b>

#### 4.7.4. Conclusions

We have presented a novel focal-plane reflector system with double sub-reflector interaction which shows excellent performance over a wide frequency range and wide scan range. It maximizes the number of simultaneously active array elements. Almost the entire array is active within a scan range of  $\pm 10^\circ$ , allowing to achieve of a high EIRP with low- to medium-power silicon-based amplifiers. It also overcomes the well-known FPA problem of a small illuminated region in the focal plane by improving it by a factor of 200 as compared to traditional prime-focus configurations see also Table 4.12. In addition, the scanning capabilities have been improved significantly as compared to classical prime-focus and double-parabolic reflectors. There is almost no beam deviation in the array plane anymore during scanning. The main operational feature of the new system is the double sub-reflector interaction. The downside of this feature is the requirement of a relatively large sub-reflector. The size is 33.5 cm x 77.4 cm with a pronounced V-shape due to the discontinuity of the function defining the sub-reflector surface.

The proposed reflector system with double sub-reflector interaction combines the advantages of phased-arrays and FPAs providing a high antenna gain within a scan range of up to  $\pm 10^\circ$ . With a feed array of overall dimensions 63.6 cm x 4 cm ( $63.6\lambda_0$  x  $4\lambda_0$ ), the gain is 15 dB higher as compared to traditional phased arrays of equivalent size.

As future work, the presented novel reflector configuration could be integrated with a wideband silicon-based phased-array feed.

# CHAPTER FIVE

## 5. FPA DESIGN AND IMPLEMENTATION

---

### 5.1. Arrays investigation<sup>1</sup>

This chapter discusses the main design challenges of wideband antenna elements which can be used in wideband focal-plane arrays and phased arrays. The impact of significant mutual coupling on the active impedance matching is presented for the case of wideband focal plane arrays (FPAs). Two novel FPA designs are presented. The array elements are based on a modified version of the well-known bow-tie antenna. The proposed array shows excellent active matching properties. It is shown that the center element of a 5x5 array, operating at a center frequency of 30 GHz, has an impedance bandwidth of 20 GHz. Moreover, a further optimized concept provides a similar bandwidth with twice as high element density.

#### 5.1.1. Introduction

Electronic phased-array antennas are used in many applications. However, there are bandwidth limitation challenges for using this technology at higher frequencies [130]. At the same time, the demand for wideband antenna arrays and focal-plane arrays (FPA) are increasing, especially in the Ku- and Ka-band. Hence, it is necessary to make an investigation of broadband array antenna elements.

This chapter presents the work which was done in the framework of the development of a wideband array for use in an FPA system, operating in the frequency band from 20-40 GHz. We will investigate the wide-band scan performance of the array in the case of a conventional phased array as well as in the case of an FPA system in which a complex field distribution needs to be generated for proper reflector illumination. We will discuss the effect of mutual coupling in FPAs and phased arrays and we will show the impact of mutual coupling on the antenna matching performance. Our goal for the FPA antenna system is to increase the element density of the array in order to obtain a larger effective isotropic radiated power (EIRP).

#### 5.1.2. Wideband array design

Paper [165] presented a connected array of five modified bow-tie antenna elements in a row with a bandwidth of 24.4 GHz (Fig. 5.1). However, the array performance was optimized only for the case of “passive array” operation, where only the central element was excited and all other array elements were matched to 50 Ohm. In the case of an active-scanned array,

<sup>1</sup>Current paragraph 5.1 is published as a conference paper: Dubok, A.; Al-Rawi, A.; Herben, M.H.A.J.; Smolders, A.B., "Wideband focal plane connected array," in 10th European Conference on Antennas and Propagation, EuCAP 2016, Davos, Switzerland, 2016, and included here in its entirety without any changes.

all elements are involved and there will be some phase difference between them (Fig. 5.2). In this situation it is necessary to consider the active reflection coefficient (ARC) [166]. The ARC of array element  $m$  can be determined by:

$$R_m(\theta_0, \varphi_0) = \sum_{n=1}^N S_{mn} a_n \quad (5.1)$$

where  $S_{mn}$  is the scattering coefficient between elements  $m$  and  $n$ ,  $a_n$  is a excitation vector,  $\theta_0$ , and  $\varphi_0$  scan angles relative to the normal of surface of the array and  $N$  is the number of array elements. In the case of scanning along only one plane, the complex excitation vector is given by:

$$a_n = \exp(-j \frac{2\pi f}{c} d_x \sin \theta_0 (n - 1)) \quad (5.2)$$

where  $d_x$  is the distance between array elements (Fig. 5.2),  $c$  - speed of light, and  $f$  - frequency of operation. Note that a uniform amplitude tapering was assumed.

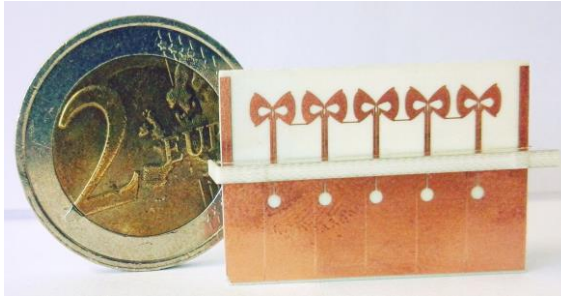


**Figure 5.1.** Cross section of a connected array of five modified bow-tie antenna elements in a row.

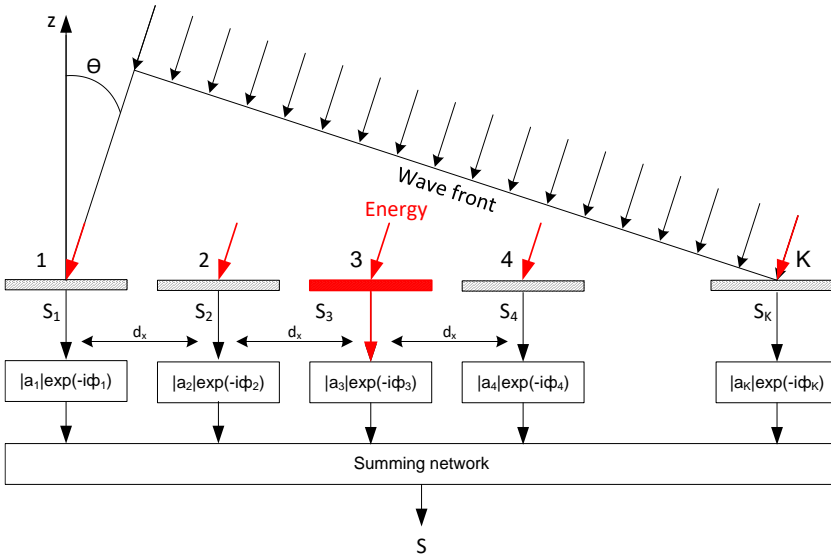


**Figure 5.2.** Excitation and mutual coupling mechanism of phased array.

In Fig. 5.3 the ARC according to (5.1) is presented for several scan angles for the configuration as shown in Fig. 5.1. The S-matrix has been calculated with CST [139]. It is clear that the bandwidth of the active reflection coefficient is significantly smaller as compared to the non-scanning situation. The bandwidth of the central array element (Fig. 5.3) is smaller than 12 GHz for scan angles larger than 10 degree. This is due to the high level of mutual coupling between the array elements in combination with the phase difference of the excitation vectors.

As a next step, we have investigated the combination of an array and reflector, forming an FPA system. In the case of FPAs, there are not only phase differences between array elements, but there is a strongly varying complex amplitude distribution. For example, for a symmetrical parabolic reflector, the field in the focal plane will have the shape of an Airy pattern (Fig. 5.4, Fig. 5.5) [145]. In addition, the phase distribution is not linear like in the case of a conventional phased array. As a result, the effect of mutual coupling on the active matching performance will differ from (5.1). Simulation results of the electric field in the focal plane for a symmetrical parabolic reflector are presented in Fig. 5.4. Simulations have been performed with GRASP [39]. From the focal field data, we can determine the complex excitation vectors  $a_n$  by means of conjugate field matching [131]. The array geometry of Fig. 5.1 has been updated to a two-dimensional array consisting of five rows of connected arrays with five modified bow-tie antenna elements in a row, see Fig. 5.6. Excitation vector data have been imported to MATLAB [167] from GRASP [39] for a 0.8 m symmetrical parabolic reflector with  $F/D = 0.6$ .

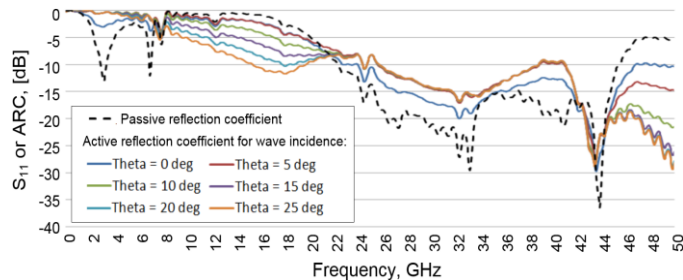


**Figure 5.3.** Passive reflection coefficient and active reflection coefficient of central element for different wave incidence on the phased array of five modified bow-tie antenna elements in a row.

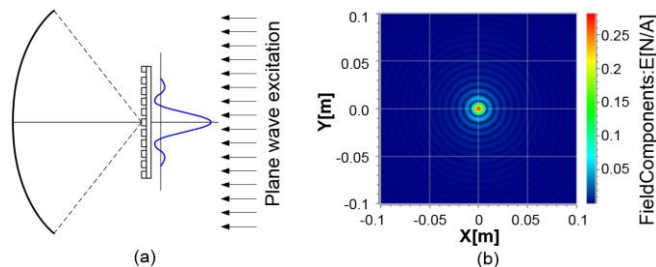


**Figure 5.4.** (a) Field propagation of reflector antenna in the focal plane (b) 2D illustration of the Airy pattern in the focal plane of a symmetrical parabolic reflector with  $F/D = 0.6$ ,  $f = 30$  GHz.

From Fig. 5.4 it is clear that there are strong amplitude differences between array elements in the case of an FPA. Thus, there are situations, where certain elements get most of the

energy due to mutual coupling. Therefore, for this element, the ARC could be significantly higher than 1. Therefore, it is more meaningful to introduce the total active antenna reflection coefficient (TARC) parameter [168] which describes the wideband properties of the whole array and can be written as:

$$\text{TARC} = \frac{\sqrt{\sum_{m=1}^N |R_m(\theta_0, \varphi_0)|^2}}{\sqrt{\sum_{m=1}^N |a_m|^2}} \quad (5.3)$$

In Fig. 5.7, the results for the FPA of Fig. 5.6, using (5.1) and (5.3), are presented. It is clear that for the central element, the frequency bandwidth remains almost the same in the case of the ARC. However, the overall array performance (TARC) shows a strong reduction in the bandwidth of approximately a factor of two due to significant mutual coupling, in combination with the specific amplitude and phase differences between the array elements.

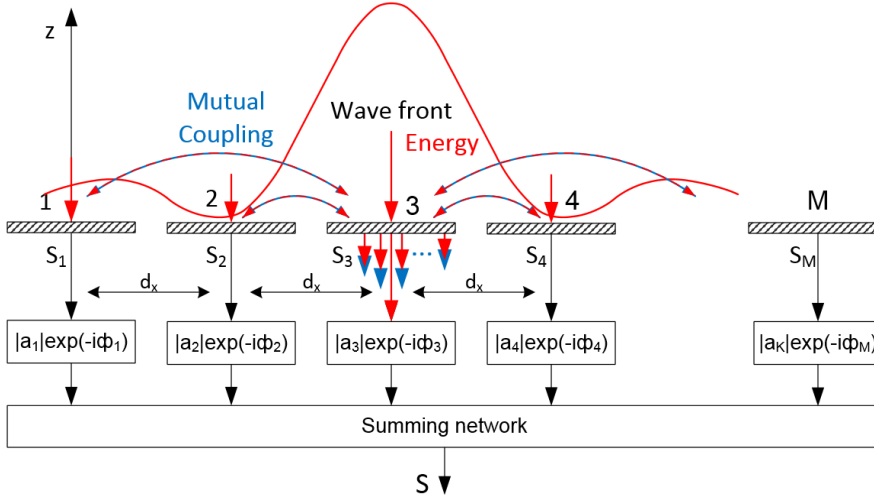


**Figure 5.5.** Excitation and mutual coupling mechanism in the case of an FPA.

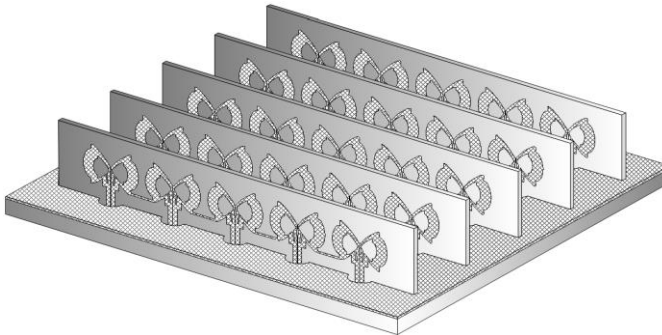


**Figure 5.6.** Cross section of the FPA consisting of five rows of connected arrays with five modified bow-tie antenna elements in a row.

### 5.1.3. 3D wideband focal plane connected-array concept

In order to improve the active wideband performance of the investigated FPA configuration, additional modifications of the array geometry should be done. Firstly, according to the paper [165], there is a direct relation between the antenna properties and its frequency band:

$$k = \frac{2\pi f_0}{c}; \quad Q \cong \frac{1}{B\eta}; \quad B = \frac{\Delta f}{f_0} \quad \Delta f(a) = \frac{1}{\eta c} \frac{8\pi^3 f_0^4 a^3}{c^2 + 4\pi^2 f_0^2 a^2} \quad (5.4)$$

where  $\eta$  represents the total antenna radiation efficiency,  $B$  is the relative bandwidth,  $c$  is the speed of light,  $f_0$  is the central frequency, and  $a$  the antenna size or boundary sphere surrounding the antenna as illustrated in Fig. 5.8 [165].

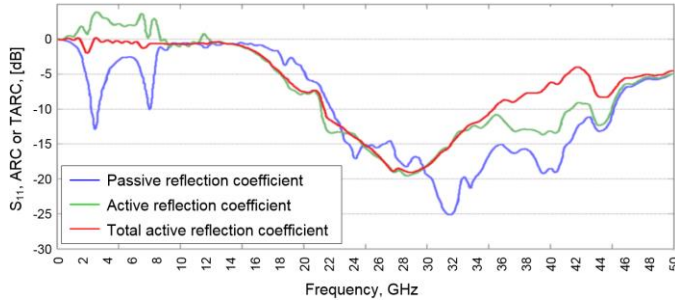


**Figure 5.7.** Passive reflection coefficient, the active reflection coefficient of the central FPA element, and the total active reflection coefficient of the complete FPA system.

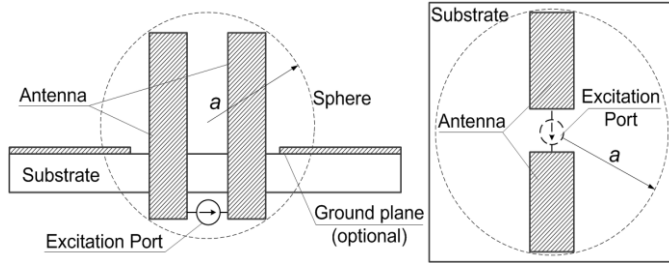


**Figure 5.8.** Illustration of boundary sphere which defines the minimum antenna size [165].

According to (5.4) it is possible to achieve the required frequency band only with antennas larger than a certain dimension or within a boundary sphere that is big enough. Since the boundary sphere surrounding the antenna three-dimensional object, it is logical to look at 3D antenna configurations as a promising design for the FPA application. These antennas will allow us to use the available space more efficiently. Moreover, for an array design, the 3D configuration will provide more flexibility for mutual coupling optimization since there are more degrees of freedom for the geometry construction. In addition, a 3D shape also provides more degrees of freedom in realizing a connected array configuration.

Secondly, the final optimization of the geometry of each array element should be done by considering the entire array configuration. According to the results of the active operation of an FPA (section 5.1.2, Fig. 5.7), it is clear that there is a significant difference between the passive and active performance. Therefore, we should optimize the geometry of the entire

array by optimizing the TARC in the case of an FPA antenna system.

The original bow-tie antenna shape has been modified to a 3D geometry by adding extra antenna elements orthogonal to the original one. Feeding is realized separately for the two orthogonal-polarization components. In this way, additional polarization control features can be implemented [169]. However, this is not part of this chapter. The configuration is presented in Fig. 5.9. Based on the comparison in [165] of connected and not-connected arrays, the single array elements of Fig. 5.9 have been combined in a 3D connected-array configuration, see Fig. 5.10. Compared to the previously presented array (section 5.1.2), there are a number of advantages like the possibility of additional polarization control features. Moreover, it has a twice as high density of array elements and, therefore, provides a higher EIRP level [15]. In addition, all gaps and line widths of the metal structures have been chosen in such a way that they are compatible with state-of-the-art PCB manufacturing design rules.

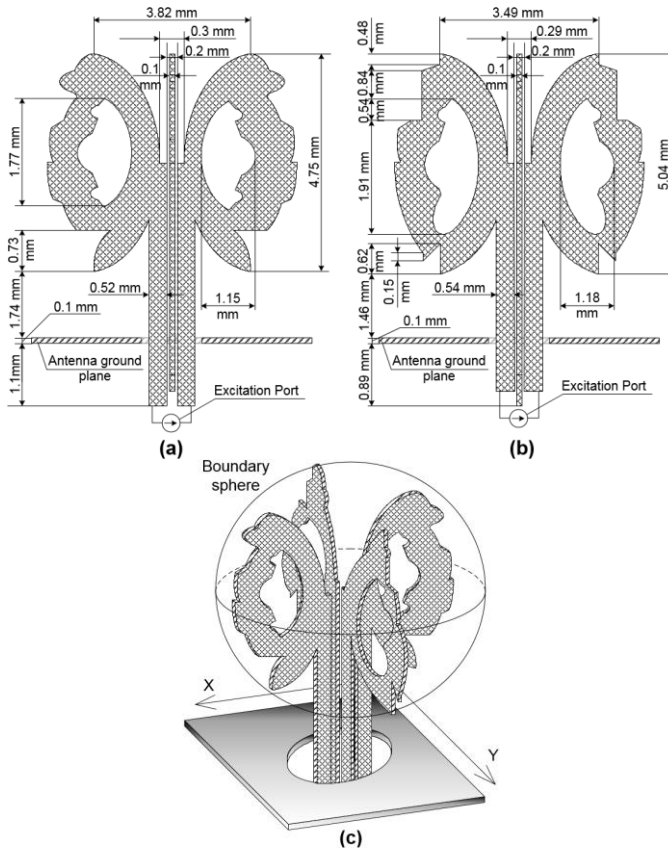


**Figure 5.9.** (a) x-axis element of the 3D Bow-Tie antenna (b) y-axis element of the 3D Bow-Tie antenna (c) Overall view of the antenna configuration in combination with the boundary sphere.

According to (5.1) and (5.3), the active performance depends not only on the passive reflection coefficients but also depends on the level of mutual coupling and the excitation vector. In the case of an FPA antenna system, the excitation vector depends on the reflector geometry and cannot be optimized within the context of the array design. Therefore, it is necessary to minimize the mutual coupling in order to improve ARC and TARC. As an

example, we have optimized the performance for the specific configuration as shown in Fig. 5.11. The FPA uses a 3x3 array, where each element is a double Bow-Tie antenna (Fig. 5.9c). In such a configuration, it is possible to simulate the mutual coupling between two central elements and the surrounding array components. This allows us to make a full analysis of the mutual coupling for the central elements. Therefore, we can optimize the central elements for minimal mutual coupling. As a result, it is possible to improve ARC for these elements. The relative positions of the array elements and the considered S-parameters for mutual coupling optimization are presented in Fig. 5.11.

From Fig. 5.11 it is clear that there is some symmetry in the array. Therefore, we only need to excite a few antenna elements during the optimization process in order to reduce the required simulation time. Four-port excitation is used during optimization (see Fig. 5.11). The main design goals are the optimization of the passive reflection coefficients of the central elements ( $S_{11}$  and  $S_{22}$ ) and the mutual coupling coefficients:  $S_{12}$ ,  $S_{13}$ ,  $S_{24}$ , and  $S_{34}$ . These mutual coupling S-parameters have been found to be most crucial for the calculation of the active reflection coefficient in the investigated frequency range. The passive reflection coefficients of the edge elements, like  $S_{33}$  and  $S_{44}$ , have been considered, however, they appear to have much less weight in the final optimization function. When larger arrays are considered, more elements need to be taken into account. However, this is beyond the scope of this article.

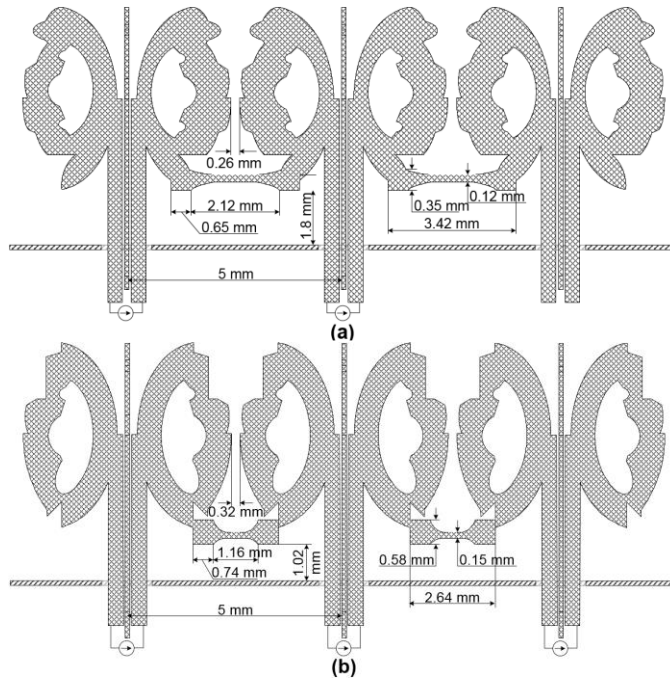


**Figure 5.10.** Cross section of the 3D wideband FPA concept: (a) x-axis elements of 3D connected array (b) y-axis elements of the 3D connected array.

The simulation results of the passive reflection coefficients are presented in Fig. 5.12. It is clear that the central array elements have a wide bandwidth of operation. For the x-axis element, the  $S_{11}$  is below -10 dB from 24 to 50 GHz, and for the y-axis element, the  $S_{22}$  is below -10 dB from 20 to 41 GHz. The performance of the edge elements ( $S_{33}$  and  $S_{44}$ ) is

significantly worse, as expected. This is due to the fact that edge elements have a different environment. Therefore, the geometry of the edge elements should ideally be different as compared to the optimized central elements. Nevertheless, the obtained passive bandwidth of the central elements is comparable with the array from section 5.1.2, despite the twice as high density of array elements. Note that in the case of a larger array size, more elements will behave like the center elements, reducing the effect of the edge elements.

The simulated mutual coupling S-parameters are presented in Fig. 5.13. It is visible that the level of mutual coupling is relatively low. The coupling between two orthogonal parts of the central element  $S_{12}$  is lower than -90 dB in all investigated frequency ranges. All other mutual coupling values,  $S_{13}$ ,  $S_{24}$ , and  $S_{34}$  are below -20 dB for almost all investigated frequencies. As a result, we have obtained a low level of mutual coupling which should provide us with a low ARC and TARC under active scan conditions.

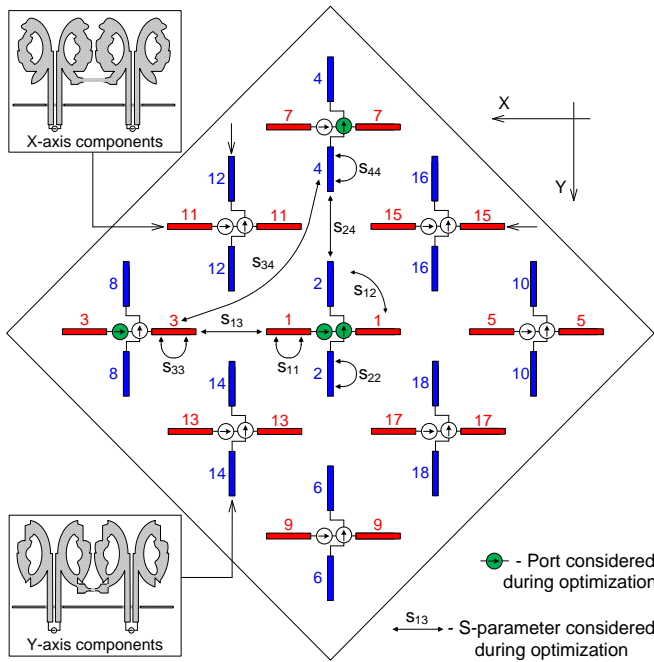


**Figure 5.11.** The relative positions of the array elements and considered S-parameters for mutual coupling optimization.

The simulated total radiation efficiency for the central elements of the investigated array is presented in Fig. 5.14. This figure also includes the predicted efficiency of the central element of the connected array of Fig. 5.6 (section 5.1.2). Compared to the efficiency of a single isolated antenna element, the efficiency deteriorated due to the mutual coupling. However, the total radiation efficiency is still higher than 60% within the required frequency band from 20 to 40 GHz for all array elements. In addition, at frequencies above 37 GHz, the 3D FPA concept shows better performance as compared to the array from section 5.1.2.

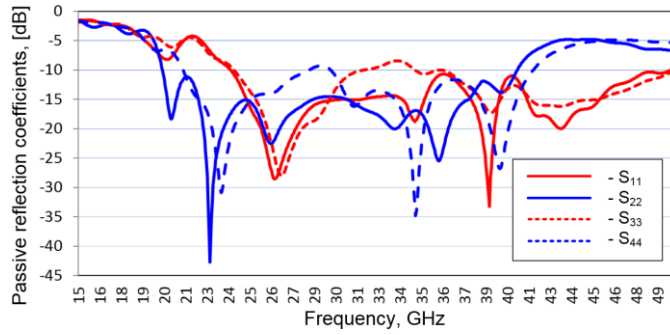


**Figure 5.12.** Simulated passive reflection coefficients.

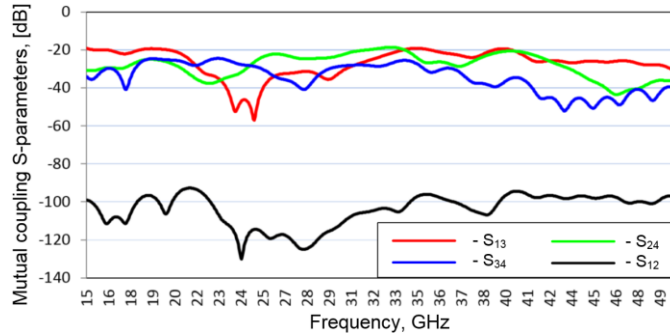


**Figure 5.13.** Simulated mutual coupling S-parameters.

Based on (5.1) and (5.2), the ARC and TARC have been calculated for our 3D FPA concept. The normal incidence of a plane wave to the reflector has been considered. The complex excitation vector of the array has been imported to MATLAB [167] from GRASP [39] for a 0.8 m symmetrical parabolic reflector with  $F/D = 0.6$ . Results are presented in Fig. 5.15. The ARC frequency band (ARC < -10 dB) for the x-axis element is from 25 to 36 GHz and for the y-axis element from 20 to 40 GHz. The TARC performance is worse as compared to the ARC, but still, a broadband performance is obtained. Further optimization is required to further improve the TARC.

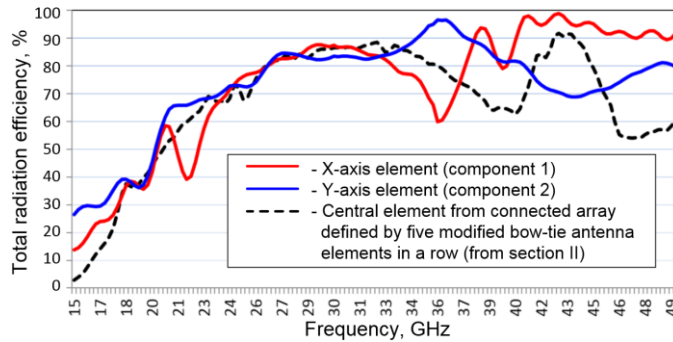


**Figure 5.14.** The simulated total radiation efficiency of the central elements in the 3D Bow-Tie antenna array in comparison with the total radiation efficiency of a connected array of Fig. 5.6.

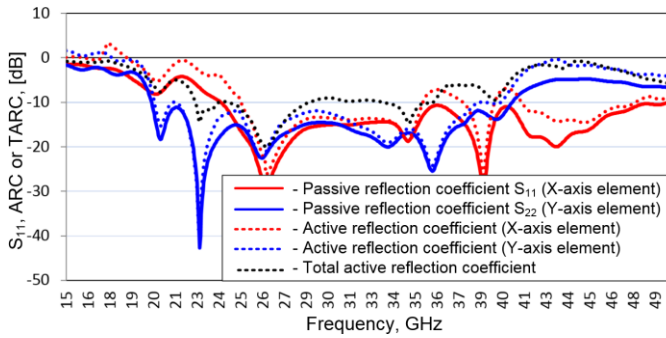


**Figure 5.15.** Passive reflection coefficient, the active reflection coefficient of the central FPA elements, and the total active reflection coefficient of the whole 3D wideband FPA concept.

#### 5.1.4. Conclusions

We have shown that wideband arrays can have issues in operation when they are used as a phased-array feed in an FPA antenna system with beam scanning. Therefore, it is necessary to investigate methods to improve both the ARC and TARC in order to obtain a wideband performance. In addition, strong mutual coupling, specifically for dense arrays, is an important challenge for a wideband FPA design.

Two versions of FPAs have been presented. Both of them have a wide passive frequency bandwidth. The first configuration is a 5x5 array providing an ARC bandwidth of almost 20 GHz for the central element and about 10 GHz TARC bandwidth of the whole array. For the second design, a dense 3x3 configuration with dual-polarized elements is used. The achieved frequency bandwidth is comparable with the first version. However, a twice as high element density is realized, providing a higher EIRP of the overall FPA system. In addition, the complex orthogonal antenna structure provides a lot of options for further improvement and realization of additional array features like polarization control. Moreover, further optimization should be done to further improve the TARC performance. This is a suggestion for future work.

## 5.2. Wideband Phased-Array Feeds for Focal Plane Arrays: Design and Implementation<sup>1</sup>

This chapter is focused on the design challenges of wideband antenna elements which can be used in phased-array feeds (PAF) for focal-plane arrays (FPAs). The PAF should support various FPA concepts and cover a wide scan range over a broad frequency range. The proposed array elements are based on a modified version of the well-known bow-tie antenna. A system-level analysis was performed for both the classical prime-focus reflector and a novel double-reflector configuration that provides a wide-scan range. We have investigated the optimal element spacing for various scan ranges. The proposed optimized array shows excellent active matching properties over a frequency band of more than one octave within a  $\pm 20^\circ$  azimuth scan range, realized with a double-reflector FPA system. A prototype FPA was realized to experimentally validate the performance of our concept.

### 5.2.1. Introduction

Electronic beam steering with phased-array antennas is a well-known concept, which is used in many applications ranging from millimeter-wave base stations for wireless communications to multi-function radars. However, there are bandwidth-limitation challenges for using this technology at higher frequencies [130]. At the same time, the requirements for wideband arrays in focal-plane arrays (FPA) are even more challenging as compared to traditional phased-array antennas. Especially Ku- and Ka-band applications are really demanding, where FPAs could be an attractive alternative to phased-array technology.

FPAs combine the benefits of phased-arrays and traditional reflector-based solutions by offering a high antenna gain, relatively low costs, and electronic beam steering over a limited field-of-view (FoV). FPAs are already widespread in the fields of radio astronomy [8], [164], and in satellite communications [9]. Moreover, emerging applications such as 5G-NR/6G, point-to-point wireless communications, and low-cost Ka-band (30-40 GHz) multi-function radar could be areas with rich possibilities for FPA implementations.

Nevertheless, there are a number of fundamental limits related to FPAs that need to be solved before this technology could become a widely accepted option to replace phased arrays. The small number of simultaneously active array elements limits the number of multiple beams or scan range [25] and achievable effective isotropic radiated power (EIRP) [26], [28], [170]. Recently, we have presented new FPA concepts that provide a high EIRP covering a wide scan and frequency range with improved realized FPA exposure [18], [21], [23], [171]. In this chapter, we will extend that work to investigate optimized phased-array feeds (PAFs) for such FPA concepts.

This chapter includes the following new scientific contributions:

- a wideband connected array concept for use in a wideband, wide-scan FPA system, operating in the frequency band from 20-40 GHz over a scan range of  $\pm 20^\circ$  in azimuth,
- exploration of the optimal element spacing for wideband PAFs based on the reflector aperture efficiency and the total radiation efficiency of the PAF,

<sup>1</sup>Current paragraph 5.2 is submitted to the IEEE Transactions on Antennas and Propagation as a journal paper: Dubok, A.; Smolders, A.B., " Wideband Phased-Array Feeds for Focal Plane Arrays: Design and Implementation," and included here in its entirety without any changes.

- experimental verification of the proposed PAF concept in combination with a novel double-reflector FPA system that provides a wide scan range.

The structure of the chapter is as follows. Section 5.2.2. describes the theoretical design challenges of active wideband antenna arrays. Section 5.2.3. compares the wideband performance and radiation efficiency of traditional bow-tie antenna arrays with arrays using our modified bow-tie antennas, and its use in combination with reflectors. Within subparagraph 5.2.3.1. the total radiation efficiency and active wideband performance with classical prime-focus reflectors are presented. Subparagraph 5.2.3.2. focuses on the aperture efficiency for such reflectors. Section 5.2.4. discusses the complete FPA system and corresponding experimental validation. The first subparagraph 5.2.4.1. presents the performance of passive arrays obtained with probe measurements. Subparagraph 5.2.4.2. discusses the measured embedded element patterns obtained for several PAF prototypes with mini SMP connectors. Subparagraph 5.2.4.3. analyses the active PAF performance with a classical prime-focus reflector and with a wide-scan complex offset double-reflector system. In subparagraph 5.2.4.4. the measured far-field patterns of a wide-scan complex offset double-reflector fed by an array of modified bow-tie antennas are presented. The last section 5.2.5. provides a system-level comparison of the proposed FPA system (subparagraph 5.2.5.1.) and compares it to equivalent phased-array configurations (subparagraph 5.2.5.2.).

### 5.2.2. Design Challenges of wideband antenna elements for PAFs

The wideband performance of PAFs is defined by a number of factors, including intrinsic frequency properties of an isolated element and mutual coupling [166]. The effect of mutual coupling in PAFs is different from traditional phased arrays since the amplitude and phase distribution in an FPA system are completely different. The impact of mutual coupling is determined by the level of the coupling itself and the applied excitation coefficients of the array elements [166]. Those coefficients are defined by the desired array far-field pattern. Consequently, the active wideband performance of an FPA is defined by the array design and by the used reflector system.

The maximum achievable bandwidth of a single isolated array element is strongly related to its dimensions. For electrically small antennas the ratio between the maximum achievable frequency bandwidth and the antenna dimension is defined by the well-known Chu-Harrington limit [132], [133], [134]. Thus, it is possible to estimate the minimum antenna size which could provide a certain frequency bandwidth around the central frequency of operation, 30 GHz in our case. As has been demonstrated in the paper [165], to cover the 20 GHz to 40 GHz band the minimum antenna size (which theoretically could provide the required frequency bandwidth) is equal to the boundary sphere with a diameter of 3.6 mm corresponding to about 72% of the free-space wavelength ( $\lambda_0$ ) divided by 2 (standard elements spacing  $\lambda_0/2$ ), where  $\lambda_0$  is the free-space wavelength at the center frequency 30 GHz.

Paper [165] presents the modified bow-tie antenna, which very efficiently uses the available space and meets the wideband performance close to the theoretical limit. It has been obtained based on the optimization of the antenna geometry based on a genetic algorithm, similar to the procedure described in [138]. At the same time, it has a fairly omnidirectional far-field pattern which could provide a nice uniform reflector illumination for an FPA application. Moreover, the total radiation efficiency of this antenna is relatively high (exceeds 90%), and the phase center position also remains constant within the investigated frequency

band, which is important when used in PAFs. The connected-array concept [141] has been used to improve the matching performance. The overall size of the proposed modified bow-tie antenna is 4.42 mm in diameter [165]. When using such an element in a PAF, the element distance is only 5 mm when a half-wavelength spacing is used at the central frequency of 30 GHz. Consequently, the neighboring array elements are going to be in close proximity to each other. This will create significant mutual coupling, and, as a result, limits the active wideband performance (Fig. 5.16) [65].

Paper [172] investigates the active performance of the array configuration of paper [165]. The active reflection coefficient (ARC) and total active reflection coefficient (TARC) [166] were analyzed. The ARC of array element  $m$  can be determined by:

$$R_m(\theta_0, \varphi_0) = \sum_{n=1}^N S_{mn} a_n \quad (5.5)$$

where  $S_{mn}$  is the scattering coefficient between element  $m$  and  $n$ ,  $a_n$  is the complex excitation coefficient,  $\theta_0$  and  $\varphi_0$  the scan angles relative to the normal of the surface of the array, and  $N$  is the number of array elements (Fig. 5.16). The TARC parameter which describes the wideband properties of the whole array can be written as:

$$\text{TARC} = \frac{\sqrt{\sum_{m=1}^N |R_m(\theta_0, \varphi_0)|^2}}{\sqrt{\sum_{m=1}^N |a_m|^2}} \quad (5.6)$$

[172] demonstrates that even for the phased array use case, where the only difference in the excitation coefficients is the phase differences between the array elements, mutual coupling significantly limits the impedance-matching bandwidth as compared to the isolated-element performance. In an FPA application, there are not only phase differences between array elements, but there is a strongly varying amplitude distribution which could lead to a further decrease in bandwidth (Fig. 5.16). This was demonstrated in [172], where a co-simulation of GRASP [39] with CST [139] and MATLAB [167] was used to demonstrate the major bandwidth reduction by a factor of two. In this case, a classical prime-focus reflector with 0.8 m diameter and  $F/D = 0.6$  was used.

In an FPA antenna system, the excitation coefficients of the PAF elements strongly depend on the reflector geometry. In the frame of this chapter, the proposed antenna geometry of [165] and [172] is investigated and further improved to provide a wideband performance when used in an FPA system. In addition, the reflector configuration of paper [23], the complex offset double-reflector that provides a wide scan range and optimized array excitation properties, is combined with the proposed array to realize a wideband performance.

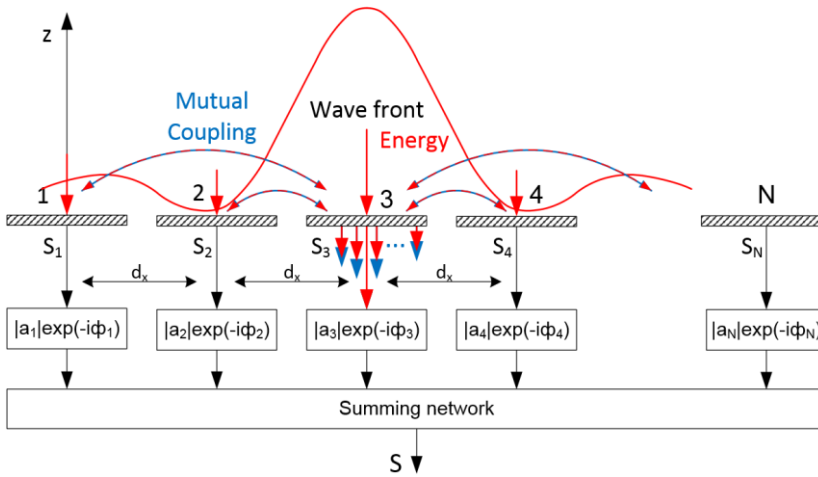


**Figure 5.16.** Excitation and mutual coupling mechanism of a PAF [172].

### 5.2.3. Integration of wideband PAFs and reflectors

As a baseline within this paragraph, the classical prime-focus reflector is used. Further in the text (section 5.2.4.3.), the complex offset double-reflector will be proposed in order to optimize the array illumination [23].

The main factors characterizing the PAF performance, presented in the first subparagraph 5.2.3.1., are the total radiation efficiency and active wideband performance. The second subparagraph 5.2.3.2. presents how the efficiency of the reflector illumination at the broadside is depending on the array type and element spacing. Further in the text (section 5.2.4.3.), we will also analyze the case of pre-defined scan ranges.

#### 5.2.3.1. PAFs total radiation efficiency and active wideband performance using a classical prime-focus reflector

Four different array configurations have been investigated in terms of the dependence of the bandwidth and total radiation efficiency on the applied element spacing. As a basic array element two different designs are used: the classical bow-tie antenna (Fig. 5.17 and Fig. 5.20), which is often used in wideband array applications [173], and the modified bow-tie antenna (Fig. 5.23 and Fig. 5.26) investigated in [165] and [172]. Both types of elements are combined into a linear array of five elements and presented in two options “not connected” (Fig. 5.17 and Fig. 5.23) and “connected” (Fig. 5.20 and Fig. 5.26) arrays. The considered elements should potentially be able to provide a high total radiation efficiency and suitable far-field patterns for the reflector illumination. As has been demonstrated in [172], connected arrays could be used to provide wideband impedance matching properties. In addition, both antenna concepts have a limited height with respect to the normal of the array face, resulting in a more stable feed phase center [135]. The latter is important in order to avoid major de-focusing of the secondary radiation pattern [136].

To estimate the active bandwidth properties of the array, it has been combined with the classical prime-focus reflector to form an FPA configuration. A model was developed in MATLAB [167], where the excitation vectors obtained with a reflector model implemented

in GRASP [39] are combined with array simulations in CST to determine the array performance (ARC and TARC) within an FPA concept for various element spacings. A classical prime-focus reflector with a 0.8 m diameter and  $F/D = 0.6$  has been used. As a first step, the broadside mode of operation has been investigated.

Simulation results of the achieved bandwidth versus element spacing using the ARC or TARC of the not-connected linear array of five bow-tie antenna elements (Fig. 5.17) are presented in Fig. 5.18. The corresponding total radiation efficiency of the stand-alone arrays is provided in Fig. 5.19 [172]. The total radiation efficiency includes the radiation efficiency and mismatch efficiency. The radiation efficiency is the ratio of the power radiated by the antenna and the power that gets into the antenna. The power not radiated is dissipated in conductors and dielectrics. The mismatch efficiency is the ratio of the incident power from the network that gets into the antenna and is not reflected or transmitted out of other ports of the array. The average efficiency of the central element is defined when one element is excited and the other elements terminated, and also could be called embedded element radiation efficiency (EERE). While the average efficiency of the whole array is defined when all elements are excited. The EERE is a product of two sub-efficiencies, namely the reflection efficiency which accounts for only the power reflected back into a certain port as a fraction of the power injected into it, whilst the other powers coupled into the surrounding passive elements are characterized by a separate sub efficiency called the decoupling efficiency, making up the other sub efficiency.

The ARC/TARC bandwidth was determined using a -10 dB limit for the reflection coefficient, based on a 50 Ohm input matching. The performance of the connected array of bow-tie antennas (Fig. 5.20) is presented in Fig. 5.21 and Fig. 5.22. The simulated performance versus element spacing for the modified bow-tie antenna is provided in Figs. 5.24-5.35 for the not-connected array and in Figs. 5.27-5.28 for the connected array.

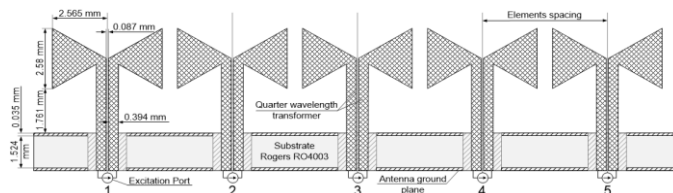


**Figure 5.17.** Cross section of an array of five bow-tie antenna elements in a row.

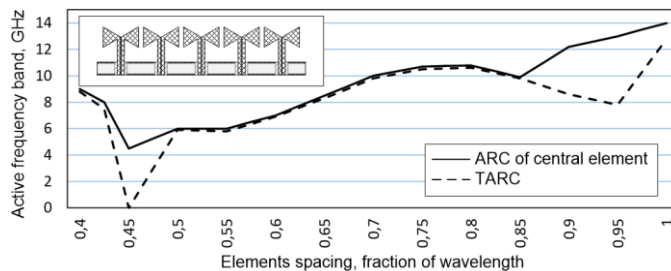


**Figure 5.18.** Impedance matching bandwidth based on the ARC of the central array element and the TARC of five bow-tie antenna elements in a row.

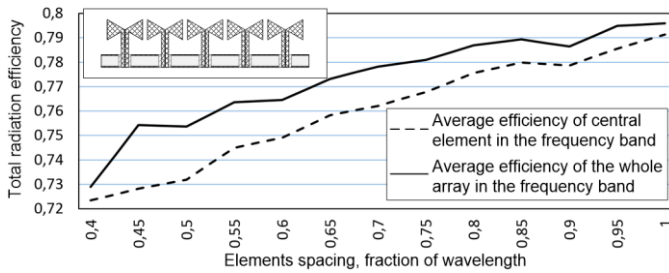


**Figure 5.19.** The simulated total radiation efficiency of the central array element and the whole array is defined by five bow-tie antenna elements in a row.

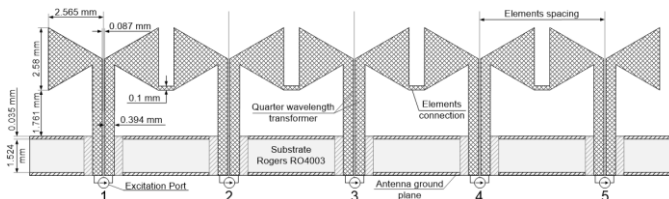


**Figure 5.20.** Cross section of a connected array of five bow-tie antenna elements in a row.

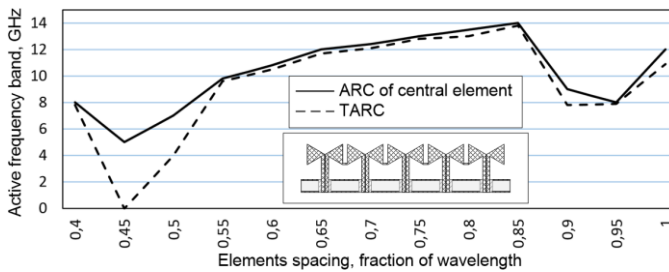


**Figure 5.21.** Impedance matching bandwidth based on the ARC of the central array element and the TARC of five connected bow-tie antenna elements in a row.

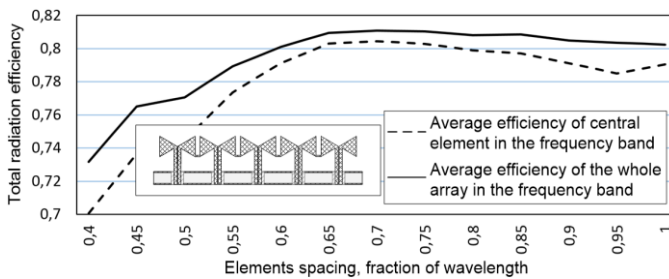


**Figure 5.22.** The simulated total radiation efficiency of the central array element and the whole array is defined by five connected bow-tie antenna elements in a row.

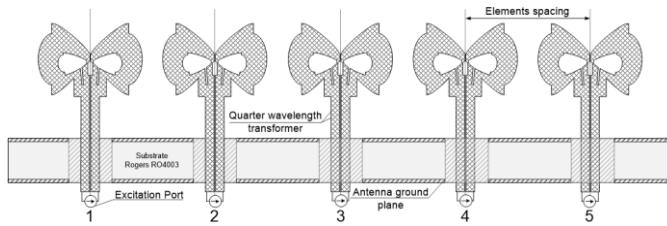


**Figure 5.23.** Cross section of an array of five modified bow-tie antenna elements in a row.

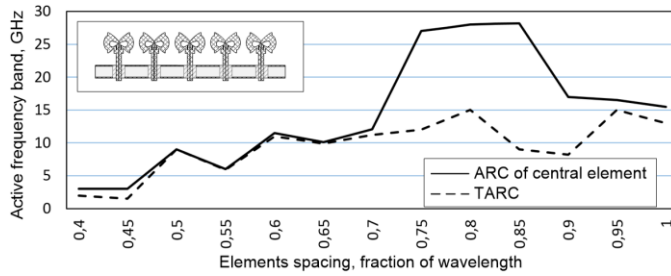


**Figure 5.24.** Impedance matching bandwidth based on the ARC of the central array element and the TARC of five modified bow-tie antenna elements in a row.

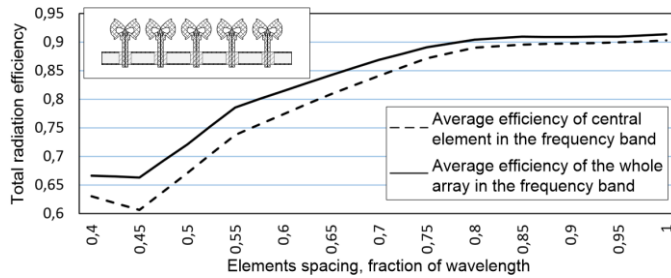


**Figure 5.25.** The simulated total radiation efficiency of the central array element and the whole array is defined by five modified bow-tie antenna elements in a row.

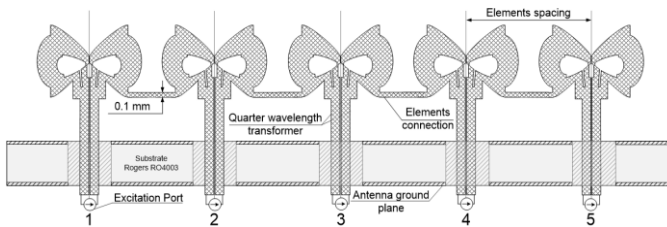


**Figure 5.26.** Cross section of a connected array of five modified bow-tie antenna elements in a row.

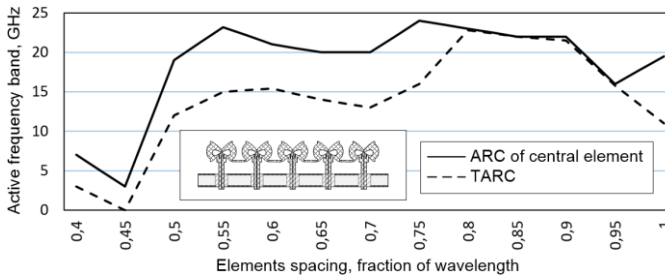


**Figure 5.27.** Impedance matching bandwidth based on the ARC of the central array element and the TARC of five connected modified bow-tie antenna elements in a row.

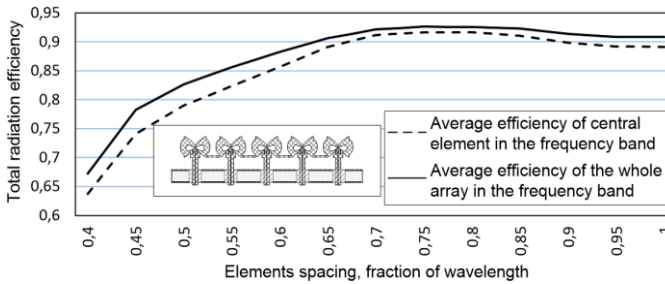


**Figure 5.28.** The simulated total radiation efficiency of the central array element and the whole array is defined by five connected modified bow-tie antenna elements in a row.

The ARCs of the not-connected (Fig. 5.18) and connected (Fig. 5.21) arrays show that the maximum bandwidth is around 14 GHz for an element spacing around  $\lambda_0$  for the not-connected array and  $0.8\lambda_0$  for the connected one. The TARC of those configurations has similar behavior and achieved bandwidth value. The ARC and TARC of the modified bow-tie antenna are significantly improved compared to the standard design. For the not-connected array (Fig. 5.24) it is possible to achieve an ARC bandwidth of more than 20 GHz using an element spacing in the range between  $0.75\lambda_0 - 0.85\lambda_0$ . However, a TARC bandwidth of 20 GHz is still not reachable. For the connected array (Fig. 5.27) an ARC bandwidth of more than 20 GHz is observed for element spacings in the range between  $0.5\lambda_0 - 0.9\lambda_0$ . While the TARC also provides a 20 GHz wideband for spacings in the range of  $0.8\lambda_0 - 0.9\lambda_0$ .

As we can see from Figs. 5.19, 5.22, 5.25, and 5.28 the total radiation efficiency shows a strong dependence on the used element spacing. For all investigated configurations the efficiency is increasing with larger element spacing until it reaches a kind of saturation. The total radiation efficiency of bow-tie arrays achieves a maximum of around 81 % (Fig. 5.19 and Fig. 5.22), while the modified bow-tie arrays reach around 93 % (Fig. 5.25 and Fig. 5.28).

### 5.2.3.2. The reflector aperture efficiency in the case of a classical prime-focus reflector

Based on the simulation results of the investigated arrays for different element spacings it is possible to conclude that wider element spacings improve the array efficiency and overall active wideband performance. However, when using such an array to feed a reflector, we need to realize a high aperture efficiency, which will put limitations on the array spacing. Therefore, it is necessary to investigate the effect of the applied element spacing on the

reflector aperture efficiency of FPAs. The aperture efficiency also defined as amplitude taper efficiency times phase efficiency is a measure of how uniform the E-field is across the antenna's aperture. In general, an antenna will have the maximum gain if the E-field is uniform in amplitude and phase across the aperture. However, the aperture fields will tend to diminish away from the main axis of the reflector, which leads to a lower gain, and this loss is captured within this parameter.

In this section, we will do this for the classical prime-focus reflector which is fed by a five-element linear array, as shown in Fig. 5.29. The far-field patterns of the individual array elements have been exported from CST [139]. The amplitude and phase of the individual elements have been adjusted by conjugate field matching according to the field distribution in the array plane for the receive case [23]. The radiated power by the feed array is normalized to  $4\pi$  Watt in order to directly determine the reflector directivity in GRASP [39]. The used classical prime-focus reflector has a diameter of 0.8 m which is equivalent to a 48 dBi directivity in the case of a 100% aperture efficiency. When the directivity is obtained using GRASP, it is possible to determine the reflector aperture efficiency with the investigated arrays of section 5.2.3.1. The efficiency is frequency dependent and thus determined for maximum, minimum, and central frequencies within the band of interest. Fig. 5.30 presents the efficiency of the reflector which is illuminated by the four types of arrays at 20 GHz, Fig. 5.31 – at 30 GHz, and Fig. 5.32 – at 40 GHz.

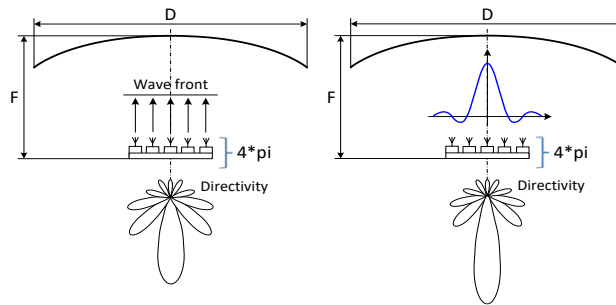


**Figure 5.29.** Directivity estimation by GRASP model with feed power normalization.

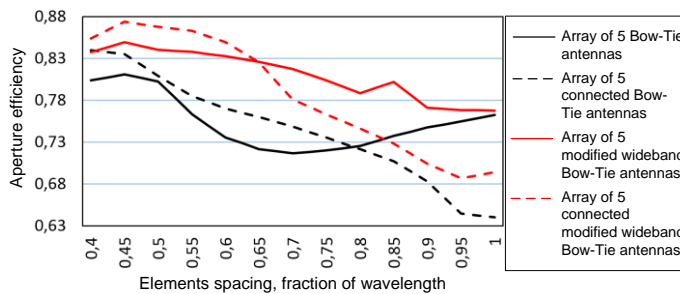


**Figure 5.30.** Aperture efficiency of the reflector illuminated by the four types of arrays,  $f = 20$  GHz.

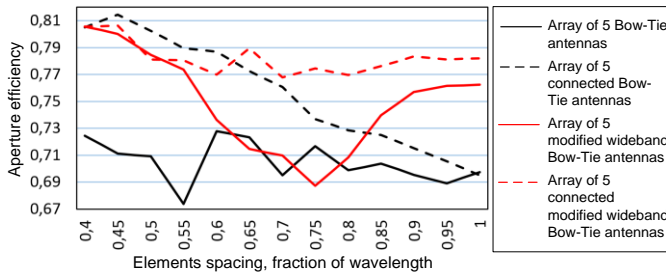


**Figure 5.31.** Aperture efficiency of the reflector illuminated by the four types of arrays,  $f = 30$  GHz.

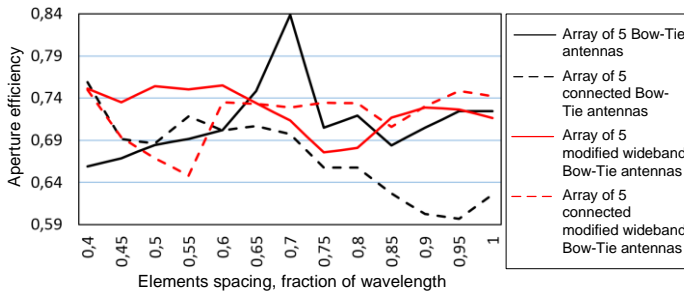


**Figure 5.32.** Aperture efficiency of the reflector illuminated by the four types of arrays,  $f = 40$  GHz.

According to Fig. 5.30 – Fig. 5.32 the reflector aperture efficiency generally decreases with increasing element spacing for 20 GHz and 30 GHz. At 40 GHz, the efficiency only weakly depends on the element spacing due to the overall lower quality of the far-field pattern of the investigated arrays. This issue will be investigated later in the chapter (see section 5.2.4.). At 20 GHz (Fig. 5.30) the efficiency is higher for the modified bow-tie antenna for all tested elements' spacings, where for spacings up to  $0.65\lambda_0$  the connected array provides the highest aperture efficiency. At 30 GHz both bow-tie and modified bow-tie antennas are performing better in the case of the connected array option, wherein the modified bow-tie array also provides high illumination efficiencies for wider element spacings beyond  $0.85\lambda_0$ . At 40 GHz, in most of the cases, the connected array of modified bow-tie antennas provides the best results.

The results of the connected array of modified bow-tie antennas with the classical prime-focus reflector are summarized in Table 5.1 for several element spacings. The justification factors are the total radiation efficiency of the central element the array, the ARC and TARC bandwidths, and the reflector aperture efficiency.

According to Table 5.1, there is a significant difference in FPA performance. Nevertheless, we can observe that only the array with a  $0.8\lambda_0$  element spacing satisfies the impedance-matching bandwidth requirement. The associated TARC bandwidth is 22.5 GHz and this is more than the required 20 GHz. Meanwhile, the array with a traditional  $0.5\lambda_0$  element spacing only provides a bandwidth of 12 GHz. In addition, the average efficiency of the whole array within the frequency band is more than 10 % higher for  $0.8\lambda_0$  than for the  $0.5\lambda_0$  case. The obvious drawback of the  $0.8\lambda_0$  configuration is the decrease in the reflector aperture efficiency. The most significant reduction is observed at 20 GHz and it is about 12 % less as

compared to the  $0.5\lambda_0$  reference case. Nevertheless, at 30 GHz the drop is only 1.1 % and for 40 GHz it is even better and provides an additional efficiency of 7.4 %. To conclude, there is some deterioration of the reflector illumination quality, but it is only significant at low-band frequencies, while at most of the frequency band, the situation is similar to the  $0.5\lambda_0$  case.

**Table 5.1** Justification of the array element spacing choice for the connected array of five modified bow-tie antenna elements based on simulation results.

Element spacing	$0.5\lambda_0$	$0.6\lambda_0$	$0.7\lambda_0$	$0.8\lambda_0$
The average efficiency of the central element in the frequency band	79 %	86 %	91 %	<b>92 %</b>
The average efficiency of the whole array in the frequency band	82.5 %	88.5 %	92.5 %	<b>93 %</b>
ARC bandwidth (central element)	18.5 GHz	21 GHz	20 GHz	<b>22.7 GHz</b>
TARC bandwidth	12 GHz	15.5 GHz	13.5 GHz	<b>22.5 GHz</b>
Aperture efficiency at 20 GHz	87 %	85 %	78.5 %	<b>75 %</b>
Aperture efficiency at 30 GHz	78 %	77.2 %	76.7 %	<b>76.9 %</b>
Aperture efficiency at 40 GHz	66 %	73.5 %	72.9 %	<b>73.4 %</b>

Based on the results of Table 5.1 the linear array with five modified bow-tie antenna elements with  $0.8\lambda_0$  element spacing is the optimal configuration when combined with the classical prime-focus reflector. Nevertheless, only broadside operation has been considered up to now. Our goal is to find an FPA concept that provides a 20 GHz bandwidth for a scan range of  $\pm 20^\circ$  in azimuth [34]. Operation over a wide scan range creates extra challenges for the impedance matching bandwidth and aperture efficiency. Thus, to satisfy those conditions the proposed array design has been further improved. In addition, the reflector has been optimized to provide a wide scan range and an optimal combination with an array feed, as presented in [23]. Details of the FPA prototyping and measurements are presented in the next section.

#### 5.2.4. FPA prototyping and measurements

Based on the results of the previous paragraph three different element spacings have been chosen for the various array configurations. The chosen designs for prototyping have a  $0.6\lambda_0$ ,  $0.7\lambda_0$ , and  $0.8\lambda_0$  element spacing. In addition, the modified bow-tie antenna introduced in [33] has been further optimized to accommodate the experiments and for manufacturability, e.g. to avoid very small dimensions.

For the classical prime-focus reflector with  $F/D = 0.6$ , the angle of the array opening towards the reflector appears to be  $\pm 40^\circ$ . Thus, the array elements have been preliminary optimized to provide the least distorted far-field pattern within the  $\pm 40^\circ$  range both in the azimuth and elevation planes. In contrast with well-known Vivaldi antennas, the overall height of the modified bow-tie antenna has been limited to ensure feed phase-center stability [135].

Similar to [33], additional design improvements have been achieved by introducing antenna slots to redistribute the currents on the antenna surface and the layered capacitor defined by the microstrip pad on the backside of the antenna. The required capacitance, dimensions, and position of the microstrip pads were optimized by means of simulation in CST [139]. The final optimization has been done for the array use-case to optimize the element performance within the array including the effect of mutual coupling. The resulting geometry of the modified bow-tie antenna element with adjusted dimensions is given in Fig. 5.33. A photo is presented in Fig. 5.34.

In order to finally verify that the use of connected arrays improves the wideband performance of FPAs, two array versions of the proposed antenna designs have been created. Fig. 5.35 presents the not-connected array of five modified bow-tie antenna elements with adjusted dimensions for manufacturing. Fig. 5.36 shows the connected array version. Each array has been created with three variations of the element spacing ( $0.6\lambda_0$ ,  $0.7\lambda_0$ , and  $0.8\lambda_0$ ).

The central gap between the differential feeding lines of the modified bow-tie antenna has been increased to  $75\text{ }\mu\text{m}$  (see Fig. 5.33). This adjustment has been realized to implement probe-based measurements. Measurement results of the (passive) input reflection coefficients using a probe are provided in subparagraph 5.2.4.1. Another series of prototypes have been realized that includes mini SMP connectors. These prototypes can be used to measure the embedded element patterns. Related results are presented in subparagraph 5.2.4.2. Subparagraph 5.2.4.3. presents the evaluation of the PAFs active scan performance. Those results have been obtained through the measurement of the complete scattering matrix. The resulting performance in combination with the classical prime-focus reflector and with the complex offset double-reflector system [23] is discussed in subparagraph 5.2.4.4.

#### **5.2.4.1. Array prototypes for probe measurements of the (passive) input reflection coefficients**

The probe measurements allow to measure the input reflection coefficients ( $S_{ii}$ ) with high accuracy using a standard probe calibration kit. For those experiments, the tested element has been attached to the probe, while the other array elements have been terminated by 50 Ohm SMD resistors. At least five copies of each array type have been manufactured. All prototypes have been measured using a Keysight Vector Network Analyzer [174]. Presented results have been deduced as the arithmetic means of all measurements to improve the reliability of the measured data. Fig. 5.37 shows a photo of all prototypes used for the probe measurements. The measurement setup is shown in more detail in Fig. 5.38. A photo of the probe-based array measurements is presented in Fig. 5.39.

The measured and simulated input reflection of a single modified bow-tie antenna element is shown in Fig. 5.40. The measurement was repeated for all available prototypes and the results were combined to provide an average measurement curve. Overall, there is a very good agreement between the model and the measured data. The realized “passive” bandwidth (with  $S_{11} < -10\text{ dB}$ ) is about 20 GHz.

The measured and simulated  $S_{ii}$  parameters of the not-connected array of five modified bow-tie antennas are presented in Fig. 5.41 for an element spacing of  $0.6\lambda_0$ , in Fig. 5.42 for an element spacing of  $0.7\lambda_0$  and in Fig. 5.43 for an element spacing of  $0.8\lambda_0$ . Due to symmetry, only the  $S_{11}$ ,  $S_{22}$ , and  $S_{33}$  curves are presented, where  $S_{33}$  corresponds to the center array element. As we could see from Figs. 5.41-5.43 there is a good agreement between simulation

and measurement. The overall bandwidth is more limited as compared to the single element case. Nevertheless, the best performance is achieved for a  $0.8\lambda_0$  element spacing. For a  $0.6\lambda_0$  and  $0.7\lambda_0$  spacing, the level of matching around 24 GHz is not sufficient.

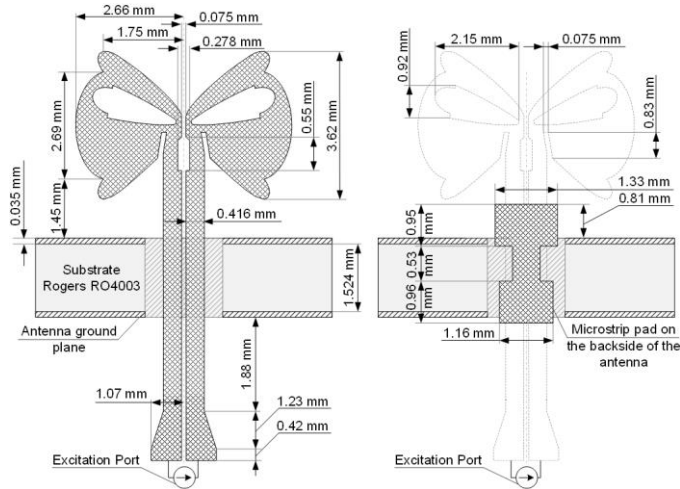


**Figure 5.33.** Single modified bow-tie antenna element with adjusted dimensions optimized for manufacturing.



**Figure 5.34.** Photo and relative size of the single modified bow-tie antenna element.

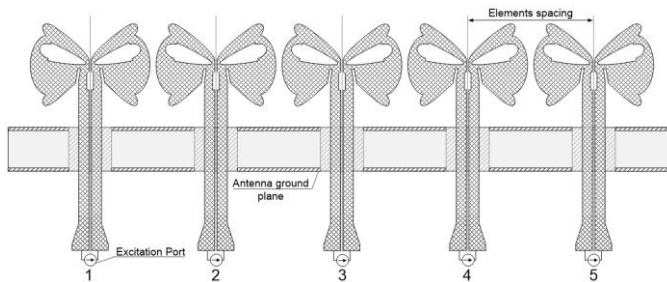


**Figure 5.35.** The not-connected array of five modified bow-tie antenna elements with adjusted dimensions for manufacturing.

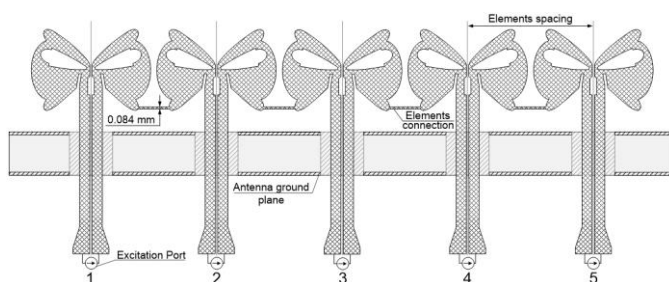


**Figure 5.36.** The connected array of five modified bow-tie antenna elements with adjusted dimensions optimized for manufacturing.

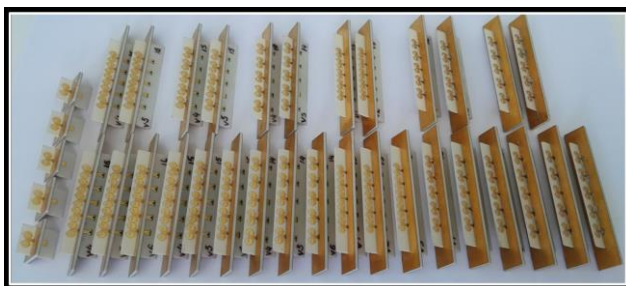


**Figure 5.37.** Photo of the prototypes for probe measurements.

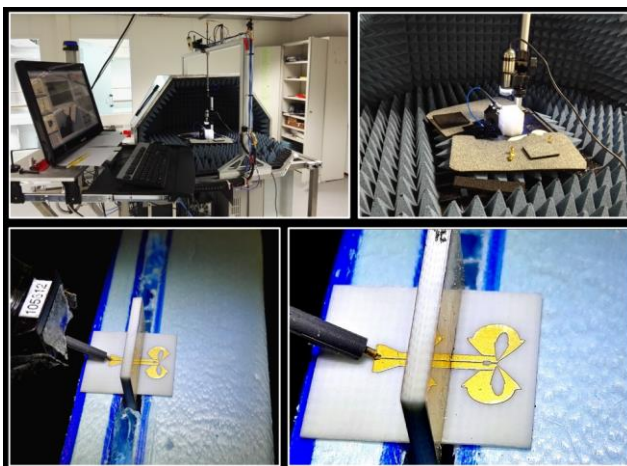


**Figure 5.38.** Probe measurements of a single modified bow-tie antenna element.

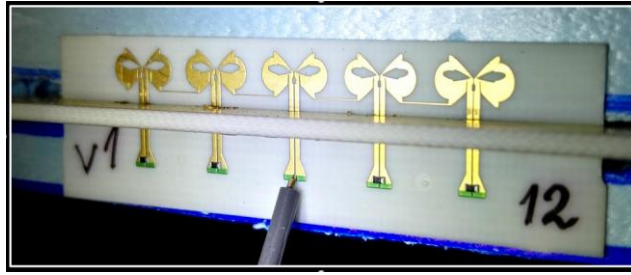


**Figure 5.39.** Probe measurements of the center element of the 5-element linear array. All other elements are terminated by 50 Ohm SMD resistors.

The measured  $S_{ii}$  of the connected array of five modified bow-tie antenna elements is shown in Fig. 5.44 for an element spacing of  $0.6\lambda_0$ , in Fig. 5.45 for an element spacing of  $0.7\lambda_0$  and in Fig. 5.46 for an element spacing of  $0.8\lambda_0$ . The overall results are significantly improved and even exceed the single element case. This can be explained by the fact that optimization has been performed for optimal operation within an array configuration. The array with a  $0.6\lambda_0$  element spacing still does not achieve a 20 GHz frequency band. However, for  $0.7\lambda_0$  and  $0.8\lambda_0$  spacing, the required bandwidth is fully reached.

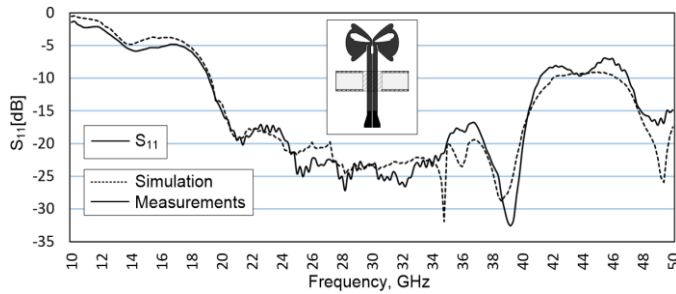


**Figure 5.40.** Measured and simulated  $S_{11}$  of a single modified bow-tie antenna element.

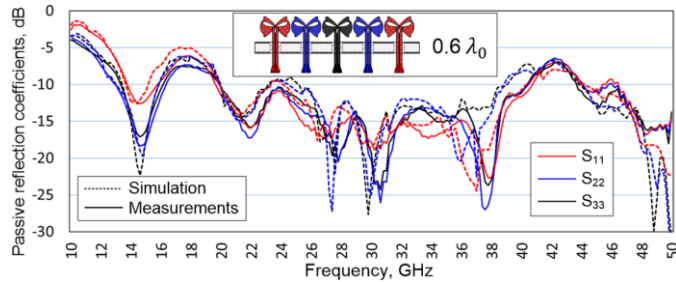


**Figure 5.41.** Measured and simulated  $S_{11}$ ,  $S_{22}$ ,  $S_{33}$ , of a not-connected array of five modified bow-tie antenna elements with element spacing  $0.6\lambda_0$ .

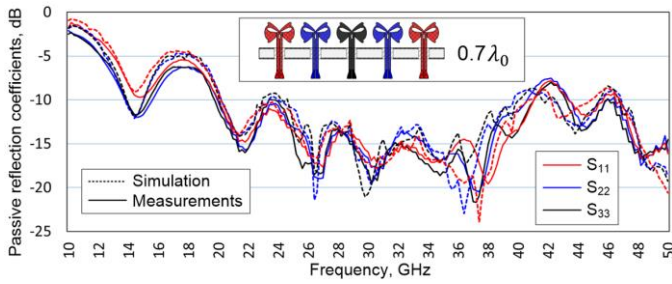


**Figure 5.42.** Measured and simulated  $S_{11}$ ,  $S_{22}$ ,  $S_{33}$ , of a not-connected array of five modified bow-tie antenna elements with element spacing  $0.7\lambda_0$ .

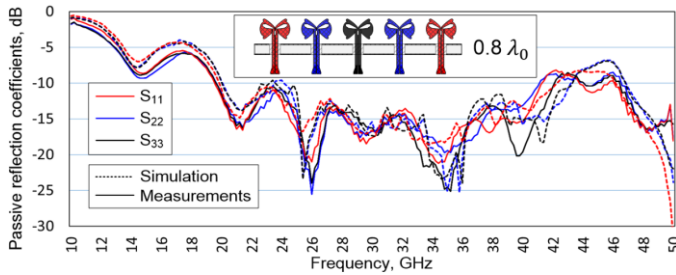


**Figure 5.43.** Measured and simulated  $S_{11}$ ,  $S_{22}$ ,  $S_{33}$ , of a not-connected array of five modified bow-tie antenna elements with element spacing  $0.8\lambda_0$ .

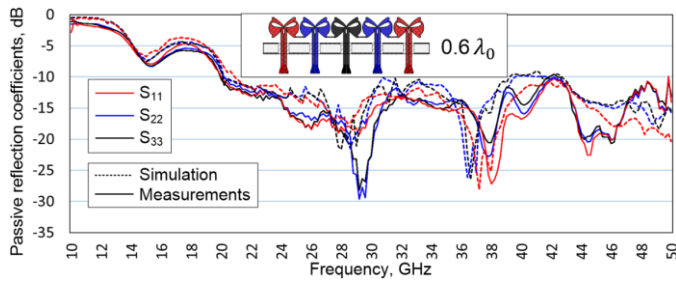


**Figure 5.44.** Measured and simulated  $S_{11}$ ,  $S_{22}$ ,  $S_{33}$ , of a connected array of five modified bow-tie antenna elements with element spacing  $0.6\lambda_0$ .

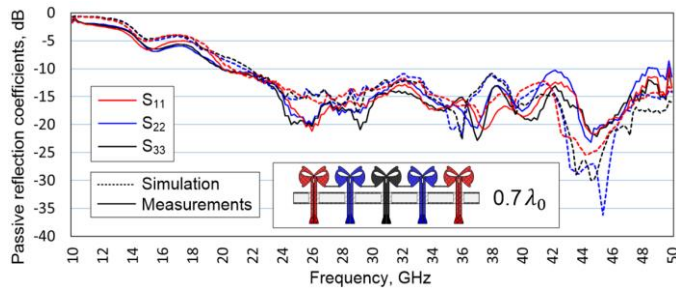


**Figure 5.45.** Measured and simulated  $S_{11}$ ,  $S_{22}$ ,  $S_{33}$ , of a connected array of five modified bow-tie antenna elements with element spacing  $0.7\lambda_0$ .

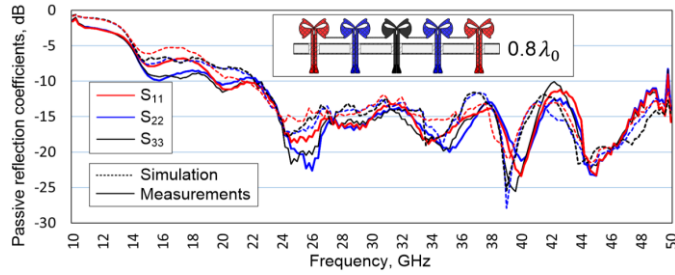


**Figure 5.46.** Measured and simulated  $S_{11}$ ,  $S_{22}$ ,  $S_{33}$ , of a connected array of five modified bow-tie antenna elements with element spacing  $0.8\lambda_0$ .

The connected array design, as has been expected, demonstrates a significantly wider bandwidth. Therefore, only the connected arrays will be considered further in the rest of the chapter. The very good agreement between simulation and measurement also confirms the applied design ideas and supports the outputs of [33] and [31], which have been based only on simulation.

The probe measurements have a few important limitations. First of all, it is not possible to measure the level of mutual coupling between elements in order to obtain a complete scattering S-matrix. As a result, it is not possible to determine the active ARC or TARC parameters. Secondly, the probe-based set-up can also not be used to measure the element patterns in an accurate way. To obtain those characteristics another series of prototypes has been realized that include wideband baluns that allow the use of mini SMP connectors.

#### 5.2.4.2. Array prototypes with mini SMP connectors for element pattern measurements

The design and geometrical details of the single modified bow-tie antenna element with a wideband balun are shown in Fig. 5.47. The size of the ground plane has been adjusted to accommodate the mini SMP connectors. The balun has been optimized for wideband performance. Fig. 5.48 shows a photo of the experimental set-up in the near-field facility at the Eindhoven University of Technology.

We used a TRL calibration [175] to accurately measure the scattering parameters. First, we measured a single isolated element. The results are provided in Fig. 5.49 ( $S_{11}$ ) and Figs. 5.50-5.52 (embedded element patterns at 20, 30, and 40 GHz)).

According to Fig. 5.49, we observe a good agreement between simulation and measurement results for a single modified bow-tie antenna element. Although the balun could limit the wideband performance, we achieved a (passive) impedance matching bandwidth of around 22 GHz.

The far-field pattern of a single array element has been optimized to provide the least distorted pattern within  $\pm 40^\circ$  in the azimuth and elevation plane. For 20 GHz (Fig. 5.50) and 30 GHz (Fig. 5.51) the far-field pattern is a hemisphere with a low directivity, which could be used for proper reflector illumination. Within  $\pm 40^\circ$  in the azimuth and elevation plane, the pattern drops by about 3 to 6 dB. For 40 GHz (Fig. 5.52), there is a significant degradation, the pattern drops up to 12 to 15 dB in the worst case. The overall agreement between simulation and measurement is relatively good for small azimuth and elevation angles. At

extreme angles ( $+90^\circ$  or  $-90^\circ$ ) there is a significant difference in results. This could be explained by the fact that the feeding cable affects the radiation pattern as well as the antenna holder.

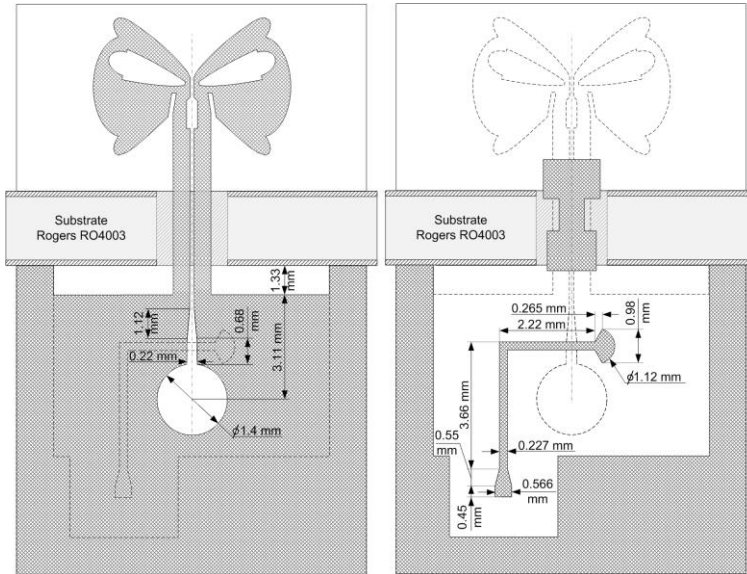


**Figure 5.47.** Single modified bow-tie antenna element with a wideband balun for connector-based measurements.



**Figure 5.48.** Impression of the connector-based measurements.

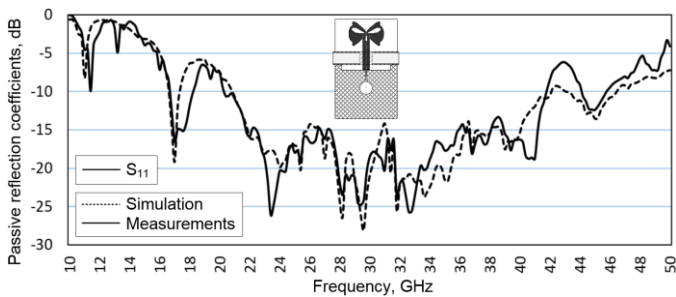


**Figure 5.49.** Measured and simulated input reflection coefficient ( $S_{11}$ ) of a single modified bow-tie antenna element with a wideband balun.

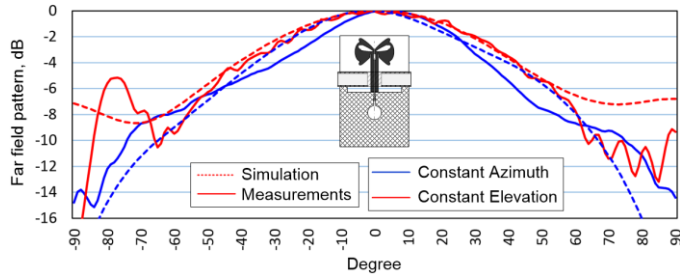


**Figure 5.50.** Measured and simulated far-field pattern in the azimuth and elevation plane of a single modified bow-tie antenna element with a wideband balun,  $f = 20$  GHz.

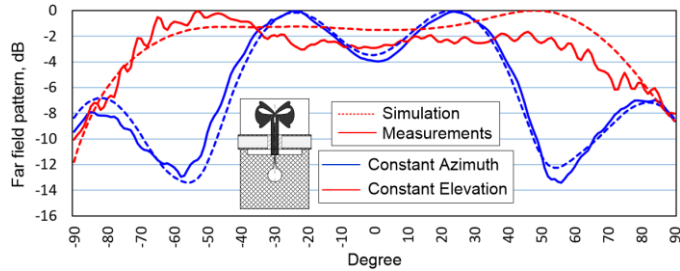


**Figure 5.51.** Measured and simulated far-field pattern in the azimuth and elevation plane of a single modified bow-tie antenna element with a wideband balun,  $f = 30$  GHz.

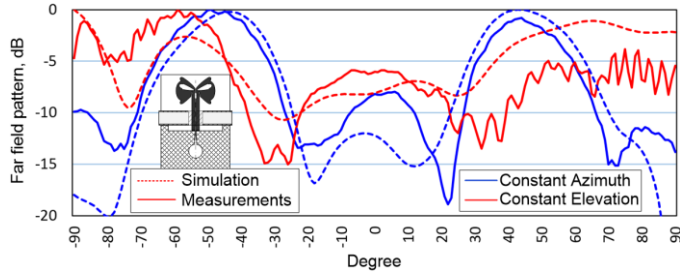


**Figure 5.52.** Measured and simulated far-field pattern in the azimuth and elevation plane of a single modified bow-tie antenna element with a wideband balun,  $f = 40$  GHz.

The next step is to investigate the performance of a connected array of five modified bow-tie antenna elements with a wideband balun, see Fig. 5.53. Similar to the measurements with the probe, three different element spacings were used ( $0.6\lambda_0$ ,  $0.7\lambda_0$ , and  $0.8\lambda_0$ ). An example of the measurement setup is presented in Fig. 5.54. Note that there is symmetry in the results for elements 1 and 5, 2 and 4.

The measured embedded element patterns in the azimuth and elevation plane at 30 GHz are presented in Figs. 5.55 – 5.63 for the 1<sup>st</sup>, 2<sup>nd</sup>, and 3<sup>rd</sup> element for the three element spacings. In addition, Figs. 5.64 – 5.65 show the frequency behavior of the embedded element pattern of the center element in the case of a  $0.8\lambda_0$  element spacing. The 2D contour plots with co- and cross-polar levels of the embedded elements patterns are shown in Fig. 5.66 for the center array element.

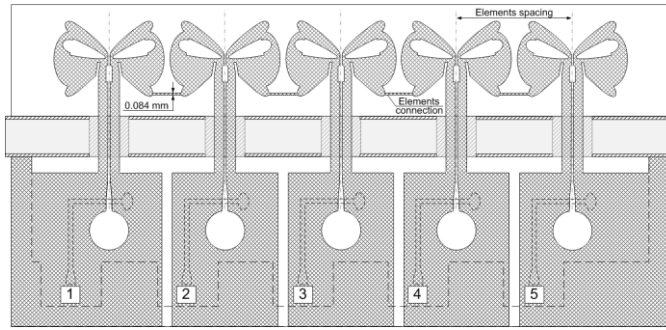


**Figure 5.53.** The connected array of five modified bow-tie antenna elements with a wideband balun for measurements through connectors.

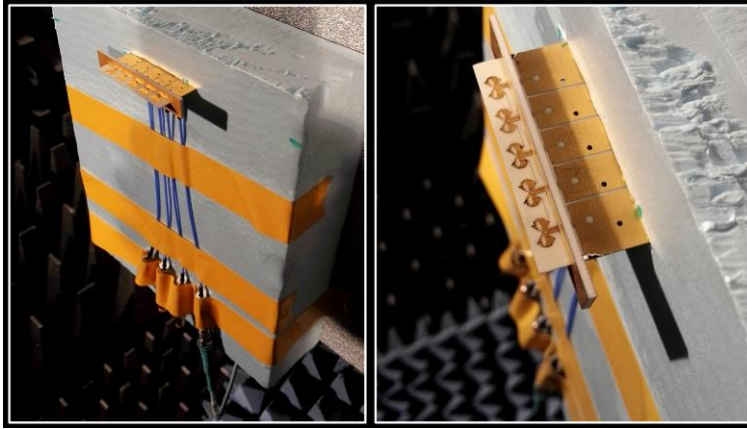


**Figure 5.54.** Measurement set-up of the connected array of five modified bow-tie antenna elements with a wideband balun.

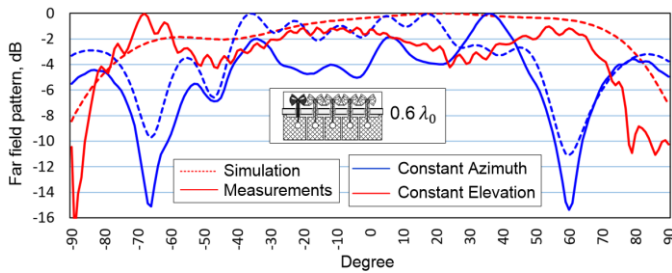


**Figure 5.55.** Measured and simulated embedded element pattern in the azimuth and elevation plane of the 1<sup>st</sup> element in the connected array of five modified bow-tie antenna elements with element spacing  $0.6\lambda_0$ ,  $f = 30$  GHz.

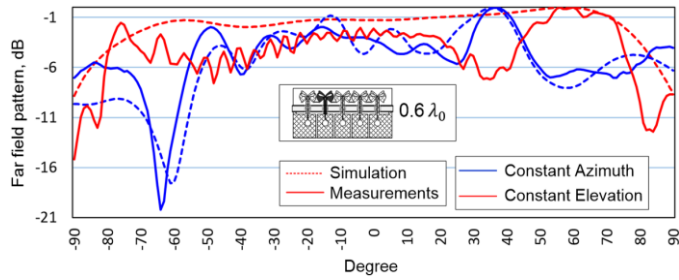


**Figure 5.56.** Measured and simulated embedded element pattern in the azimuth and elevation plane of the 2<sup>nd</sup> element in the connected array of five modified bow-tie antenna elements with element spacing  $0.6\lambda_0$ ,  $f = 30$  GHz.

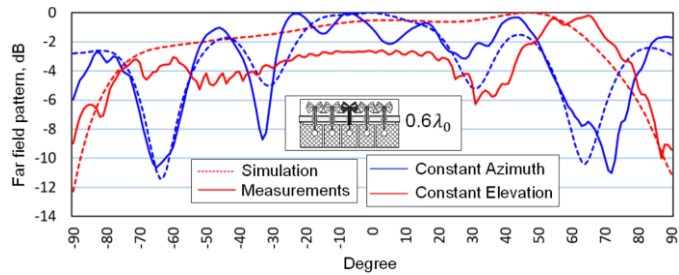


**Figure 5.57.** Measured and simulated embedded element pattern in the azimuth and elevation plane of the 3<sup>rd</sup> (central) element in the connected array of five modified bow-tie antenna elements with element spacing  $0.6\lambda_0$ ,  $f = 30$  GHz.

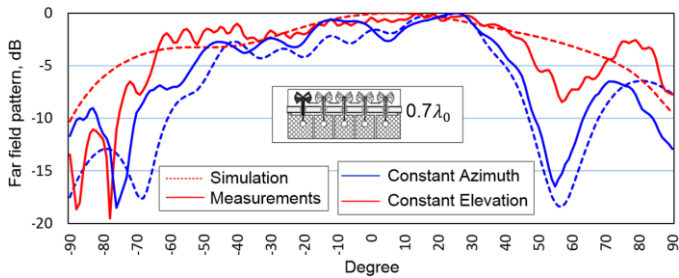


**Figure 5.58.** Measured and simulated embedded element pattern in the azimuth and elevation plane of the 1<sup>st</sup> element in the connected array of five modified bow-tie antenna elements with element spacing  $0.7\lambda_0$ ,  $f = 30$  GHz.

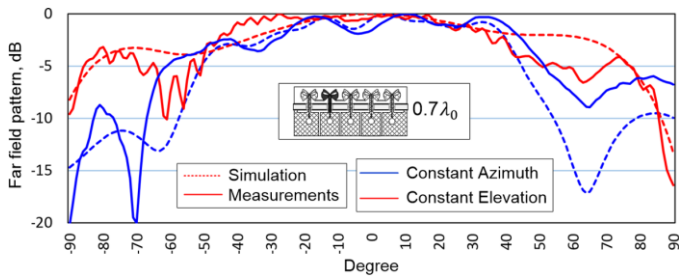


**Figure 5.59.** Measured and simulated embedded element pattern in the azimuth and elevation plane of the 2<sup>nd</sup> element in the connected array of five modified bow-tie antenna elements with element spacing  $0.7\lambda_0$ ,  $f = 30$  GHz.

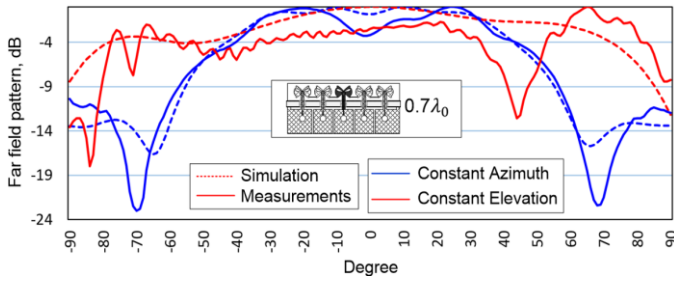


**Figure 5.60.** Measured and simulated embedded element pattern in the azimuth and elevation plane of the 3<sup>rd</sup> (central) element in the connected array of five modified bow-tie antenna elements with element spacing  $0.7\lambda_0$ ,  $f = 30$  GHz.

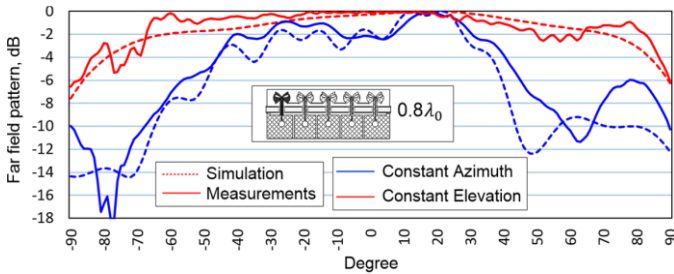


**Figure 5.61.** Measured and simulated embedded element pattern in the azimuth and elevation plane of the 1<sup>st</sup> element in the connected array of five modified bow-tie antenna elements with element spacing  $0.8\lambda_0$ ,  $f = 30$  GHz.

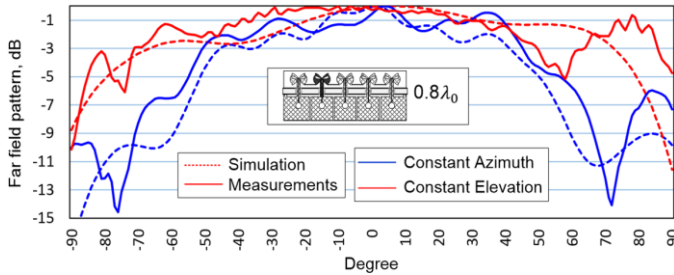


**Figure 5.62.** Measured and simulated embedded element pattern in the azimuth and elevation plane of the 2<sup>nd</sup> element in the connected array of five modified bow-tie antenna elements with element spacing  $0.8\lambda_0$ ,  $f = 30$  GHz.

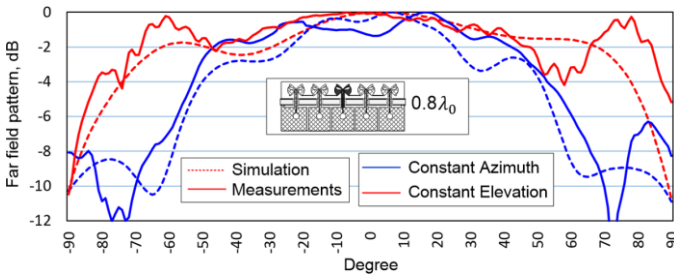


**Figure 5.63.** Measured and simulated embedded element pattern in the azimuth and elevation plane of the 3<sup>rd</sup> (central) element in the connected array of five modified bow-tie antenna elements with element spacing  $0.8\lambda_0$ ,  $f = 30$  GHz.

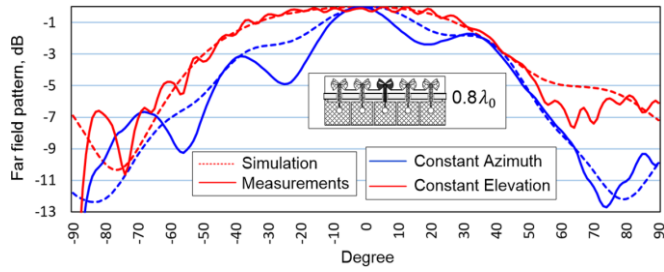


**Figure 5.64.** Measured and simulated embedded element pattern in the azimuth and elevation plane of the 3<sup>rd</sup> (central) element in the connected array of five modified bow-tie antenna elements with element spacing  $0.8\lambda_0$ ,  $f = 20$  GHz.

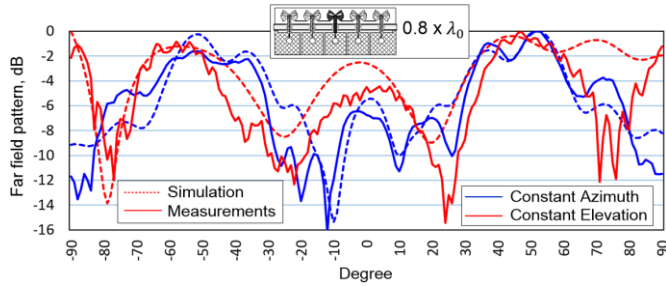


**Figure 5.65.** Measured and simulated embedded element pattern in the azimuth and elevation plane of the 3<sup>rd</sup> (central) element in the connected array of five modified bow-tie antenna elements with element spacing  $0.8\lambda_0$ ,  $f = 40$  GHz.

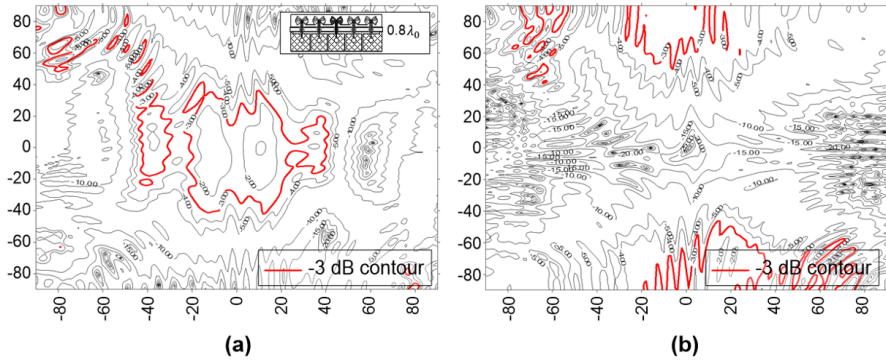


**Figure 5.66.** Measured a) co-polar (b) cross-polar 2D far-field contour image of 3<sup>rd</sup> (central) element in the connected array of five modified bow-tie antenna elements with element spacing  $0.8\lambda_0$ ,  $f = 30$  GHz.

As we can observe from the measured embedded element patterns, there is a clear difference between arrays with different element spacings. For all examined elements (array elements 1, 2, and 3 of Fig. 5.53) with narrow element spacing ( $0.6\lambda_0$ ) there is significant distortion of the patterns, see Fig. 5.55, Fig. 5.56, and Fig. 5.57. For this case, within  $\pm 40^\circ$  in azimuth and elevation plane, the pattern drops up to 9 dB. For  $0.7\lambda_0$  element spacing (Fig. 5.58, Fig. 5.59, and Fig. 5.60) the overall quality is better, but the maximum observed roll-off is also up to 9 dB. The best-obtained patterns are related to a  $0.8\lambda_0$  element spacing, see Fig. 5.61, Fig. 5.62, and Fig. 5.63. The distributions are smooth and within  $\pm 40^\circ$  in the

azimuth and elevation plane, the pattern drops only up to 3 dB in the measurement results. In addition, the frequency behavior of the array with  $0.8\lambda_0$  element spacing (Fig. 5.63 – Fig. 5.64) demonstrates that there are more or less smooth distributions within a  $\pm 40^\circ$  angular range, similar to the single element pattern. Only at higher frequencies (Fig. 5.65), there is a significant drop up to 16 dB at 40 GHz. At the same time, the 2D far-field contour images (Fig. 5.66) show relatively low cross-polar components. The 2D far-field contour images also validate that the -3 dB contour is located within  $\pm 40^\circ$  in the azimuth and elevation plane. This means that the dominant part of the energy is going to contribute to the reflector illumination.

#### 5.2.4.3. Evaluation of the active wideband performance of the PAF with the classical prime-focus reflector and the complex offset double-reflector system

The next step is to determine the ARC and TARC of the connector-based prototypes. For that purpose, we need to postprocess the measured S-matrix. The TARC is the most informative characteristic since it illustrates the combined performance of the whole array within the required frequency range.

To determine the TARC of an FPA, it is required to specify the used reflectors. In GRASP two different reflector configurations have been simulated. The first one is again the classical prime-focus reflector with  $F/D = 0.6$ . The other configuration is the double-reflector antenna with improved scan capabilities - the complex offset double-reflector as introduced by our research group in [23]. This design is presented in Fig. 5.67. The wide scan range of this reflector has been achieved by using the idea of discontinuous surfaces. This idea is illustrated in Fig. 5.68. The operation of this design has been validated by measurements with the prototype of Fig. 5.69 [23].

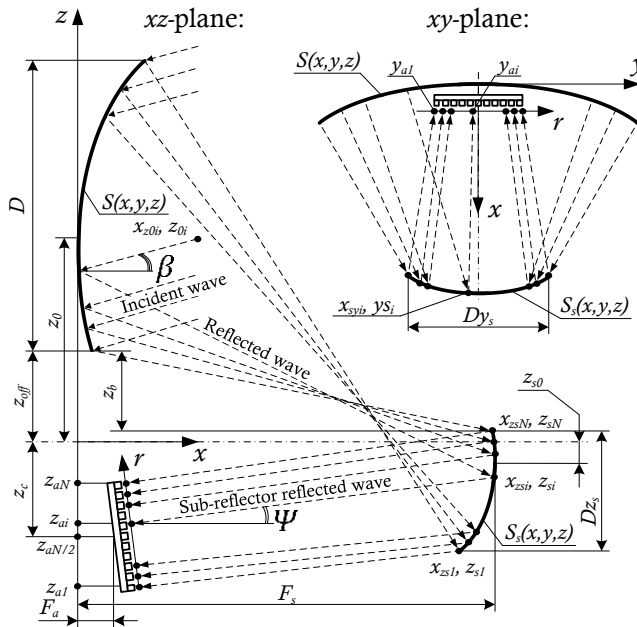
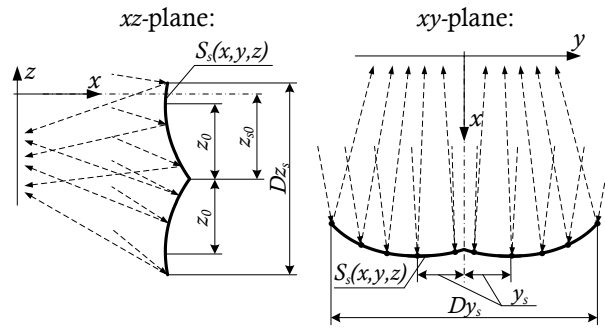
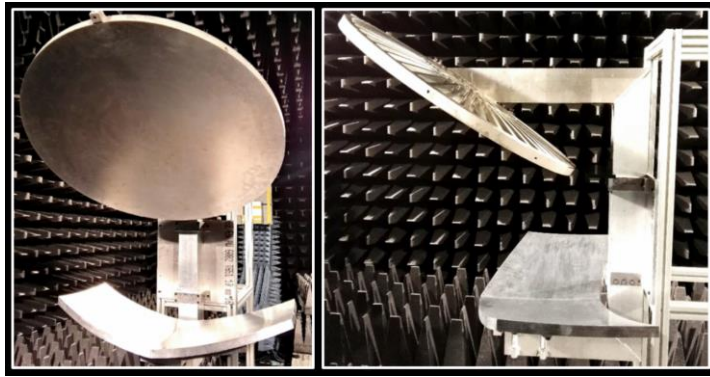


Figure 5.67. Complex offset double-reflector model [23].



**Figure 5.68.** The complex offset double-reflector model with discontinuities in the sub-reflector [23].



**Figure 5.69.** Photo of the prototype using the complex offset double-reflector setup [23].

The excitation coefficients from the reflectors have been obtained from GRASP simulations [39] and have been combined with the measured S-matrix to prove the wideband performance. Thus, the obtained TARC results contain both simulations and actual measurements. In the text below those results are called “measurements”. In its turn, the TARC “simulation” results are obtained from the simulation of the array in CST [139] plus the simulated excitations from GRASP [39].

Three different arrays have been tested with element spacing of  $0.6\lambda_0$ ,  $0.7\lambda_0$  and  $0.8\lambda_0$ , where  $\lambda_0 = 1$  cm. All arrays are related to the connected configuration with five modified bow-tie antenna elements with mini SMP connectors. In addition, for the configuration with element spacing of  $0.8\lambda_0$ , the excitation coefficients have been obtained in the case of an incoming plane wave with the angle of incidence equal to  $5^\circ$ ,  $10^\circ$ ,  $15^\circ$ , and  $20^\circ$ . This allows us to determine the performance in the case of scanning as well.

Figs. 5.70-5.74 present the measured and simulated TARC with element spacing of  $0.8\lambda_0$  for broadside operation and scanning up to  $20^\circ$ . Fig. 5.75 shows the TARC with an element spacing of  $0.7\lambda_0$ , and Fig. 5.76 – with an element spacing of  $0.6\lambda_0$ . In addition, Figs. 5.77 – Fig. 5.80 present summaries of the TARC results for various scan angles and element spacings for both the classical prime-focus and complex offset double-reflector system.

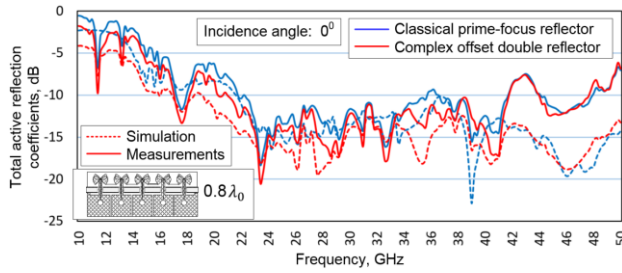


**Figure 5.70.** TARC of the connected array of five modified bow-tie antenna elements with element spacing  $0.8\lambda_0$  in combination with reflectors based on simulated and measured S-parameters for broadside operation.

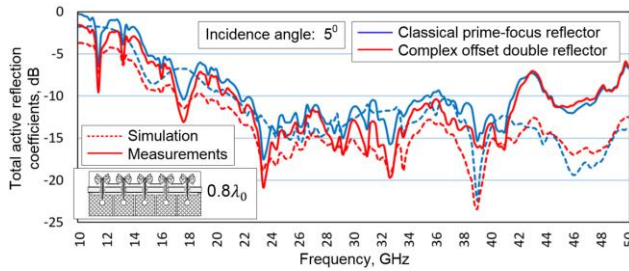


**Figure 5.71.** TARC of the connected array of five modified bow-tie antenna elements with element spacing  $0.8\lambda_0$  in combination with reflectors based on simulated and measured S-parameters for incidence angle  $5^\circ$ .

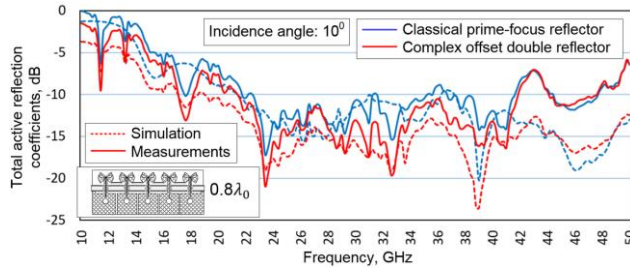


**Figure 5.72.** TARC of the connected array of five modified bow-tie antenna elements with element spacing  $0.8\lambda_0$  in combination with reflectors based on simulated and measured S-parameters for incidence angle  $10^\circ$ .

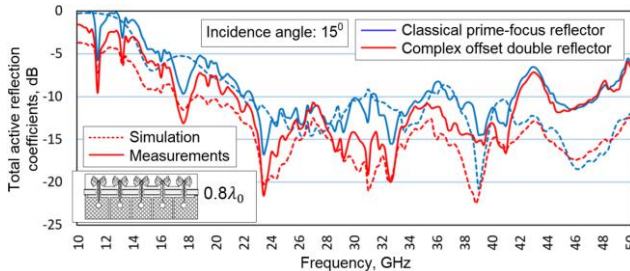


**Figure 5.73.** TARC of the connected array of five modified bow-tie antenna elements with element spacing  $0.8\lambda_0$  in combination with reflectors based on simulated and measured S-parameters for incidence angle  $15^\circ$ .

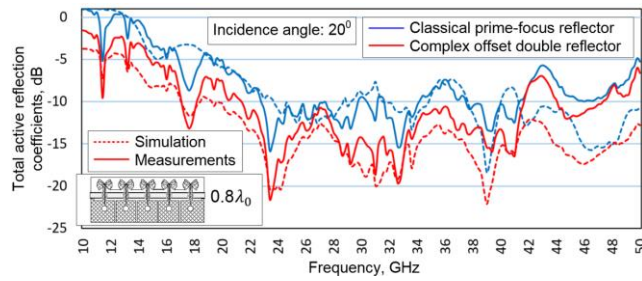


**Figure 5.74.** TARC of the connected array of five modified bow-tie antenna elements with element spacing  $0.8\lambda_0$  in combination with reflectors based on simulated and measured S-parameters for incidence angle  $20^\circ$ .

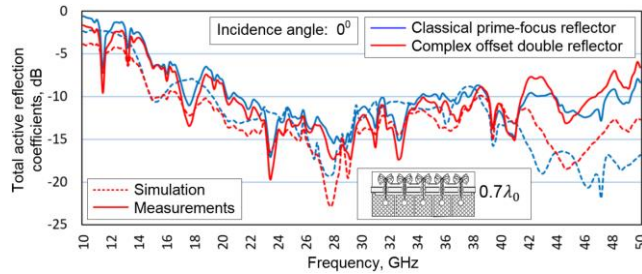


**Figure 5.75.** TARC of the connected array of five modified bow-tie antenna elements with element spacing  $0.7\lambda_0$  in combination with reflectors based on simulated and measured S-parameters for broadside operation.

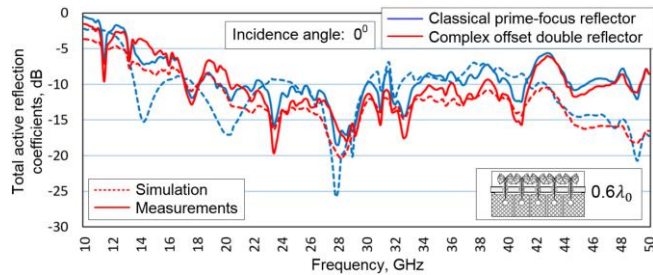


**Figure 5.76.** TARC of the connected array of five modified bow-tie antenna elements with element spacing  $0.6\lambda_0$  in combination with reflectors based on simulated and measured S-parameters for broadside operation.

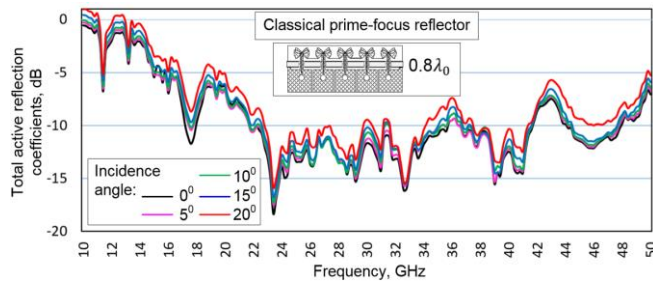


**Figure 5.77.** TARC of the connected array of five modified bow-tie antenna elements with element spacing  $0.8\lambda_0$  in combination with classical prime-focus reflector based on measured S-parameters for different incidence angle.

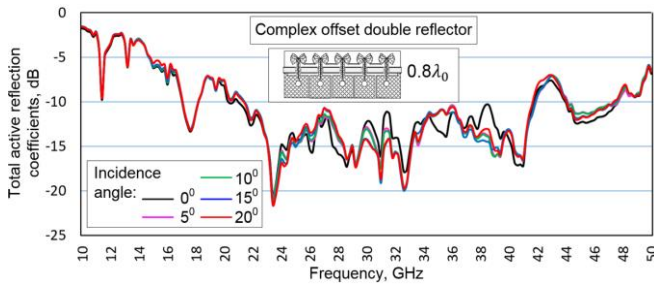


**Figure 5.78.** TARC of the connected array of five modified bow-tie antenna elements with element spacing  $0.8\lambda_0$  in combination with the complex offset double-reflector based on measured S-parameters for different incidence angle.

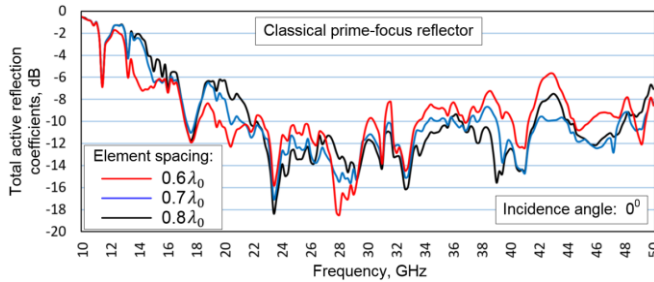


**Figure 5.79.** TARC of the connected array of five modified bow-tie antenna elements with different element spacings in combination with a classical prime-focus reflector based on measured S-parameters for broadside operation.

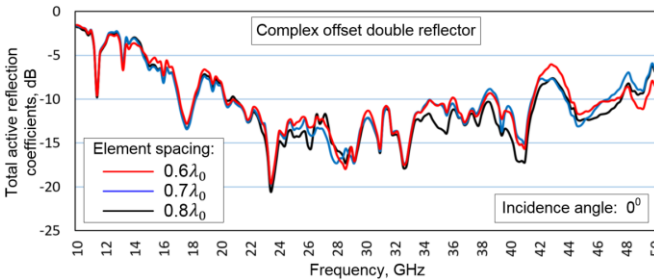


**Figure 5.80.** TARC of the connected array of five modified bow-tie antenna elements with different element spacings in combination with a complex offset double-reflector based on measured S-parameters for broadside operation.

In Fig. 5.70 – Fig. 5.76 we see a very good agreement between simulation and measurement up to 40 GHz, for frequencies higher than 40 GHz there is a significant difference. This could be related to the wideband balun which limits the wideband performance. In addition, Fig. 5.70 – Fig. 5.76 demonstrate that the array excitation by the complex offset double-reflector leads to better wideband performance as compared to the classical prime-focus reflector. This is nice evidence that the concept of field optimization of the reflector works well. This reflector provides a more uniform field distribution and linear phase shift between array elements. This leads to a reduced effect of mutual coupling between array elements and, as a result, provides a wider active frequency bandwidth. The difference between the applied reflectors is less significant for limited scan angles ( $0^\circ$  -  $10^\circ$ ), see Fig.

5.70 – Fig. 5.72, and quite significant in the case of wide-angle scanning, see Fig. 5.73 and Fig. 5.74. This is expected since the complex offset double-reflector is optimized for wide-scan performance.

The scan angle has a pronounced effect on the TARC. For the classical prime-focus reflector, in Fig. 5.77, the TARC curve increases about 2 – 4 dB in the range from  $0^\circ$  to  $20^\circ$ . Of course, that limits the frequency band since the overall level of matching is about -15 dB – -8 dB. For the complex offset double-reflector of Fig. 5.78, there is almost no variation within the required scan range. Again, this is expected since the scan performance of the reflector has been optimized. The broadside operation is a little bit different since at broadside scan the reflectors have a very wide field distribution with two separated maxima (bi-focal distribution) and the array is located between them [23].

The most crucial factor in achieving a wideband TARC performance is the element spacing, see Fig. 5.79 and Fig. 5.80. We observe that even with the optimized reflector configuration it is not possible to achieve a good TARC level over a bandwidth of 20 GHz if the element spacing is less than  $0.8\lambda_0$ . The bandwidth obtained with the classical prime-focus reflector (Fig. 5.79) is totally unacceptable even for broadside operation. The results of Fig. 5.78 – Fig. 5.80 are summarized in Table 5.2. This table presents a clear comparison between the classical prime-focus reflector and the complex offset double-reflector. In addition, the TARC variation for different element spacings is clearly visible, especially for the classical prime-focus reflector which is not optimized for wide-angle scanning FPAs. Of course, with wider element spacing we lose some reflector performance, but, as has been demonstrated, the quality of the embedded element patterns could be improved with wider element spacing, as has been shown in section 5.2.3.2. Also, it is important to notice that in a real application, the array should be two-dimensional using significantly more elements. In Section 5.2.5.1. an FPA with about 200 elements is presented to analyze the potential FPA system capability.

**Table 5.2** Realized impedance matching bandwidth based on the measured TARC of the connected array of five modified bow-tie antenna elements.

Reflector type	Classical prime-focus reflector	Complex offset double-reflector
Broadside operation with element spacing $0.6\lambda_0$	7.3 GHz	17.7 GHz
Broadside operation with element spacing $0.7\lambda_0$	13.1 GHz	17.9 GHz
Broadside operation with element spacing $0.8\lambda_0$	14.2 GHz	<b>21.6 GHz</b>
Scan angle of angle $5^\circ$ , with element spacing $0.8\lambda_0$	13.7 GHz	<b>21 GHz</b>
Scan angle of $10^\circ$ , with element spacing $0.8\lambda_0$	13.7 GHz	<b>20.8 GHz</b>
Scan angle of $15^\circ$ , with element spacing $0.8\lambda_0$	12.5 GHz	<b>20.6 GHz</b>
Scan angle of $20^\circ$ , with element spacing $0.8\lambda_0$	6.8 GHz	<b>20.1 GHz</b>

#### 5.2.4.4. Far-field pattern measurements of the complex offset double-reflector fed by modified bow-tie antennas

Before investigating the FPA system capability it is necessary to measure the far-field pattern of the complex offset double-reflector with the designed modified bow-tie antenna. This evaluation allows to compare the measured secondary far-field patterns of the combination of reflector and antenna feed with our FPA model implemented in GRASP/CST/MATLAB.

Unfortunately, it was not possible to use the whole array as a feed. Therefore, the single array element has been used to feed the complex offset double-reflector, see Fig. 5.81. Note that a combination of the proposed reflector with the designed array is presented in [27], where an LNA chip with an optical beamforming network has been used to feed the designed array.

In [23] a horn antenna has been used in combination with the complex offset double-reflector to prove the scan performance and to validate the reflector concept with a well-known feed. Unfortunately, the horn antenna is not wideband enough, the frequency range is limited to 26.4 GHz – 40.1 GHz. Thus, it is necessary to use the designed modified bow-tie antenna to test the reflector far-field properties and scan capability in the required 20 GHz – 40 GHz operational band.

The near field test facility of the Eindhoven University of Technology was used, as shown in Fig. 5.81. To test the required scan capability up to  $\pm 20^\circ$  in the azimuth plane, a modified bow-tie antenna has been placed at different positions along the array plane. For each of these positions, the radiation patterns have been measured.

According to [23], the complex offset double-reflector requires to have an array length of 28 cm to provide a  $\pm 20^\circ$  scan range in the azimuth plane. Thus, we first measured the far-field patterns with the feed located in the center of the array (Fig. 5.82 – Fig. 5.84) and then shifted the feed in steps of 2 cm until it reaches the edge of the array at 14 cm shift (Fig. 5.85 – Fig. 5.91). Figs. 5.82–5.84 present the far-field patterns in the azimuth plane, 2D far-field images, and 2D far-field contour images with the bow tie placed at the center of the array at 20 GHz, 30 GHz, and 40 GHz, respectively.

Figs. 5.85–5.91 present the far-field patterns at 30 GHz for various feed displacements in the range between 2–14 cm. These figures also show the frequency dependence of the far-field pattern. The agreement between simulation and measurement is in all cases quite good. The differences in sidelobe levels are mainly due to the large support structure of the reflector in the prototype, see also Fig. 5.81. This was not included in the simulation. The complex offset double-reflector has a bi-focal field distribution in the array plane for the receive case [23]. Thus, the far-field of the reflector is a bi-focal kind of distribution when only a single array element is used. The difference between the co-polar and cross-polar components of the electric field is sufficiently high (about 20 dB) in all investigated scan positions over the frequency band of interest. For the maximum feed displacement of 14 cm (Fig. 5.91), the main lobe deviation is about  $19^\circ$ . This is less than the expected  $20^\circ$ , but could be improved somewhat by using additional phase control in a complete array-fed system.

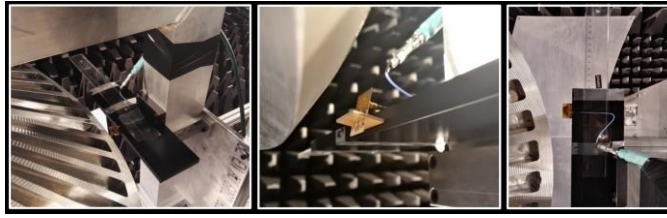


**Figure 5.81.** Photo of the experimental set-up using a single modified bow-tie antenna element to measure the far-field patterns of the complex offset double-reflector system.

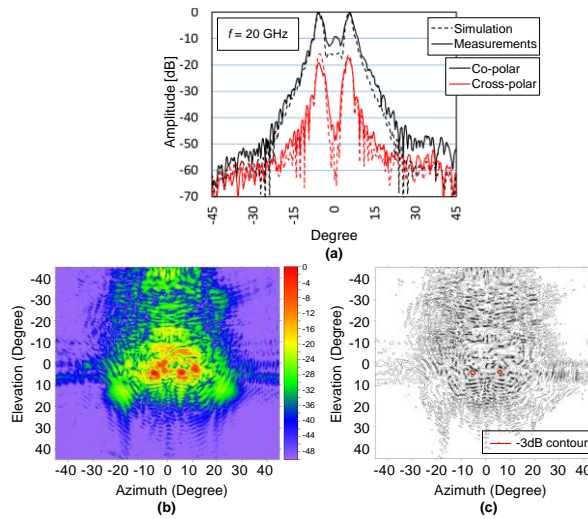


**Figure 5.82.** (a) Far-field pattern in azimuth plane (b) 2D far-field image (c) 2D far-field contour image of single modified bow-tie antenna feed at the center of the array,  $f = 20$  GHz.

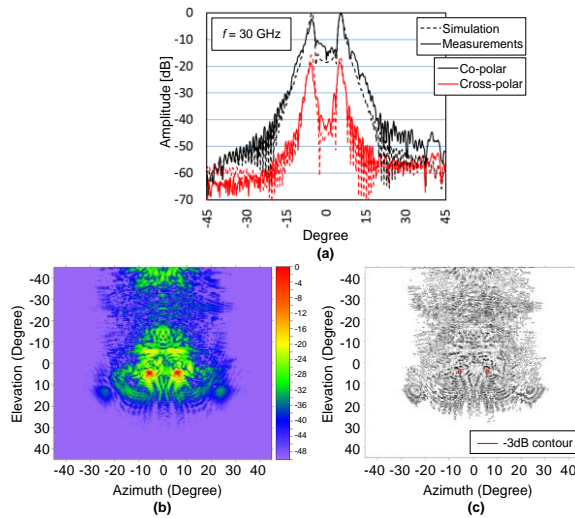


**Figure 5.83.** (a) Far-field pattern in azimuth plane (b) 2D far-field image (c) 2D far-field contour image of single modified bow-tie antenna feed at the center of the array,  $f = 30$  GHz.

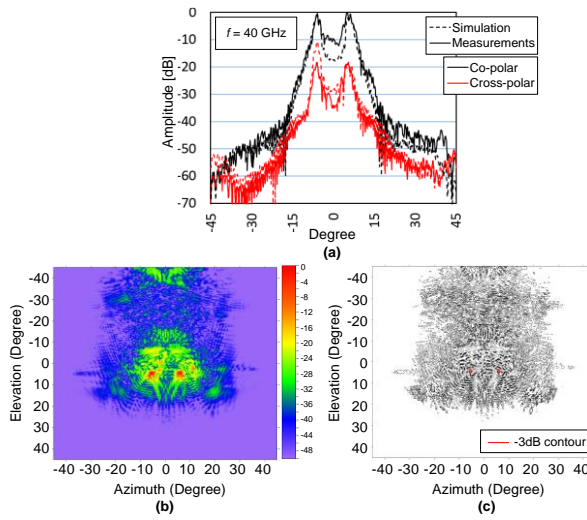


**Figure 5.84.** (a) Far-field pattern in azimuth plane (b) 2D far-field image (c) 2D far-field contour image of single modified bow-tie antenna feed at the center of the array,  $f = 40$  GHz.

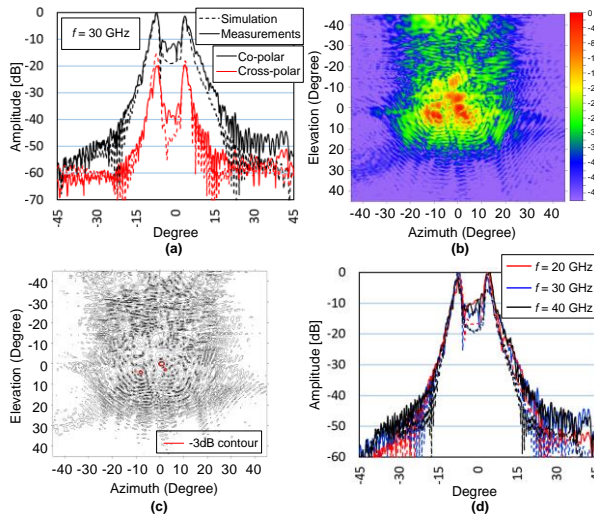


**Figure 5.85.** (a) The far-field pattern in the azimuth plane (b) 2D far-field image (c) 2D far-field contour image,  $f = 30$  GHz, (d) Far-field pattern in the azimuth plane for different frequencies with antenna feed displaced 2 cm from the array center.

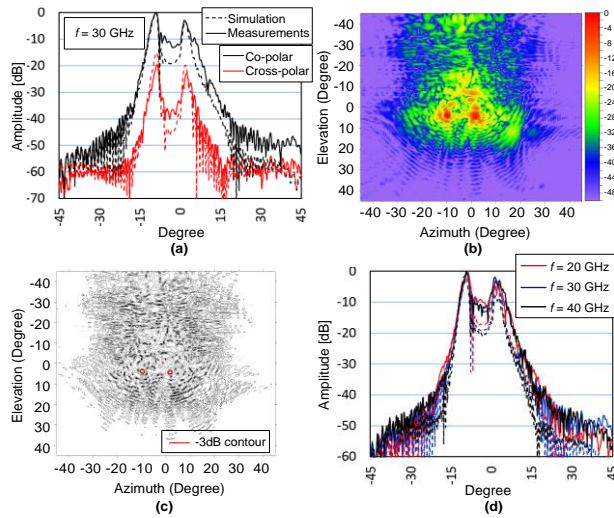


**Figure 5.86.** (a) The far-field pattern in the azimuth plane (b) 2D far-field image (c) 2D far-field contour image,  $f = 30$  GHz, (d) Far-field pattern in the azimuth plane for different frequencies with antenna feed displaced 4 cm from the array center.

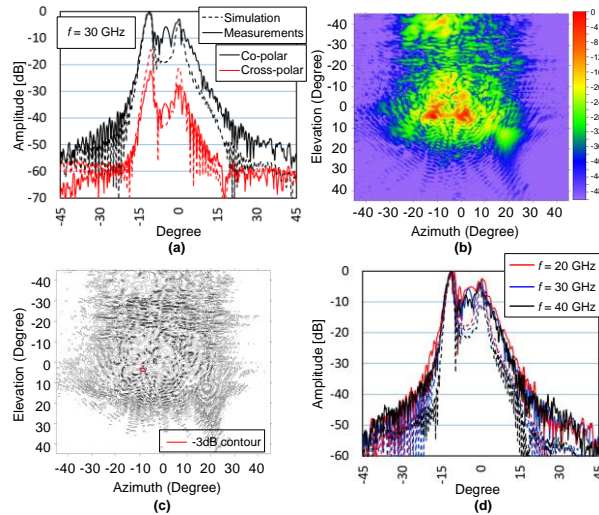


**Figure 5.87.** (a) The far-field pattern in the azimuth plane (b) 2D far-field image (c) 2D far-field contour image,  $f = 30$  GHz, (d) Far-field pattern in the azimuth plane for different frequencies with antenna feed displaced 6 cm from the array center.

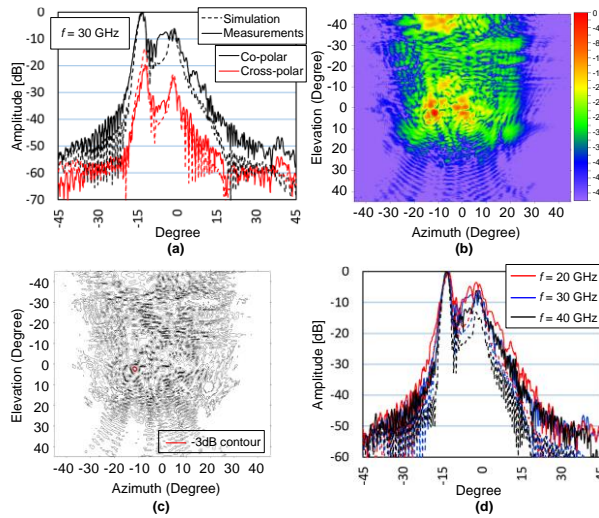


**Figure 5.88.** (a) The far-field pattern in the azimuth plane (b) 2D far-field image (c) 2D far-field contour image,  $f = 30$  GHz, (d) Far-field pattern in the azimuth plane for different frequencies with antenna feed displaced 8 cm from the array center.

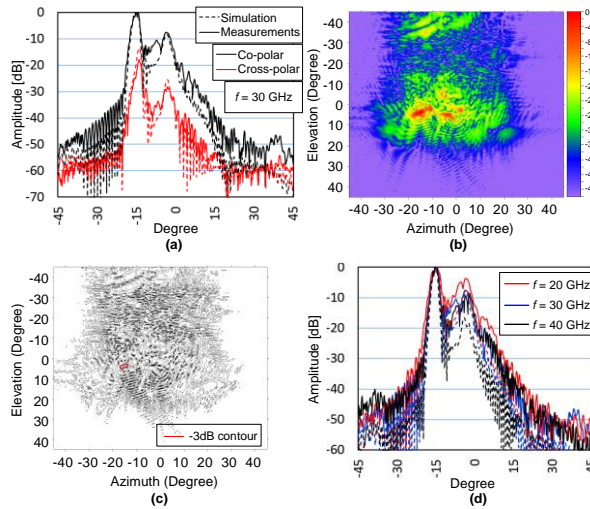


**Figure 5.89.** (a) The far-field pattern in the azimuth plane (b) 2D far-field image (c) 2D far-field contour image,  $f = 30$  GHz, (d) Far-field pattern in the azimuth plane for different frequencies with antenna feed displaced 10 cm from the array center.

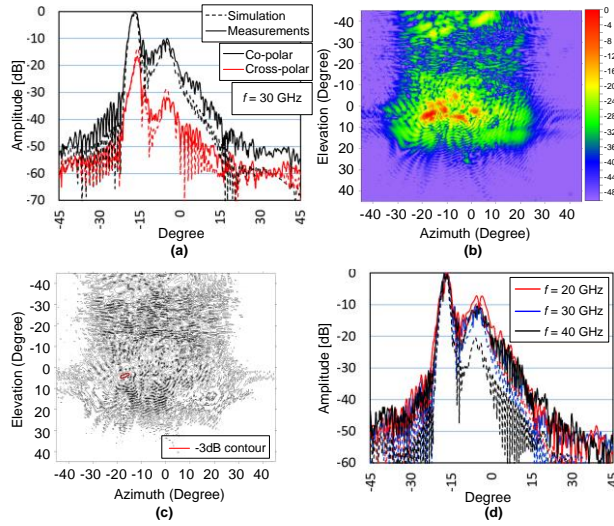


**Figure 5.90.** (a) The far-field pattern in the azimuth plane (b) 2D far-field image (c) 2D far-field contour image,  $f = 30$  GHz, (d) Far-field pattern in the azimuth plane for different frequencies with antenna feed displaced 12 cm from the array center.

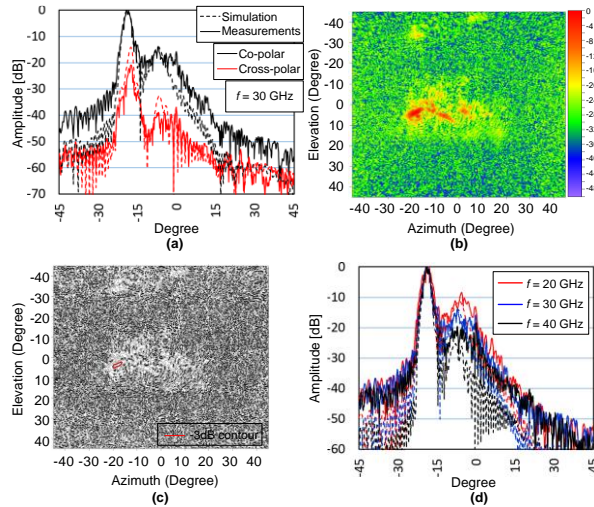


**Figure 5.91.** (a) The far-field pattern in the azimuth plane (b) 2D far-field image (c) 2D far-field contour image,  $f = 30$  GHz, (d) Far-field pattern in the azimuth plane for different frequencies with antenna feed displaced 14 cm from the array center.

### 5.2.5. FPA system capability

In the previous sections, we have investigated and experimentally validated the FPA performance using small linear arrays of bow-tie elements. A very good agreement between measurements and simulations has been obtained. What we still miss is the overall performance when the reflector system is fed by a large number of array elements. For that purpose, a two-dimensional array with about 200 elements is simulated in combination with the complex offset double-reflector configuration. Note that the array size is determined by

the reflector design, thus the actual number of elements depends on the element spacing. Results are presented in subparagraph 5.2.5.1. To estimate the overall expediency of such FPAs systems the equivalent phased-array configuration has been analyzed in subparagraph 5.2.5.2. and compared against our proposed FPAs.

### 5.2.5.1. FPA system analysis

In [23] arrays of horn antennas have been used to determine the scan performance of the realized reflector prototype. The horn antenna has a limited frequency range between 26.4 GHz – 40.1 GHz. In addition, mutual coupling between array elements was ignored as well as feed mismatch efficiency and phase efficiency.

In this section, we will use the connected array of modified bow-tie antennas with three different elements spacings ( $0.6\lambda_0$ ,  $0.7\lambda_0$  and  $0.8\lambda_0$ , where  $\lambda_0 = 1$  cm) to determine the overall system-level performance. The array dimensions are chosen based on the required dimension of the complex offset double-reflector configuration [23]. Thus, the size of the arrays is 28 cm in length and 4 cm in width. As a result, the array with  $0.8\lambda_0$  element spacing has 180 elements, with  $0.7\lambda_0$  – 200 elements, and with  $0.6\lambda_0$  – 230 elements. The far-field pattern of each array element has been simulated in CST [139] and then imported to GRASP [39]. In GRASP the conjugate field matching coefficients have been applied to each antenna element. In this way, the directivity includes the radiation efficiency of the reflector, taper efficiency, spill-over efficiency, polarization efficiency, and potential blockage efficiency. In addition, all effects of mutual coupling between array elements are also included. However, since power normalization was used, mismatch efficiency and phase efficiency in the array are not included, so the array radiates all energy with perfect phase and amplitude, but with a realistic embedded element pattern.

The simulated set-up is illustrated in Fig. 5.92. For broadside operation investigations were done at 20 GHz, 30 GHz, and 40 GHz. The scan performance has been explored at 30 GHz with scan angles  $0^\circ$ ,  $5^\circ$ ,  $10^\circ$ ,  $15^\circ$ , and  $20^\circ$ . Fig. 5.93, Fig. 5.94, and Fig. 5.95 show present the realized directivity patterns of the complex offset double-reflector configuration at the broadside with element spacing varying between  $0.6\lambda_0$  and  $0.8\lambda_0$ . The  $90^\circ$ -cuts correspond to the scan plane or the azimuth plane. In the  $0^\circ$ -plane, the patterns show similar behavior as the classical prime-focus reflector. Fig. 5.96, Fig. 5.97, and Fig. 5.98 show the performance versus element spacing in the case of scanning. Excitations of the array elements have been adjusted to realize the scan performance up to  $20^\circ$ . We can observe that for a scan range of  $\pm 15^\circ$ , the directivity drop is limited to only a few dB and remains above 40 dBi. This proves the concept viability of this reflector system and designed array feed. Table 5.3 and Table 5.4 summarize the realized directivity and reflector efficiencies.

It is important to notice that the proposed complex offset double-reflector configuration (see Fig. 5.67) uses the reflector elevation incline  $\beta$  as one of the geometrical parameters optimized by geometrical optics (GO) code [155], [158]. This parameter is equal to  $40^\circ$  which is also visible in the photo of the prototype in Fig. 5.69. According to [23] this incline could significantly improve the reflector scan properties, but it limits the effective area of the main reflector with a cosine from this angle. Thus, the maximum directivity of the tested system is potentially 23.4% less than for a classical prime-focus reflector of the same size. This factor is considered during the estimation of reflector efficiencies. An alternative reflector system with improved scan performance and without this issue is presented in [171].

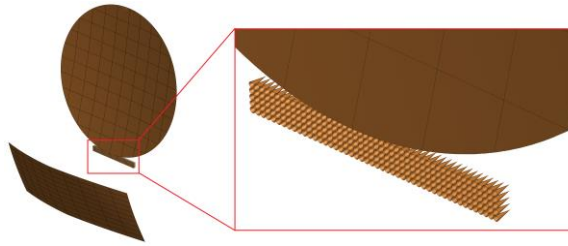


**Figure 5.92.** The complex offset double-reflector configuration fed by a connected array of modified bow-tie antennas.

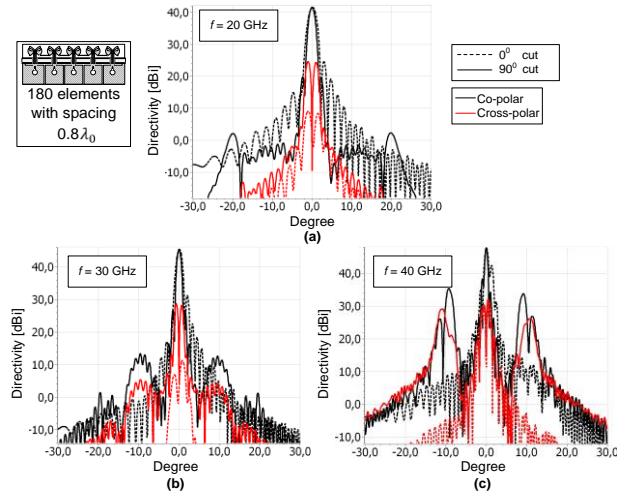


**Figure 5.93.** Directivity pattern of the complex offset double-reflector fed by an array of connected modified bow-tie antennas with element spacing of  $0.8\lambda_0$  at 30 GHz for (a)  $f = 20$  GHz, (b)  $f = 30$  GHz, (c)  $f = 40$  GHz.

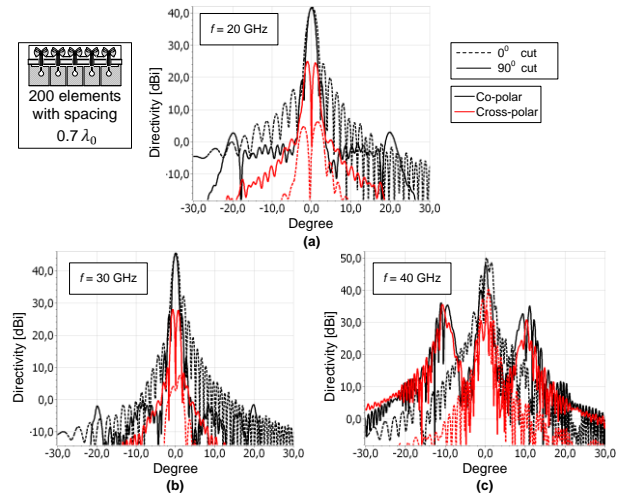


**Figure 5.94.** Directivity pattern of the complex offset double-reflector fed by an array of connected modified bow-tie antennas with element spacing of  $0.7\lambda_0$  at 30 GHz for (a)  $f = 20$  GHz, (b)  $f = 30$  GHz, (c)  $f = 40$  GHz.

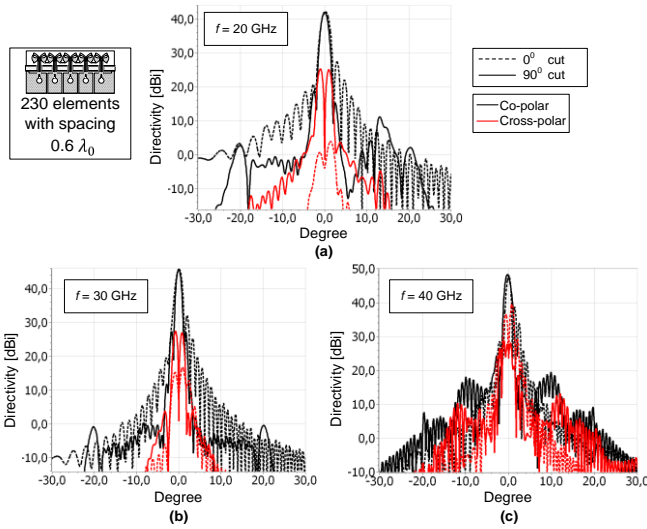


**Figure 5.95.** Directivity pattern of the complex offset double-reflector fed by an array of connected modified bow-tie antennas with element spacing of  $0.6\lambda_0$  at 30 GHz for (a)  $f = 20$  GHz, (b)  $f = 30$  GHz, (c)  $f = 40$  GHz.

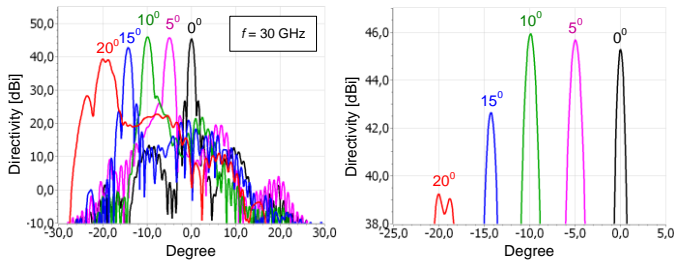


**Figure 5.96.** Directivity pattern of the complex offset double-reflector fed by an array of connected modified bow-tie antennas with element spacing of  $0.8\lambda_0$  for different scan angles,  $f = 30$  GHz.

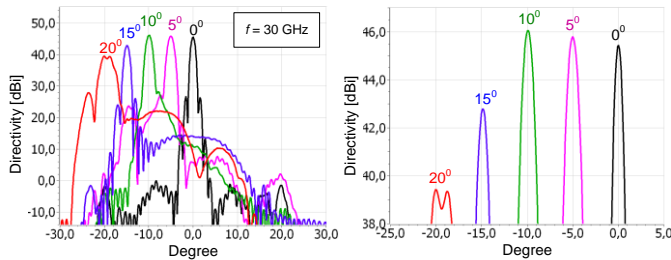


**Figure 5.97.** Directivity pattern of the complex offset double-reflector fed by an array of connected modified bow-tie antennas with element spacing of  $0.7\lambda_0$  for different scan angles,  $f = 30$  GHz.

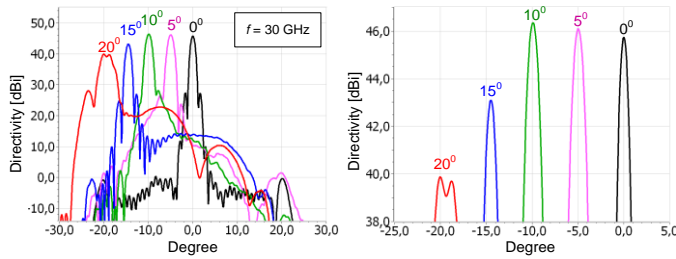


**Figure 5.98.** Directivity pattern of the complex offset double-reflector fed by an array of connected modified bow-tie antennas with element spacing of  $0.6\lambda_0$  for different scan angles,  $f = 30$  GHz.

**Table 5.3** Performance of the system with different array element spacings.

Array type, number of array elements, and element spacing ( $\lambda_0 = 1$ cm)		Directivity [dBi]			Reflector aperture efficiency, %		
		Frequency, GHz			Frequency, GHz		
		20	30	40	20	30	40
The array of modified bow-tie antennas	180 elements, $0.8\lambda_0$	41.50	45.28	47.76	65.26	69.12	68.87
	200 elements, $0.7\lambda_0$	41.67	45.44	47.92	67.71	71.75	71.40
	230 elements, $0.6\lambda_0$	41.97	45.74	48.22	72.59	76.88	76.54
The array of horn antennas [23]	180 elements, $0.8\lambda_0$	-	45.80	48.01	-	77.97	72.91
	200 elements, $0.7\lambda_0$	-	45.91	48.18	-	79.95	75.94
	230 elements, $0.6\lambda_0$	-	46.07	48.24	-	82.94	76.82

**Table 5.4** Scan performance of the system with different array element spacings at 30 GHz.

Array type, number of array elements and element spacing ( $\lambda_0 = 1$ cm)		Directivity [dBi]				Efficiency, %			
		Scan angle, deg				Scan angle, deg			
		5	10	15	20	5	10	15	20
The array of modified bow-tie antennas	180 elements, $0.8\lambda_0$	45.67	45.92	42.64	39.23	75.9	81.42	38.99	18.29
	200 elements, $0.7\lambda_0$	45.79	46.05	42.79	39.42	78.1	83.78	40.41	19.11
	230 elements, $0.6\lambda_0$	46.09	46.34	43.16	39.87	83.6	89.68	43.96	21.16

According to Table 5.3, there is a trade-off between the size of the feed array, the number of antennas, and the realized efficiency. Higher directivities and reflector efficiencies are obtained by using a smaller array grid and more array elements. Nevertheless, the difference is not more than a few percent between the array of 180 and 230 elements. At the same time, we know that wideband properties are only realizable for the array with  $0.8\lambda_0$  element spacing. Thus, the slight directivity drop is probably an acceptable price to pay in the design process of a complete FPA system. Overall, the achieved directivity with our array of modified bow-tie antennas is lower than for an array with ideal horn antennas. However, it is important to notice that for an array of horn antennas even a  $0.8\lambda_0$  element spacing is physically not possible to realize in practice since the horn antennas are simply too large. Thus, the results for the array of horn antennas from [23] should be seen as an orientation point. The results obtained with the modified bow-tie antennas are more realistic and include mutual coupling and realistic embedded element patterns. However, only a few percent degradations in efficiency is observed when compared to an array of horns.

The results of Table 5.4 demonstrate that the best directivity is achieved with scan angles

around  $10^\circ$ . This could be explained by the fact that the reflector is optimized for operation within  $\pm 20^\circ$  scan in the azimuth plane and the  $10^\circ$  scan angle is in the middle of this range. In addition, the embedded element patterns of the array elements also have maxima between  $10^\circ$  and  $30^\circ$  (see also Fig. 5.52). As a result, the directivity performance with the proposed modified bow-tie antennas could be better at some scan angles as compared to the case of horn antennas.

### 5.2.5.2. Equivalent phased-array configuration

As a final step, it is interesting to compare our realized FPAs performance with conventional phased-arrays configurations. For that purpose, we have created equivalent phased-array configurations with modified bow-tie antennas for three different element spacings ( $0.6\lambda_0$ ,  $0.7\lambda_0$ , and  $0.8\lambda_0$ ). The array with  $0.8\lambda_0$  element spacing has 180 elements, with  $0.7\lambda_0$  – 200 elements, and with  $0.6\lambda_0$  – 230 elements. The far-field pattern of each array element has been simulated in the CST [139] and then imported to GRASP [39]. In GRASP it is possible to combine the fields of all array elements with the proper phase to form the phased array. Using the feed power normalization, we can obtain the reflector directivity. This way the directivity is including all effects of mutual coupling between array elements and realistic element patterns.

Fig. 5.99, Fig. 5.100, and Fig. 5.101 show the performance at broadside over the frequency band, for  $0.8\lambda_0$ ,  $0.7\lambda_0$ , and  $0.6\lambda_0$  element spacing, respectively. Fig. 5.102, Fig. 5.103, and Fig. 5.104 show the performance in the case of scanning up to  $20^\circ$ . Table 5.5 and Table 5.6 summarize the realized directivity and array efficiencies. In all cases, a uniform tapering was used.

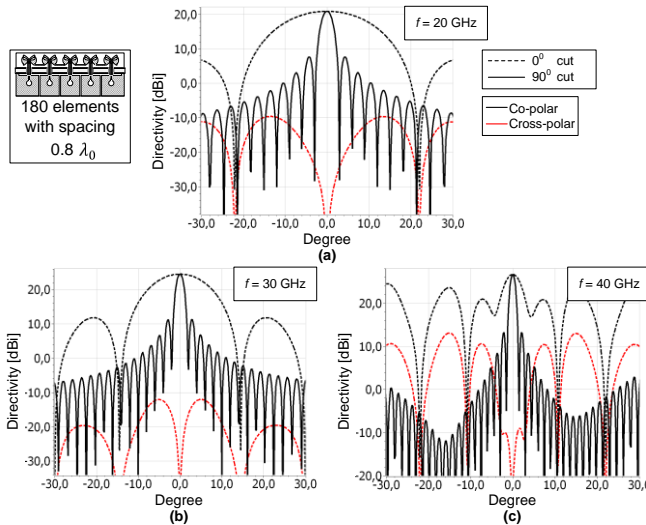


**Figure 5.99.** Directivity pattern of the equivalent phased array of modified bow-tie antennas with element spacing of  $0.8\lambda_0$  at 30 GHz for (a)  $f = 20$  GHz, (b)  $f = 30$  GHz, (c)  $f = 40$  GHz.

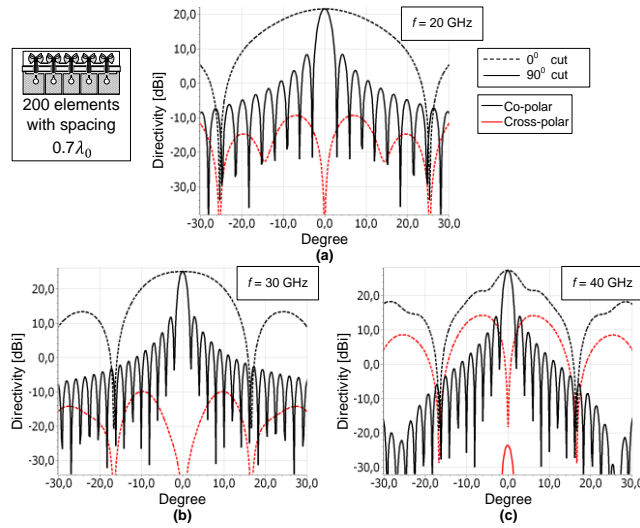


**Figure 5.100.** Directivity pattern of the equivalent phased array of modified bow-tie antennas with element spacing of  $0.7\lambda_0$  at 30 GHz for (a)  $f = 20$  GHz, (b)  $f = 30$  GHz, (c)  $f = 40$  GHz.

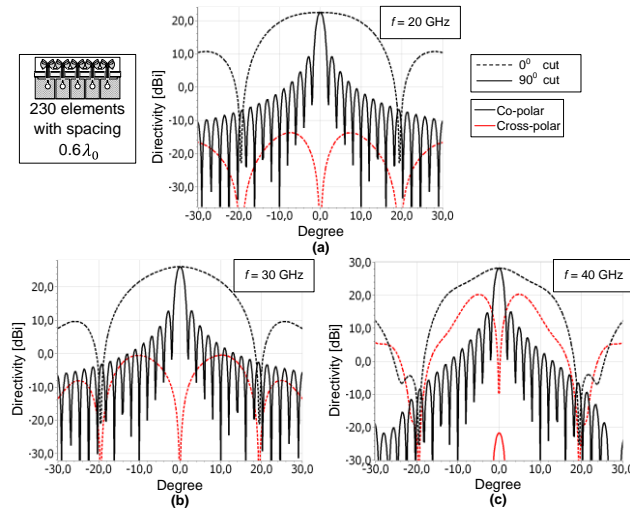


**Figure 5.101.** Directivity pattern of the equivalent phased array of modified bow-tie antennas with element spacing of  $0.6\lambda_0$  at 30 GHz for (a)  $f = 20$  GHz, (b)  $f = 30$  GHz, (c)  $f = 40$  GHz.

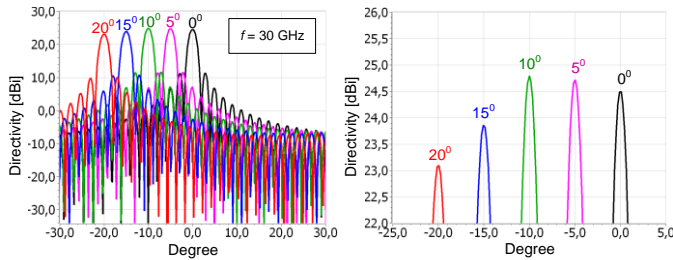


**Figure 5.102.** Directivity pattern of the equivalent phased array of modified bow-tie antennas with element spacing of  $0.8\lambda_0$  for different scan angles,  $f = 30$  GHz.

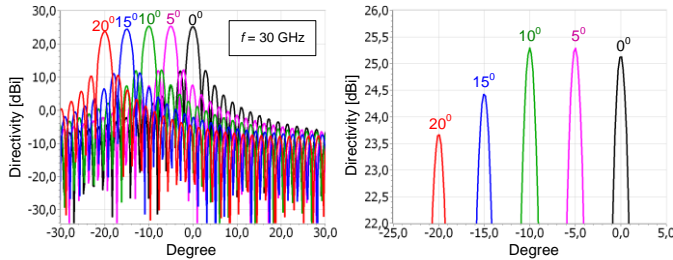


**Figure 5.103.** Directivity pattern of the equivalent phased array of modified bow-tie antennas with element spacing of  $0.7\lambda_0$  for different scan angles,  $f = 30$  GHz.

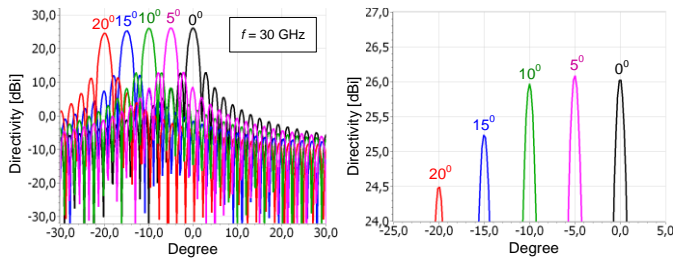


**Figure 5.104.** Directivity pattern of the equivalent phased array of modified bow-tie antennas with element spacing of  $0.6\lambda_0$  for different scan angles,  $f = 30$  GHz.

The investigated phased arrays have the same dimensions and number of elements as the feeds of the studied FPAs, 28 cm in length and 4 cm in width. The main difference when comparing a phased array with an FPA is the directivity level, which is at least 20 dB higher for FPAs.

**Table 5.5** Performance of the equivalent phased array of modified bow-tie antennas.

Array type, number of array elements and element spacing ( $\lambda_0 = 1$ cm)		Directivity [dBi]			Efficiency, %		
		Frequency, GHz			Frequency, GHz		
		20	30	40	20	30	40
A phased array of modified bow-tie antennas	180 elements, $0.8\lambda_0$	20.88	<b>24.49</b>	26.69	78.61	80.25	74.82
	200 elements, $0.7\lambda_0$	21.5	<b>25.12</b>	27.3	81.65	83.48	77.67
	230 elements, $0.6\lambda_0$	22.4	<b>26.02</b>	28.21	87.36	89.39	83.27

**Table 5.6** Scan performance of the equivalent phased array of modified bow-tie antennas at 30 GHz.

Array type, number of array elements and element spacing ( $\lambda_0 = 1$ cm)		Directivity [dBi]				Efficiency, %			
		Scan angle, deg				Scan angle, deg			
		5	10	15	20	5	10	15	20
Phased array of modified bow-tie antennas	180 elements, $0.8\lambda_0$	24.72	24.79	23.86	23.09	86.38	93.93	84.58	82.73
	200 elements, $0.7\lambda_0$	25.28	25.29	24.42	23.66	88.58	94.94	87.06	85.47
	230 elements, $0.6\lambda_0$	26.09	25.97	25.24	24.49	92.73	96.82	91.72	90.68

For an array with 180 elements, the highest directivity is observed at scan angles around  $10^\circ$ , with 200 elements – around  $5^\circ$  and  $10^\circ$ , and for 230 elements – around  $5^\circ$ . This is related to the embedded element pattern shape. The overall directivity drop is about 1.5 dB within the scan range of  $20^\circ$  while for FPAs it has been around 6 dB. This of course shows that the overall scan performance of an FPA is still less productive than traditional phased arrays. Nevertheless, this drop is fully compensated by the significantly higher directivity of PFAs.

According to Table 5.5 and Table 5.6, like in the case of an FPA, there is a trade-off between the size of the feed array, the number of antennas, and the realized efficiency. Higher directivities and efficiencies are also obtained by using a smaller array grid and more array elements. As we can observe in Table 5.5 and Table 5.6, the phased arrays efficiencies are higher than the corresponding reflector efficiencies (see Table 5.3 and Table 5.4). So, this means that for a phased array a sufficient number of array elements is more crucial than improving the mutual coupling between array elements or the shape of the embedded element patterns. For PFAs those factors are important as well, but the overall beamforming is much more complicated. As a result, PFAs have more difficulties to achieve a wideband performance. Thus, the actual reflector aperture efficiency could be sacrificed by using an array with wider element spacing. This wider element spacing in combination with our optimized reflector allows to achieve an active bandwidth of more than 20 GHz in the K and Ka-band for a  $20^\circ$  scan range.

### 5.2.6. Conclusions

Future FPA antenna systems require a wide bandwidth, a wide scan range, and a high level of integration and co-optimization between the reflector system and array feed. In this chapter, an array design with wideband capabilities is proposed and investigated against well-known antenna designs. The factors that determine the performance are investigated and analyzed for the proposed design. A large number of prototypes have been manufactured and tested to support the design ideas. The proposed design using modified bow-tie antennas allows us to achieve good active matching properties over a frequency band of more than one octave. At the same time, other relevant characteristics, like a high total radiation efficiency, phase-center stability, and reflector aperture efficiency remain at an acceptable level. In addition, a novel reflector design was proposed to realize wide-scan FPAs. This concept was tested in combination with the designed array feed. The demonstrated simulations and measurements fully support the feasibility studies of both reflector and array concepts of [33], [31], and [23].

The presented connected array of modified bow-tie antennas achieves an active impedance matching bandwidth (based on the TARC) of more than 20 GHz within the scan range of

$\pm 20^\circ$  with the complex offset double-reflector configuration. This wideband performance has been achieved with only a relatively small sacrifice on the reflector aperture efficiency. The demonstrated tradeoff between array element spacing and FPA far-field properties allows to satisfy the TARC requirements. Both simulation and measurement demonstrate a good agreement of the scattering matrix and far-field patterns for a single antenna, for arrays, and for reflectors in combination with the arrays.

We have also shown that an FPA system based on our complex offset double-reflector fed by an array of 200 connected modified bow-tie antennas outperforms a conventional phased array using the same type of element for a scan range of  $\pm 20^\circ$ .

# CHAPTER SIX

## 6. FPA DEMONSTRATOR<sup>1,2</sup>

---

### Summary

A wide-scan and broadband focal-plane array (FPA) concept is introduced that provides high antenna gain and effective isotropic radiated power (EIRP) with electronic beam steering within a relatively large field-of-view (FoV) up to  $\pm 20^\circ$ . The antenna uses a bi-focal double-reflector concept that optimizes the illumination of the focal-plane region. In this way, we have reduced the required size of the feed array and have maximized the number of simultaneously active array elements. By using a photonics beamformer, a broadband system for the 20 – 40 GHz band can be created with a fiber-based interface to a central processing unit. This hybrid antenna system proves to be a very interesting concept for future 5G and beyond-5G millimeter-wave base stations, two-way satellite communication systems, and point-to-point wireless backhaul systems. A silicon BiCMOS low noise amplifier and a photonic integrated circuit for the optical beamformer have been developed and integrated into the overall system. A system-level demonstrator was developed and experimentally validated in receive mode. Our concept provides an antenna gain of more than 40 dBi over a FoV of  $\pm 15^\circ$  at 28.5 GHz.

### 6.1. Introduction

The continuously growing need for higher data rates in wireless communications drives new applications into the millimeter-wave (mm-wave) frequency domain. Emerging applications include base stations for 5G wireless communication, two-way satellite communication, point-to-point wireless backhaul, and commercial radar [1], [2], [3], [4]. These mm-wave applications would benefit from using advanced phased-array technologies. Phased arrays offer the ability of fast electronic beam-steering, multi-beam operation, adaptive pattern shaping and MIMO (Multiple-Input-Multiple-Output) capabilities. However, traditional full phased-array solutions have major limitations: they are far too expensive and have a very high-power consumption due to the low efficiency of state-of-the-art mm-wave integrated circuits [5], [6]. In addition, phased arrays have high complexity and

<sup>1</sup>Current chapter is published as a journal paper: Smolders, A.B., Dubok, A., Tessema, N.M., Chen, Zhe, Al-Rawi, A.N.H., Johannsen, U., Bressner, T.A.H., Milosevic, D., Gao, H., Tangdiongga, E., Gerini, G., Baltus, P.G.M., Geurts, Marcel & Koonen, A.M.J., "Building 5G millimeter-wave wireless infrastructure: wide-scan focal plane arrays with broadband optical beamforming," IEEE Antennas and Propagation Magazine, 2018, and included here in its entirety without any changes.

<sup>2</sup>Only paragraph 6.3 of this chapter is written by the thesis author and the overall chapter is used to demonstrate the system concept.

provide a limited operational bandwidth [7]. An alternative to phased-arrays is the focal-plane array (FPA), which is a hybrid solution that combines the best of both worlds: the robustness, low cost and large bandwidth of conventional reflector-based antenna systems and the flexibility and adaptivity of phased-arrays. However, conventional FPA systems [176], [177] have a limited field-of-view (FoV) and are often used in narrow-band applications. In this chapter, we will investigate how these limitations can be overcome.

Fig. 6.1 shows two target applications of FPAs. Base stations for mm-wave 5G should provide massive-MIMO capabilities and should be able to cover urban macro-cell sizes up to 300 m [2]. This requires a large antenna gain in order to overcome the non-line-of-sight (NLOS) propagation loss, which can be as high as 140 dB. Fig. 6.1(a) shows an illustration of such a base station utilizing the FPA concept, providing high antenna gain and a highly effective isotropic radiated power (EIRP). The base station provides omnidirectional coverage in the azimuth (horizontal) direction and limited beam scanning in elevation. Note that the  $360^\circ$  azimuth coverage could be split into several sections. Another application that is considered is Ka-band two-way satellite communication as illustrated in Fig. 6.1(b). In this case, multiple satellites operating at different frequency bands can be addressed simultaneously. In order to obtain a wide instantaneous bandwidth, we propose to use a novel optical beamforming system that can be controlled by the home communication controller.

In order to explore the limitations of FPAs, we have developed a system demonstrator with the following set of challenging design goals:

- large operational bandwidth between 20-40 GHz,
- wide FoV with a scan range of  $\pm 20$  degrees in the azimuth direction (horizontal plane),
- limited FoV in the elevation plane,
- antenna directivity larger than 40 dBi with an overall efficiency of 80%,
- use of low-cost silicon BiCMOS technology to realize the RF electronics,
- use of integrated photonic chips to realize a compact wideband optical beamformer that is connected to a central processing unit using low-cost optical fibers.

In this way, we comply with the requirements of two-way satellite communications. In addition, the demonstrator can be used to cover a sector of an mm-wave 5G base station. The use of optical fibers to connect the remote antenna station to the central site also allows us to use this concept in future beyond5G systems utilizing distributed massive MIMO (DM-MIMO) in which multiple remote antenna stations within a single urban macro-cell are used to further enhance the capacity of the wireless network [178].

In this chapter, we will describe the design and experimental validation of the complete antenna system including FPA, feed array with integrated silicon electronics, and an optical beamformer using photonic integrated circuits which are connected to a remote central processing unit by means of optical fibers. The demonstrator that was realized operates in receive mode.

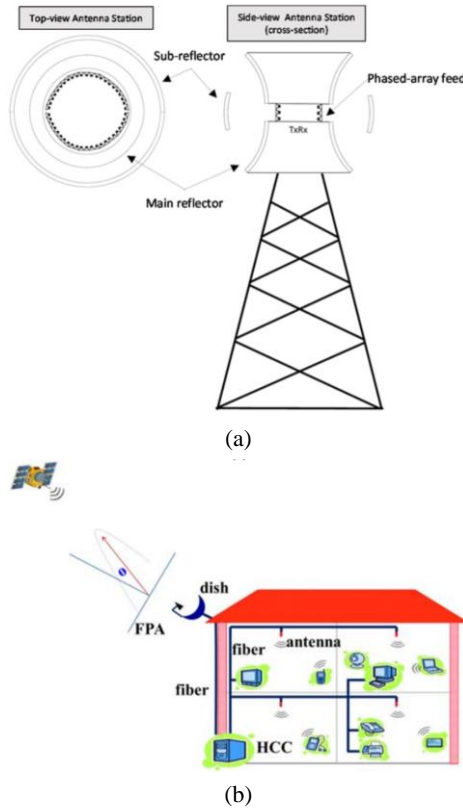


**Figure 6.1.** Examples of applications (a) base station for 5G mm-wave (massive) MIMO, (b) Ka-band two-way satellite communication. Beamforming to multiple satellites is established with an FPA with optical beamforming. The control of the FPA is provided by the home communication controller (HCC).

The outline of this chapter is as follows. In Section 6.2, the overall system concept is introduced. In Section 6.3, the scan limitations of FPA systems are explored. A double-reflector bi-focus concept is proposed that provides a wide FoV. Section 6.4 introduces the optical beamformer for which a new photonic integrated circuit was developed using ring resonators. Section 6.6 is devoted to the design of BiCMOS low-noise amplifiers with a large dynamic range and integrated with a 4x1 wideband linear feed array. Finally, in Section 6.7, the measurement results of the system demonstrator are presented.

## 6.2. Overall system concept

The basic set-up of the overall antenna system is illustrated in Fig. 6.2. It consists of an FPA antenna built up from a main reflector with diameter  $D$  and a phased-array feed located at a distance  $F$  from the main reflector. The incident field illuminates the reflector. As a result, a focused field distribution will be generated in the focal region of the array. A phased-array feed receives this incident field. In Fig. 6.2(a), the basic symmetric parabolic reflector configuration is shown. Later on in this chapter, we will extend this concept by adding a shaped sub-reflector and shape the offset main reflector in order to optimize the FoV. In receive mode (Fig. 6.2(b)), each of the  $N$  antenna elements in the phased-array feed is

connected to a low-noise amplifier (LNA) and external modulator (EM) that provides amplification and conversion to the optical domain. The optical beamformer generates  $M$  beams simultaneously by using  $M$  laser diodes of which the emission wavelengths are separately tunable. The phase shifts between the antenna elements are achieved by optical phase shifters, i.e. micro-ring resonators. The phase shift in a micro-ring resonator depends periodically on the wavelength and on the refractive index of the optical micro-ring waveguide [36]. By positioning the wavelength of each tunable laser diode individually on the slope of one of the group delay peaks, a different group delay (and thus phase shift) at each wavelength can be obtained. This allows the simultaneous reception of  $M$  radio beams for which the antenna reception patterns are individually adjustable, by remotely wavelength-tuning the laser diodes in the central site. There is an important note, that the multiple beams are tuned simultaneously. After wavelength de-multiplexing at the central site, individual amplitude weighing of each of the received wavelength channels is done to provide the optimal conjugate match of the incident field in the focal plane of the FPA [29]. In transmit mode (Fig. 6.2(c)), multiple beams are generated by using multiple tunable optical wavelengths.

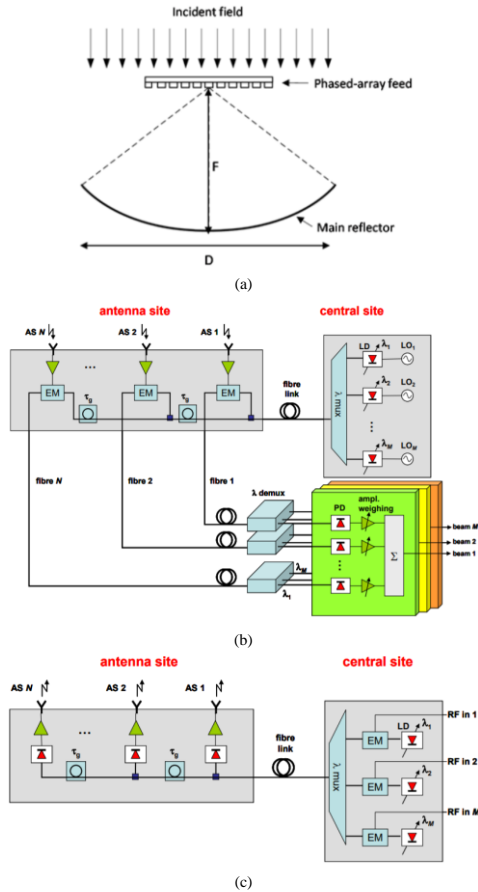


**Figure 6.2.** Overall system concept (a) basic form of a single-dish FPA antenna, (b) optical beamforming network in receive mode consisting of  $N$  antenna nodes that generate  $M$  simultaneous beams, (c) optical beamforming network in transmit mode generating multiple beams by using multiple tunable optical wavelengths.

### 6.3. Broadband wide-scan focal-plane arrays

The FoV of a classical parabolic prime-focus FPA (Fig. 6.2(a)) is very limited. Only a very small number of antenna elements in the phased-array feed are illuminated simultaneously. In [162] it was shown that for a prime-focus FPA with  $F/D = 0.6$ , only 3.1% of all active array elements are used at the same time for a scan range up to  $3^\circ$  and aperture efficiency of 80%. In the case of transmitting, this would result in a low EIRP and would exclude the use of low-cost silicon-based RF integrated circuits. For even larger scan-angles the situation becomes even more dramatic. A way to improve this is by using a double-parabolic reflector FPA as shown in Fig. 6.3. The double-reflector configuration of Fig. 6.3(a) significantly improves the number of simultaneously active elements as compared to a single-reflector FPA. For a configuration with  $F_m/D_m = 0.6$  up to 9.1% of the array elements are active at the same time when scanning up to  $3^\circ$  [162]. However, a major drawback of the double-reflector configuration of Fig. 6.3(a) is the so-called magnification factor  $M_a$  [38], which states that the incident angle seen by the phased-array feed is a factor  $M_a$  larger as compared to the incidence angle  $\theta_0$ . As a result, the required number of array elements to support a certain scan range is much larger.

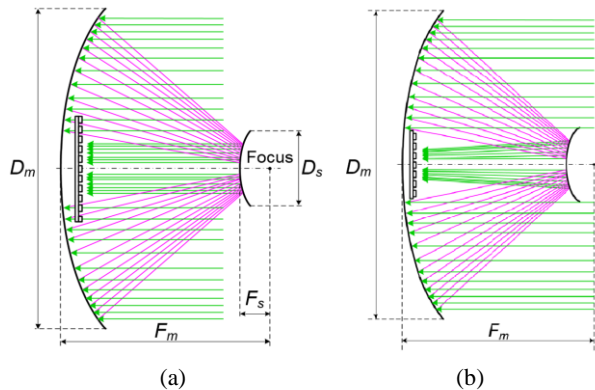


**Figure 6.3.** Double-reflector FPAs with (a) symmetrical double-parabolic reflector, (b) optimized ring-focus double reflector.

This situation can be improved by optimizing the shape of the sub-reflector. In this way, up to 22.7 % of the array elements are active simultaneously for scan angles up to  $3^\circ$ . For a configuration operating at 30 GHz, this would require an array feed size of about 115 mm, with element spacing of  $\lambda_0/2=5$  mm at this frequency. However, our application requires a much larger FoV. This can be achieved by using a more complex double-reflector system with a shaped bi-focus sub-reflector as illustrated in Fig. 6.4. An offset configuration is used to avoid blocking from the relatively large reflector. The required array size for scanning up to  $\pm 20^\circ$  with an aperture efficiency of 80% is now 280 mm at 30 GHz of which 21.4% of the array elements are active simultaneously to create a single beam.

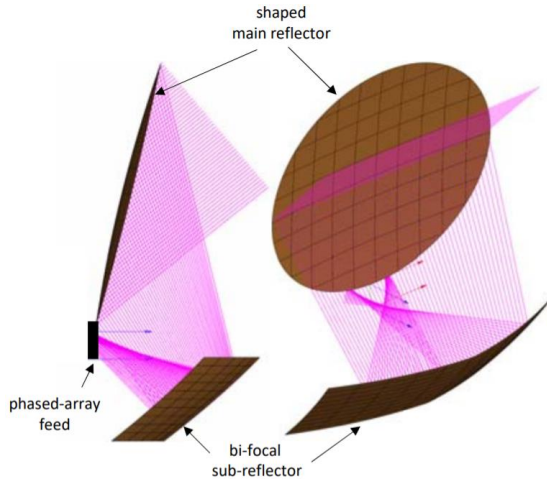


**Figure 6.4.** Optimized offset double-reflector FPA with a bi-focus shaped sub-reflector providing a scan range up to  $20^\circ$ . The wave trajectory of an incident wave is shown. Key dimensions of optimized configuration are: main reflector size is 80 cm, sub-reflector size is 83 cm by 25.5 cm, the focal length of sub-reflector  $F_s=79$  cm, and offset between main and sub-reflector  $z_{off}=10$  cm.

#### 6.4. Optical beamforming using ring resonators

As discussed in section 6.2, an optical beamforming network provides wideband beamforming control of an FPA antenna system with the capability to create multiple beams by using multiple wavelengths for the lasers. The optical beamformer utilizes true time delay (TTD), implemented in a photonic integrated circuit (PIC). The beamforming control is enabled by an optical micro-ring resonator (ORR) which provides a continuously tunable delay via thermos-optic tuning. Thermo-optic tunability in an ORR is enabled via a heater. The schematic structure of a thermally-tunable ORR is shown in Fig. 6.5(a). The heaters generate a phase shift on the waveguide due to thermally induced change in the refractive index.

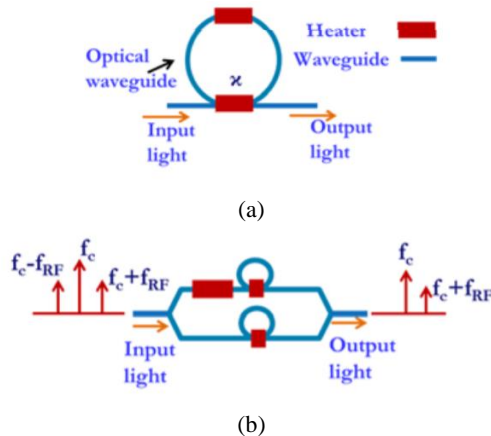


**Figure 6.5.** Schematic of (a) an Optical Micro ring resonator (ORR) (b) Optical Sideband Filter (OSBF).

The principle of operation involves thermal control of the power coupling ratio  $\kappa$  via a heater within the coupling section which controls the amount of power fed into the feedback loop of an ORR [128], [179] - [180]. Accordingly, the amount of time the input light stays inside the ORR is controlled and hence the generated time delay by the optical beamformer is continuously tuned. The relation of the generated time delay in an ORR with  $\kappa$  is graphically illustrated in Fig. 6.6. For decreasing values of  $\kappa$ , increased ORR delay is generated. A second heater on the feedback loop of an ORR enables fine tuning of the ORR delay response. Because of the spectral periodicity in an ORR delay response, several unique delay values can be tuned simultaneously with the use of multiple input wavelengths. This allows generating multiple radio beams via multiple wavelengths in a single ORR [128], [181].

The ORR functionality is supported by an optical sideband filter (OSBF) which converts a double side-band modulated signal into a single side-band signal and band limits the signal. This relaxes the delay bandwidth requirement of an ORR TTD [180]. A typical OSBF implementation is shown in Fig. 6.5(b). Via the use of thermo-optic tunability of its heating elements, the OSBF can be configured to a desired shape.

We realized a four-channel optical beamformer implementation (with four input and four output fibers) based on ORR delay in an integrated circuit. It is fabricated and packaged as shown in Fig. 6.7. The optical beamforming chip is realized in a  $\text{Si}_3\text{N}_4$  integration platform, because of its low-loss and thermo-optic features [128]. The optical chip is transparent only to transverse electromagnetic (TE) polarization. The optical beamformer chip is placed on a PCB for the wire bonding of the DC power-supply contacts pads of the ORR heaters. Embedded arrays of voltage drivers supply a DC voltage for the thermo-optic tuning of the ORRs. The voltage level is controlled on a computer via digital-to-analog (DAC) units. The packaging has a mechanism to stabilize the temperature of the optical beamformer chip via thermoelectric cooling (TEC) controllers. The electro-packaging facilitates system integration of the TTD chip within the optical beamformer system. As a result, the packaged optical beamforming chip is used in the system demonstrator presented in section 6.6.

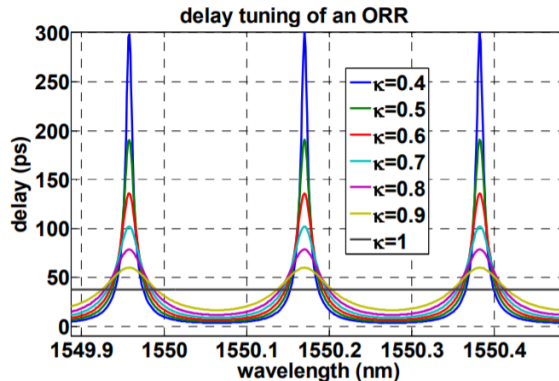


**Figure 6.6.** Simulated group delay response (for an ORR with a free spectral range of 0.21 nm (26.5 GHz)), as a function of power coupling ratio  $\kappa$ .

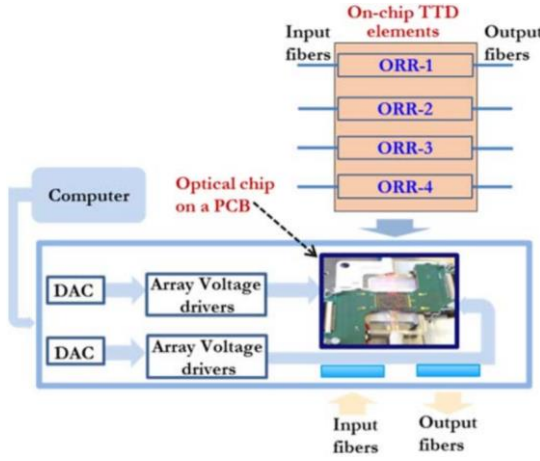


**Figure 6.7.** Electro-optically packaged TTD chip on the Si<sub>3</sub>N<sub>4</sub> platform for a four-channel radio beamformer (with 4 ORRs).

### 6.5. Active phased-array feed using low-noise amplifiers with a large dynamic range

In this hybrid RF-optical system, broadband LNA is one of the bottlenecks. The LNA should provide a low noise figure and high gain over a large operational bandwidth to satisfy the sensitivity and dynamic range requirements. A high power gain of at least 25 dB is required since the LNAs should drive the optical modulators. In addition, the LNA should be realized in low-cost silicon technology to ensure future integration with other analog and digital electronic circuits. Furthermore, the packaged LNA should fit within the array grid spacing that is required in our FPA concept. Fig. 6.8(a) shows a photo of the realized phased-array feed, consisting of four wideband bowtie like antennas [165] - [172] connected to high-gain LNAs which are connected via a rat-race balun to RF cables used to validate the performance of the active 4x1 array. The differential antenna elements are directly matched to the input of the LNA to ensure a low overall noise figure and good power matching. The packaging concept is illustrated in Fig. 6.8(b). The silicon LNA chips and bond wires are covered with black glob-top material as can be observed in Fig. 6.8(a).

The input noise-matching network is the most crucial part of this LNA to ensure both noise matching and power matching. The common-emitter (CE) structure with inductive degeneration and series input inductor is widely used in LNA designs to achieve simultaneous noise- and power matching [182] - [183]. However, the matching condition is only valid within a narrow frequency band if the input matching network only uses a single inductor-capacitor ( $LC$ ) tank. To achieve both broadband power- and noise matching, a dual- $LC$  tank matching method was previously proposed in [184] and implemented in a cascade structure. The equivalent small-signal model of the dual- $LC$  tank matching network is shown in Fig. 6.9, which consists of a shunt tank ( $L1, C1$ ), a series ( $L2, C2$ ) tank, and an equivalent resistance  $R_{EQ}$ . Both shunt and series tanks are resonant at the same radial frequency  $\omega_C$ . The input impedance,  $Z_{IN}$ , can be expressed as a function of the radial frequency  $\omega$  and  $R_{EQ}$ :

$$Z_{IN} = \left[ j\omega C_1 \left( 1 - \frac{\omega_C^2}{\omega^2} \right) + \frac{1}{\left( j\omega L_2 \left( 1 - \frac{\omega_C^2}{\omega^2} \right) + R_{EQ} \right)} \right]^{-1} \quad (6.1)$$

The  $Z_{IN}$  curves are shown in Fig. 6.9 with  $R_{EQ}$  changing from 30 to 70  $\Omega$ . The blue dashed circle indicates the region in which the reflection coefficient ( $\Gamma_{IN}$ ) is below -10 dB. Clearly, the  $S_{11}$  bandwidth is extended when  $R_{EQ}$  is decreased.

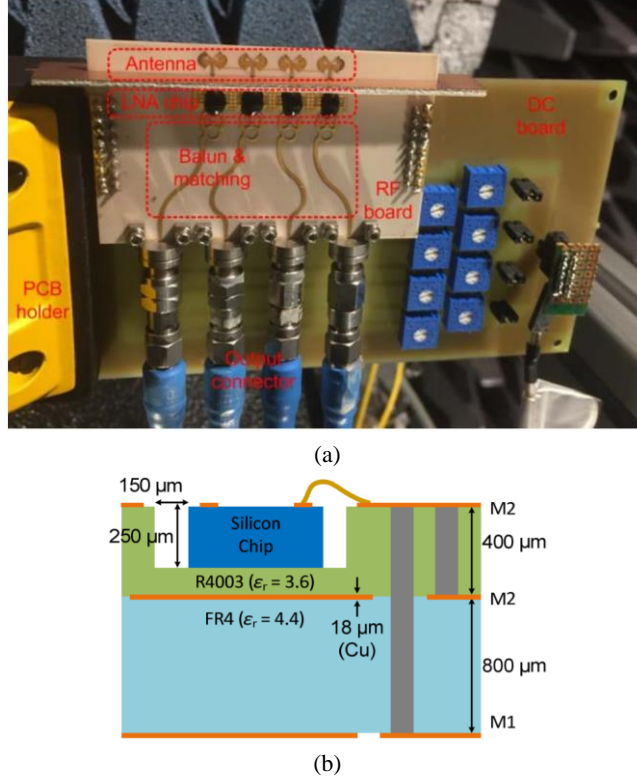


**Figure 6.8.** (a) Photo of the 4x1 linear feed array with SiGe BiCMOS LNAs, (b) cross-section of the packaging concept. The silicon chips and bond wires are covered with black glob-top material.

The dual- $LC$  tank can also be applied for broadband noise matching. The output impedance of the matching network ( $Z_S$ ) is shown in Fig. 6.10. The minimal noise figure of the transistor is achieved under the noise matching condition of  $Z_S = Z_{OPT}$ , where  $Z_{OPT}$  is the optimal noise impedance of the transistor. If  $Z_S = Z_{OPT} = Z_{IN}^*$ , we can realize simultaneous noise- and power matching. For an inductively-degenerated CE structure (Fig. 6.10) with the effect of the load ignored, the input impedance  $Z_{IN}$  and the optimal noise source impedance  $Z_{OPT}$  are found by:

$$Z_{OPT} \approx \frac{\sqrt{g_m R_B / 2}}{\omega(C_{BE} + C_{BC})} + j \left[ \frac{1}{\omega(C_{BE} + C_{BC})} - \omega L_E \right] \quad (6.2)$$

$$Z_{IN} \approx \frac{g_m L_E}{C_{BE}} + R_B - j \left[ \frac{1}{\omega(C_{BE} + M C_{BC})} - \omega L_E \right] \quad (6.3)$$

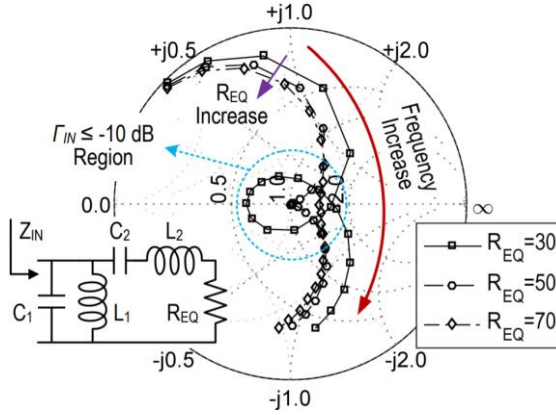


**Figure 6.9.** Simulated  $Z_{IN}$  of a dual-LC tank matching network for different values of  $R_{EQ}$  (30/50/70  $\Omega$ ). Frequency increases from 10 to 50 GHz by 5 GHz per step. The dashed circle indicates the region of  $\Gamma_{IN} < -10$  dB.

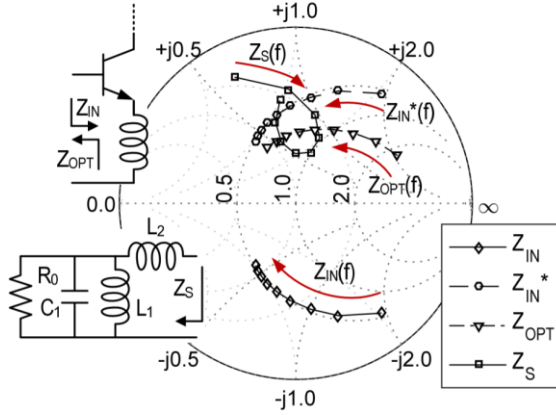


**Figure 6.10.** Simulated input impedance  $Z_{IN}$  (and its conjugate  $Z_{IN}^*$ ) and the optimal noise impedance  $Z_{OPT}$  of an inductively degenerated CE structure and simulated output impedance  $Z_S$  of the dual-LC tank matching network.  $R_0$  is the source resistance. Frequency increases from 10 to 50 GHz by 5 GHz per step.

where  $C_{BE}$  and  $C_{BC}$  represent the base-emitter and base-collector capacitances,  $R_B$  is the equivalent base resistance,  $g_m$  is the trans-conductance,  $L_E$  is the degeneration inductance and  $M$  is a coefficient related to the Miller effect. The difference between  $Z_{IN}$  and  $Z_{OPT}$  is mainly due to  $R_B$  and  $C_{BC}$  [185], whereas it is alleviated by  $L_E$ . Simulation results are provided in Fig. 6.10, showing the curves of  $Z_S$ ,  $Z_{IN}$ , and  $Z_{OPT}$  versus frequency. Obviously,  $Z_{IN}$  and  $Z_{OPT}$  deviate from each other at all frequencies, thus there is no ideal case of a simultaneous power and noise match.  $Z_S$  crosses both  $Z_{IN}$  and  $Z_{OPT}$  twice at different frequencies, which indicates that  $Z_S$  provides a wideband matching situation.

The final design of the LNA was realized in a silicon-germanium (SiGe) BiCMOS technology [186] and was experimentally validated on a probe station using a fully calibrated four-port vector network analyzer setup (for S-parameter measurement) and a two-port spectrum analyzer for noise figure and linearity measurements. The results are summarized and compared with other LNAs in Table 6.1. We can conclude that this LNA can support this

wireless-optical link by providing a power gain of 28.5 dB and a noise figure of 3.1 dB with an 8 GHz bandwidth. To cover a broader bandwidth, two or more LNAs should be put in parallel.

**Table 6.1.** Performance summary and comparison of the BiCMOS LNA chip.

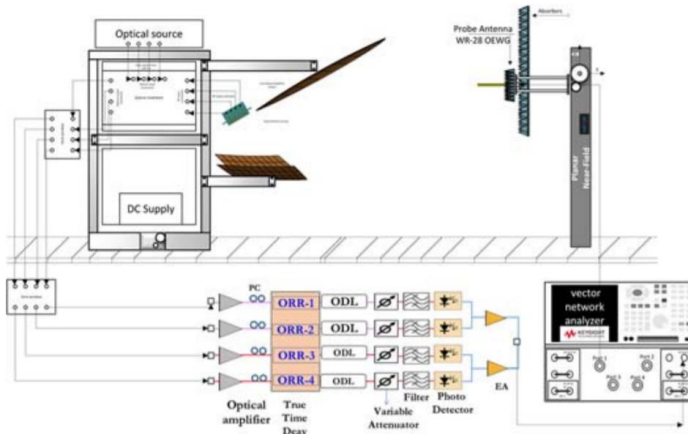
	This work	TMTT 2015 [187]	ASSCC 2016 [184]	MWCL 2007 [185]
Gain (dB)	28.5	26	10.5	23.5
3-dB Gain BW (GHz)	29-37	25-34*	17-43	31-35*
NF (dB)	3.1-4.1	2.1-3.5	2.5-4.0	2.6-3.2
$S_{11} < -10$ dB BW (GHz)	24-40	N/A	17-50	26-40*
IIP3 (dBm)	-12.5 to -7	-5@31GHz	1.8 to 5.9	-19.5@30GHz
Power (mW)	80	134	24	11
Technology	0.25 $\mu$ m SiGe	0.25 $\mu$ m SiGe	0.25 $\mu$ m SiGe	0.12 $\mu$ m SiGe

### 6.6. System demonstrator

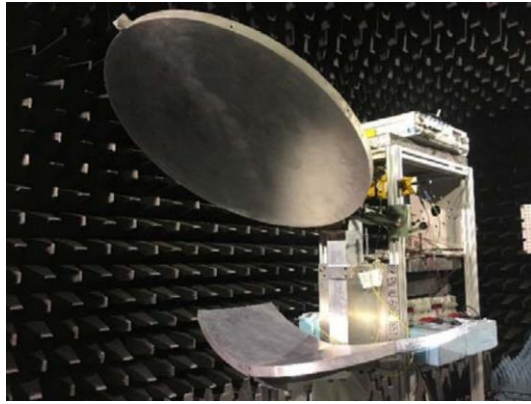
The overall system demonstrator is shown in Fig. 6.11. It operates in receive mode and consists of the optimized offset double-reflector FPA with the 4x1 active phased-array feed of Fig. 6.8(a) which is connected to the four-channel optical beamformer. The feed array is positioned in the center of the focal plane. Measurements have been performed in the near-field test facility of the Eindhoven University of Technology.

A detailed block diagram of the optical beamformer setup is shown in Fig. 6.12. The first part of the optical beamformer (consisting of lasers and the optical Mach-Zehnder (MZM) modulators) is placed inside the anechoic chamber and is connected with the rest of the optical beamforming system outside the anechoic chamber via a 10 meter optical fiber link.

The output of two lasers tuned at  $\lambda_1$ :1545.398 nm and  $\lambda_2$ :1546.033 nm are used to supply a continuous wave (CW) light input to the four optical beamformer channels. The output of the four active antenna elements supplies four 28 GHz signals input to the optical beamformer. The conversion of the RF signals from each antenna element into the optical domain is realized using separate MZMs via intensity modulation. The optical signals are then transported outside of the anechoic chamber via the four 10 meter optical fiber links. Then, optical amplifiers (OAs) compensate for any optical loss in the modulators. Erbium-Doped Fiber Amplifiers are used as OAs. Polarization controllers (PC) are used to align the light into TE-mode prior to being input into the packaged TTD chip for efficient fiber-to-chip coupling. The thermo-optic tuning of the ORRs is used to control the generated time delay of the optical beamformer as explained in section 6.4. The measured delay versus heater voltage is shown in Fig. 6.13. Any amplitude imbalance is controlled by variable power attenuators (VAtt). After further optical amplifications and double side-band to single side-band conversion via two optical filters, a 2x1 optical combination of the signals is used to generate 2x1 beamforming. After photodetection, a power combiner is used to generate the 4x1 beamformer output.



(a)



(b)

**Figure 6.11.** System demonstrator in the near-field scanner antenna test facility. It consists of a wide-scan double-reflector FPA with a 4-element active phased array feed (see Fig. 6.8(a)) connected to the optical beamformer. This antenna system is connected to a remote central processing unit using optical fibers. The main reflector size is 80 cm, sub-reflector size is 83 cm by 25.5 cm. The focal length of sub-reflector  $F_s = 79$  cm.

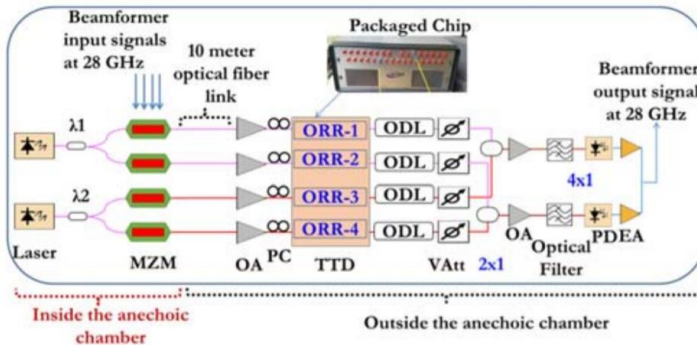


**Figure 6.12.** Optical beamformer setup in the system demonstrator (MZM: Mach-Zehnder modulator, OA: optical amplifiers, ODL: optical delay lines, Vatt: variable attenuator, PD: photo-detectors, EA electrical amplifiers).

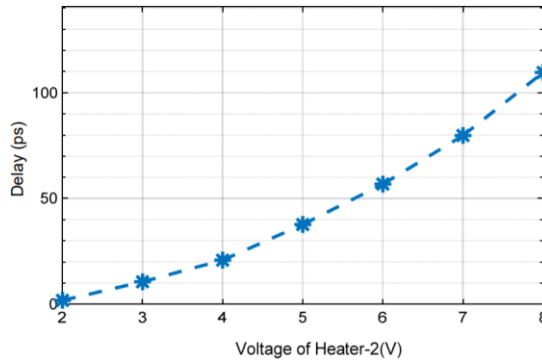


**Figure 6.13.** Measured single-channel delay versus thermo-optic control voltage of the optical beamformer measured in the demonstrator set-up.

We have measured the antenna far-field patterns of the single channels and compared the response with our simulation model. Fig. 6.14 shows the measured antenna pattern at 28 GHz for a single channel. Clearly, the bi-focal behavior of the double-reflector FPA can be observed. The somewhat higher measured sidelobes are due to the large construction required to accommodate the supporting equipment of the optical beamformer (see Fig. 6.11(b)). In a full-operating system, we would require about 200 active array elements in order to cover the entire scan range of  $\pm 20^\circ$ . Fig. 6.15 shows the predicted antenna gain of our system. Clearly, scanning up to  $\pm 15^\circ$  can be done with only a limited loss in gain. Further optimization of the double-reflector FPA is required to improve the performance at larger scan angles.

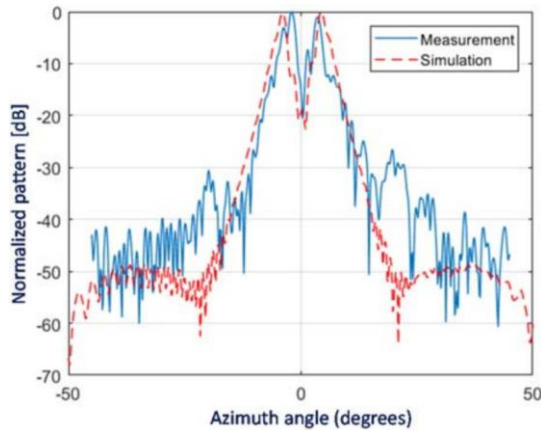


**Figure 6.14.** Measured far-field antenna pattern of a single-channel of the complete demonstrator system at the output of optical beamformer, frequency is 28.5 GHz.

## 6.7. Conclusions and future research directions

It is shown that it is possible to use focal-plane-arrays with a high antenna gain for beam-steering with a relatively large field-of-view up to  $\pm 20^\circ$ . By using an optical beamformer, a wideband system for the 20-40 GHz band can be created with a fiber-based interface to a central processing unit. This hybrid antenna system proves to be a very interesting candidate to be used in future 5G and beyond-5G mm-wave base-stations and in two-way satellite

communication systems. We have developed integrated circuits for the most critical components in our system, the low-noise amplifier with high gain and the optical beamformer chip using ring-resonators. A system-level demonstrator was developed that operates in receive mode. Experimental results provide a good correlation with the predicted performance.

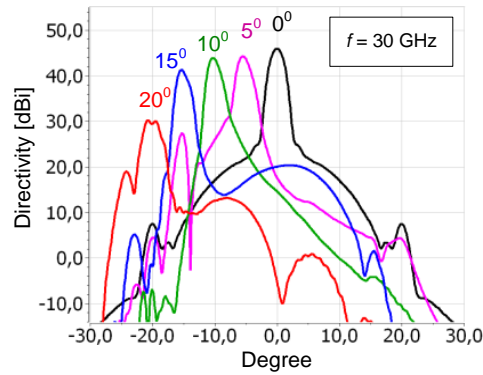


**Figure 6.15.** Predicted directivity of the double-reflector FPA when using a feed-array with 200 active elements.

# CHAPTER SEVEN

## 7. FOCAL-PLANE ARRAYS WITH IMPROVED SCAN CAPABILITIES<sup>1</sup>

---

### Summary

This chapter investigates the limits of focal plane array technology by studying a double-reflector antenna system with wide-angle scan capabilities. The proposed reflector configurations are analyzed in terms of effective isotropic radiated power (EIRP) maximization, minimization of the required total number of array elements for a wide-scan range, and the highest number of simultaneously active array elements of the phased-array feed. Presented configurations have capabilities to operate in the scan range up to  $\pm 30^\circ$  in azimuth and  $\pm 3^\circ$  in elevation. It has been demonstrated how different optimizations could allow to build systems with varying performance in terms of the key operation parameters, like array size, effective isotropic radiated power (EIRP), and the number of active array elements. A detailed analysis is provided that demonstrates the potential applicability of this concept in future millimeter-wave applications.

### 7.1. Introduction

Focal-plane arrays (FPAs) form a promising antenna technology allowing to combine the benefits of reflector-based systems that provide high antenna directivities and phased-arrays which are traditionally used for multi-beam and electronic beam-scanning applications. As a result, FPAs are widely used in radio astronomy [8], satellite and point-to-point communications [9], and low-cost Ka-band (30-40 GHz) multi-function radars. An interesting area of research is to investigate if FPAs can be used to realize base stations (also referred to as remote radio units) for future millimeter-wave (mm-wave) wireless communications infrastructure to meet the demands of 5G and beyond.

One of the main limiting factors of existing solutions for mm-wave 5G base stations is the limited range and insufficient power budget due to the lack of system directivity [16], [17]. This leads to the necessity to use a huge number of array elements when using traditional phased array based systems. The FPA concept could solve those issues if it would be possible to design FPA systems with wide-scan capabilities. The proposed concept should demonstrate improved performance compared to the traditionally used phased arrays in terms of required array elements.

<sup>1</sup>Current chapter is published as a journal paper: Dubok, A.; Smolders, A.B., "Focal-Plane Arrays with Improved Scan Capabilities," IEEE Antennas and Propagation Magazine, 2022, and included here in its entirety without any changes.

Traditionally, reflector systems have limited scanning potential and are dedicated to applications that required high directivity within an extremely narrow angular section. Classical reflectors focus the received wavefront on a relatively small spot in the focal plane. Multi-beam operation with such reflectors is normally done by placing a few separate feeds in the focal plane. This approach only works well over a relatively small angular range, since the point in the focal plane on which the energy is focused deviates strongly with increasing offset angle [18], [19], even for small offset angles w.r.t. broadside.

The use of arrays as feeds for reflector systems allows to scan the main beam over a wider angular range. At the same time, the focusing properties of traditional reflectors significantly deteriorate during scanning. As a result, only a small number of active array elements are typically used in the focal plane [18], [21], [22], [23]. This limits the number of simultaneously available beams or scan range [24], [25] and limits the achievable effective isotropic radiated power (EIRP) [26], [27], [28]. At the same time, the required array size grows dramatically with increased scan range requirements. Nevertheless, the array feed could compensate for the reflector defocusing to achieve a high level of EIRP over the entire scan range. At the same time, mutual reposition of the reflector and array feed, the so-called axial displacement of the array, allows to increase in the number of involved array elements within the required scan range [29]. Moreover, the previously presented paper [23] demonstrates that it is possible to optimize the scan performance of FPAs and to improve its scan capabilities. In [23] we have investigated a complex offset double-reflector system as illustrated in Fig. 7.1 and Fig. 7.2, which provides a scan range of  $\pm 20^\circ$  in the azimuth plane. Our model uses a geometrical optics (GO) approach, which applies Snell's law according to [153], [154] and [155]. When we describe the reflector surface as a mathematical function and divide the surface into a finite number of points, it is possible to find the normal at each point of the reflector. Based on Snell's law, the reflected wave in each reflector point can be calculated. In this way, the field distribution in the array plane can be determined, resulting in a cost-function used in our optimization process.

In this chapter we will bring the concept of [23] to the next level by investigating the following research challenges:

- investigate the maximum achievable scan range that FPA systems can provide, in particular for the double-reflector model with wide-scan capabilities,
- decrease the beam deviation in the focal plane region during scanning,
- investigate the most crucial factors of wide scanning FPAs,
- explore configurations with a wide illumination area of the array to maximize the EIRP,
- develop a wideband FPA system, operating over a wide operational bandwidth in K- and Ka-band between 20-40 GHz.

Similar to [23], we will work at a frequency of 30 GHz. It is important to note that the results of array size minimization are not only related to a certain scan range, but also to the reflector sizes. It is obvious, that a larger main reflector could provide a higher directivity, but it will require a larger array as well.

The structure of the chapter is as follows. Section 7.2 describes the concept of a complex offset double-reflector model optimized for different optimization goals. The situation with

sub-reflectors is more complicated and is discussed in section 7.3 where we will show reflector optimization results for a minimum array size for different sizes of the sub-reflectors. Both the length and height of the sub-reflectors have been varied for those optimizations. The last section 7.4 discusses the most challenging optimization of the required array size for two-dimensional scanning with fixed sizes of the reflectors. In addition to the previously used azimuth scan range up to  $\pm 30^\circ$ , an additional elevation scan range up to  $\pm 3^\circ$  is demonstrated.

## 7.2. Double-reflector antenna with improved scan capabilities

The traditional problems for FPAs with a wide-scan range are twofold: (1) we need to use a relatively large array to compensate for the beam deviation while scanning; (2) we need to use a sufficient number of active array elements to meet the required EIRP level. At the same time, the array elements are costly in such systems and the idea is to use them as much as possible. It is required to have a mechanism to connect the defined properties of the system, required directivity, scan range, and overall dimensions, with the properties of the array, like array size, the number of involved elements, and the distribution of amplitude and phase along the array. Knowing such relations, it is possible to find a way to control, optimize, and improve the FPA properties over the entire scan range. Such a method as a strictly deterministic mathematical algorithm has been proposed by the authors in [23]. The necessity to control additional parameters like amplitude and phase along the array is highlighted in [21], [188], [189], [190], [191], [129].

The concept presented in [23] investigates a complex offset double-reflector model (Fig. 7.1 and Fig. 7.2) for a scan range of  $\pm 20^\circ$  in the azimuth plane without scanning in the elevation plane. The size of the array in the elevation plane has been fixed to 4 cm and in the azimuth plane the size is subject of optimization. The main reflector size is 0.8 m in diameter which provides a maximum directivity of 48dBi at 30 GHz. The maximum sub-reflector size is limited to 83 cm x 30 cm. The obtained configuration has been used to construct a prototype for experimental validation (see Fig. 7.3). The simulation and measurement results confirm the proposed method, proves that the optimization algorithm works well, and allows to significantly improve the performance within a pre-defined scan range. Nevertheless, the question about the applicability of the proposed method for other optimization goals has not been disclosed. In addition, other scan range requirements could also lead to other optimal configurations. Thus, in the frame of this chapter additional investigations are done.

In the proposed configuration of paper [23], the reflector elevation incline angle  $\beta$  acts as one of the geometrical parameters optimized by GO [192], [193], see Fig. 7.1. This incline is also visible in the photo of the prototype in Fig. 7.3. It is important to note that this parameter has been limited during optimization with a maximum value for up to  $40^\circ$ . It is obvious that with a higher elevation incline, the effective area of the main reflector will be lower, reduced according to  $\cos\beta$ . As a result, the directivity of the reflector system will degrade with increasing  $\beta$ . At the same time, as will be demonstrated in this chapter, the introduction of this elevation aspect could improve the optimization results for reflector minimization during scanning. To find a balanced solution within this chapter, the reflector optimizations have been done for three different maximum values of  $\beta$  defined in the optimization code. Like in [23], one compilation of optimization limits the maximum value for  $\beta$  to  $40^\circ$ , which is related to a 23.4% potential loss of directivity. Two other cases limit the maximum  $\beta$  to  $20^\circ$  and  $0^\circ$ ,

which is equivalent to a potential loss of directivity of 6% and 0%, respectively.

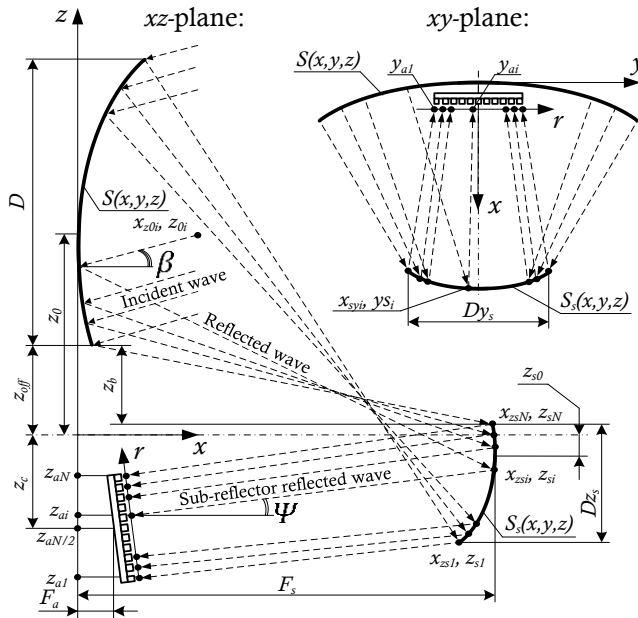


**Figure 7.1.** Complex offset double-reflector model [23].

In [23] the optimization has been done for a “complex” or multi-variable set of optimization goals. This set is a combination of the minimum required array size to realize a certain scan range, the maximization of the ratio of active versus non-active array elements, and the minimization of the amplitude and phase errors along the array. Depending on the FPA application, different optimization goals could be more relevant than others. Thus, to cover the technology applicability it is necessary to investigate optimization goals that improve a certain aspect of the FPA. For example, the overall number of array elements could be minimized by minimizing the array dimension during operation within the required scan range. Nevertheless, the foundation stone is the optimization of the ratio of active versus the total number of array elements of the FPA within the scan range. As we know, the focusing properties of traditional reflectors significantly deteriorate during scanning. As a result, only a small number of active array elements are typically used in the focal plane. This limits the FPA technology and makes it vulnerable compared to phased arrays.

We will introduce a new parameter RATA, which represents the Ratio between the number of Active array elements contributing to the reflector illumination for a certain scan angle to the Total number of Array elements [23]. The RATA will vary over the scan range, between a minimum and maximum value, as illustrated in Fig. 7.4. A high RATA results in a high EIRP level.

Fig. 7.4 presents the typical situation for classical prime-focused reflectors. For larger scan angles, the focusing properties of the reflector deteriorate and the beam is broadened in the array plane. As a result, the number of active array elements is at its minimum for broadside operation and increases with scanning, reaching a maximum at the maximum scan incline.

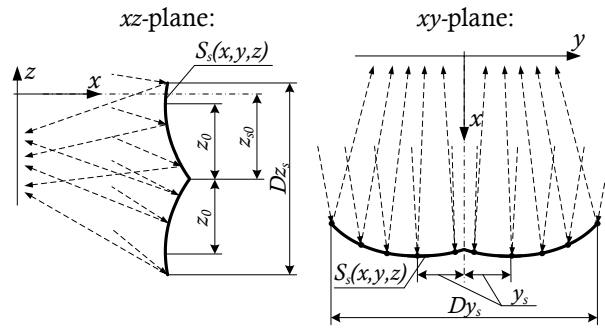


**Figure 7.2.** Complex offset double-reflector model with discontinuities of the three-dimensional offset reflector [23].

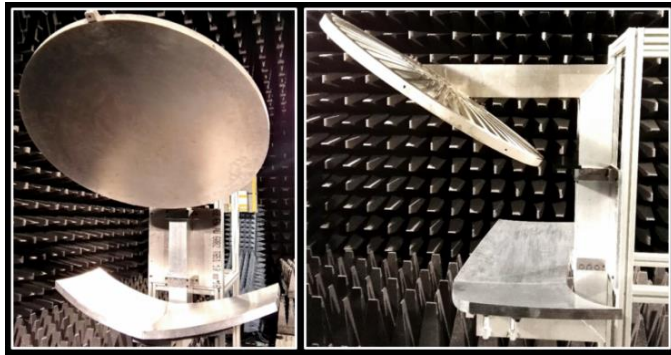


**Figure 7.3.** Photo of the prototype using a complex offset double-reflector setup [23].

For classical prime-focused reflectors, the field distribution in the focal plane is presented as an Airy pattern with a ring-like distribution. The aperture efficiency is found by integrating the electric field on the focal plane along the aperture and normalizing it to the total power received by the reflector [194]. An aperture efficiency of 100% for any distribution of the electric field in the array plane could be achieved only by using an infinitely large aperture radius. The array element is considered active if it is included in the aperture radius related to an aperture efficiency of 80% [162]. It is obvious that for different reflector configurations that operate within a defined scan range, the field distribution in the focal plane could take various forms. Nevertheless, the definition of “active array element” remains relevant [23].

Within this chapter, we will extend the optimization method of the paper [23] by investigating in subparagraph 7.2.1 how the multi-variable optimization can be extended to more extreme scan ranges up to  $\pm 30^\circ$ . Next to this, alternative optimization goals will be investigated. Subparagraph 7.2.2 presents the results of optimizations for the maximization of the peak EIRP only or optimization of the maximum RATA only. Subparagraph 7.2.3 presents the results of maximizing the minimum RATA that can occur in a certain scan range (Fig. 7.4). Subparagraph 7.2.4 demonstrates the combination of goals of subsections 7.2.2 and 7.2.3, by maximizing the peak EIRP for broadside operation and improve the minimum RATA over the entire scan range. In subparagraph 7.2.5 we look at the minimum array size which could serve the required scan range. Subparagraph 7.2.6 summarizes the results achieved by different optimization methods.

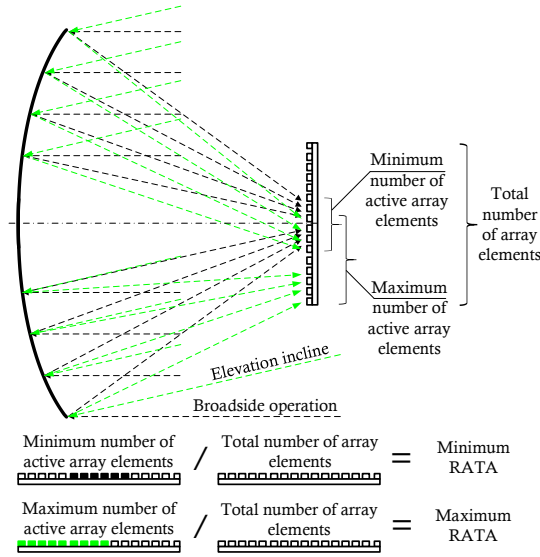


**Figure 7.4.** Maximum and minimum RATA of FPA within the scan range.

For all optimizations, we have used a fixed array size of 4 cm in the elevation plane. The main reflector size is 0.8 m in diameter and the maximum allowed sub-reflector size is 100 cm x 45 cm.

### 7.2.1. Multi-variable optimization goal

Within this subparagraph, the optimization results for 21 different reflectors configurations for a multi-variable optimization goal are presented. The configurations vary based on the maximum required scan range and are based on the maximum allowed angle  $\beta$  of the reflector configuration, see Fig. 7.1. The scan range starts from  $0^\circ$  (broadside operation) and increases up to  $\pm 30^\circ$  maximum. Each scan range corresponds to different optimized reflector configurations. The multi-variable set of optimization goals combines the root mean square (RMS) amplitude and phase error along the array, minimum array size, and maximization of the RATA. Note that the definitions of the RMS amplitude and phase errors along the array are provided in [23]. The optimization set combines those goals with the same weighting coefficients as in the paper [23].

Table 7.1 contains the optimization results of the complex offset double-reflector models for  $\beta$  limited to  $40^\circ$ , Table 7.2, and Table 7.3 for  $20^\circ$  and  $0^\circ$ , respectively.

A comparison between reflector configurations with different limits on  $\beta$  is presented in Fig. 7.5 for varying array sizes, in Fig. 7.6 for the RATA, and in Fig. 7.7 for the RMS amplitude and phase errors along the array.

An azimuth scan range of  $0^\circ$  corresponds to broadside operation only. If we do not scan, the minimum and maximum RATA are always equal to 100% since there is no beam deviation related to scanning. As a result, for broadside, we only optimize the array size minimization and the RMS amplitude and phase error along the array.

In the case of scanning, it is possible to optimize the RATA of the reflector configuration

within a defined scan range. Each scan range corresponds to the different optimized reflector configurations and to different values of the minimum and maximum RATA. For example, the configuration optimized to operate within a scan range of  $\pm 20^\circ$  will have a certain value for the minimum and maximum RATA within this  $\pm 20^\circ$  range. The configuration optimized to work within  $\pm 30^\circ$  is going to be different and will have other values of minimum and maximum RATA.

**Table 7.1.** Optimization results with the multi-variable goal for the complex offset double-reflector model for  $\beta = 40^\circ$ .

	Azimuth scan range, deg						
	0	$\pm 5$	$\pm 10$	$\pm 15$	$\pm 20$	$\pm 25$	$\pm 30$
Array size, cm	0.2	6.2	11.6	20.5	21.7	27.7	40.63
Maximum RATA, %	100	99.53	95.73	44.07	61.25	50.66	20.75
Minimum RATA, %	100	35.75	24.91	6.45	5.27	5.05	6.48
Amplitude uniformity maximum RMS error, %	0.03	3.50	6.68	5.52	8.27	6.40	4.73
Phase linearity maximum RMS error, deg	0.17	1.56	2.88	4.23	5.48	7.69	9.18

**Table 7.2.** Optimization results with the multi-variable goal for the complex offset double-reflector model for  $\beta = 20^\circ$ .

	Azimuth scan range, deg						
	0	$\pm 5$	$\pm 10$	$\pm 15$	$\pm 20$	$\pm 25$	$\pm 30$
Array size, cm	0.3	9.9	20.5	34.4	43.2	79.7	121.3
Maximum RATA, %	100	61.48	62.46	39.65	61.53	41.71	42.14
Minimum RATA, %	100	3.15	0.99	2.18	6.73	26.60	34.36
Amplitude uniformity maximum RMS error, %	0.05	4.24	8.75	9.12	16.67	12.12	17.82
Phase linearity maximum RMS error, deg	0.21	1.79	3.59	5.38	7.46	10.47	12.87

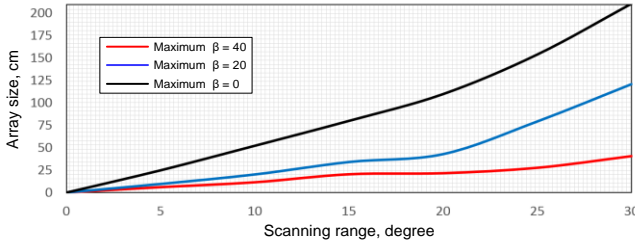
**Table 7.3.** Optimization results with multi-variable goal for the complex offset double-reflector model for  $\beta = 0^\circ$ .

	Azimuth scan range, deg						
	0	$\pm 5$	$\pm 10$	$\pm 15$	$\pm 20$	$\pm 25$	$\pm 30$
Array size, cm	0.04	24.9	52.3	80.1	110	154.2	210.9
Maximum RATA, %	100	3.63	7.75	10.76	13.74	13.33	24.59
Minimum RATA, %	100	2.67	4.04	4.66	5.75	1.93	8.56
Amplitude uniformity maximum RMS error, %	0.01	0.25	1.16	2.48	4.36	5.92	14.87
Phase linearity maximum RMS error, deg	2.32	3.26	4.71	6.31	7.74	7.23	6.86

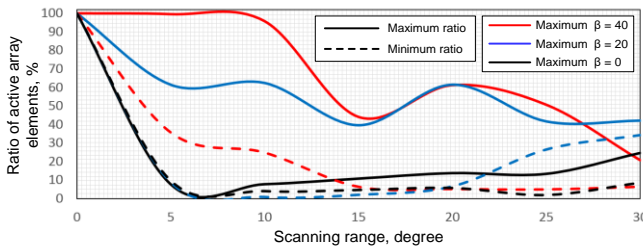
When only optimizing the maximum RATA, we improve the best-case operation, the best-case peak EIRP. At other scan angles, the RATA might be much lower. On the other hand, when we only optimize the minimum RATA, we improve the RATA over the whole scan range. Both optimization goals could be combined with a certain proportion. Those could be interesting for radar applications since system sensitivity could be optimized in a certain direction and balanced with a minimum required sensitivity in other directions.

Table 7.1 contains the results of the reflector optimization for  $\pm 20^\circ$  scanning with a limit of  $40^\circ$  of the maximum  $\beta$ , see Fig. 7.5. This is the same optimization requirement as for the proposed configuration in the paper [23]. The required minimum array size, which was 28 cm in paper [23] based on physical optics (PO) simulations in GRASP [39], is now reduced to 21.7 cm in this chapter based on the GO optimization code. The slight improvement can be explained by the fact that in [23] the sub-reflector length has been limited to 83 cm due to

the prototype production restrictions, while in this chapter the maximum dimension the of sub-reflector size has been limited to 1 m.



**Figure 7.5.** Array size for the complex offset double-reflector model optimized for a multi-variable goal.



**Figure 7.6.** RATA for the complex offset double-reflector model optimized for a multi-variable goal.

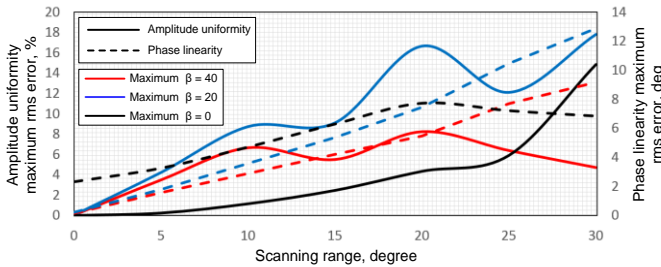


**Figure 7.7.** RMS amplitude uniformity and phase linearity error along the array for the complex offset double-reflector model optimized for a multi-variable goal.

From Fig. 7.5, it is clear that the required array size is increasing with increased scan range quite linearly. In addition, there is a clear difference versus an incline angle. A limit of  $\beta$  to  $20^\circ$  results in an increase of the required array size of almost a factor 3 for a scan range of  $\pm 30^\circ$  as compared to the situation of a  $40^\circ$  limit of  $\beta$ . In case  $\beta$  is not provided, the required array size is more than 5 times larger as compared to the maximum value for  $\beta = 40^\circ$ . From Fig. 7.6 we can observe a similar trend for the RATA. Both the maximum and the minimum RATA show a degradation with strict limits on  $\beta$  and degradation for wider scan ranges. Thus, it is obvious that some degradation in directivity could be acceptable to significantly reduce the array size and, as a result, the number of array elements for a wide-scan range.

Fig. 7.7. shows the mixed dependence of amplitude uniformity and phase linearity RMS error along the array for various values of the reflector elevation incline angle.

### 7.2.2. Maximization of EIRP within the defined scan range

Within this subparagraph, the optimization results for another 21 different reflectors configurations when maximizing the EIRP are presented. As in the previous case, the configurations vary based on the maximum required scan range and are based on the maximum allowed  $\beta$  angle.

For this optimization, it is possible to create a situation where the entire array is active for a certain scan angle, so we could achieve a maximum RATA of 100%. Thus, in this case, a second-order optimization factor has been used. The minimization of the overall array dimension is applied if the maximum RATA achieves 100%.

Within this chapter, we investigate the use case when the maximum RATA is optimized for broadside operation. If the maximum RATA for this optimization achieves 100%, this means that this configuration has all elements active for broadside operation and at the same time capable to provide scanning within the defined scan range (of course with less RATA than 100% for non-broadside operation) and achieves all of that with a minimum required array size. An example of such a system is presented in Fig. 7.8.

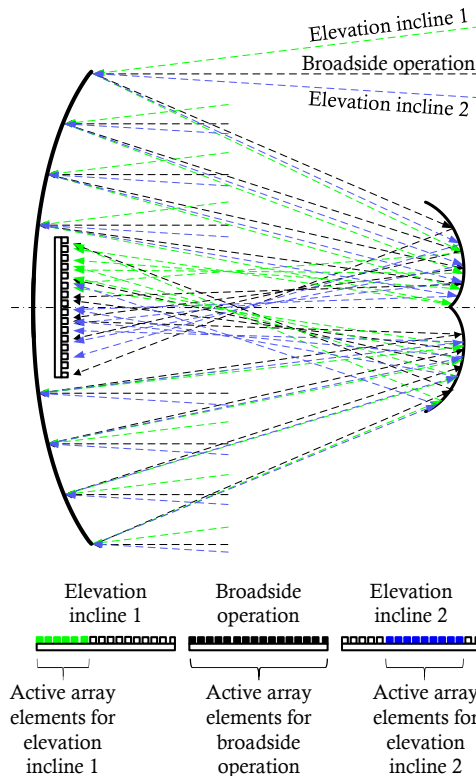


**Figure 7.8.** Illustration of an FPA with scanning capabilities and with the maximum RATA equal to 100% for broadside operation.

Table 7.4 contains the optimization results of complex offset double-reflector models for  $\beta$  limited to  $40^\circ$ , Table 7.5, and Table 7.6 for  $20^\circ$  and  $0^\circ$ , respectively.

A comparison between the reflector configurations is presented in Fig. 7.9 for varying array size, in Fig. 7.10 for the RATA, and in Fig. 7.11 for the RMS amplitude uniformity and phase linearity error along the array.

**Table 7.4.** Optimization results for EIRP maximization using a multi-variable goal for the complex offset double-reflector model for  $\beta = 40^\circ$ .

	Azimuth scan range, deg					
	$\pm 5$	$\pm 10$	$\pm 15$	$\pm 20$	$\pm 25$	$\pm 30$
Array size, cm	<b>6.82</b>	<b>8.97</b>	<b>13.66</b>	<b>18.062</b>	<b>26.69</b>	<b>40.6</b>
Maximum RATA, %	<b>100</b>	<b>100</b>	<b>100</b>	<b>100</b>	<b>100</b>	<b>100</b>
Minimum RATA, %	2.14	11.06	6.63	9.84	29.41	56.84
Amplitude uniformity maximum RMS error, %	4.73	6.01	8.86	12.17	12.62	17.63
Phase linearity maximum RMS error, deg	1.54	2.88	4.28	5.63	7.41	10.66

**Table 7.5.** Optimization results for EIRP maximization using a multi-variable goal for the complex offset double-reflector model for  $\beta = 20^\circ$ .

	Azimuth scan range, deg					
	$\pm 5$	$\pm 10$	$\pm 15$	$\pm 20$	$\pm 25$	$\pm 30$
Array size, cm	<b>9.3</b>	<b>17</b>	<b>35.8</b>	<b>42.6</b>	<b>89.8</b>	<b>118.2</b>
Maximum RATA, %	<b>100</b>	<b>100</b>	<b>100</b>	<b>100</b>	<b>100</b>	<b>100</b>
Minimum RATA, %	3.12	4.03	34.47	24.66	52.09	49.94
Amplitude uniformity maximum RMS error, %	6.53	11.55	18.69	23.11	38.69	54.34
Phase linearity maximum RMS error, deg	1.88	3.96	6.10	7.87	10.83	14.25

**Table 7.6.** Optimization results for EIRP maximization using a multi-variable goal for the complex offset double-reflector model for  $\beta = 0^\circ$ .

	Azimuth scan range, deg					
	$\pm 5$	$\pm 10$	$\pm 15$	$\pm 20$	$\pm 25$	$\pm 30$
Array size, cm	<b>9.67</b>	<b>46.7</b>	90.6	102.5	162.2	210.8
Maximum RATA, %	<b>100</b>	<b>100</b>	<b>89.61</b>	<b>74.88</b>	<b>45.10</b>	<b>24.62</b>
Minimum RATA, %	4.56	47.63	61.15	47.65	41.46	8.55
Amplitude uniformity maximum RMS error, %	6.28	24.43	33.34	33.16	28.13	14.88
Phase linearity maximum RMS error, deg	2.48	4.41	6.07	7.01	11.47	6.87

Table 7.4 and Table 7.5 show the optimized results with a maximum  $\beta$  of  $40^\circ$  and  $20^\circ$ , respectively. As we can see from those tables, within the investigated azimuth scan range up to  $\pm 30^\circ$ , there is always a situation for each reflector when the entire array is active. Thus, in those tables, the array size is also optimized for minimum dimensions. Table 7.6 contains the results of the reflector optimization without the possibility of elevation incline. As we can observe, this implies a more challenging situation on the peak EIRP optimization and only within a limited scan range up to  $\pm 10^\circ$ , it is possible to achieve the situation that all array elements are active for broadside operation. For scan ranges beyond  $\pm 10^\circ$ , the optimization is done only for peak EIRP and does not include the array size minimization.

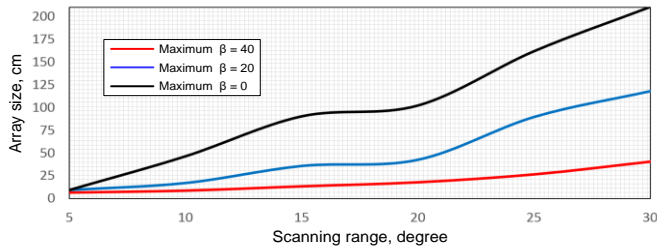


**Figure 7.9.** Array size for the complex offset double-reflector model optimized for EIRP maximization.

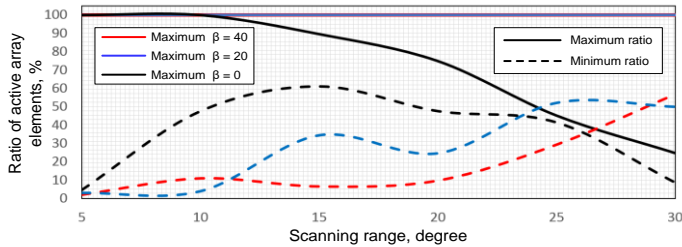


**Figure 7.10.** RATA for the complex offset double-reflector model optimized for EIRP maximization.

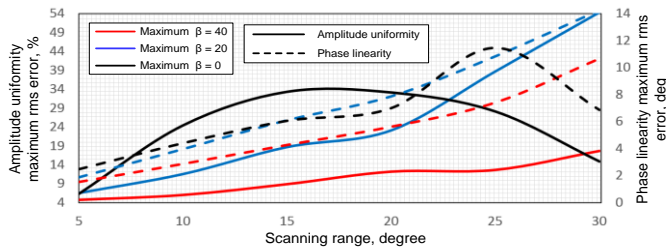


**Figure 7.11.** RMS amplitude uniformity and phase linearity error along the array for the complex offset double-reflector model optimized for EIRP maximization.

Similarly to the previous optimization, Fig. 7.9 shows that the required array size is increasing with increased scan range in an almost linear way and with a stricter limit of the maximum  $\beta$ . Moreover, the limit on  $\beta$  limits the optimized peak EIRP as we could see in Fig. 7.10. For  $\beta = 40^\circ$  and  $\beta = 20^\circ$  the maximum RATA is equal to 100% for all investigated scan ranges. Whereas for  $\beta = 0^\circ$ , the maximum RATA is decreasing linearly with increasing azimuth scan range. On the other hand, the minimum RATA is the highest when  $\beta = 0^\circ$ . This means that the difficulty to achieve the highest peak EIRP is in some way compensated by a higher minimum RATA.

The RMS amplitude uniformity and phase linearity error along the array, as shown in Fig. 7.11, demonstrates the overall increase for wider scan ranges.

### 7.2.3. Minimum RATA

Within this subparagraph, the optimization results for 21 different reflectors configurations

toward increasing the minimum RATA are presented. The lowest RATA value within the scan range characterizes how efficient array elements are used. Normally, this parameter is a weak spot of traditional reflector configurations. Classical prime focused reflectors have a very low RATA while scanning, so most of the array elements remain inactive [170], [144]. The complex offset double-reflector model of [23] allows to have about a quarter of the array elements to be active within a  $\pm 20^\circ$  scan range. Here we will explore if we can further improve the minimum RATA at the cost of deteriorating other characteristics.

Table 7.7 contains the optimization results for maximizing the minimum RATA for  $\beta$  limited to  $40^\circ$ , Table 7.8, and Table 7.9 for  $20^\circ$  and  $0^\circ$ , respectively.

A comparison between reflector configurations with different limits on  $\beta$  is presented in Fig. 7.12 for the array size, in Fig. 7.13 for the RATA, and in Fig. 7.14 for the RMS error of the amplitude uniformity and phase linearity along the array.

**Table 7.7.** Optimization results for the maximization of the minimum RATA using a multi-variable goal for the complex offset double-reflector model for  $\beta = 40^\circ$ .

	Azimuth scan range, deg					
	$\pm 5$	$\pm 10$	$\pm 15$	$\pm 20$	$\pm 25$	$\pm 30$
Array size, cm	38.4	28.27	33.3	35.9	41.8	47.2
Maximum RATA, %	99.96	99.04	98.64	99.99	99.61	95.69
Minimum RATA, %	<b>99.95</b>	<b>99.02</b>	<b>98.54</b>	<b>97.28</b>	<b>95.22</b>	<b>91.68</b>
Amplitude uniformity maximum RMS error, %	14.97	9.11	11.28	13.15	15.47	16.79
Phase linearity maximum RMS error, deg	4.56	3.39	5.93	7.47	10.18	12.99

**Table 7.8.** Optimization results for the maximization of the minimum RATA using a multi-variable goal for the complex offset double-reflector model for  $\beta = 20^\circ$ .

	Azimuth scan range, deg					
	$\pm 5$	$\pm 10$	$\pm 15$	$\pm 20$	$\pm 25$	$\pm 30$
Array size, cm	37.8	69.4	69.3	95.7	96.4	107.9
Maximum RATA, %	99.86	99.32	98.16	92.98	77.99	99.96
Minimum RATA, %	<b>99.83</b>	<b>99.31</b>	<b>98.15</b>	<b>82.83</b>	<b>70.46</b>	<b>56.99</b>
Amplitude uniformity maximum RMS error, %	13.62	28.29	26.03	35.32	30.81	48.59
Phase linearity maximum RMS error, deg	4.50	5.56	9.93	13.69	14.83	17.26

**Table 7.9.** Optimization results for the maximization of the minimum RATA using a multi-variable goal for the complex offset double-reflector model for  $\beta = 0^\circ$ .

	Azimuth scan range, deg					
	$\pm 5$	$\pm 10$	$\pm 15$	$\pm 20$	$\pm 25$	$\pm 30$
Array size, cm	85.5	82.5	94.4	141.3	162.2	210.7
Maximum RATA, %	99.96	86.44	75.85	63.85	45.10	24.62
Minimum RATA, %	<b>99.89</b>	<b>84.34</b>	<b>72.29</b>	<b>59.77</b>	<b>41.46</b>	<b>8.55</b>
Amplitude uniformity maximum RMS error, %	34.55	27.48	26.98	35.66	28.12	14.88
Phase linearity maximum RMS error, deg	4.49	8.13	10.44	14.25	11.47	6.87

According to Tables 7.7, 7.8, and 7.9, it is not possible to achieve a situation where the entire array remains active within the whole scan range. The minimum RATA is always less than 100% when there is a scan capability realized. Nevertheless, we could see that a dedicated optimization of the complex offset double-reflector allows to obtain results radically different from classical prime focused reflectors. If the prime focused reflector without reflector elevation incline has a RATA of about 19% for  $20^\circ$  elevation incline [23],

the corresponding complex offset double-reflector (see Table 7.9) optimized for  $\pm 20^\circ$  scan range has a minimum RATA of almost 60%.

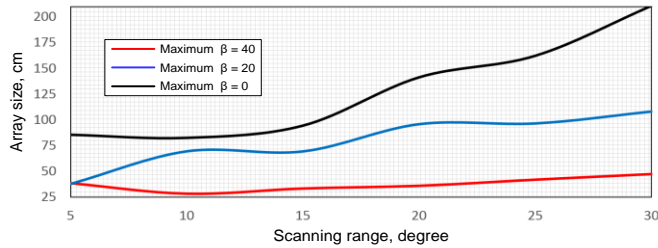


**Figure 7.12.** Array size for the complex offset double-reflector model optimized for maximization of the minimum RATA.

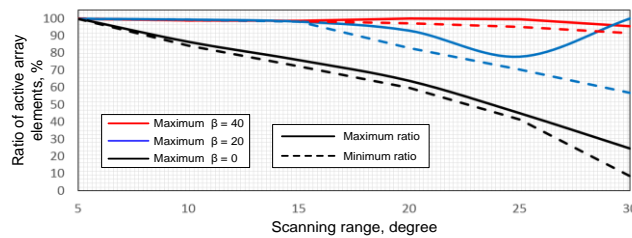


**Figure 7.13.** RATA for the complex offset double-reflector model optimized for maximization of the minimum RATA.

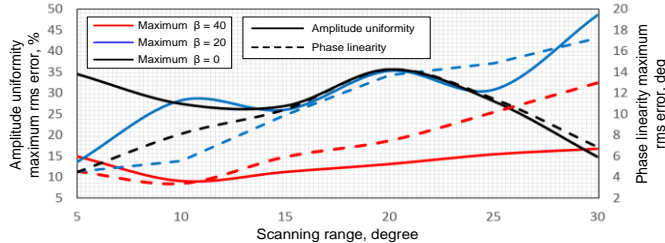


**Figure 7.14.** RMS error of amplitude uniformity and phase linearity along the array for the complex offset double-reflector model optimized for maximization of the minimum RATA.

The costs of the achieved RATA improvement are visible in Fig. 7.12. The sizes of the required arrays are significantly larger than for other types of optimizations. In addition, even for a limited scan range, a larger array is required. For reflectors with an elevation incline up to  $40^\circ$ , the array is almost independent of the scan range. For a strict limit to  $\beta = 0^\circ$ , the array size remains almost constant up to the  $15^\circ$  scan range and then linearly increases.

The RATA of Fig. 7.13 demonstrates that up to a  $15^\circ$  scan range, it is possible to keep almost the entire array in active mode for configurations with maximum  $\beta$  of  $20^\circ$  and  $40^\circ$ . As we know, a  $\beta$  equal to  $40^\circ$  corresponds to a potential loss of directivity of 23.4% and for a  $\beta$  value of  $20^\circ$  to 6%. This fact proves that some compromise towards a potential directivity drop and improvements of the array illumination by the reflector, in terms of a RATA increase, could be done. For  $\beta$  equal to  $0^\circ$  the maximum and minimum RATA strongly decreases for wider scan ranges.

### 7.2.4. Maximization of EIRP and the minimum RATA

As we can see in the previous subparagraphs, the optimization of the minimum RATA is leading to the fact that the maximum RATA is also increasing. In addition, the optimization toward peak EIRP is possible using up to 100% of the active array elements for most of the configurations. Thus, it is interesting to combine those goals in one optimization. Both the peak EIRP and the minimum RATA are optimized with equal optimization weight within this paragraph. The optimization outcomes are again presented for 21 different reflectors configurations.

When we look at the results of subparagraph 7.2.2 there is no need for a second-order optimization factor like array size minimization in this case. As it has been demonstrated the minimum RATA never achieves 100% within a nonzero scan range. Thus, the combined goal never could be satisfied fully.

Table 7.10 contains the optimization results for  $\beta$  limited to  $40^\circ$ , Table 7.11, and Table 7.12 for  $20^\circ$  and  $0^\circ$ , respectively.

A comparison between reflector configurations with different limits on  $\beta$  is presented in Fig. 7.15 for array size, in Fig. 7.16 for the RATA, and in Fig. 7.17 for the RMS amplitude and phase linearity error along the array.

**Table 7.10.** Optimization results for the maximization of EIRP and minimum RATA for the complex offset double-reflector model for  $\beta = 40^\circ$ .

	Azimuth scan range, deg					
	$\pm 5$	$\pm 10$	$\pm 15$	$\pm 20$	$\pm 25$	$\pm 30$
Array size, cm	42.79	50.3	52.66	60.7	48.6	58.23
Maximum RATA, %	<b>99.97</b>	<b>100</b>	<b>100</b>	<b>100</b>	<b>99.99</b>	<b>100</b>
Minimum RATA, %	<b>99.95</b>	<b>99.25</b>	<b>96.80</b>	<b>96.84</b>	<b>95.28</b>	<b>91.25</b>
Amplitude uniformity maximum RMS error, %	17.76	19.81	20.44	22.76	18.63	22.72
Phase linearity maximum RMS error, deg	4.86	5.47	8.36	12.09	12.12	16.19

**Table 7.11.** Optimization results for the maximization of EIRP and minimum RATA for the complex offset double-reflector model for  $\beta = 20^\circ$ .

	Azimuth scan range, deg					
	$\pm 5$	$\pm 10$	$\pm 15$	$\pm 20$	$\pm 25$	$\pm 30$
Array size, cm	37.8	69.6	69.7	72.4	82	115.5
Maximum RATA, %	<b>99.96</b>	<b>99.34</b>	<b>98.15</b>	<b>100</b>	<b>100</b>	<b>98.08</b>
Minimum RATA, %	<b>99.82</b>	<b>99.29</b>	<b>98.13</b>	<b>95.85</b>	<b>79.87</b>	<b>56.11</b>
Amplitude uniformity maximum RMS error, %	13.62	28.37	26.20	28.97	33.86	48.01
Phase linearity maximum RMS error, deg	4.51	5.58	9.98	13.97	16.60	17.05

**Table 7.12.** Optimization results for the maximization of EIRP and minimum RATA for the complex offset double-reflector model for  $\beta = 0^\circ$ .

	Azimuth scan range, deg					
	$\pm 5$	$\pm 10$	$\pm 15$	$\pm 20$	$\pm 25$	$\pm 30$
Array size, cm	90.5	81.1	86	145.5	162.2	210.8
Maximum RATA, %	<b>99.97</b>	<b>99.99</b>	<b>81.29</b>	<b>61.15</b>	<b>45.11</b>	<b>24.62</b>
Minimum RATA, %	<b>99.89</b>	<b>97.96</b>	<b>76.00</b>	<b>57.39</b>	<b>41.46</b>	<b>8.56</b>
Amplitude uniformity maximum RMS error, %	37.51	31.29	27.61	34.97	28.13	14.88
Phase linearity maximum RMS error, deg	6.08	8.86	8.33	14.07	11.47	6.87

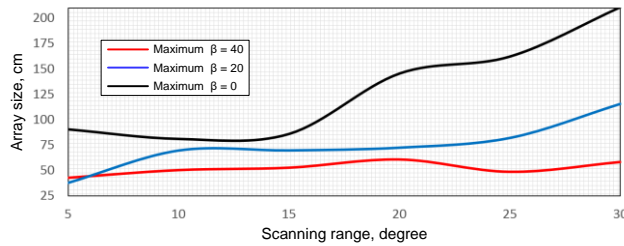


**Figure 7.15.** Array size for the complex offset double-reflector model optimized for maximization of EIRP and minimum RATA.

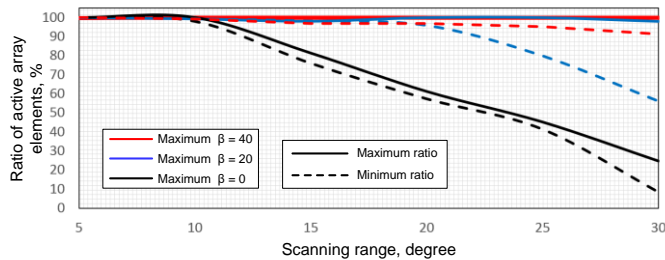


**Figure 7.16.** RATA for the complex offset double-reflector model optimized for maximization of EIRP and minimum RATA.

As we could see from Tables 7.10, 7.11, and 7.12 for the combined goal the maximum RATA could achieve 100%. This means that within a scan range, there is a certain scan angle when all array elements are going to be involved. For optimization results with a maximum reflector incline angle up to  $40^\circ$  (Table 7.10), the minimum RATA is also relatively close to 100%. Thus, it is possible to claim that for  $\beta$  maximally equal to  $40^\circ$ , the optimization goal is almost satisfied within the investigated scan range and it is possible to build an FPA with maximum use of the array elements.

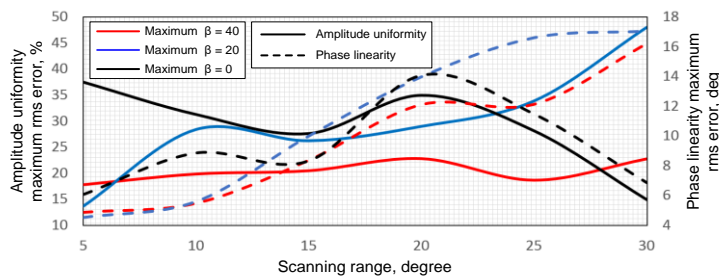


**Figure 7.17.** RMS error of amplitude uniformity and phase linearity along the array for the complex offset double-reflector model optimized for maximization of EIRP and minimum RATA.

Like the optimization results of the previous subparagraph the cost of the improvement is the need for a larger overall array size, see Fig. 7.15. For reflectors with  $\beta$  up to  $20^\circ$  and  $40^\circ$  the array size almost does not depend on the scan range. In the case  $\beta = 0^\circ$  the array size remains almost constant up to a  $15^\circ$  scan range and then increases further for wider scan ranges.

According to Fig. 7.16, the maximum RATA stays almost up to 100% for a  $\pm 30^\circ$  scan range for a maximum  $\beta$  of  $40^\circ$ , within  $\pm 20^\circ$  – for a maximum  $\beta$  of  $20^\circ$ , and  $\pm 10^\circ$  – for a maximum  $\beta$  of  $0^\circ$ .

### 7.2.5. Array size minimization

From a cost point of view, the most important configuration could be the one that minimizes the overall number of required array elements. In other words, to optimize the shape of the reflector to achieve a minimum array size that could provide the required performance over the specified scan range. Within this subparagraph, the optimization results for 21 different reflectors configurations toward array size minimization are presented. It is important to notice that the obtained optimization results are scalable with the size of the reflectors and relevant only for the chosen sizes and proportions of the main and sub-reflectors.

Table 7.13 contains the optimization results of array minimization for  $\beta$  limited to  $40^\circ$ , Table 7.14, and Table 7.15 for  $20^\circ$  and  $0^\circ$ , respectively.

A comparison between reflector configurations with different limits on  $\beta$  is presented in Fig. 7.18 for the array size, in Fig. 7.19 for the RATA and in Fig. 7.20 for the RMS of amplitude uniformity and phase linearity error along the array.

**Table 7.13.** Optimization results for array size minimization for the complex offset double-reflector model for  $\beta = 40^\circ$ .

	Azimuth scan range, deg					
	$\pm 5$	$\pm 10$	$\pm 15$	$\pm 20$	$\pm 25$	$\pm 30$
Achieved minimum array size, cm	<b>4.3</b>	<b>8.6</b>	<b>12.8</b>	<b>15.1</b>	<b>21.9</b>	<b>32.83</b>
Maximum RATA, %	99.97	99.98	99.98	99.32	99.99	54.07
Minimum RATA, %	17.31	13.97	14.78	27.32	7.54	47.81
Amplitude uniformity maximum RMS error, %	2.74	5.71	8.52	10.21	11.66	7.87
Phase linearity maximum RMS error, deg	1.76	2.88	4.19	5.40	6.99	8.76

**Table 7.14.** Optimization results for array size minimization for the complex offset double-reflector model for  $\beta = 20^\circ$ .

	Azimuth scan range, deg					
	$\pm 5$	$\pm 10$	$\pm 15$	$\pm 20$	$\pm 25$	$\pm 30$
Achieved minimum array size, cm	<b>6.88</b>	<b>12.94</b>	<b>26.07</b>	<b>40.6</b>	<b>75.6</b>	<b>108.7</b>
Maximum RATA, %	99.96	100	53.03	28.06	36.93	57.08
Minimum RATA, %	6.58	4.12	1.68	1.79	32.09	41.05
Amplitude uniformity maximum RMS error, %	4.37	8.42	9.27	7.92	8.69	29.50
Phase linearity maximum RMS error, deg	1.83	3.66	5.21	6.66	9.49	10.95

**Table 7.15.** Optimization results for array size minimization for the complex offset double-reflector model for  $\beta = 0^\circ$ .

	Azimuth scan, deg					
	$\pm 5$	$\pm 10$	$\pm 15$	$\pm 20$	$\pm 25$	$\pm 30$
Achieved minimum array size, cm	<b>10.2</b>	<b>18.2</b>	<b>42.6</b>	<b>87.9</b>	<b>123.9</b>	<b>210.2</b>
Maximum RATA, %	99.16	88.79	18.82	8.64	28.47	24.55
Minimum RATA, %	3.55	2.96	2.32	1.22	23.67	8.45
Amplitude uniformity maximum RMS error, %	7.11	10.77	5.28	3.29	12.95	14.79
Phase linearity maximum RMS error, deg	2.13	4.24	6.05	7.40	7.81	6.87

According to Tables 7.13, 7.14, and 7.15, it is possible to achieve significant array compactness compared to the previous cases. In addition, we could see that dedicated optimization of the complex offset double-reflector allows to obtain significantly different array sizes as compared to a similar configuration presented in the paper [23] where for  $\pm 20^\circ$  scanning an array length of 28 cm length was required. In the dedicated optimization of this subparagraph, the configuration with the same  $\beta$  just requires a maximum length of 15.1 cm to provide the same scan range. This is achieved due to the dedicated optimization and due to the larger sub-reflector size up to 1 m, against 83 cm of the paper [23].

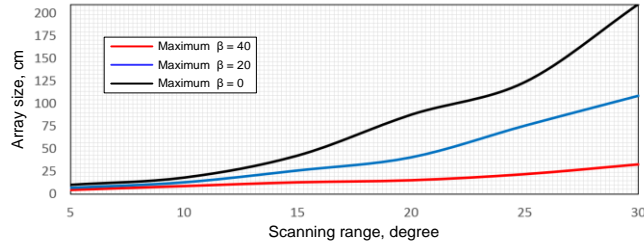


**Figure 7.18.** Array size for the complex offset double-reflector model optimized for array size minimization.

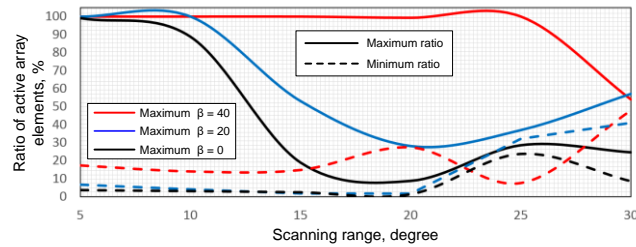


**Figure 7.19.** RATA for the complex offset double-reflector model optimized for array size minimization.

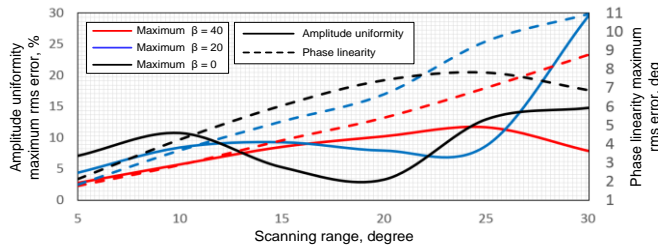


**Figure 7.20.** RMS error of amplitude uniformity and phase linearity along the array for the complex offset double-reflector model optimized for array size minimization.

The overall optimized array sizes almost increase quadratically with the scan range according to Fig. 7.18. For smaller scan ranges, the elevation inclines practically do not affect the required array size. However, with the increase of scan range, the difference between configuration limits becomes more pronounced and achieves a ratio of more than 6 for a  $\pm 30^\circ$  scan range between  $\beta = 0^\circ$  and  $\beta = 40^\circ$ .

The RATA of Fig. 7.19 demonstrates that there are certain scan angles when a significant part of the array will be active. However, the minimum RATA during scanning is significantly reduced compared to the dedicated optimization for RATA maximization (see subparagraph 7.2.2). Combined with the factor that optimization toward a compact array also minimizes the overall number of elements, we can conclude that there will be certain scan angles where the number of active elements is really low.

### 7.2.6. Summary of optimizations

An overview of the required array size for the different optimization goals presented in the previous subparagraphs is provided in Fig. 7.21 for reflector configurations with maximum  $\beta=40^\circ$ , Fig. 7.22 –  $20^\circ$ , and Fig. 7.23 –  $0^\circ$ , respectively.

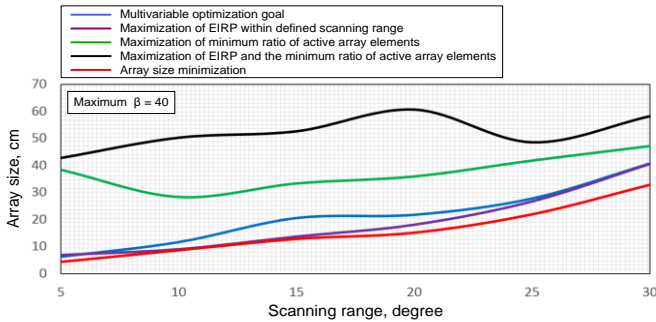


**Figure 7.21.** Array size for the complex offset double-reflector model with  $\beta=40^\circ$  optimized for different goals.

As we could see there is a tradeoff between different array characteristics. We could minimize the array size and have more complicated beamforming or have a significant RATA within all scan ranges, but with a relatively large array size. Interesting to notice is that the most significant difference between the required array sizes is observed for cases where the maximum  $\beta$  is equal to  $40^\circ$ , see Fig. 7.21. For other values of  $\beta$ , it is more difficult to optimize the reflector for a certain optimization goal, see Figs. 7.22 and 7.23. Moreover, the increase in the required scan range also minimizes the output optimization results. The required array sizes of Figs. 7.22 and 7.23 are becoming the same or almost the same for the scan range of  $\pm 30^\circ$ . Those factors demonstrate that there is a clear limit on reflector designs with improved scanning capabilities. Scan ranges wider than  $\pm 30^\circ$  are not advisable since it is impossible to improve the reflector to obtain acceptable characteristics of the array. In addition, the optimization effect will be significant only if there are compromises on the directivity that the reflectors could provide as compared to classical reflector configurations.

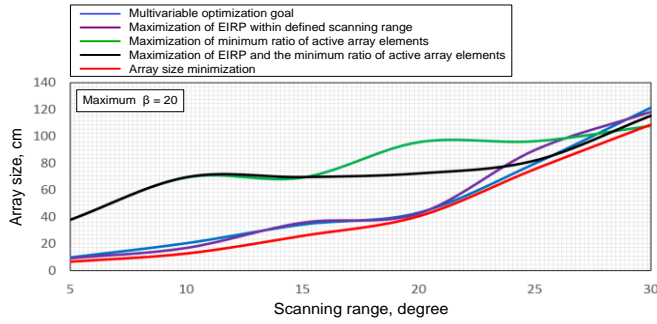


**Figure 7.22.** Array size for the complex offset double-reflector model with  $\beta = 20^\circ$  optimized for different goals.

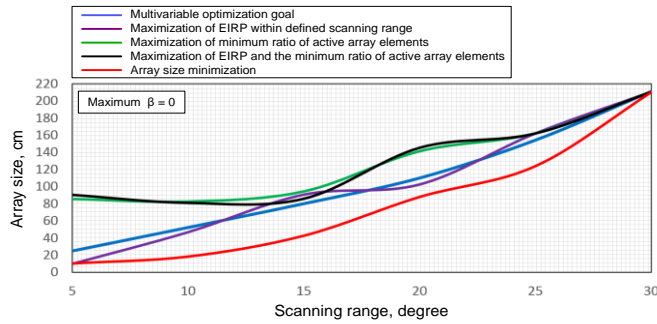


**Figure 7.23.** Array size for the complex offset double-reflector model with  $\beta = 0^\circ$  optimized for different goals.

### 7.3. Array size minimization for different sub-reflector sizes

The previously presented optimization results of the array size minimization are relevant for a certain size of the main and sub-reflectors. The size of the main reflector defines the directivity of the whole system. In addition, scaling the main reflector size will cause scaling of the required sub-reflector and array. The RATA will remain the same. Normally the main reflector is the bulkiest part of the system and defines the required directivity, while the sub-reflector could be a bit smaller and stretched out in one of the dimensions to provide scan capabilities. Thus, it is interesting to investigate how the sub-reflector size could affect the scan capabilities of the whole system.

Within this section, the optimization results for 49 different reflectors configurations toward array length minimization are presented for different sub-reflector sizes. The investigation is done for a complex offset double-reflector model with  $\beta$  of  $40^\circ$ . The required scan range has been fixed to  $\pm 20^\circ$  in the azimuth plane. In the orthogonal non-scanning plane, the width of the array has been fixed to 4 cm. The sub-reflector sizes  $D_{Y_s}$  vary from 80 cm to 110 in the scanning plane and  $D_{Z_s}$  from 15 cm to 30 cm in the orthogonal plane.

The optimization results of the array size minimization are presented in Table 7.16 and Fig. 7.24, the maximum RATA - in Table 7.17 and Fig. 7.25, the minimum RATA - in Table 7.18 and Fig. 7.26, the RMS error of amplitude uniformity - in Table 7.19 and Fig. 7.27, the RMS error of phase linearity - in the Table 7.20 and Fig. 7.28.

According to Table 7.16, there is an optimum size of the sub-reflector for a defined reflector specification. We could see that the minimum array size is achieved with a sub-reflector size of 90 - 100 cm in the scan plane and 25 cm in the orthogonal plane. Both dimensions are affecting the achieved size of the array. In Fig. 7.24 we can see the limitation of  $Dz_s$  has a significant effect on the array size. In addition, it is important to notice that a further increase in the dimensions of the sub-reflectors does not help to minimize the array size further.

The maximum RATA (Table 7.17 and Fig. 7.25) depends on the sub-reflector size in a straightforward way. With increasing sub-reflector size, the maximum number of simultaneously involved elements within the defined scan range is also increasing. It is achieving almost 100% for a maximum  $Dz_s$  of 30 cm. The minimum RATA (Table 7.18 and Fig. 7.26) in its turn has a mixed dependence. However, some of the sub-reflector sizes achieve a minimum RATA of up to 40%. For example, one of the smallest achieved arrays corresponded to a  $Dz_s$  equal to 25 cm and  $Dy_s$  - 90 cm.

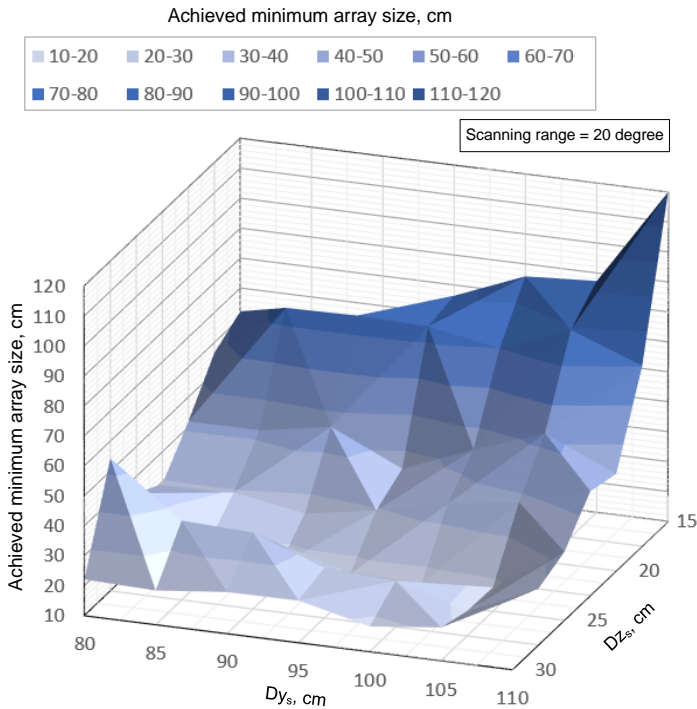


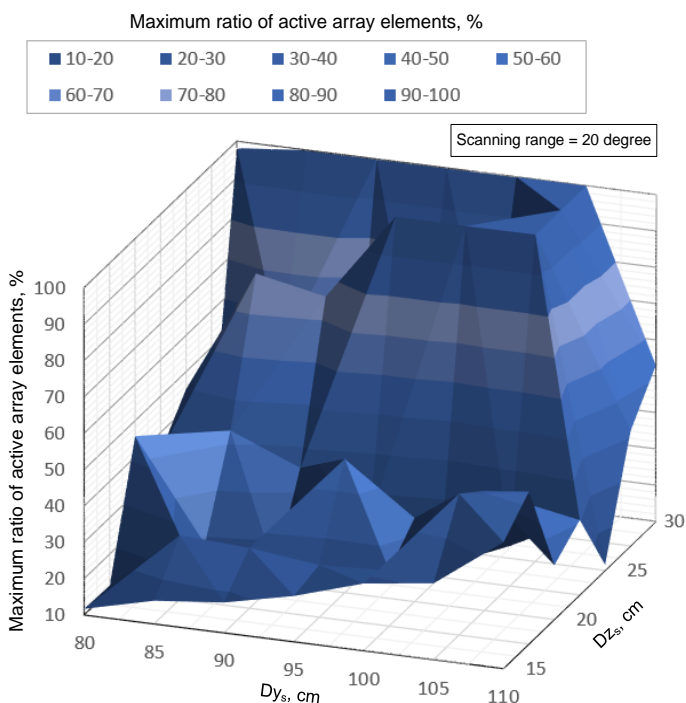
**Figure 7.24.** Achieved minimum array size of the complex offset double-reflector for different sub-reflector sizes.

**Table 7.16.** Achieved minimum array size of the complex offset double-reflector for different sub-reflector sizes.

Achieved minimum array size, cm								
		$D_{ys}, \text{ cm}$						
		80	85	90	95	100	105	110
$D_{zs}, \text{ cm}$	15	62.2	64.5	63.6	76.4	85.9	87.3	120.3
	17.5	56.6	74.6	75.0	74.4	69.9	79.2	70.2
	20	41.9	41.9	46.1	35.1	44.5	52.9	42.4
	22.5	29.3	29.4	25.4	29.4	34.6	38.2	44.8
	25	34.4	20.0	16.1	16.5	16.1	18.0	32.8
	27.5	54.3	36.5	35.5	26.7	25.4	18.3	28.8
	30	22.1	21.4	23.9	24.1	18.4	21.1	33.4

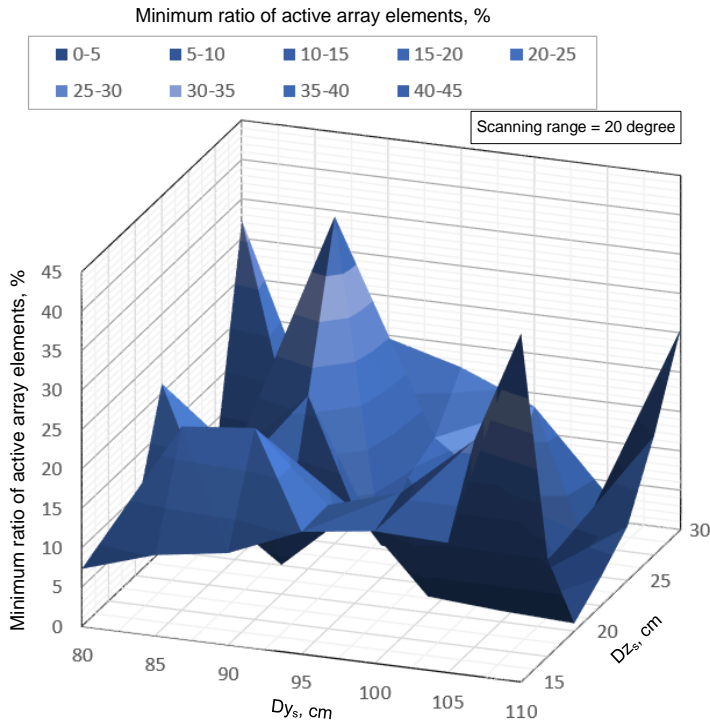
**Table 7.17.** Maximum RATA of the complex offset double-reflector model for different sub-reflector sizes.

Maximum RATA, %								
		$D_{ys}, \text{ cm}$						
		80	85	90	95	100	105	110
$D_{zs}, \text{ cm}$	15	11.69	16.37	18.35	22.59	28.48	30.99	44.75
	17.5	11.35	27.64	26.69	24.38	25.31	48.91	51.93
	20	45.75	18.45	13.84	46.82	33.01	42.98	24.93
	22.5	34.66	43.01	35.17	23.99	12.82	21.03	30.62
	25	45.21	79.49	75.59	99.99	99.88	99.99	11.53
	27.5	21.99	50.97	21.87	42.70	49.93	99.99	41.59
	30	98.13	99.99	99.99	99.98	99.98	100	52.95

**Figure 7.25.** Maximum RATA of the complex offset double-reflector for different sub-reflector sizes.

**Table 7.18.** Minimum RATA of the complex offset double-reflector for different sub-reflector sizes.

Minimum RATA, %								
		$Dy_s$ , cm						
		80	85	90	95	100	105	110
$Dz_s$ , cm	15	7.30	10.23	11.66	15.52	16.77	16.48	44.26
	17.5	5.92	23.34	24.32	15.71	18.49	26.32	12.32
	20	7.29	10.29	3.72	11.80	2.05	1.38	0.98
	22.5	21.18	13.58	21.99	4.12	3.52	2.13	3.62
	25	4.84	7.35	41.53	9.53	3.21	2.29	6.84
	27.5	4.84	11.56	8.68	11.39	4.69	1.49	15.12
	30	32.30	9.22	19.66	17.11	13.30	3.24	25.50

**Figure 7.26.** Minimum RATA of the complex offset double-reflector for different sub-reflector sizes.**Table 7.19.** RMS error of amplitude uniformity of the complex offset double-reflector for different sub-reflector sizes.

Amplitude uniformity maximum RMS error, %								
		$Dy_s$ , cm						
		80	85	90	95	100	105	110
$Dz_s$ , cm	15	1.74	2.85	3.28	4.99	7.27	8.13	21.62
	17.5	1.52	8.39	6.85	5.27	7.93	20.11	21.92
	20	11.89	3.58	4.09	9.85	10.21	15.52	7.33
	22.5	5.59	7.26	2.55	4.46	2.96	5.50	9.31
	25	9.90	10.86	7.35	8.51	8.41	12.26	1.11
	27.5	6.54	10.70	2.27	6.26	7.90	11.64	6.32
	30	13.23	14.90	15.64	15.89	12.27	14.18	10.08

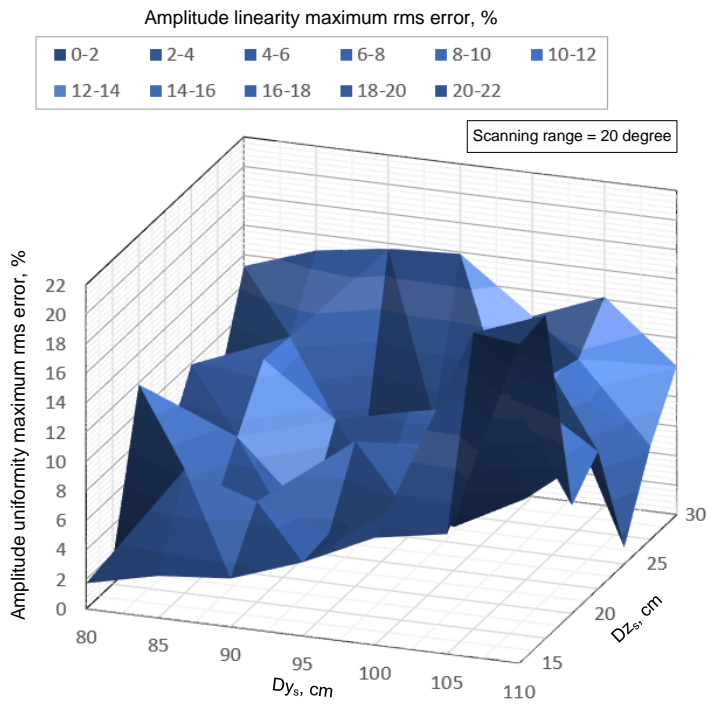


**Figure 7.27.** RMS amplitude uniformity error of the complex offset double-reflector model for different sub-reflector sizes.

**Table 7.20.** RMS phase linearity error of the complex offset double-reflector model for different sub-reflector sizes.

Phase linearity maximum RMS error, deg								
		$Dy_s$ , cm						
		80	85	90	95	100	105	110
$Dz_s$ , cm	15	2.39	2.31	2.74	2.28	2.09	2.41	0.87
	17.5	3.26	2.83	2.89	3.32	3.42	3.25	4.24
	20	4.37	4.45	4.45	4.86	4.86	5.15	5.22
	22.5	5.00	4.71	5.18	4.78	5.15	5.41	5.88
	25	5.82	5.26	5.36	5.58	5.67	6.31	6.34
	27.5	5.42	5.13	5.49	5.59	5.73	6.02	6.72
	30	6.00	5.70	6.32	6.32	5.94	5.99	7.56

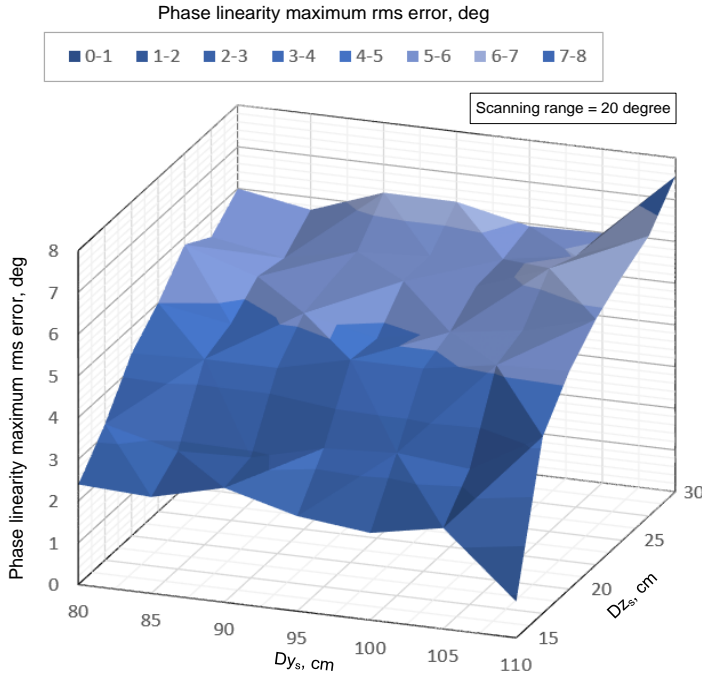


**Figure 7.28.** RMS phase linearity error of the complex offset double-reflector model for different sub-reflector sizes.

#### 7.4. Array size minimization for two-dimensional scanning

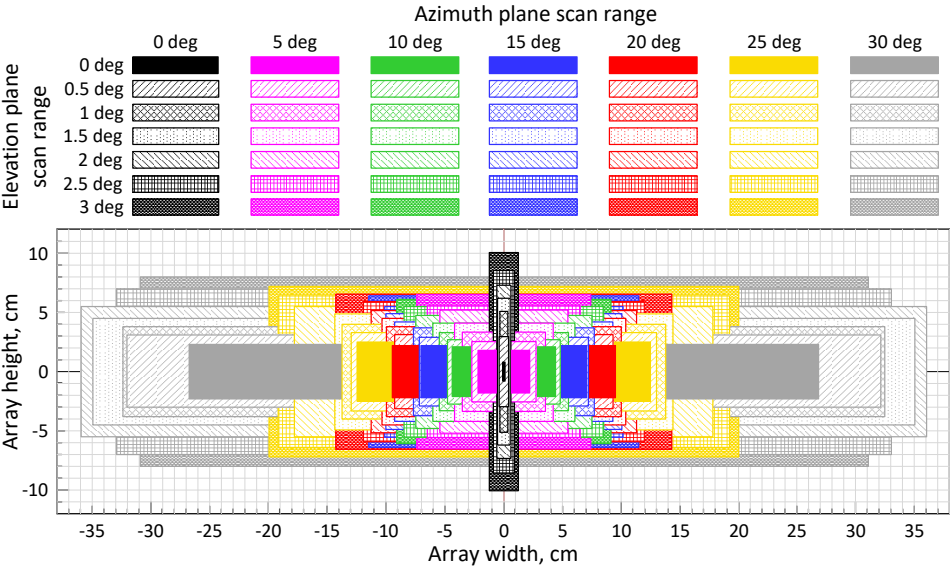
Next to scanning in the azimuth plane, scanning in elevation could be very useful, for example, to compensate for antenna tower vibrations due to wind, which could lead to a beam misalignment of a few degrees [15]. Thus, in addition to the wide-scan capabilities in the azimuth plane, it is crucial to have a limited scanning functionality in the opposite orthogonal plane. In the previous paragraph, we have seen that the sizes of both sub-reflectors affect the minimum required array size.

Within this subparagraph, the optimization results for 49 different reflectors configurations toward array size minimization are presented for scanning in two planes. Like the previous cases, the scanning in azimuth is investigated in the range up to  $\pm 30^\circ$ . In the orthogonal elevation plane, the scan range is limited to  $\pm 3^\circ$ . The investigation is done for a complex offset double-reflector with  $\beta=40^\circ$ . The sub-reflector size is 100 cm x 45 cm. The desired array size is minimized in the main scanning plane and remains equal to 4 cm in the elevation plane.

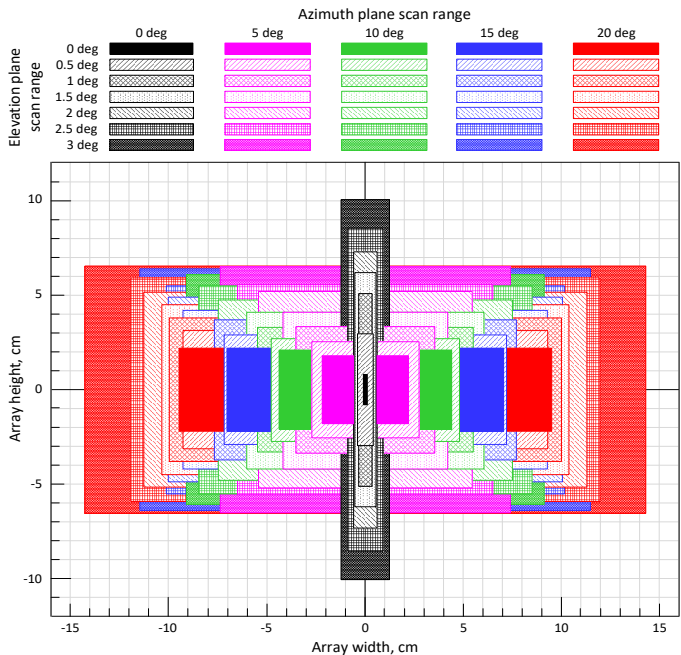
Table 7.16 presents the optimization results of the array size and associated dimensions. Figs. 7.29 and 7.30 present a comparative analysis of the minimum required array size for different scan ranges in azimuth and elevation. Fig. 7.31 presents the same results in a 3-D surface chart. The maximum RATA is presented in Table 7.22 and Fig. 7.32, the minimum RATA - in Table 7.23 and Fig. 7.33, the RMS error of amplitude uniformity - in Table 7.24 and Fig. 7.34, the RMS error of phase linearity - in Table 7.25 and Fig. 7.35.

**Table 7.21.** Achieved minimum array size for the complex offset double-reflector model for two-dimensional scanning.

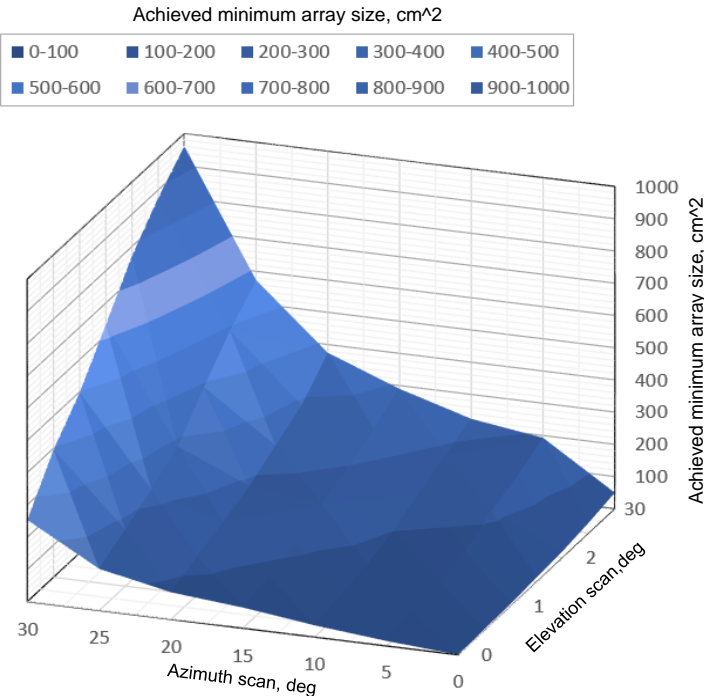
Achieved minimum array size, length, cm, width cm, area, cm <sup>2</sup>								
		Azimuth scan range, deg						
		0	±5	±10	±15	±20	±25	±30
Elevation scan range, deg	0	0.1x3.1 0.3	4.4x3.6 15.5	8.9x4.1 36.5	14.2x4.5 64.1	19x4.4 83.9	25.1x5.2 129	53.7x4.7 253
	±0.5	0.8x5.9 4.5	5.5x5.1 27.8	9.7x5.4 52.7	14.5x5.8 83.4	18.6x6.4 118.5	25.9x6.7 174.8	64.5x6.1 396.0
	±1	0.7x10.1 6.8	7.2x6.6 47.8	10.9x6.7 73.7	15.4x7.4 113.7	19.6x7.7 150.7	27.5x8.1 222.7	64.9x7.6 498.0
	±1.5	1.1x12.4 13.5	8.5x8.2 69.1	12.1x8.2 98.8	18.7x8.4 158.3	20.7x9 186.4	28.7x9.8 282.8	69.4x9.1 634.0
	±2	1.3x14.7 19.7	11x10.4 114.9	15.3x9.5 145.6	20.3x9.8 198.8	22.7x10.5 237.6	35.6x11 391.3	71.1x10.8 771.0
	±2.5	1.9x17.2 32.5	13.3x11.4 151.5	17.1x10.8 185.7	21.7x11.1 241.3	24.1x11.8 286.4	38.4x12.8 490.8	65.7x13.3 876.0
	±3	2.5x20.1 49.9	14.8x13 192.9	18.4x12.2 224.3	22.9x12.6 290.0	28.6x13.1 374.6	39.5x14.5 573.0	61.8x15.5 961.0



**Figure 7.29.** Array size for two-dimensional scanning with the complex offset double-reflector. Azimuth scan range up to  $\pm 30^\circ$  and elevation scan range up to  $\pm 3^\circ$ .



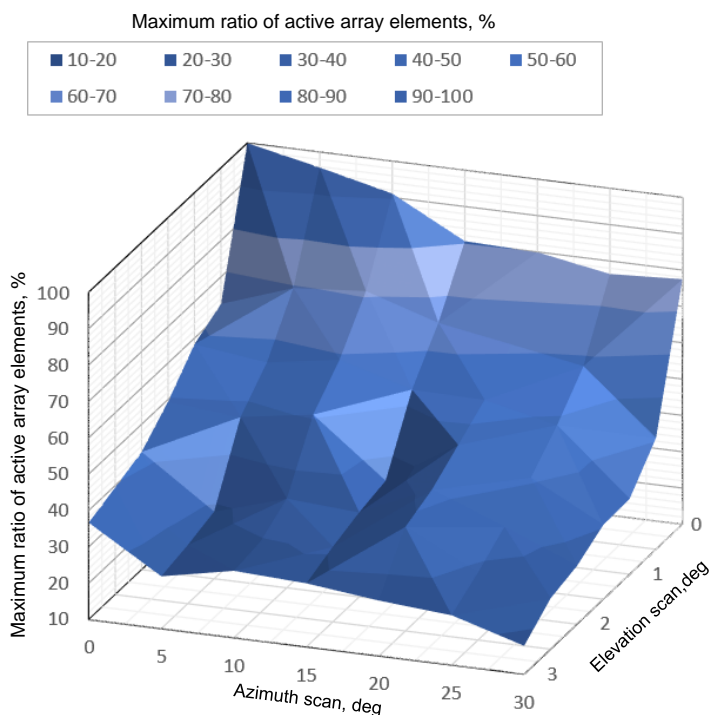
**Figure 7.30.** Array size for two-dimensional scanning with the complex offset double-reflector. Azimuth scan range up to  $\pm 20^\circ$  and elevation scan range up to  $\pm 3^\circ$ .



**Figure 7.31.** Achieved minimum array size of the complex offset double-reflector for two-dimensional scanning.

**Table 7.22.** Maximum RATA of the complex offset double-reflector for two-dimensional scanning.

Maximum RATA, %								
		Azimuth scan range, deg						
		0	$\pm 5$	$\pm 10$	$\pm 15$	$\pm 20$	$\pm 25$	$\pm 30$
Elevation scan range, deg	0	100	95.75	91.08	80.48	79.93	76.43	77.48
	$\pm 0.5$	62.56	69.44	71.11	64.84	61.45	57.94	40.65
	$\pm 1$	58.34	55.82	59.04	53.34	53.01	48.56	30.78
	$\pm 1.5$	49.41	47.63	50.81	35.10	47.47	40.94	30.45
	$\pm 2$	42.42	28.49	34.57	33.26	41.97	34.25	26.02
	$\pm 2.5$	39.47	26.11	29.59	30.66	38.63	28.51	23.96
	$\pm 3$	36.67	24.40	28.41	27.46	25.22	23.70	17.78

**Figure 7.32.** Maximum RATA of the complex offset double-reflector for two-dimensional scanning.**Table 7.23.** Minimum RATA of the complex offset double-reflector for two-dimensional scanning.

Minimum RATA, %								
		Azimuth scan range, deg						
		0	$\pm 5$	$\pm 10$	$\pm 15$	$\pm 20$	$\pm 25$	$\pm 30$
Elevation scan range, deg	0	100	34.26	20.75	11.81	10.24	20.78	51.91
	$\pm 0.5$	46.58	14.14	9.94	5.23	5.59	10.65	28.20
	$\pm 1$	43.17	6.50	6.77	6.39	5.35	5.29	20.84
	$\pm 1.5$	34.54	5.63	7.26	3.62	3.94	2.54	17.29
	$\pm 2$	26.89	4.95	3.18	2.85	3.15	6.91	12.69
	$\pm 2.5$	22.79	6.53	2.37	2.28	2.46	3.27	8.82
	$\pm 3$	20.63	5.23	1.95	1.76	1.58	1.36	5.19

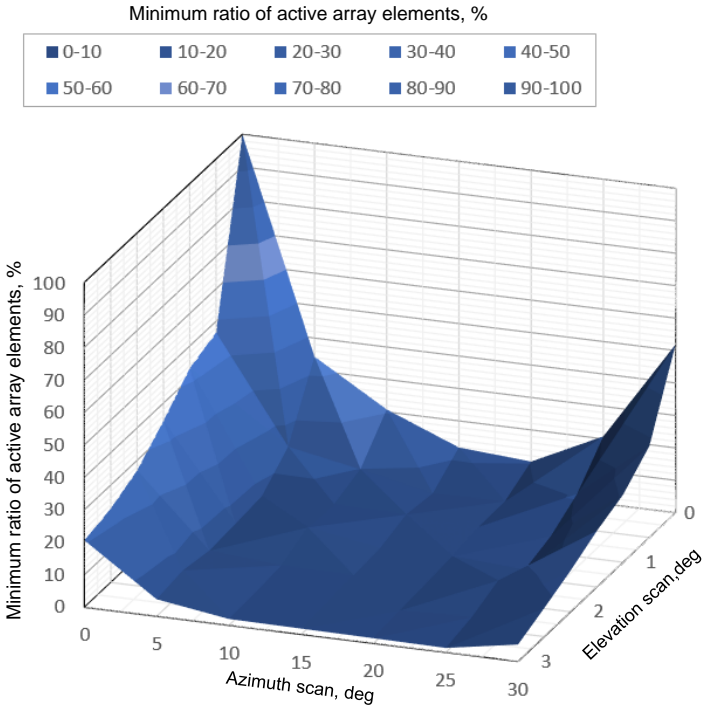


**Figure 7.33.** Minimum RATA of the complex offset double-reflector for two-dimensional scanning.

**Table 7.24.** RMS error of amplitude uniformity of complex offset double-reflector model for different two-dimensional scanning.

Amplitude uniformity maximum RMS error, %								
		Azimuth scan range, deg						
		0	±5	±10	±15	±20	±25	±30
Elevation scan range, deg	0	9.16	10.35	12.74	12.06	11.43	13.62	23.14
	±0.5	9.98	10.22	12.90	15.28	16.51	13.25	13.47
	±1	14.01	10.25	12.44	13.49	14.29	13.06	13.45
	±1.5	13.83	10.38	13.13	11.99	14.27	16.50	14.50
	±2	13.52	10.18	11.53	12.22	12.88	15.07	14.24
	±2.5	13.93	10.65	11.48	11.99	12.70	13.20	16.48
	±3	14.54	10.65	11.51	12.02	12.54	12.43	11.82

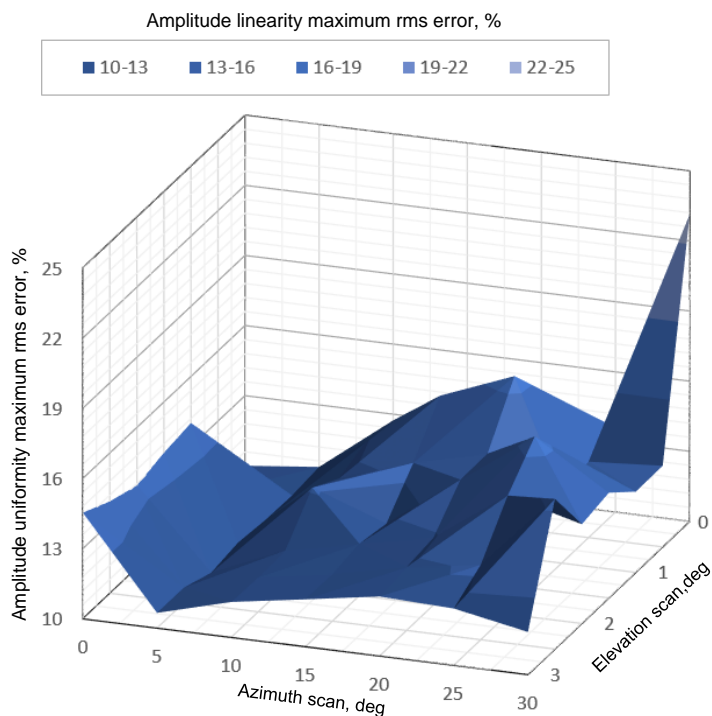


**Figure 7.34.** RMS error of amplitude uniformity of complex offset double-reflector model for different two-dimensional scanning.

**Table 7.25.** RMS error of phase linearity of complex offset double-reflector model for two-dimensional scanning.

		Phase linearity maximum RMS error, deg						
		Azimuth scan range, deg						
		0	±5	±10	±15	±20	±25	±30
Elevation scan range, deg	0	14.45	11.12	11.44	11.75	11.88	12.02	13.12
	±0.5	11.07	11.10	11.38	11.52	11.51	11.80	12.91
	±1	11.82	11.10	11.35	11.46	11.39	11.75	12.88
	±1.5	11.82	11.10	11.34	11.42	11.29	11.55	12.99
	±2	11.82	11.10	11.20	11.20	11.19	11.46	12.93
	±2.5	11.83	11.11	11.18	11.19	11.12	11.26	11.75
	±3	11.82	11.12	11.18	11.16	11.16	11.18	11.50

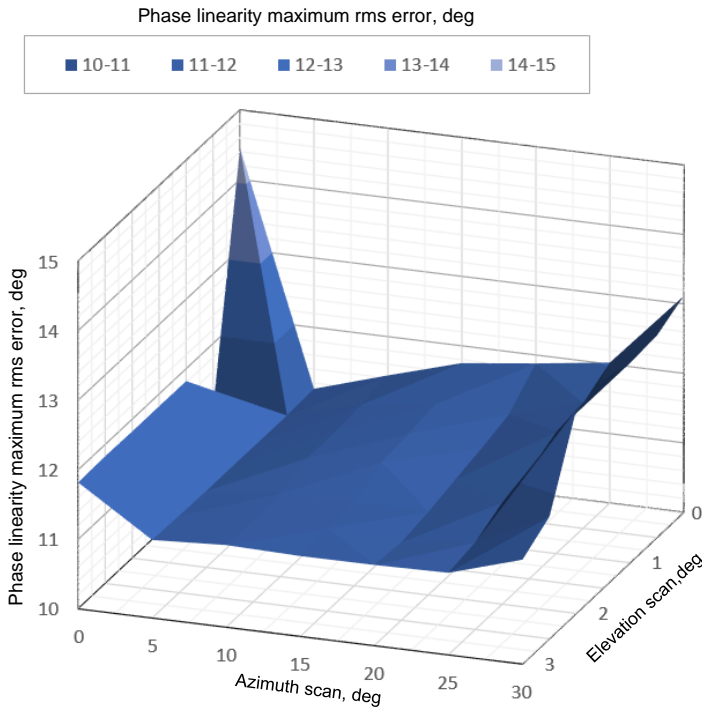


**Figure 7.35.** RMS error of phase linearity of the complex offset double-reflector model for two-dimensional scanning.

According to Table 7.21, as has been expected, the minimum required array size strongly depends on the scanning requirements in both planes. We can observe this in Figs. 7.29 and 7.30 that scanning in the elevation plane makes the array size minimization much more challenging. For example, for scanning up to  $\pm 20^\circ$  in the azimuth plane (red color in Figs. 7.29 and 7.30) the required array size is significantly larger in both dimensions if there is scanning in the elevation plane. For  $0^\circ$  scan in elevation, the array size is: 19 cm x 4,4 cm, whereas for  $\pm 3^\circ$  we obtain a size of 28,6 cm x 13,1 cm. The main reason is the difficulty to avoid blockage when we scan in the elevation plane. In addition, the focusing properties of the reflectors are sacrificed for wider scanning. The overall shapes of the reflector are more stretched in the azimuth plane where the main scanning is provided. Fig. 7.31 shows the array size versus the scan range. As could be expected a larger array size is required for an increased scan range in one of the planes.

The maximum RATA (Table 7.22 and Fig. 7.32) depends quite straightforward on the scan requirements. As could be expected for zero scans in both planes, all array elements are all-time active. With increasing scan range the maximum RATA is gradually decreasing and achieves a minimum for the widest scan ranges in both planes.

The minimum RATA (Table 7.23 and Fig. 7.33) has a maximum value for the non-scanning cases. For other situations, it is significantly lower and demonstrates that most of the array elements are not involved in two-dimensional scanning. The most challenging situation occurs for an elevation scan range up to  $\pm 3^\circ$ . In this case, the RATA drops to a few percent due to the significant beam deviation and limited focusing properties in the offset

plane.

Traditionally, the parabolic shape is considered the most common type of surface for classical prime focus reflectors [145]. It is also well-known that a spherical reflector could provide a minimum beam deviation during scanning [150]. Nevertheless, the situation for the investigated complex offset double-reflector is more complicated. The main reflector shape for different scan ranges is presented in Table 7.26, for the sub-reflector – in Table 7.27.

**Table 7.26.** Main reflector shape of the complex offset double-reflector for two-dimensional scanning. “H” stands for a hyperbolic shape and “P” – for a parabolic shape.

Main reflector shape								
		Azimuth scan range, deg						
		0	$\pm 5$	$\pm 10$	$\pm 15$	$\pm 20$	$\pm 25$	$\pm 30$
Elevation scan range, deg	0	H	P	P	P	H	P	P
	$\pm 0.5$	H	P	P	P	H	P	P
	$\pm 1$	H	P	P	P	P	H	P
	$\pm 1.5$	H	H	H	H	P	H	H
	$\pm 2$	H	H	H	H	P	H	P
	$\pm 2.5$	H	H	P	P	P	P	P
	$\pm 3$	H	P	P	P	P	P	P

**Table 7.27.** The sub-reflector shape of the complex offset double-reflector for two-dimensional scanning. “H” stands for a hyperbolic shape and “P” – for a parabolic shape.

Sub-reflector shape								
		Azimuth scan range, deg						
		0	$\pm 5$	$\pm 10$	$\pm 15$	$\pm 20$	$\pm 25$	$\pm 30$
Elevation scan range, deg	0	H	H	H	H	H	P	H
	$\pm 0.5$	H	H	H	H	H	P	H
	$\pm 1$	H	H	H	H	H	P	H
	$\pm 1.5$	H	H	H	H	H	H	H
	$\pm 2$	H	H	H	H	H	H	H
	$\pm 2.5$	H	H	H	H	H	H	P
	$\pm 3$	H	H	H	H	H	H	P

From Tables 7.26 and 7.27 we could see that parabolic reflector shapes are not always the optimal solutions. It really depends on the scanning requirements. For the main reflector, the parabolic shape has a mixed variation of hyperbolic and parabolic shapes whereas the optimal shape of the sub-reflector is always a hyperbolic shape.

## 7.5. Conclusion

Within this chapter, a detailed analysis of FPA configurations has been presented in terms of technology limits for wide-angle scanning. It has been shown how different optimizations could allow building systems with various performances in terms of key operating parameters like array size, EIRP, and the RATA.

It is possible to improve the best-case operation or create configurations where the entire array is active for a certain scan angle, with a maximum RATA of 100%. For instance, reflector configurations can be obtained with all elements active for broadside operation. At the same time, these configurations are capable to provide scanning within the defined range at the expense of a much lower RATA.

For improving the overall array performance, we only optimize the minimum RATA or improve the RATA over the whole scan range. The minimum RATA is always well below 100% when there is a scan capability realized. Nevertheless, we have shown that this parameter can be significantly improved using optimization. The proposed double-reflector is optimized for a  $\pm 20^\circ$  scan range and provides a minimum RATA of almost 60% while for classical prime-focused reflectors, this is equal to 19% only.

It is also possible to significantly reduce the required array size by a dedicated optimization. With a size of the main reflector of 80 cm, the minimum array size to provide  $\pm 20^\circ$  azimuth scanning is equal to 15.1 cm x 4 cm while for a classical prime focused reflector the array size is 52 cm x 9 cm [23]. The required minimum array size is significantly larger in both dimensions when we also require additional scanning in the elevation plane.

The ratio between the main and sub-reflector can also be subject to optimization. We have shown that there are optimum dimensions of the sub-reflector in order to achieve a minimum array size.

Overall, it has been shown that there is a tradeoff between different FPA characteristics. It is possible to minimize the array size and, at the same time, have a smaller number of active array elements or have a significant RATA within all scan ranges, but with a relatively large array size.

## 8. CONCLUSION AND RECOMMENDATIONS

---

The thesis has addressed the FPA technology, and more specifically an antenna system capable to operate in the frequency band of 20-40 GHz with a scan range up to  $\pm 20^\circ$  in the azimuth plane. The aim of the project has been to develop a hybrid system that combines the benefits of phased arrays and traditional reflector-based solutions. Next to this, an array design to be used as a wideband phased-array feed (PAF) is proposed and investigated against state-of-the-art antenna designs. The factors that determine the active wideband performance are investigated and analyzed for the chosen configuration of the reflector and array. Several prototypes have been manufactured and tested to support the design ideas. The proposed design allows us to get good active matching properties over a frequency band of more than one octave. This is based on the active reflection coefficient and the total active antenna reflection. At the same time, other relevant characteristics, like total radiation efficiency, phase-center stability, and reflector aperture efficiency remain at an acceptable level. In addition, an innovative reflector design was proposed for a wide scan range up to  $\pm 20^\circ$  in the azimuth plane and was tested in combination with the designed array feed. The demonstrated simulations and measurements fully support the visibility study of both reflector and array designs.

### 8.1. Thesis overview

In chapter 3 an overview of the main design challenges of FPAs has been provided. The main focus was to explore wideband concepts for the phased array feed and issues of scanning with the reflector. The proposed modified bow-tie antenna has been investigated and analyzed as a single element. It demonstrated excellent input matching properties over a frequency band of more than one octave and nearly reaches the theoretical Chu-Harrington limit. The reflector configuration for a narrow scan range has been proposed as a double-reflector concept. This design allows expanding the illuminated region of the array by a factor of 60 as compared to traditional prime-focus configurations. The proposed configuration also decreases the magnification factor by a factor of 2.5, as compared to the double-parabolic configuration for a  $\pm 1.5^\circ$  scan range. As a starting point for the reflector analysis for a wide-scan range application, a solid mathematical analysis of reflector shaping for wide-angle scanning was presented. Parabolic, hyperbolic, and spherical reflectors were defined based on the geometrical optics method in order to have the smallest deviation of the focused beam during wide-angle scanning. It has been demonstrated that it is possible to expand the illuminated region of the array by a factor of 3 for parabolic reflectors with axial displacement. In addition, it has been verified that the spherical reflector has the smallest deviation from the axis of revolution during wide-angle scanning.

Chapter 4 described the optimization algorithm based on geometrical optics for reflector optimization for wide scan-range applications with limited computational effort. The main result of this procedure is the new complex offset double reflector configuration for a

wideband FPA which is optimized for Ka-band applications with a scan range of  $\pm 20^\circ$  in the azimuth plane. The proposed reflector configuration was capable to maximize the number of simultaneously active array elements of the PAF and minimize the required total number of array elements for this wide scan range. To realize an aperture efficiency of at least 80% at 30 GHz, this concept has half of the antenna elements in the array be active during scanning for a scan range of  $\pm 10^\circ$  and at least a quarter of the array elements to be active for a scan range of  $\pm 20^\circ$ . This is a major improvement as compared to the scan capabilities of focal-plane arrays based on conventional single and double-parabolic reflector configurations. In addition, the FPA configuration has been optimized for wideband optical TTD beamforming which requires a linear phase distribution along the array elements. The phase linearity was obtained with an rms error of  $2.81^\circ$  at 30 GHz. The experiments from the realized prototype demonstrated good agreement between simulation and measurement and fully prove the required scan performance over a  $\pm 20^\circ$  scan range. The prototype demonstrated a high directivity up to 46 dBi at 30 GHz and 48 dBi at 40 GHz and aperture efficiency up to 83 % at 30 GHz and 77 % at 40 GHz.

An additional output of the optimization algorithm is the possibility to design more complex reflector configurations with multiple interactions. The design presented in chapter 4 fully combines the advantages of phased arrays in terms of wide-angle scanning and FPA systems in terms of high antenna gain. There is almost no beam deviation in the array plane anymore during scanning. The main operational feature of the new system is the double sub-reflector interaction. This FPA system achieved a 15 dB higher antenna gain as compared to a phased array with a size equal to the feed array of the proposed reflector system. Based on a minimum required 80% aperture efficiency at 30 GHz, the illuminated array region is increased by a factor of 200 as compared to traditional prime-focus configurations. In addition, the FPA configuration significantly reduces the required overall array size by a factor of 1.5 as compared to conventional double-parabolic reflector configurations. The proposed concept maximizes the percentage of active array elements up to 90% within the required scan range of  $\pm 10^\circ$  along the azimuth plane. Since almost the whole array is active, a high EIRP could be obtained with this configuration. The downside of this feature is the requirement of a relatively large sub-reflector. The size is 33.5 cm x 77.4 cm with a pronounced V-shape due to the discontinuity of the function defining the sub-reflector surface.

In chapter 5 several array designs were investigated in detail including the design challenges to obtain a wideband performance during scanning, issues for reflector aperture efficiency, and integration of wideband PAFs and reflectors. The array elements were based on a modified version of the well-known bow-tie antenna. The analysis was performed for both the classical prime-focus reflector and for a novel double reflector configuration that provides a wide-scan range. The optimal element spacing for various scan ranges was investigated. The proposed optimized array demonstrated excellent active matching properties over a frequency band of more than one octave and within a  $\pm 20^\circ$  azimuth scan range, realized with the double-reflector FPA. Multiple FPA prototypes were realized to validate the performance of our concept. The active wideband performance has been achieved with a limited sacrifice of the reflector aperture efficiency. The demonstrated tradeoff between array element spacing and FPA far-field properties allows to satisfy the design requirements of the total active reflection coefficient (TARC). Both simulation and measurement results demonstrate good agreements of the S-matrix and far-field patterns for a single antenna, for arrays, and for reflectors in combination with the PAFs.

Chapter 6 was focused on the FPA system-level demonstrator, which is the result of the collaboration of several sub-project into one system concept. The broadband wide-scan focal-plane array designed in this thesis was combined with optical beamforming using ring resonators and low-noise amplifiers with a large dynamic range. A system-level demonstrator was experimentally validated in receive mode. The concept provided an antenna gain of more than 40 dBi over a FoV of  $\pm 15^\circ$  at 28.5 GHz. It has been demonstrated that it is possible to use focal-plane arrays with a high antenna gain for beam-steering with a relatively large field-of-view up to  $\pm 20^\circ$ . By using an optical beamformer, a wideband system for the 20-40 GHz band can be created with a fiber-based interface to a central processing unit. Experimental results provided a good correlation with the predicted performance.

In chapter 7 it has been shown that the proposed double-reflector antenna system with wide-angle scan capabilities could be extended and further optimized for different use cases, for two-dimensional scanning in the frame of various design limits. The proposed reflector configurations were analyzed in terms of EIRP maximization, minimization of the required total number of array elements for a wide-scan range, and the highest number of simultaneously active array elements of the phased-array feed. Presented configurations have capabilities to operate in the scan range up to  $\pm 30^\circ$  in azimuth and  $\pm 3^\circ$  in elevation. It has been demonstrated how different optimizations could allow building systems with varying performance in terms of key operation parameters like array size, EIRP, and the number of active array elements. A detailed analysis was provided that demonstrates the potential applicability of this concept in future millimeter-wave applications.

## 8.2. Recommendations

Future FPA antenna systems require active wideband performance, wide-scan range operation, and a high level of integration and co-optimization between the reflector system and array feed. At the same time, the cost-related parameters should be carefully controlled in order for FPAs to compete with traditional phased arrays. This thesis presents outcomes that would make PFAs competitors to the phased arrays for a number of applications where the limited scan capability of FPAs could be improved and be sufficient. Nevertheless, there are a wide variety of PFAs characteristics which are required further development and improvements.

Based on the research presented in the thesis it is possible to specify the number of most promising recommendations for further development in the field of wideband FPAs with improved scanning capabilities:

- Extension of the GO model to include more flexibility in the reflector's shaping. Within this thesis, the surfaces of the investigated reflectors are described as second-order polynomial functions. This allows the investigation of traditional elliptical, spherical, and hyperbolic reflectors with different discontinuities, axial displacement, and different mutual positions of reflectors and arrays. Nevertheless, it is possible to use other types of functions to describe the reflector surface like polynomials of higher order. In addition, we can investigate the possibility to describe different parts of the reflectors by different functions. Those will allow to provide further reflector optimizations for dedicated reflector illumination and scanning capability.

- Increased scan range by using shaped main reflectors. Within this thesis, the surface of the main reflector has been described differently in elevation and azimuth planes. This has been done in order to satisfy different scanning requirements in those orthogonal planes. As could be expected scanning demands in the azimuth plane are significantly more challenging than in elevation. Nevertheless, the overall shape of the main reflector has been a traditional circular dish. It is possible to significantly improve the scanning properties if to reshape the main dish and extend its dimension in the more demanding scanning plane. The best example of such a design is a torus reflector antenna which has a wider dimension in the horizontal plane to provide increased scan range in the azimuth.
- Further extend the idea of reflector optimization to obtain  $360^\circ$  azimuth scanning. This could be done by creating the reflector from a circular disk with the surface of revolution around the vertical. For this design, only part of the reflector could be involved for certain azimuth scans and effective use of the array will be created by reflector optimization. A conceptual example of such a system is presented in Fig. 8.1. This type of reflector could be interesting for base station applications and compete with phased arrays in the field of mobile communication. Nevertheless, the idea requires extensive optimization and evaluation against traditionally used based stations.
- Investigation of cost minimization and control of cost-related parameters. It is obvious that the applicability of FPA is only possible in applications where there is a clear price benefit compared to the well-known phased arrays. Thus, it is important to analyze and compare not only the RF performance of the FPAs compared to phased arrays but to take into account cost-related factors. For example, the required array feed size should be minimized as well as further improvement of the RATA is required. As we know the most costly part of FPAs are PAFs where each element requires amplitude and phase tuning. The most beneficial optimization is to use all available array elements as much as possible within the whole scan range, in other words, to maximize the RATA. This could be the main priority for FPAs design and could be achieved by further improvement of the optimization algorithm for this dedicated goal.
- As shown in chapter 3, the frequency band is a tradeoff to the size of the array element, since the array element should be large enough to be capable to provide the minimum required frequency band. In its turn, the size of the array element will limit the available element spacing within an array. This could affect the mutual coupling within the array as a result of the active wideband performance. In addition, the element spacing defines the quality of the far-field pattern provided by the reflector. Thus, further investigation and optimization are required of the trade-off between achievable wideband performance and quality of the FPAs far field pattern.

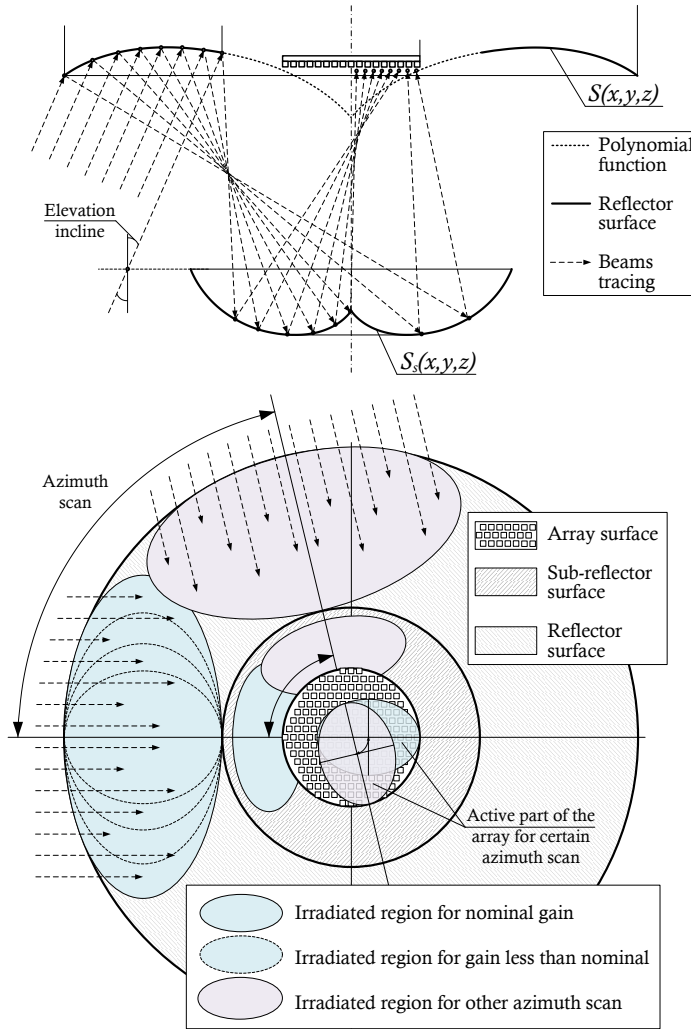


**Figure 8.1.** Reflector base station with  $360^\circ$  azimuth scanning.

- In this thesis it is claimed that reflector and PAF have been mutually optimized for better performance. This has been done from the perspective of an optimization of field uniformity along the array surface and optimization of the reflector illumination by the array within a wide scanning range. Nevertheless, the PAF and reflector always have been simulated separately by field export-import functions of CST [138] and GRASP [39]. Thus, the next step could be an investigation of combined simulation models where the effect of mutual reflection from the reflector and PAF could be taken into account. For example, using Ansys HFSS [194] with applying hybrid boundaries methods.
- The proposed reflector design in this thesis is based on the multi-variable optimization goal, including the minimum required array size to realize a certain scan range, the maximization of the ratio of active versus non-active array elements, and the minimization of the amplitude and phase errors along the array.

The goals have been combined in one function by balanced coefficients and optimized for scanning with a reflector up to  $\pm 20^\circ$  in the azimuth plane. The choice of balanced coefficients is an open question, which could be investigated further. In addition, it is important to study further how those balances between different characteristics could be matched the best with different requirements of the FPAs. Improving one of the performance aspects of the FPAs causes the design restriction or need to increase the cost or complexity of other design parameters. Every variation in FPA's requirements will lead to a different optimization process and a different balance between design characteristics. Overall exploring the different optimization processes is an essential recommendation for future research.

## BIBLIOGRAPHY

---

- [1] Parkvall S., Dahlman E., Furuskär A., and Frenne. M., "NR - The new 5G," *IEEE Communications Standards Magazine*, 2017.
- [2] 3. T. R. 3. V14.0.0, "Study on Scenarios and Requirements for Next Generation Access Technologies (Release 14)," 2016.
- [3] DeBoer D.R., et al., "Australian SKA Pathfinder: A High-Dynamic Range Wide-Field of View Survey," *Proceedings of the IEEE*, vol. 97, no. 8, pp. 1507-1521, 2009.
- [4] Adela B.B., Zeijl P.T.M. van, Johannsen U., Smolders A.B., "On-chip antenna integration for millimeter-wave single-chip FMCW radar," *IEEE Transactions on Antennas and Propagation*, vol. 64, no. 8, 2016.
- [5] Hajimiri A., Hashemi H., Natarajan A., Guan X., Komijani A., "Integrated Phased Array Systems in Silicon," *Proceedings of the IEEE*, vol. 93, no. 9, pp. 1637-1655, 2005.
- [6] Essing J.A.J., Leenaerts D.M.W., and Mahmoudi R., "A 27GHz, 31dBm power amplifier in a 0.25um SiGe: BiCMOS technology," in *Proceeding of Bipolar/BiCMOS Circuits and Technology Meeting (BCTM)*, Coronado, CA, USA, 2014.
- [7] Smolders A.B., "Design and construction of a broadband wide-scan angle phased-array antenna with 4096 radiating elements, Phased Array Systems, and Technology," in *IEEE International Symposium*, 1996.
- [8] Benthem, P; Kant, G.W.; Wijnholds, S.J.; Arts, M.J.; Maaskant, R.; Ruiter, M.; van der Wal, E., "Aperture array development for future large radio telescopes," in *Proceedings of the 5th European Conference Antennas and Propagation (EUCAP)*, 05/2011.
- [9] Zamanifekri, A.; Smolders, A.B., "Optimum configuration of focal plane arrays for satellite communication," in *2013 IEEE International Symposium on Antennas and Propagation & USNC/URSI National Radio Science Meeting*, 07/2013.
- [10] Cooley, M., "Phased Array Fed Reflector (PAFR) antenna architectures for space-based sensors," in *IEEE Aerospace Conference Proceedings*, 06/2015.
- [11] Brookner, E, "Phased array radars-past, present and future," *RADAR 2002*, pp. 104-113, 2002.
- [12] Dubok A., Al-Rawi A., Gerini G., Smolders A. B., "Reflector Synthesis for Wide-Scanning Focal Plane Arrays," *IEEE Transactions on Antennas and Propagation*, vol. 67, no. 3, 2019.
- [13] Ivashina M. V., van 't Klooster C. G. M., "Focal Fields in Reflector Antennas and Associated Array Feed Synthesis for High-Efficiency Multi-Beam Performances," in *25<sup>th</sup> ESA Antenna Workshop on Satellite Antenna Technology*, Noordwijk, The Netherlands, 2002.

- [14] Verheijen, M. A. W. and Oosterloo, T. A. and van Cappellen, W. A. and Bakker, L. and Ivashina, M. V. and van der Hulst, J. M., "Apertif, a focal plane array for the WSRT," in *AIP Conference Proceedings*, 2008.
- [15] Al-Rawi, A.; Dubok, A.; Herben, M.H.A.J.; Smolders, A.B., "Point-to-point Radio Link Variation at E-band and Its Effect on Antenna Design," in *Progress In Electromagnetics Research Symposium Proceedings*, Prague, Czech Republic, July 2015.
- [16] Shu S., Theodore S. R., Mansoor S., Pan T., Jianhua Z., Peter J. S., "Propagation Models and Performance Evaluation," *IEEE TRANSACTIONS ON VEHICULAR TECHNOLOGY*, vol. 67, no. 9, pp. 8422-8439, 2018.
- [17] Johannsen U., Bressner T., Elsakka A, Smolders A.B., Johansson M/, "Base Station Antenna Systems for mm-Waves," in *Proceedings of the International Symposium on Antennas and Propagations*, 2020.
- [18] Dubok, A.; Al-Rawi, A.; Herben, M.H.A.J.; Gerini, G.; Smolders, A.B., "Wide-angle scanning reflector configuration for focal plane arrays," in *2016 IEEE International Symposium on Antennas and Propagation, APS/URSI*, Fajardo, Puerto Rico, 26 June - 1 July 2016.
- [19] Pelorossi, F.; Toso, G.; Angeletti, P., "On the Scanning Properties of Imaging Antennas Based on Dual Confocal Paraboloidal Reflectors," *Progress In Electromagnetics Research*, vol. 37, p. 95–107, 2014.
- [20] Huber S., Rommel T., Patyuchenko A., Laskowski, P., "A Reflector Based Digital Beamforming Demonstrator," in *European Conference on Synthetic Aperture Radar (EUSAR)*, 2014.
- [21] Dubok, A; Al-Rawi, A; Tessema, N; Tangdionga, E; Herben, M.H.A.J; Gerini, G; Smolders, A. B, "Double Reflector Configuration for Optimal Exposure of Wideband Focal Plane Arrays with Optical Beamforming," *IEEE Transactions on Antennas & Propagation*, no. 10.1109/TAP.2017.2709620, 2017.
- [22] Dubok, A.; Al-Rawi, A.; Gerini, G.; Smolders, A.B., "Extreme Scanning Focal-plane Arrays using a Double," *Transactions on Antennas and Propagation. Communication*, vol. 68, no. 7, pp. 5686-5690, 2020.
- [23] Dubok A., Al-Rawi A., Gerini G., Smolders A. B., "Reflector Synthesis for Wide-Scanning Focal Plane Arrays," *IEEE Transactions on Antennas and Propagation*, vol. 67, no. 3, 2019.
- [24] Toso, G., "The Beauty of Multibeam Antennas," in *Proceedings of the 9<sup>th</sup> European Conference on Antennas and Propagation (EUCAP)*, Lisbon, Portugal, 12-17 April 2015.
- [25] Ng Mou Kehn, M.; Shafai, L., "Characterization of dense focal plane array feed for parabolic reflectors in achieving closely overlapping or widely separated multiple beams," *Radio Sci.*, vol. 44(3), 25 June 2009.
- [26] Al-Rawi, A; Dubok, A; Geluk, S.J; de Hon, B.P; Herben, M.H.A.J.; Smolders, A.B., "Increasing the EIRP by using FPA-fed reflector antennas," in *IEEE International Symposium on Antennas and Propagation (APSURSI)*, Fajardo, Puerto Rico, 2016.
- [27] Smolders, A.B., Dubok, A., Tessema, N.M., Chen, Zhe, Al-Rawi, A.N.H., Johannsen, U., Bressner, T.A.H., Milosevic, D., Gao, H., Tangdionga, E., Gerini, G., Baltus, P.G.M., Geurts, Marcel & Koonen, A.M.J., "Building 5G millimeter-

- wave wireless infrastructure: wide-scan focal plane arrays with broadband optical beamforming," *IEEE Antennas and Propagation Magazine*, 2018.
- [28] Al-Rawi, A.; Dubok, A.; Herben, M.H.A.J.; Smolders, A.B., "Point-to-point Radio Link Variation at E-band and Its Effect on Antenna Design," in *Progress In Electromagnetics Research Symposium Proceedings*, Prague, Czech Republic, July 2015.
  - [29] Al-Rawi, A., Dubok, A., Geluk, S.J., Herben, M.H.A.J. & Smolders, A.B., "A comparative study on the parabolic and spherical FPA-fed reflector antenna," in *10<sup>th</sup> European Conference on Antennas and Propagation, EuCAP 2016*, Davos, Switzerland, 2016.
  - [30] Al-Rawi, A.; Dubok, A.; Geluk, S.J.; de Hon, B.P.; Herben, M.H.A.J.; Smolders, A.B., "Increasing the EIRP by using FPA-fed reflector antennas," in *IEEE International Symposium on Antennas and Propagation (APSURSI)*, Fajardo, Puerto Rico, 2016.
  - [31] Dubok, A.; Al-Rawi, A.; Herben, M.H.A.J.; Smolders, A.B., "Wideband focal plane connected array," in *10<sup>th</sup> European Conference on Antennas and Propagation, EuCAP 2016*, Davos, Switzerland, 2016.
  - [32] Ferendeci, Altan M., "Smart electronic phase control for phased array antennas," in *Aerospace and Electronics Conference (NAECON)*, Fairborn, OH, USA, 14-16 July 2010.
  - [33] A. Dubok, A. Al-Rawi, M. Herben, and A. B. Smolders, "Fundamental challenges for wideband antenna elements in focal-plane arrays," in *The 9th European Conference on Antennas and Propagation*, Lisbon Portugal, 2015.
  - [34] FREEBEAM project, <http://www.nwo.nl/onderzoek-en-resultaten/onderzoeksprojecten/40/2300173540.html>.
  - [35] Marpaung D.; Roeloffzen, C.; Heideman, R.; Leinse, A.; Sales, S.; Capmany, J., "Integrated microwave photonics," *Laser & Photon*, vol. 7(4), p. 506–538, 2013.
  - [36] Burla, M.; Marpaung, D. A. I.; Zhuang, L.; Rezaul Khan, M.; Leinse, A.; Beeker, W.; Hoekman, M.; Heideman, R. G.; Roeloffzen, C. G. H., "Multiwavelength-Integrated Optical Beamformer Based on Wavelength Division Multiplexing for 2-D Phased Array Antennas," *Journal of Lightwave Technology*, vol. 32, no. 20, pp. 3509- 3520, October 15, 2014.
  - [37] Tessema, N.M.; Cao, Z.; Dubok, A.; Tangdiongga, E.; Smolders, A.B.; Koonen, A.M.J., "A Si3N4 PIC for optically controlled 2D radio beamforming in satellite communications," in *MWP 2015: 2015 International Topical meeting on Microwave Photonics (MWP)*, Paphos, Cyprus, 26-29 October 2015.
  - [38] Zimmerman, M.; Lee, S.W.; Houshmand, B.; Rahmat-Samii, Y.; Acosta, R., "A Comparison of Reflector Antenna Designs for Wide-Angle Scanning," in *ASA Technical Memorandum 101459. NASA Technology Workshop for Earth Science Geostationary Platforms*, Hampton, Virginia, USA, September 21-22, 1988.
  - [39] TICRA Software, <http://www.ticra.com/products/software/grasp>.
  - [40] R. C. Spencer, C. J. Sletten, and J. E. Walsh, "Correction of spherical aberration by a phased line source," in *Proc. National Electronics Conference*, vol. 5. *National Engineering Conference, inc.*, 1949.
  - [41] A. Love, "Spherical reflecting antennas with corrected line sources," *Proc. IRE*,, vol. 10, no. 5, p. 529–537, 1962.

- [42] W. E. Gordon, "Arecibo Ionospheric Observatory," *Science*, vol. 146, p. 26–30, 1964.
- [43] R. M. W. M. a. H. J. C. Sletten, "Corrective line sources for paraboloids," *Antennas and Propagation, IRE Transactions*, vol. 6, no. 3, p. 239–251, 1958.
- [44] R. J. Mailloux, "Hybrid antennas," *The Handbook of Antenna Design, ser. IEE electromagnetic waves series*, vol. 1, p. 415–465, 1982.
- [45] R. N. A. a. W. C. D. J. L. J. Ricardi, "A mechanically fixed radar antenna with scanning capability," *Massachusetts Inst. of Tech. Lexington Lincoln Lab., Tech. Rep. 315G-2*, 1961.
- [46] C. F. a. H. L. H. Ward, "Gca radars: Their history and state of development," *Proc. IEEE*, vol. 62, no. 6, p. 705–716, 1974.
- [47] S. J. B. a. W. A. Imbriale, "Array feed synthesis for correction of reflector distortion and vernier beam steering," *IEEE Trans. Antennas Propag*, vol. 36, no. 10, p. 1351–1358, 1988.
- [48] P. L. a. R. Martin, "Efficient aberration correction with a transverse focal plane array technique," *Proc. IRE International Convention Record*, vol. 12, p. 125–131, 1964.
- [49] A. W. R. a. M. J. Withers, "Beam-scanning primary feed for parabolic reflectors," *Electronics Letters*, vol. 5, p. 39–41, 1969.
- [50] P. Shelton, "Multiple-feed systems for objectives," *IEEE Trans. Antennas Propag*, vol. 13, no. 6, p. 992–994, 1965.
- [51] E. A. Ohm, "A proposed multiple-beam microwave antenna for earth stations and satellites," *Bell Systems Technical Journal*, vol. 53, p. 1657–1665, 1974.
- [52] S.-W. L. a. R. M. V. Galindo-Israel, "Synthesis of a laterally displaced cluster feed for a reflector antenna with application to multiple beams and contoured patterns," *IEEE Trans. Antennas Propag*, vol. 26, no. 2, p. 220–228, 1978.
- [53] E. Ohm, "Multifixed-beam satellite antenna with full area coverage and a rain-tolerant polarization distribution," *IEEE Trans. Antennas Propag.*, vol. 29, no. 6, p. 937–943, 1981.
- [54] T. S. B. S. G. H. a. Y. K. C. G. T. Poulton, "Rigorous design of an antenna for AUSSAT-B," *IEEE AP-S Int. Symp. Digest*, vol. 4, p. 1900–1903, 1990.
- [55] G. T. Poulton and S. G. Hay, "Efficient design of shaped reflectors using successive projections," *Electronics Letters*, vol. 27, no. 23, p. 2156–2158, 1991.
- [56] H. T. Y. M. a. T. O. K. Tokunaga, "Electric design and prototype development of phased array feed for onboard reflector antennas," *Electronics and Communications in Japan*, vol. 84, no. 6, p. 22–31, 2001.
- [57] W. L. W. a. J. M. Howell, "Communications satellite antennas with on-orbit pattern flexibility," *Microwave Journal*, vol. 8, p. 22–43, 2004.
- [58] P. K. a. R. G. R. Sorbello, "Feed array and beam forming network design for a reconfigurable satellite antenna," *IEEE AP-S Int. Symp. Digest*, vol. 18, p. 78–81, 1980.
- [59] P. Balling, "Digital beamforming antenna RF design and analysis impact of amplifier errors," in *8th COST 260 Meeting on Smart Antenna Computer-Aided Design & Technology*, Rennes, France, 2000.

- [60] T. S. Bird, "Mode coupling in a planar circular waveguide array," *Microwaves, Optics, and Acoustics*, vol. 3, no. 5, p. 172–180, 1979.
- [61] T. S. Bird, "Analysis of mutual coupling in finite arrays of different-sized," *IEEE Trans. Antennas Propag.*, vol. 38, no. 2, p. 166–172, 1990.
- [62] T. S. B. a. D. G. Bateman, "Mutual coupling between rotated horns in a ground plane," *IEEE Trans. Antennas Propag.*, vol. 42, no. 7, p. 1000–1006, 1994.
- [63] T. S. Bird, "Improved solution for mode coupling in different-sized circular apertures and its application," *IEE Proc. H: Microwaves Antenna. Propag.*, vol. 143, no. 6, p. 457–464, 1996.
- [64] T. S. Bird, "Mutual coupling in arrays of coaxial waveguides and horns," *IEEE Trans. Antennas Propag.*, vol. 52, no. 3, p. 821–829, 2004.
- [65] Balanis C. A., *Antenna Theory - Analysis and Design*, New Jersey: John Wiley & Sons, 2005.
- [66] J. Hung, J. A. Encinar, *Reflectarray antennas*, John Wiley and Sons Ltd, 2007.
- [67] E. D. T. Emerson and J. M. Payne, "Multi-feed systems for radio telescopes," in *Astron. Soc. Pac. Conf.*, Tucson, AZ, 1994.
- [68] W. E. W. T. S. B. M. J. D. R. D. E. K. C. F. R. F. H. M. W. S. R. A. V. R. L. W. a. A. E. W. L. Staveley-Smith, "The Parkes 21 cm multibeam receiver," *Astron. Soc. Aust.*, vol. 13, p. 243–248, 1996.
- [69] J. F. Johansson, "Fundamental limits for focal-plane array efficiency," in *Multi-feed systems for radio telescopes, ser. Astron. Soc. Pac. Conf.*, Tucson, AZ, 1994.
- [70] B. Veidt, "Focal-plane array architectures: horn clusters vs. phase-array techniques," in *International Square Kilometre Array Steering Committee, SKA Memo 71*, 2006.
- [71] D. B. Hayman, "Beamforming and Evaluation of Focal Plane Arrays for Radio Astronomy," in *Doctor thesis*, Sydney, 2011.
- [72] S. G. Hay, "Comparison of single-ended and differential beamforming on the efficiency of a checkerboard phased array feed in offset and front-fed reflectors," in *Eu. Conf. on Antennas and Propagation (EuCAP)*, 2010.
- [73] O. A. I. R. M. W. A. v. C. L. B. a. T. O. M. V. Ivashina, "Off-axis beam performance of focal plane arrays for the Westerbork Synthesis Radio Telescope—initial results of a prototype system," in *IEEE AP-S Int. Symp. Digest*, Charleston, SC, 2009.
- [74] M. V. W. v. C. L. B. G. H. a. M. I. T. Oosterloo, "Apertif—the focal-plane array system for the WSRT," in *Widefield Science and Technology for the SKA, SKADS Conference*, Chateau de Limelette, Belgium, 2009.
- [75] J. B. a. S. Hay, "Achievable field of view of checkerboard phased array feed," in *Int. Conf. on Electromagnetics in Advanced Applications (ICEAA)*, 2010.
- [76] A. W. R. a. M. J. Withers, "Beam-scanning primary feed for parabolic reflectors," *Electronics Letters*, vol. 5, p. 39–41, 1969.
- [77] J. B. a. P. C. T. Bird, "Multiple-beam dual-offset reflector antenna with an array feed," *Electronics Letters*, vol. 14, no. 14, p. 439–441, 1978.
- [78] T. S. Bird, "Contoured-beam synthesis for array-fed reflector antennas by field correlation," *Proc. Inst. Elect. Eng. Microwaves*, vol. 129, p. 293–298, 1982.

- [79] M. F. J. M. F. A. M. a. S. C. N. S. F. Maharimi, "Impact of number elements on array factor in linear arrays antenna," *IEEE 8th International Colloquium on Signal Processing and its Applications*, p. 296–299, 2012.
- [80] S. K. R. a. M. Q. Tang, "Stepped-reflector antenna for dual-band multiple beam Satellite communications payloads," *IEEE Transactions on Antennas and Propagation*, vol. 54, no. 3, pp. 801–811, 2006.
- [81] C. F. a. H. L. H. Ward, "Gca radars: Their history and state of development," *Proc. IEEE*, vol. 62, no. 6, p. 705–716, 1974.
- [82] P. L. a. R. Martin, "Efficient aberration correction with a transverse focal plane array technique," *Proc. IRE International Convention Record*, vol. 12, p. 125–131, 1964.
- [83] S. J. B. a. W. A. Imbriale, "Array feed synthesis for correction of reflector distortion and vernier beamsteering," *IEEE Trans. Antennas Propag*, vol. 36, no. 10, p. 1351–1358, 1988.
- [84] T. J. C. a. P. J. Napier, "The focal plane coherence function of an imaging antenna and its use in measuring and correcting aberrations," *Radio Sci.*, vol. 23, p. 739–748, 1988.
- [85] R. Padman, "Optical fundamentals for array feed," in *Multifeed systems for radio telescopes, ser. Astron. Soc. Pac. Conf.*, Tucson, AZ, 1994.
- [86] K. B. a. Y. Rahmat-Samii, "An array-compensated spherical reflector antenna for a very large number of scanned beams," *IEEE Trans. Antennas Propag.*, vol. 53, no. 11, p. 3547–3555, 2005.
- [87] A. W. R. a. D. E. N. Davies, "Electronically controllable primary feed for profile-error compensation of large parabolic reflectors," *Proc. IEE*, vol. 117, no. 2, p. 351–358, 1970.
- [88] W. T. S. W. L. Smith, "A pattern synthesis technique for array feeds to improve radiation performance of large distorted reflector antennas," *IEEE Trans. Antennas Propag.*, vol. 40, p. 57–62, 1992.
- [89] L. L. P. a. A. G. Pino, "Synthesis of array feeds for optimum illumination of reflector antennas and low spillover," *Microwave Opt Technol Lett*, vol. 15, no. 5, p. 334–338, 1997.
- [90] A. W. R. a. D. E. N. Davies, "Electronically controllable primary feed for profile-error compensation of large parabolic reflectors," *Proc. IEE*, vol. 117, no. 2, p. 351–358, 1970.
- [91] S.-W. L. a. R. M. V. Galindo-Israel, "Synthesis of a laterally displaced cluster feed for a reflector antenna with application to multiple beams and contoured patterns," *IEEE Trans. Antennas Propag.*, vol. 26, no. 2, p. 220–228, 1978.
- [92] T. S. B. S. G. H. a. Y. K. C. G. T. Poulton, "Rigorous design of an antenna for AUSSAT-B," *IEEE AP-S Int. Symp. Digest*, vol. 4, p. 1900–1903, 1990.
- [93] G. T. P. a. S. G. Hay, "Efficient design of shaped reflectors using successive projections," *Electronics Letters*, vol. 27, no. 23, p. 2156–2158, 1991.
- [94] W. L. W. a. J. M. Howell, "Communications satellite antennas with on-orbit pattern flexibility," *Microwave Journal*, vol. 8, p. 22–43, 2004.

- [95] K. F. W. J. L. J. W. D. J. J. R. F. a. R. D. N. B. D. Jeffs, "Signal processing for phased array feeds in radio astronomical telescopes," *IEEE J. Sel. Topics Signal Process.*, vol. 2, no. 5, p. 635–646, 2008.
- [96] K. F. W. B. D. J. J. R. F. a. R. B. C. K. Hansen, "Interference mitigation using a focal plane array," *Radio Sci.*, vol. 40, 2005.
- [97] K. F. W. R. F. R. N. J. L. D. J. J. W. M. E. a. A. S. B. D. Jeffs, "Interference cancellation with a focal plane array," in *Presentation at NROA, Green Bank*, 2007.
- [98] L. B. a. P. A. T. Gunaratne, "Broadband beamforming of focal plane array (FPA) signals using real-time spatiotemporal 3D FIR frustum digital filters," *IEEE Trans. Antennas Propag.*, vol. 59, no. 6, p. 2029–2040, 2011.
- [99] J. E. a. M. R. B. Pueo, "Precise control of beam direction and a beamwidth of linear loudspeaker arrays," *Processing Workshop Proceedings, 2004 Sensor Array and Multichannel Signal*, p. 538–541, 2004.
- [100] M. K. a. P.-S. K. M. Ivashina, "Optimal number of elements and element spacing of wide-band focal plane arrays for a new generation radio telescope," in *Antennas and Propagation, 2007. EuCAP 2007. The Second European Conference*, 1–7, 2007.
- [101] M. K. P.-S. K. a. R. M. M. Ivashina, "Decoupling efficiency of a wideband Vivaldi focal plane array feeding a reflector antenna," *Antennas and Propagation, IEEE Transactions on*, vol. 57, no. 2, p. 373–382, 2009.
- [102] J. B. A. F. G. G. H. H. A. I. a. A. N. A. Baryshev, "Progress in antenna-coupled kinetic inductance detectors," *Terahertz Science and Technology, IEEE Transactions on*, vol. 1, no. 1, p. 112–123, 2011.
- [103] T. B. K. E. a. P. H. D. Hayman, "Experimental demonstration of focal plane array beamforming in a prototype radiotelescope," *Antennas and Propagation, IEEE Transactions on*, vol. 58, no. 6, p. 1922–1934, 2010.
- [104] R. N. J. d. V. N. R. a. E. L. D. Glynn, "Realization of a focal plane array receiver system for radio astronomy applications," in *Microwave Conference, 2009. EuMC 2009*, 2009.
- [105] B. K. T. G. Y. P. K. a. S. W. J. Leech, "Experimental investigation of a low-cost, high-performance focal-plane horn array," *Terahertz Science and Technology, IEEE Transactions on*, vol. 2, no. 1, p. 61–70, 2012.
- [106] J. B. W. v. C. G. K. a. J. d. V. A. van Ardenne, "Extending the field of view with phased array techniques: Results of European SKA research," *Proceedings of the IEEE*, vol. 97, no. 8, p. 1531–1542, 2009.
- [107] A. M. a. P. Smith, "Scanning capabilities of large parabolic cylinder reflector antennas with phased-array feed," *IEEE Transactions on Antennas and Propagation*, vol. 29, no. 3, pp. 455–462, 1981.
- [108] M. N. M. K. a. L. Shafai, "Characterization of dense focal plane array feeds for parabolic reflectors in achieving closely overlapping or widely separated multiple beams," *RADIO SCIENCE*, vol. 44, 2009.
- [109] M. N. M. K. P. K. a. R. M. M. V. Ivashina, "Decoupling Efficiency of a Wideband Vivaldi Focal Plane Array Feeding a Reflector Antenna," *IEEE Transactions on Antennas and Propagation*, vol. 57, no. 2, pp. 373–382, 2009.
- [110] O. I. R. M. W. v. C. a. T. O. M. Ivashina, "An optimal beamforming strategy for wide-field surveys with phased-array-fed reflector antennas," *Antennas and Propagation, IEEE Transactions on*, vol. 59, no. 6, p. 1864–1875, 2011.

- [111] M. I. K. P. P. N. C. C. N. S. S. S. A. I. D. H. a. K. K. O. Iupikov, "Dense focal plane arrays for push broom satellite radiometers," in *Antennas and Propagation (EuCAP), 2014 8th European Conference*, 2014.
- [112] K. P. P. N. N. S. S. S. M. I. O. I. A. I. D. H. a. K. K. C. Cappellin, "Novel multi-beam radiometers for accurate ocean surveillance," in *Antennas and Propagation (EuCAP), 2014 8th European Conference on*, 2014.
- [113] N. F. C. a. Y. J. G. S. Gao, "Guest editorial: Antennas for satellite communications," *IEEE Transactions on Antennas and Propagation*, vol. 63, p. 1186–1190, 2015.
- [114] K. J. M. a. E. Lier, "Theoretical and experimental study of interference in multibeam active phased array transmit antenna for satellite communications," *IEEE Transactions on Antennas and Propagation*, vol. 52, no. 2, pp. 587–592, 2004.
- [115] C. C. A. P. G. E. C. F. V. a. E. V. A. Bosisio, "Analysis and applications of short-distance site diversity techniques for 20/30 GHz communication links," *Proceedings of GLOBECOM*, pp. 749–753, 1995.
- [116] M. V. M. W. a. Q. W. P. Stoica, "Optimal direction finding with partially calibrated arrays in spatially correlated noise fields," *Proceedings of 1994 28th Asilomar Conference on Signals, Systems and Computers*, pp. 643–647, 1994.
- [117] Y. H. R. S. a. F. A. A. Zaghloul, "Advances in multibeam communications satellite antennas," *Proceedings of the IEEE*, vol. 78, no. 7, p. 1214–1232, 1990.
- [118] M. N. M. K. a. L. Shafai, "Characterization of dense focal plane array feeds for parabolic reflectors in achieving closely overlapping or widely separated multiple beams," *Radio Science*, vol. 44, no. 3, 2009.
- [119] A. Kumar, "An array fed dual reflector antenna at 36 GHz," *Digest on Antennas and Propagation Society International Symposium*, vol. 3, p. 1590–1593, 1989.
- [120] A. Z. a. E. D. G. B. S. L. S. S. R. M. Sorbello, "20-GHz mmic modules," *COMSAT al Review*, vol. 16, no. 2, p. 339–373, 1986.
- [121] A. Z. a. A. B. Smolders, "Optimum configuration of focal plane arrays for satellite communication," in *2013 IEEE Antennas and Propagation Society International Symposium (APSURSI)*, 2013.
- [122] K. F. W. a. P. Russer, "Quantifying the noise penalty for a mutually coupled array," in *IEEE AP-S Int. Symp. Digest*, San Diego, CA, 2008.
- [123] M. R. a. D. George, "Estimation of coupled noise in low noise phased array antennas," *IEEE Trans. Antennas Propag.*, vol. 59, no. 6, p. 1846–1854, 2011.
- [124] S. G. H. a. J. D. O'Sullivan, "Analysis of common-mode effects in a dual-polarized planar connected-array antenna," *Radio Sci.*, vol. 43, p. 1–9, 2008.
- [125] J. B. d. V. M. I. M. Z. V. N. a. N. R. J. Simons, "Design of a focal plane array system at cryogenic temperatures," in *Eu. Conf. on Antennas and Propagation (EuCAP)*, 2006.
- [126] J. F. B. J. a. K. W. R. Norrod, "Development of cryogenic phased array feeds for radio astronomy antennas," in *IEEE Int. Symp. on Phased Array Systems and Technology*, 2010.
- [127] K. F. W. J. L. J. W. D. J. J. R. F. a. R. D. N. B. D. Jeffs, "Signal processing for phased array feeds in radio astronomical telescopes," *IEEE J. Sel. Topics Signal Process.*, vol. 2, no. 5, p. 635–646, 2008.

- [128] N. Tessema, "Optical control of radio beam steering for broadband satellite communication," *Technische Universiteit Eindhoven, Doctoral thesis*, 2017.
- [129] Burla, M.; Marpaung, D. A. I.; Zhuang, L.; Rezaul Khan, M.; Leinse, A.; Beeker, W.; Hoekman, M.; Heideman, R. G.; Roeloffzen, C. G. H., "Multiwavelength-Integrated Optical Beamformer Based on Wavelength Division Multiplexing for 2-D Phased Array Antennas," *Journal of Lightwave Technology*, vol. 32, no. 20, pp. 3509- 3520, October 15, 2014.
- [130] Genderen P. van, "State-of-the-Art and Trends in Phased Array Radar," *Perspectives on Radio Astronomy: Technologies for Large Antenna Arrays*, Edited by A. B. Smolders and M. P. Haarlem, Published by ASTRON, p. 354, 2000.
- [131] Ivashina M. V., Kehn M.N.M., Kildal P.-S., Maaskant R., "Decoupling Efficiency of a Wideband Vivaldi Focal Plane Array Feeding a Reflector Antenna," *IEEE Transactions on Antennas and Propagation*, vol. 57, no. 2, p. 373 – 382, 2009.
- [132] Best S. R., Hanna D. L., "Performance and comparison of Fundamental Small-Antenna design," *IEEE Antenna and Propagation Magazine*, vol. 52, no. 1, 2010.
- [133] Chu, L.J., "Physical Limitations of Omni-Directional Antennas," *Journal of Applied Physics*, vol. 19, no. 12, pp. 1163-1175, 1948.
- [134] Sievenpiper D. F., et al., "Experimental Validation of Performance Limits and Design Guidelines for Small Antennas," *IEEE Transactions on Antennas and Propagation*, vol. 60, no. 1, pp. 8-19, 2012.
- [135] Tokan N. T., "Optimization of the UWB Feed Antenna Position in Reflector Applications," *International Journal of Antennas and Propagation*, no. Article ID 961818, 2014.
- [136] Kildal P.-S., "Combined E - and H - plane phase centers of antenna feeds," *IEEE Transactions on Antennas and Propagation*, vol. 31, no. 1, p. 199 – 202, 1983.
- [137] Smolders A.B., Arts M.J., "Wide-band antenna element with an integrated balun," in *Proceedings of the International IEEE Antennas & Propagation Symposium*, Atlanta, Georgia, 1998.
- [138] Tran D., Paraforou V., Yarovoy A., "A novel 1-decade super wideband UHF antenna for GPR and impulse radio applications," in *Proceedings of the 8th European Conference on Antennas and Propagation (EUCAP)*, The Hague, Netherlands, 2014.
- [139] CST GmbH, "www.cst.com".
- [140] Chen Y., Yang S., Nie Z., "A novel wideband antenna array with tightly coupled octagonal ring elements," *Progress In Electromagnetics Research*, vol. 124, p. 55– 70, 2012.
- [141] Cavallo D., "Connected array antennas: analysis and design," Doctoral degree 07-11-2011; the Eindhoven University of Technology, Department of Electrical Engineering, ISBN: 978-94-6191-035-6, 220 p.
- [142] M. Ng Mou Kehn and L. Shafai, "Characterization of dense focal plane array feed for parabolic reflectors in achieving closely overlapping or widely separated multiple beams," *Radio Sci.*, vol. 44(3), 25 June 2009.
- [143] Hayman, D.B., "Encircled power study of the focal plane field for estimating focal plane array size," *2005 IEEE Antennas and Propagation Society International Symposium*, vol. 3A, pp. 371-374, 2015.

- [144] Zimmerman, M.; Lee, S.W.; Houshmand, B.; Rahmat-Samii, Y.; Acosta, R., "A Comparison of Reflector Antenna Designs for Wide-Angle Scanning," in *ASA Technical Memorandum 101459. NASA Technology Workshop for Earth Science Geostationary Platforms*, Hampton, Virginia, USA, September 21-22, 1988.
- [145] Minnett, H. C.; Thomas, B. M., "Fields in the image space of symmetrical focusing reflectors," *Institution of electrical engineers*, vol. 115, no. 1419-1430, 1968.
- [146] Toso, G., "The Beauty of Multibeam Antennas," in *Proceedings of the 9th European Conference on Antennas and Propagation (EUCAP)*, Lisbon, Portugal, 12-17 April 2015.
- [147] Pelorossi, F.; Toso, G.; Angeletti, P., "On the Scanning Properties of Imaging Antennas Based on Dual Confocal Paraboloidal Reflectors," *Progress In Electromagnetics Research*, vol. 37, p. 95–107, 2014.
- [148] Morgan, S. "Some examples of generalized Cassegrainian and Gregorian antennas," *IEEE Transactions on Antennas and Propagation*, vol. 12(6), pp. 685 - 691, November 1964.
- [149] Granet C., "A simple procedure for the design of classical displaced-axis dual-reflector antennas using a set of geometric parameters," *IEEE Antennas and Propagation Magazine*, vol. 41, no. 6, pp. 64 - 72, 1999.
- [150] Dubok, A.; Al-Rawi, A.; Herben, M.H.A.J.; Gerini, G.; Smolders, A.B., "Wide-angle scanning reflector configuration for focal plane arrays," in *2016 IEEE International Symposium on Antennas and Propagation, APS/URSI*, Fajardo, Puerto Rico, 26 June - 1 July 2016.
- [151] Li T., "Study of the spherical reflector as wide-angle Scanning antennas," *IRE Trans. Antennas Propagat*, Vols. AP-7, no. 3, pp. 223-226, 1959.
- [152] Dubok, A.; Al-Rawi, A.; Tessema, N.; Tangdiongga, E.; Herben, M.H.A.J.; Gerini, G.; Smolders, A. B., "Double Reflector Configuration for Optimal Exposure of Wideband Focal Plane Arrays with Optical Beamforming," no. 10.1109/TAP.2017.2709620, 2017.
- [153] Guenther, A. H.; Pedrotti, L. S.; Roychoudhuri, C.; *Fundamentals of Photonics*, Waco, TX: Storrs, CT : University of Connecticut, 2000.
- [154] F. J. S. Moreira, J. R. Bergmann, "Classical axis-displaced dual-reflector antennas for omnidirectional coverage," *IEEE Transactions on Antennas and Propagation*, pp. 159-163, 2005.
- [155] B.S. Westcott, F.A. Stevens, F. Brickell, "GO synthesis of offset dual reflector," *IEE Proceedings H - Microwaves, Optics, and Antennas*, vol. 128, no. 1, pp. 11-18, 1981.
- [156] Born, M.; Wolf, E.; Bhatia, A. B.; Clemmow, P. C.; *Principles of Optics: Electromagnetic Theory of Propagation, Interference, and Diffraction of Light*, Cambridge University Press, 1999.
- [157] C. Dragone; M. J. Gans, "Imaging reflector arrangements to form a scanning beam using a small array," *The Bell System Technical Journal*, vol. 58, no. 2, p. 501 – 515, 1979.
- [158] Hay, S.G.; "A double-edge-diffraction Gaussian-series method for efficient physical optics analysis of dual-shaped-reflector antennas," *IEEE Transactions on Antennas and Propagation*, vol. 53, no. 8, pp. 2597 - 2610, 08 August 2005.

- [159] Mrstik A. and Smith P., "Scanning capabilities of large parabolic cylinder reflector antennas with phased-array feed," *IEEE Transactions on Antennas and Propagation*, vol. 29, no. 3, pp. 455 - 462, 1981.
- [160] C. Cappellin et al., "Novel multi-beam radiometers for accurate ocean surveillance," in *8th Eur. Conf. Antennas and Propagation*, The Hague, 2014, pp. 3531–3535.
- [161] Westcott B.S., Stevens F.A., Brickell F., "GO synthesis of offset dual reflector," *IEE Proceedings H - Microwaves, Optics, and Antennas*, vol. 128, no. 1, pp. 11-18, 1981.
- [162] Dubok, A; Al-Rawi, A; Tessema, N; Tangdiongga, E; Herben, M.H.A.J; Gerini, G; Smolders, A. B., "Double Reflector Configuration for Optimal Exposure of Wideband Focal Plane Arrays with Optical Beamforming," *IEEE Transactions on Antennas & Propagation*, no. 10.1109/TAP.2017.2709620, 2017.
- [163] Dragone C.; Gans M. J., "Imaging reflector arrangements to form a scanning beam using a small array," *The Bell System Technical Journal*, vol. 58, no. 2, p. 501 – 515, 1979.
- [164] Hayman, D.B.; Bird, T.S.; Esselle, K.P., "Experimental Demonstration of Focal Plane Array Beamforming in a Prototype Radiotelescope," *IEEE Transactions on Antennas and Propagation*, vol. 58, no. 6, pp. 1922 - 1934, 2010.
- [165] Dubok, A; Al-Rawi, A; Herben, M.H.A.J; Smolders, A. B, "Fundamental challenges for wideband antenna elements in focal-plane arrays," in *The 9th European Conference on Antennas and Propagation*, Lisbon Portugal, 2015.
- [166] Gomez-Tagle J., "Broadband characterization of the active reflection coefficient of finite-sized phased array microstrip antennas," in *Phased Array Systems and Technology, 2000. Proceedings. 2000 IEEE International Conference*, Dana Point, CA, 2000.
- [167] MATLAB Software, <http://nl.mathworks.com/products/matlab>.
- [168] Manteghi M., "Broadband characterization of the total active reflection coefficient of multiport antennas," in *Antennas and Propagation Society International Symposium*, Columbus, OH, USA, 2003.
- [169] Smolders A.B., Johannsen U., "Axial ratio enhancement for circularly-polarized millimeter-wave phased-arrays using a sequential rotation technique," *IEEE Transactions on Antennas and Propagation*, vol. 59, no. 9, pp. 3465-3469, 2011.
- [170] Hayman, D.B., "Encircled power study of the focal plane field for estimating focal plane array size," *2005 IEEE Antennas and Propagation Society International Symposium*, vol. 3A, pp. 371-374, 2015.
- [171] Dubok, A.; Al-Rawi, A.; Gerini, G.; Smolders, A.B., "Extreme scanning double shaped-reflector antenna with multiple interactions for focal plane array applications," *IEEE Transactions on Antennas and Propagation*, vol. 68, no. 7, pp. 5686-5690, 2020.
- [172] Dubok, A.; Al-Rawi, A.; Herben, M.H.A.J.; Smolders, A.B., "Wideband focal plane connected array," in *10th European Conference on Antennas and Propagation, EuCAP 2016*, Davos, Switzerland, 2016.
- [173] Smolders A.B., Hampson G., "Deterministic RF nulling in phased arrays for the next generation radio telescopes," *IEEE Antennas and Propagation Magazine*, 2002

- [174] V. N. A. -. Keysight, "<https://www.keysight.com/nl/en/assets/7018-01698/technical-overviews/5989-7603.pdf>," [Online]".
- [175] I. W. B. a. S. B. Rolles, "Calibration-measurement unit for the automation of vector network analyzer measurements," *Adv. Radio Sci.*, vol. 6, p. 27–30.
- [176] Rohrdantz B., Jaschke T., Reuschel T., Radziejewski S., Sieganschin A., Jacob A. F., "An Electronically Scannable Reflector Antenna Using a Planar Active Array Feed at Ka-Band," *IEEE Transactions on Microwave Theory and Techniques*, vol. 65, no. 5, pp. 1650-1661, 2017.
- [177] Mou Kehn M. Ng, Shafai L., "Characterization of dense focal plane array feed for parabolic reflectors in achieving closely overlapping or widely separated multiple beams," *Radio Sci.*, vol. 44, no. 3, 2009.
- [178] Rogolin R. et al., "Scalable synchronization and reciprocity calibration for distributed multiuser MIMO," *IEEE Trans. Wireless Commun.*, vol. 13, no. 4, pp. 1815-1831, 2014.
- [179] Han X. et al., "A tunable optical waveguide ring resonator for microwave photonic filtering," in *IEEE International Topical Meeting on Microwave Photonics (MWP)*, Alexandria, VA, 2013, 2013.
- [180] Bogaerts W., Heyn P. De, Vaerenbergh T. van, Vos K. De, Kumar S., "Silicon microring resonators," *Laser & Photon.*, vol. 6, p. 47–73, 2012.
- [181] Tessema N.M., Cao Z., Zantvoort J.H.C. van, Mekonnen K.A., Trinidad A.M., Tangdionga E., Smolders A.B., Koonen A.M.J., "K-band RF Multi-Beamformer Using Si<sub>3</sub>N<sub>4</sub> TTD for Home-Satellite," in *Optical Fiber Communication Conference, OSA Technical Digest (Optical Society of America)*, (online), 2017.
- [182] Gao H., Ma Q., Leenaerts D.M.W., and Mahmoudi R., "A 48-61 GHz LNA in 40-nm CMOS with 3.6 dB minimum NF employing a metal slotting method," in *IEEE Radio Frequency Integrated Circuits Symposium*, San Francisco, California, USA, 2016.
- [183] Ma Q., Leenaerts D., and Mahmoudi R., "A 30GHz 2dB NF low noise amplifier for Ka-band applications," in *IEEE Radio Frequency Integrated Circuits Symposium*, Montreal, QC, 2012.
- [184] Chen Z., Gao H., Leenaerts D.M.W., Milosevic D., and Baltus P.G.M., "A 16–43 GHz low-noise amplifier with 2.5–4.0 dB noise figure," in *IEEE Asian Solid-State Circuits Conference (A-SSCC)*, 2016.
- [185] Min B.W., Rebeiz G.M., "Ka-Band SiGe HBT Low Noise Amplifier Design for Simultaneous Noise and Input Power Matching," *IEEE Microwave and Wireless Components Letters*, vol. 17, no. 12, pp. 891- 893, 2007.
- [186] Deixler P. et al., "QUBiC4X: An  $fT/f_{max} = 130/140$ GHz SiGe: CBiCMOS manufacturing technology with elite passives for emerging microwave applications," in *Bipolar/BiCMOS Circuits and Technology, Proceedings of the 2004 Meeting*, 2004.
- [187] Ma Q., Leenaerts D.M.W., Baltus P.G.M., "Silicon-Based True-TimeDelay Phased-Array Front-Ends at Ka-Band," *IEEE Transactions on Microwave Theory and Techniques*, vol. 63, no. 9, pp. 2942-2952, 2015.
- [188] Tessema, N.M., Cao, Z., van Zantvoort, J.H.C., Dubok, A., Tangdionga, E., Smolders, A.B. & Koonen, A.M.J., "Radio beam-steering via tunable Si<sub>3</sub>N<sub>4</sub> optical

- delays for multi-Gbps K-band satellite communication," in *Optical Fiber Communications and Exhibition Conference (OFC)*, Anaheim, California, 2016.
- [189] Tessema, N.M., Cao, Z., van Zantvoort, J.H.C., Mekonnen, K.A., Dubok, A., Tangdiongga, E., Smolders, A.B. & Koonen, A.M.J., "A tunable Si<sub>3</sub>N<sub>4</sub> integrated true time delay circuit for optically-controlled K-band radio beamformer in satellite communication," *Journal of Lightwave Technology*, vol. 34, no. 20, 2016.
- [190] Tessema, N.M.; Cao, Z.; Dubok, A.; Tangdiongga, E.; Smolders, A.B.; Koonen, A.M.J., "A Si<sub>3</sub>N<sub>4</sub> PIC for optically controlled 2D radio beamforming in satellite communications," in *MWP 2015: 2015 International Topical meeting on Microwave Photonics (MWP)*, Paphos, Cyprus, 26-29 October, 2015.
- [191] Trinidad, A.M., Tessema, N., Cao, Z., van Zantvoort, J.H.C., Dubok, A., Al-Rawi, A.N.H., Tangdiongga, E., Smolders, A.B. & Koonen, A.M.J., "Optical beamformer for K-band smart antenna systems," in *Optical Fiber Communications Conference and Exposition, OFC 2018 - Proceedings*, 2018.
- [192] Westcott B.S., Stevens F.A., Brickell F., "GO synthesis of offset dual reflector," *IEEE Proceedings H - Microwaves, Optics, and Antennas*, vol. 128, no. 1, pp. 11-18, 1981.
- [193] Hay, S.G., "A double-edge-diffraction Gaussian-series method for efficient physical optics analysis of dual-shaped-reflector antennas," *IEEE Transactions on Antennas and Propagation*, vol. 53, no. 8, pp. 2597 - 2610, 08 August 2005.
- [194] H. D.B., "Encircled power study of the focal plane field for estimating focal plane array size," *IEEE Antennas and Propagation Society International Symposium*, vol. 3, no. A, pp. 371-374, 2005.
- [195] Born, M.; Wolf, E.; Bhatia, A. B.; Clemmow, P. C., *Principles of Optics: Electromagnetic Theory of Propagation, Interference, and Diffraction of Light*, Cambridge University Press, 1999.
- [196] Lee, Min & Song, Ickho & Seokho, Yoon & Park, So, "Evaluation of directivity for planar antenna arrays," *Antennas and Propagation Magazine, IEEE*, vol. 42, pp. 64 - 67, 2000.
- [197] Puskely J., Aslan Y., Roederer A., Yarovoy A., "SIW Based Antenna Array with Power Equalization in Elevation Plane for 5G Base Stations," in *12th European Conference on Antennas and Propagation (EuCAP 2018)*, 2018.
- [198] Ferendeci, Altan M., "Smart electronic phase control for phased array antennas," in *Aerospace and Electronics Conference (NAECON)*, Fairborn, OH, USA, 14-16 July 2010.
- [199] S. J. B. a. W. A. Imbriale, "Array feed synthesis for correction of reflector distortion and vernier beamsteering," *IEEE Trans. Antennas Propag*, vol. 36, no. 10, p. 1351–1358, 1988.



# LIST OF PUBLICATIONS

---

## Patents

- [P1] Dubok A., Al-Rawi, A., Smolders, A.B., "Extreme scanning focal-plane arrays using a double-reflector concept with uniform array illumination", Issued Sep 12, 2019, US PCT/EP2019/055153.
- [P2] Al-Rawi, A., Dubok A., Herben, M.H.A.J., Smolders, A.B., "High-efficiency e-band antenna system", Issued Sep 12, 2019, US PCT/EP2019/055760.

## Journal Papers

### *Ph.D. based papers*

- [J1] Dubok, A., Smolders, A.B., "Wideband Phased-Array Feeds for Focal Plane Arrays: Design and Implementation," submitted to IEEE Transactions on Antennas and Propagation, 2022.
- [J2] Dubok, A., Smolders, A.B., "Focal-Plane Arrays with Improved Scan Capabilities," IEEE Transactions on Antennas and Propagation (Early Access), 2022.
- [J3] Dubok, A.; Al-Rawi, A.; Gerini, G.; Smolders, A.B., "Extreme scanning double shaped-reflector antenna with multiple interactions for focal plane array applications," IEEE Transactions on Antennas and Propagation, vol. 68, no. 7, pp. 5686-5690, 2020.
- [J4] Dubok A., Al-Rawi A., Gerini G., Smolders A. B., "Reflector Synthesis for Wide-Scanning Focal Plane Arrays," IEEE Transactions on Antennas and Propagation, vol. 67, no. 3, 2019.
- [J5] Smolders, A.B., Dubok, A., Tessema, N.M., Chen, Zhe, Al-Rawi, A.N.H., Johannsen, U., Bressner, T.A.H., Milosevic, D., Gao, H., Tangdiongga, E., Gerini, G., Baltus, P.G.M., Geurts, Marcel & Koonen, A.M.J., "Building 5G millimeter-wave wireless infrastructure: wide-scan focal plane arrays with broadband optical beamforming," IEEE Antennas and Propagation Magazine, 2018.
- [J6] Dubok, A; Al-Rawi, A; Tessema, N; Tangdiongga, E; Herben, M.H.A.J; Gerini, G; Smolders, A. B; "Double Reflector Configuration for Optimal Exposure of Wideband Focal Plane Arrays with Optical Beamforming," no. 10.1109/TAP.2017.2709620, 2017.

*Other papers*

- [J7] Tessema, N.M., Cao, Z., van Zantvoort, J.H.C., Mekonnen, K.A., Dubok, A., Tangdiongga, E., Smolders, A.B. & Koonen, A.M.J., "A tunable Si<sub>3</sub>N<sub>4</sub> integrated true time delay circuit for optically-controlled K-band radio beamformer in satellite communication," *Journal of Lightwave Technology*, vol. 34, no. 20, 2016.
- [J8] Dubok, A. & Smolders, A. B., "Miniaturization of robust UHF RFID antennas for use on perishable goods and human bodies", *IEEE Antennas and Wireless Propagation Letters*. 13, 1, pp. 1321-1324, 2014.

**Publications in peer-reviewed conferences***Ph.D. based papers*

- [C1] Dubok, A.; Al-Rawi, A.; Herben, M.H.A.J.; Gerini, G.; Smolders, A.B.; "Wide-angle scanning reflector configuration for focal plane arrays," in 2016 IEEE International Symposium on Antennas and Propagation, APS/URSI, Fajardo, Puerto Rico, 26 June - 1 July 2016.
- [C2] Dubok, A.; Al-Rawi, A.; Herben, M.H.A.J.; Smolders, A.B., "Wideband focal plane connected array", 10th European Conference on Antennas and Propagation, EuCAP 2016, Davos, Switzerland, 2016.
- [C3] Dubok A., Al-Rawi A., Herben M., Smolders A. B., "Fundamental challenges for wideband antenna elements in focal-plane arrays," in The 9th European Conference on Antennas and Propagation, Lisbon Portugal, 2015.

*Other papers*

- [C4] Narayanan, S., Al-Rawi, A., Dubok, A., de Hon, B. P. & Smolders, A. B., "Gain-maximization of FPA-fed reflectors by means of linear regression", 2019 IEEE International Symposium on Antennas and Propagation and USNC-URSI Radio Science Meeting, pp. 469-470, Jul 2019.
- [C5] Trinidad, A.M., Tessema, N., Cao, Z., van Zantvoort, J.H.C., Dubok, A., Al-Rawi, A.N.H., Tangdiongga, E., Smolders, A.B. & Koonen, A.M.J., "Optical beamformer for K-band smart antenna systems," in Optical Fiber Communications Conference and Exposition, OFC 2018 - Proceedings, 2018.
- [C6] Al-Rawi, A; Dubok, A; Geluk, S.J; de Hon, B.P; Herben, M.H.A.J.; Smolders, A.B.;, "Increasing the EIRP by using FPA-fed reflector antennas," in IEEE International Symposium on Antennas and Propagation (APSURSI), Fajardo, Puerto Rico, 2016.
- [C7] Tessema, N.M., Cao, Z., van Zantvoort, J.H.C., Dubok, A., Tangdiongga, E., Smolders, A.B. & Koonen, A.M.J., "Radio beam-steering via tunable Si<sub>3</sub>N<sub>4</sub> optical delays for multi-Gbps K-band satellite communication," in Optical Fiber Communications and Exhibition Conference (OFC), Anaheim, California, 2016.
- [C8] Al-Rawi, A., Dubok, A., Geluk, S.J., Herben, M.H.A.J. & Smolders, A.B., "A comparative study on the parabolic and spherical FPA-fed reflector antenna," in

10th European Conference on Antennas and Propagation, EuCAP 2016, Davos, Switzerland, 2016.

- [C9] Tessema, N.M.; Cao, Z.; Dubok, A.; Tangdiongga, E.; Smolders, A.B.; Koonen, A.M.J.; "A Si<sub>3</sub>N<sub>4</sub> PIC for optically controlled 2D radio beamforming in satellite communications," in MWP 2015: 2015 International Topical meeting on Microwave Photonics (MWP), Paphos, Cyprus, 26-29 October, 2015.
- [C10] Al-Rawi, A.; Dubok, A.; Herben, M.H.A.J.; Smolders, A.B.; "Point-to-point Radio Link Variation at E-band and Its Effect on Antenna Design," in Progress In Electromagnetics Research Symposium Proceedings, Prague, Czech Republic, July 2015.
- [C11] Dubok, A. & Smolders, A. B., "Increased operational range for implantable UHF RFID antennas", Proceedings of the 8th European Conference on Antennas and Propagation (EuCAP 2014), 6-11 April 2014, The Hague, The Netherlands, pp. 1749-1753, 2014.
- [C12] Dubok, A., Coenen, T. J., Zamanifekri, A. & Smolders, A. B., "Robust UHF RFID antennas in complex environments", Proceedings of the 7th European Conference on Antennas and Propagation (EUCAP), 8-12 April 2013, Gothenburg, Sweden. Piscataway: Institute of Electrical and Electronics Engineers, pp. 1636-1640, 2013.



# ACKNOWLEDGMENTS

---

At last, my Ph.D. path is almost over. It has been a long way, sometimes pleasant, sometimes tough in the 10 years, which anyway passed quite fast. Nevertheless, it has been a nice journey together with a lot of friends and colleagues who helped and supported me along the way, for whom I am really grateful.

First of all, I want to thank all my colleagues from the EM group for the great time I had during my Ph.D. In particular, I would like to thank my first promotor Bart Smolders for providing me with lots of freedom for creativity and all the crazy ideas touched on within the project, and of course for spending a lot of time reading and verifying those ideas in my manuscripts.

Furthermore, I wish to thank my second promotor, Giampiero Gerini for active support during the project, as well as the other members of my Ph.D. committee, i.e., Marianna Ivashina, A.M.J. (Ton) Koonen, Peter G.M. Baltus, and Mark Bentum.

I wish to thank all company members assigned to the FREEBEAM project for professional collaboration throughout the whole project development, to Kave Kianush (Catena), Corne Stoffels (Thales), Gie-Han Tan (ESO), Peter de Maagt (ESA), Paul van Dijk and Chris Roeloffzen (SATRAX), Frank Karelse (STW), Jeffrey Vermeer (TNO). Special thanks to Wim van Cappellen and Albert van Duin (ASTRON) for help with PCB prototyping and to Domine Leenaerts and Marcel Geurts (NXP) for help with SMD elements soldering, and, in addition, to NWO-TTW for the project financial support. There are also special thanks to Erwin Dekkers, John Meulendijks, and Peter Minten for the reflector manufacturing.

Here, are special acknowledgments to Ad Reniers for support during measurements and for sharing life wisdom during office discussions. Special gratitude to Suzanne Kuijlaars for all the administrative things she did in the past years. Additionally, I want to thank Anton Tijhuis, Huib Visser, Bas P. de Hon, Martijn van Beurden, Matti Herben, Rob Maaskant, Peter Smulders, Ulf Johannsen, Rob Mestrom, Anne Roc'h, Rainier van Dommele, and many others.

Of course, I want to thank my FREEBEAM project colleagues Zhe Chen and Netsanet Tessema for productive collaboration within the whole project. Big gratitude to all my friends and office mates, with whom we had not only a lot of work to do but a lot of entertainment as well outside the university, to Ali Al-Rawi, Ronis Maximidis, Bedilu Adela, Qiang Liu, and Subin Narayanan. Also, I like to thank my EM group colleagues, Alhassan Aljarosha, Teun van den Biggelaar, Radovan Bojanic, Thomas Bressner, Sander Bronckers, Roeland Dilz, Amr Elsakka, Sander Floris, Sander Geluk, Lu Huang, Adedayo Omisakin, Elles Raaijmakers, Maarten van Rossum, Rabia Syeda, Dian Tresnawan, Ellaheh Barzegar, and many others.

Special thanks to my Philips colleagues who supported me in not stopping the Ph.D. work

and finalizing the thesis. Especially to Wouter Numan, Flip Reijnen, Roberto Cairo, and Guy Dohmen, to Timo Paardenkooper for highlighting the value of education, and to many others, and Philips overall for constant wish to move further.

Special gratitude to Leon Kaufmann and Rian van Gaalen for a chance to be a PDEng student in TU/e. Thanks to you, I ended up and have been in the Netherlands and now here already for more than 10 years.

Big gratitude to all my friends, to Sultan Jumayev, Olga Kupriyanova, Oleksii Rudenko, Yuliya Pestserava, Satoru Sakai, Manolis Chrysillos, Oleg Matveichuk, Lena Filatova, Natsuru Sakai, Giulia De Martino, Massimo Michelini, Svetlana Marmutova.

Last, but certainly not least, I wish to thank my wife and parents, who always supported me no matter what.

# CURRICULUM VITAE

---

Aleksei Dubok was born on 22-05-1987 in Pskov, Russia.

After finishing the B.Sc. degree (cum laude) in 2008 at Saint Petersburg State Electrotechnical University in Saint Petersburg, he studied the M.Sc. at the same university. In 2010 he graduated (cum laude) within the Electrical Engineering faculty on the microwave, optical, and digital means of telecommunications. He studied the second M.Sc. at the Lappeenranta University of Technology in Lappeenranta Finland. In 2011 he graduated within the Electrical Engineering faculty on power electronics. After that, he studied the PDEng (Professional Doctorate in Engineering) at the Eindhoven University of Technology in Eindhoven, The Netherlands, and graduated in 2013. From 2013 he started a Ph.D. project at the same university of which the results are presented in this dissertation.

He has been employed from 2007 till 2010 as an Engineer-Developer of radio communications systems at TELROS integration in Saint Petersburg. Since 2017 he is employed at Philips in Best, The Netherlands as an RF Hardware Designer in the field of Magnetic resonance imaging.